

An Investigation on the Structure/Property Relationships of  
Solid State Welding Processes in a Titanium Matrix Composite  
Alloy (Ti6Al4V + 10 wt.% of TiC)

Von der Fakultät für Ingenieurwissenschaften, Abteilung Maschinenbau  
der  
Universität Duisburg-Essen

zur Erlangung des akademischen Grades

DOKTOR-INGENIEUR

genehmigte Dissertation

von

Antonio Augusto Monaco da Silva

aus

Porto Alegre – Brasilien

Referent: Univ.-Prof. Dr.-Ing. Alfons Fischer  
Korreferent: Univ.-Prof. Dr.-Ing. Karl-Heinz Schwalbe  
Tag der mündlichen Prüfung: 26. Januar 2006

**An Investigation on the Structure/Property Relationships of Solid State Welding Processes in a Titanium Matrix Composite Alloy (Ti6Al4V + 10 wt.% of TiC)**

**ABSTRACT**

TiC particulate reinforced Ti6Al4V metal matrix composites (Ti6Al4V+10 wt.% TiC) have high strength-to-weight ratio and good high temperature properties. Although this class of composite clearly perform better than the matrix alloy itself, the successful application of such particulate-reinforced materials depends on the availability of proven joining techniques that can produce high quality joints. Due to the high chemical reactivity of titanium that may lead to a chemical interaction with the reinforcing material a poor fusion welding performance is commonly observed in these materials making solid-state diffusion bonding and rotary friction welding potential processes to produce complex structural components.

Despite recent advances in processing and manufacturing technology of Ti6Al4V+10 wt.% TiC there is still a lack of understanding in the solid state joining possibilities and its microstructural changes and mechanical properties. The main objective of this work is to investigate and analyse the feasibility of joining the particulate-reinforced composite alloy by rotary friction welding and diffusion bonding processes. It is also aimed the determination and establishment of the microstructure/properties relationships of the resultant welds as well as to investigate the bonding mechanisms and understand the weldability aspects of friction welded and diffusion bonded Ti6Al4V+10 wt.% TiC. Metallurgical characterization of both base material and welded joints was performed using Optical and Scanning Electron Microscope. Mechanical assessment was accomplished using tensile, microflat tensile and fracture toughness tests.

A microstructural examination of the friction-welded joints has revealed two distinct welding zones (transformed and recrystallized zone as well as heat affected zone); while no metallurgical transformation has occurred in the diffusion bonding process. In the case of rotary friction welding best results were associated with low rotational speed and low friction pressure; while in the diffusion bonding process the best results were associated with a bonding temperature and pressure of 1000°C and 5MPa together with bonding times ranging from 35 and 60 minutes.

## **Untersuchung des Zusammenhangs von Struktur und Eigenschaften von in fester Phase geschweißten Titan-Matrix-Verbundwerkstoffen (Ti6Al4V + 10 Gew.-% TiC)**

### **ZUSAMMENFASSUNG**

Die mit TiC verstärkten Ti6Al4V metallischen Verbundwerkstoffe (Ti6Al4V+10 Gew.-% TiC) weisen eine hervorragende gewichtsspezifische Festigkeit, welche auch bei höheren Temperaturen erhalten bleibt, auf. Obwohl die Eigenschaften der Verbundwerkstoffe im Vergleich zu denen der Basislegierung deutlich verbessert sind, hängt die erfolgreiche industrielle Einführung dieser partikelverstärkten Werkstoffe hauptsächlich von der Wahl bzw. Entwicklung eines geeigneten Fügeverfahrens ab. Dieses Verfahren muss in der Lage sein qualitativ hochwertige Verbindungen erzeugen zu können. Aufgrund der ausgeprägten chemischen Reaktionsfähigkeit von Titan, die zu einer unerwünschten Wechselwirkung mit dem Verstärkungsmaterialien führen kann, ist die Leistungsfähigkeit von Schmelzschweißverfahren in qualitativer Hinsicht nicht ausreichend. Daher eignen sich Fügeverfahren in fester Phase wie das Diffusionsschweißen und das Rotationsreibschweißen zur Herstellung von komplexen Komponenten.

Trotz der jüngsten Fortschritte in der Bearbeitungs- und Produktionstechnologie von Ti6Al4V+10 Gew.-% TiC ist das Schweißen solcher Materialien mit Fügeverfahren in fester Phase sowie die damit verbundene Veränderung von Mikrostruktur und mechanischen Eigenschaften nicht ausreichend untersucht worden. Die Untersuchung und Analyse von mit Rotationsreib- und Diffusionsschweißverfahren gefügten Verbundwerkstoffen steht daher im Fokus dieser Arbeit. Die Darstellung der Wechselbeziehung zwischen der ausgebildeten Mikrostruktur und den mechanischen Eigenschaften der geschweißten Verbindungen ist ein weiteres Ziel. Ebenso erfolgt die Untersuchung der Fügemechanismen und Aspekte der Schweißbarkeit von reib- und diffusionsgeschweißten Ti6Al4V+10 Gew.-% TiC im Rahmen dieser Arbeit.

Die metallurgische Charakterisierung des Grundwerkstoffes und der Schweißverbindung erfolgte sowohl mit Hilfe der optischen als auch der Rasterelektronenmikroskopie. Zur Beurteilung und Bewertung der mechanischen Eigenschaften wurden Zug-, Mikroflachzug- und Bruchzähigkeitsversuche durchgeführt.

Die mikrostrukturelle Untersuchung der reibgeschweißten Verbindungen zeigten zwei ausgeprägte Zonen in der Schweißnaht. Zum einen die transformierte und rekristallisierte Zone und zum anderen die Wärmeeinflusszone. Die diffusionsgeschweißten Verbindungen zeigten keine metallurgischen Transformationen.

## ACKNOWLEDGEMENTS

I would like to thank Prof. Dr. A. Fischer, Prof. Dr. K.-H Schwalbe and Dr. J.F. dos Santos for the supervision of this work and valuable discussions.

I would like also to thank GKSS Forschungszentrum GmbH for giving me the opportunity to develop and perform this work and in particular to the Head of the Joining Technology Group, Dr. Jorge Fernandez dos Santos who has always supported my work with his valuable discussions and suggestions.

I would like to acknowledge Dr. Celso Roberto Ribeiro for his valuable contributions to the development of this work and for his support during the accomplishment of this investigation. I would like also to thank a number of colleagues that have helped me during this work especially Dr. Axel Mayer for his valuable contributions and helping as well as the other colleagues from the Joining Technology Group (GKSS – Germany) and from the Laboratório de Metalurgia Física (LAMEF/UFRGS – Brasil).

Many thanks go to Prof. Telmo Roberto Strohaecker and Prof. Afonso Reguly from LAMEF/UFRGS for their continuous support and valuable discussions as well for giving me the opportunity of starting my academic research experience in LAMEF/UFRGS.

I am also in debt with Petra Fischer of the GKSS metallographic laboratory, Stefan Riekher and Hans Mackel from the WMF group for their support in the mechanical testing as well as Karl-Heinz Bohm for performing the diffusion bonding process. In addition, I am grateful to Dave Dent and Gordon Blakemore from Circle Technical Services for the possibility of using their welding system throughout the whole work. I am also in debt to Susan Abkowitz from Dynamet Technology Inc. for the donation of the composite base material.

Special thanks goes to my Brazilian family, Marcos, Cecilia, Fernanda, Wilma, Lorena, Tanane, Marco, Rafa and Tati as well as to my Spanish family, Eva, Mila, Javier, Maite and Liher for their great support during these years.



---

**CONTENTS**

<b>ABSTRACT .....</b>	<b>II</b>
<b>ZUSAMENFASSUNG .....</b>	<b>III</b>
<b>ACKNOWLEDGEMENTS.....</b>	<b>IV</b>
<b>1 INTRODUCTION .....</b>	<b>1</b>
<b>2 STATE OF ART .....</b>	<b>5</b>
<b>2.1 General Metal Characteristics .....</b>	<b>5</b>
<b>2.2 Phases and Structures of Titanium and its Alloys .....</b>	<b>5</b>
2.2.1 Unalloyed or Commercially Pure (CP) Titanium .....	6
2.2.2 Alpha Alloys .....	6
2.2.3 Alpha-Beta Alloys .....	7
2.2.4 Beta Alloys .....	7
<b>2.3 Alpha + Beta Alloy Ti6Al4V .....</b>	<b>8</b>
<b>2.4 Advanced Titanium Alloys.....</b>	<b>9</b>
2.4.1 Metal Matrix Composites (MMCs).....	10
2.4.2 Titanium Matrix Composites (TMCs) .....	12
2.4.2.1 Discontinuously Reinforced Titanium Matrix Composite (Ti6Al4V+TiC particles).....	15
2.4.2.2 Extent of Reaction between TiC Particles and Ti6Al4V Matrix .....	18
2.4.2.3 Fracture Behaviour and Failure Mechanisms of Particle Reinforced MMCs.....	20
2.4.2.4 Fracture Toughness Behaviour of Particle Reinforced MMCs .....	24
<b>2.5 Solid State Welding Processes.....</b>	<b>27</b>
2.5.1 Friction Welding (FW) .....	28
2.5.1.1 Rotational Speed.....	35
2.5.1.2 Pressure (Forging and Friction).....	35
2.5.1.3 Heating Time .....	37
2.5.1.4 Burn-Off.....	37
2.5.2 Diffusion Bonding .....	38
2.5.2.1 Microasperity Deformation .....	41
2.5.2.2 Diffusion-Controlled Mass Transport.....	42
2.5.2.3 Interface Migration .....	43
2.5.2.4 Influence of the Diffusion Bonding Parameters on the Process .....	43
2.5.3 Joining of MMCs and TMCs .....	45
2.5.3.1 Friction Welding of MMCs and TMCs .....	47
2.5.3.1.1 Particle Fracture Phenomenon in Particulate-Reinforced Friction Welding.....	48
2.5.3.1.2 Dynamic Recrystallization.....	50
2.5.3.2 Diffusion Bonding of MMCs and TMCs.....	50

---

<b>3</b>	<b>EXPERIMENTAL PROCEDURE</b>	<b>53</b>
3.1	Methodology	53
3.2	Titanium Matrix Composite - TMC (Ti6Al4V+10 wt.% of TiC)	53
3.3	Friction Welding Process	54
3.3.1	Friction Welding Equipment	54
3.3.2	Friction Welding Studs Configuration	56
3.3.3	Friction Welding Parameter Matrices	56
3.4	Diffusion Bonding Process	58
3.4.1	Diffusion Bonding Equipment and Specimens Configuration	58
3.4.2	Diffusion Bonding Parameter Matrix	59
3.5	Non-Destructive Tests (NDT)	60
3.6	Metallurgical Characterization	60
3.6.1	Macrostructural Characterization	60
3.6.2	Microstructural Characterization	61
3.6.3	Optical Microscopy (OM)	61
3.6.4	Scanning Electron Microscopy (SEM)	61
3.6.5	Image Analysis	62
3.6.6	Determination of $\beta$ Grain Size	62
3.7	Mechanical Characterization	63
3.7.1	Microhardness	63
3.7.2	Tensile Test	63
3.7.3	Microflat Tensile Test	66
3.7.4	Fracture Toughness Testing ( $K_{IC}$ )	67
<b>4</b>	<b>RESULTS AND DISCUSSION</b>	<b>69</b>
4.1	Metallurgical and Mechanical Characterisation of the Ti6Al4V+10 wt.% TiC Base Material Composite Alloy	69
4.1.1	Metallurgical Characterisation - Ti6Al4V+10 wt.% TiC	69
4.1.1.1	Image Analysis of the Base Material	73
4.1.2	Mechanical Characterisation - Ti6Al4V+10 wt.% TiC	75
4.1.2.1	Microhardness	75
4.1.2.2	Tensile Tests	76
4.1.2.2.1	Room Temperature Tensile Tests	76
4.1.2.2.1.1	Fracture Surface Analysis of the Tensile Specimens	77
4.1.2.2.2	High Temperature Tensile Tests	79
4.1.2.3	Fracture Toughness Tests	81
4.1.2.3.1	Fracture Surface Analysis of the Fracture Toughness Specimens	87

---

<b>4.2 Metallurgical and Mechanical Characterisation of the Ti6Al4V+10 wt.% TiC Friction</b>	
<b>Welded Joints.....</b>	<b>88</b>
4.2.1 Friction Welding Process.....	88
4.2.2 Metallurgical Characterisation of the Friction Welded Joints .....	94
4.2.2.1 Image Analysis of the Friction Welded Joints.....	103
4.2.3 Mechanical Characterisation of the Friction Welded Joints .....	106
4.2.3.1 Microhardness .....	106
4.2.3.2 Tensile Tests.....	107
4.2.3.2.1 Longitudinal Section Analysis of the Fracture Surface of the Tensile Specimens	109
4.2.3.2.2 Fracture Surface Analysis of the Tensile Specimens.....	111
4.2.3.3 Fracture Toughness Tests .....	115
4.2.3.3.1 Modelling the Fracture Toughness of the Particulate-Reinforced Material (Base Material and Friction Welded joints).....	122
4.2.3.4 Fracture Surface Analysis of the Fracture Toughness Specimens.....	126
<b>4.3 Metallurgical and Mechanical Characterisation of the Ti6Al4V+10 wt.% TiC Diffusion</b>	
<b>Bonded Joints.....</b>	<b>129</b>
4.3.1 Diffusion Bonding .....	129
4.3.2 Metallurgical Characterisation of the Diffusion Bonded Joints.....	130
4.3.3 Metallurgical Characterisation of the Diffusion Bonded Joints.....	134
4.3.3.1 Microhardness .....	134
4.3.3.2 Microflat Tensile Tests.....	135
<b>5 CONCLUSIONS.....</b>	<b>140</b>
<b>6 SUGGESTIONS FOR FUTURE WORK.....</b>	<b>142</b>
<b>7 REFERENCES .....</b>	<b>143</b>
<b>LIST OF FIGURES .....</b>	<b>159</b>
<b>LIST OF TABLES .....</b>	<b>164</b>
<b>CURRICULUM VITAE – ANTONIO AUGUSTO MONACO DA SILVA .....</b>	<b>166</b>

## 1 INTRODUCTION

Materials and materials processing have entered a new era. Where metals and alloys once dominated, advanced materials, such as polymers, ceramics, intermetallic compounds and composites with polymeric, metallic, ceramic and intermetallic matrices have entered to extend applications. Titanium matrix composites (TMCs), such as the particle reinforced Ti6Al4V+10 wt.% TiC, can be included in this new era opening new perspectives for applications such as sporting goods and aerospace structures. The use of advanced materials is very attractive to material scientists and high-technology industries, usually for specific applications in which their special properties can be tailored and used to great advantage exploiting the desirable properties and minimizing those less desirable features.

Advanced materials require novel joining techniques; therefore, developments in new structural materials research should be conducted in parallel with that into weldability aspects. Among the modern joining processes used in engineering, the solid-state techniques such as diffusion bonding and rotary friction welding are intensively used in materials sensitive to fusion welding processes. Solid-state joining processes operate without melting of the base metal, usually by the application of high pressure, thus limiting the extent of metallurgical reactions that may cause welding defects such as cracking, porosity or formation of intermetallic compounds. Bonding is achieved by the introduction of mechanical, electrical or thermal energy and/or diffusion. Nowadays these processes play an important role in key technology industries helping to develop complex structures such as airframes, offshore accommodation units, pipelines, among other components.

Titanium is a low-density metallic element that is abundant and widely distributed throughout earth's crust (concentration of about 0.6%). It was discovered in a mineral (rutile -  $\text{TiO}_2$ ) by W. Gregor and M. Klaproth in 1790; however, only in the last 50 years or so has this metal gained strategic importance due to its mechanical and physical properties and alloying characteristics [1-3]. Titanium and its alloys have two principal virtues: a high strength-to-weight ratio and an outstanding corrosion resistance. Several applications and structural components take advantage of these two main characteristics such as aerospace and marine structures (aircraft, skin and engine components) as well as petrochemical and chemical processing equipments [1-3]. Nowadays, the titanium technology encompasses a variety of products and processes, including oxide dispersion-strengthened powder metallurgy, superplastic forming and diffusion bonding, TMCs and titanium base ordered-intermetallic compounds [3-5].

One of the most widely used titanium alloy, accounting for more than 50% of all titanium tonnage in the world is the alpha+beta Ti6Al4V, which contains aluminum (6 wt.%) and vanadium (4 wt.%) allowing the presence of both alpha and beta phases in the final microstructure [6-8]. It has a good combination of strength and toughness as well as an excellent corrosion resistance [9]. The Ti6Al4V alloy is unique in that it combines attractive properties with inherent workability, good weldability (with atmospheric protection) and commercial availability that lead to reliable and economic usage [10]. Despite of its good weldability high heat inputs and fast cooling rates during fusion welding frequently lead to local microstructural changes which, in turn, change the welded joint local mechanical behaviour and the overall performance of welded components. Therefore, solid state joining processes play an important role in titanium alloys welding avoiding fusion welding problems and eliminating expensive solders, electrodes, fluxes or shielding gases.

The need for enhanced materials for high performance structures and specific applications created the possibility for design and use of new materials such as the metal matrix composites (MMCs). This class of material has attracted great interest in recent years owing to their superior strength-to-weight ratio, high resistance to elevated temperature and better wear resistance than many materials. MMCs consist of two distinctly different materials: matrix (typically an aluminium or titanium alloy) and reinforcement (fibre, whisker or particle) [11]. Among all the materials used as matrix, titanium is one of the most utilised particularly due to their unique mechanical properties, corrosion resistance and low density. A class of MMCs referred to as titanium matrix composite (TMCs) consisting of a titanium alloy matrix and a reinforcement is being identified as one of the enabling technologies for many applications in both military and commercial arena to meet design requirements for materials displaying high strength and stiffness-to-density ratios at moderate to high temperatures (400°C to 800°C) [12,13].

The most significant drawback for a widespread use of TMCs in several applications is the high cost of the fabrication process. Several attempts were made in order to modify the manufacturing process to reduce TMCs cost. One of these attempts was using advanced P/M technology which has provided the key to a low cost new TMCs class. This material is a particulate reinforced composite with a titanium matrix alloy (Ti6Al4V) and ceramic or intermetallic additions (TiC, TiB<sub>2</sub> or TiAl) at various loading levels. The process utilised to produce this material is known as CHIP (Cold and Hot Isostatic Pressing) that has been recognized as a practical and economic method for fabricating fully dense titanium-alloy

components to a near net shape [5,14]. Titanium carbide, among all others, is the most successful particulate addition to date, imparting both strengthening effects and bulk elastic modulus enhancement. Tensile properties comparison of this composite with those of the matrix alloy indicates that the elevated-temperature yield and tensile strength as well as the elastic modulus increase 10-15% to about 650°C. As expected, strength increases and ductility decreases, with increasing particle loading. Additionally, while conventional titanium alloys typically display poor tribological properties as a result of ceramic-particle addition, the wear resistance is significantly improved [14].

The successful engineering application of TMCs depends on their weldability aspects and welding techniques that can produce high quality joints. With this in mind, solid state welding processes would be a natural choice during fabrication since the joints have good mechanical properties and the process is easily automated. Furthermore, TMCs have proved to be quite sensitive to fusion joining processes. Indeed, the high chemical reactivity of titanium may lead to chemical interaction with the reinforcing material, having a deleterious effect on the mechanical properties of the joint [15].

### **Motivation**

It is well established that TMCs have higher specific strength and modulus of elasticity as well as good high temperature properties; however, there are some problems in its widespread use such as reliable fabrication process, degradation of the mechanical properties (interfacial reaction between the reinforcement and the matrix) and secondary processing, especially joining. When using fusion welding to join particulate TMCs several problems may occur such as segregation due to differences in density between the matrix and the particulate; formation of undesirable eutectic structures as well as chemical reactions due to the contact between the molten metal and the reinforcement. Therefore, solid-state welding processes represent an excellent alternative when it comes to welding of particulate TMCs; however, despite recent advances in processing and manufacturing technology there is a lack of understanding in the solid state joining possibilities and its microstructural changes and mechanical properties.

### **Objectives**

The objectives of the present investigation are:

- to investigate and analyse the feasibility of joining the Ti6Al4V + 10 wt.% TiC composite by rotary friction welding and diffusion bonding processes;

- to evaluate the metallurgical and mechanical properties of the base material and the welds;
- to investigate the bonding mechanisms and understand the weldability aspects of friction-welded and diffusion-bonded Ti6Al4V + 10 wt.% TiC composites;
- to determine the effect of the solid-state processes parameters on the microstructure and properties of the composite alloy;
- to determine the microstructure/property relationships of Ti6Al4V + 10wt.% TiC welds.

### **Outline of the Thesis**

The general presentation of the thesis is divided into several chapters, including an introduction, a state of the art, the experimental procedure, the results and discussion as well as the conclusions. Initially it is presented a general introduction about the composite material and the solid state welding processes utilised in this investigation giving an idea to the reader about the general characteristics of the material and welding processes as well as the motivation and objectives of the investigation. In this chapter it is also shown the importance of the solid-state joining techniques on the advanced materials in engineering applications. In chapter 2 it is presented a literature review of the welding processes as well as the composite material (Ti6Al4V+10 wt.% TiC) and its mechanical and metallurgical properties. Important features about processing/manufacturing and failure mechanisms are also shown as well as a study of the parameter influence on the mechanical and metallurgical properties of the friction-welded and diffusion bonded joints, and the solid state joining possibilities for TMCs and MMCs alloys with general characteristics of the resultant welded joints. Chapter 3 shows a detailed description of the experimental procedure used in this investigation presenting the mechanical and metallurgical techniques utilized to characterize the resultant welded joints and base material. The welding parameter matrices of both joining processes are also presented showing all the different joining parameters used to perform the friction welding and diffusion bonding processes. Chapter 4 shows the results and discussion of this investigation where it is presented a detailed metallurgical and mechanical characterisation of the base material as well as of the welded joints resulting in the determination of the structure/property relationships. It is also presented a fracture analysis showing the micromechanisms of fracture of the resultant welded joints and base material. Finally some concluding remarks are made and some recommendations for further research are given.

## 2 STATE OF ART

### 2.1 General Metal Characteristics

Titanium is widely distributed being its concentration of about 0.6% making it the fourth most abundant of structural metals (after aluminium, iron and magnesium). This abundance is to some extent illusory, in that it is not so frequently found in economically extractable concentrations. Metal concentrated sources are ilmenite, titanomagnetite, rutile, anatase and brookite [2]. Titanium has a density of  $4.50 \text{ g/cm}^3$  [1,3,12,16,17] and a Young's modulus ranging from 103 to 115 GPa [3,12,17]; for its alloys the density varies between 4,30 and  $5.10 \text{ g/cm}^3$  while the modulus can range from 75 to 130 GPa [12,18]. Titanium and its alloys have melting points higher than those of steels, but maximum useful temperatures for structural applications generally range from 425 to 540°C due to elevated-temperature strength and creep resistance along with pickup of interstitial impurities (oxygen, nitrogen and hydrogen) because of the chemical reactivity of titanium [1,3,16]. It has exceptional ability to passivate in solutions based on the formation of a stable, protective oxide layer leading to an exceptional aqueous corrosion resistance. Combination of high strength, stiffness, good toughness and corrosion resistance, as well as low density provided by various titanium alloys at a very low to moderately elevated temperatures allows weight savings in aerospace structures as well as in petrochemical and marine environment applications [10].

### 2.2 Phases and Structures of Titanium and its Alloys

Titanium exists in two crystallographic forms. At room temperature, unalloyed titanium has a hexagonal close-packed (hcp) crystal structure referred to as alpha ( $\alpha$ ) phase. Between 882°C and 885°C pure titanium undergoes an allotropic transformation to a body-centred cubic (bcc) structure known as beta ( $\beta$ ) phase [1-3,10,12,16,17,19-23]. This allotropic behaviour allows complex variations in the microstructure and more diverse strengthening opportunities than those of other nonferrous alloys [16]. The transformation temperature is known as  $\beta$  transus temperature and is defined as the lowest equilibrium temperature at which the material is 100%  $\beta$ . However, this temperature is only valid for laboratory-pure titanium; the inevitable presence of oxygen in commercially pure titanium and other alloying elements in different titanium alloys raise this transition temperature [24]. The allotropic transformation temperature can be also altered by the addition of alloying elements depending on the type and amount of alloy contents. According to their influence on the  $\alpha$ - $\beta$ -transition temperature the alloying elements are divided into three groups: neutral (zirconium and tin);  $\alpha$



stabilizers, such as aluminium, carbon and oxygen, that increase the temperature at which  $\alpha$  phase is stable, and  $\beta$  stabilizers, such as vanadium, niobium and molybdenum that stabilize the  $\beta$  phase at lower temperature [1,2,10,12,16-21,23,25]. The manipulation of these crystallographic variations through alloying additions and thermomechanical processing is the basis for the development of a wide range of alloys and properties. Based on this, besides CP titanium, it can be classified into three major categories according to the predominant phases present in microstructure:  $\alpha$ ,  $\alpha+\beta$  and  $\beta$  alloys [1-3,10,12,16-21,25]. These families can be further subdivided to near- $\alpha$ , near- $\beta$  and metastable- $\beta$  alloys [18,19].

### 2.2.1 Unalloyed or Commercially Pure (CP) Titanium

CP titanium has minimum titanium contents ranging from about 98 to 99.5 wt.% and is usually selected for its excellent corrosion resistance especially in applications where high strength is not required [1,10,16]. The yield strength of the unalloyed grades varies from less than 170 MPa to over 485 MPa simply as a result of variation in the interstitial and impurity levels. Oxygen and iron are primary variants in these grades, but nitrogen, carbon and silicon are also important impurities that can greatly affect the mechanical properties. Grades of higher purity are lower in strength, hardness and transformation temperature than those higher in interstitial content [1,10]. The CP titanium microstructure depends upon whether it has been cold worked and on the type of annealing. In addition, upon cooling from the  $\beta$ -region, the structure will depend upon the cooling process, as this affects the  $\beta$ -to- $\alpha$  transformation, and hence the final  $\alpha$  grain size and shape [23]. At room temperature, the CP microstructure is 100%  $\alpha$ -crystal structure. As amounts of impurities increase, small, but increasing amounts of  $\beta$  are observed, usually at the  $\alpha$  grain boundaries [16]. Typical examples of CP alloys are Ti0.3Mo0.8Ni (Grade 12) and Ti0.2Pd (Grades 7 and 11).

### 2.2.2 Alpha Alloys

Titanium and its alloys with  $\alpha$  stabilizers either single or in combination are hcp at ordinary temperatures and are classified as  $\alpha$  alloys. Satisfactory strength, toughness, creep resistance and weldability characterize these alloys. Furthermore, the absence of ductile-brittle transformation renders the  $\alpha$  alloys suitable for cryogenic applications. Generally they have creep resistance superior to  $\beta$  alloys and are preferred for high temperature applications. Extra-low-interstitial (ELI) grades retain ductility and toughness at cryogenic temperatures. Unlike  $\alpha$ - $\beta$  and  $\beta$  alloys,  $\alpha$  alloys cannot be strengthened by heat treatment. Strengthening

mechanisms are cold work, cold work and anneal to control the  $\alpha$  grain size as well as solute additions for solid solution strengthening [23]. Alloys that contain small additions of  $\beta$  stabilizers (Ti8Al1Mo1V or Ti3Al2.5V) have been classified as near- $\alpha$  alloys. Although they contain some retained  $\beta$  phase, these alloys consist primarily of  $\alpha$  and behave more like conventional  $\alpha$  alloys than  $\alpha$ - $\beta$  alloys [1-3]. An example of  $\alpha$  alloy is Ti5Al2.5Sn.

### 2.2.3 Alpha-Beta Alloys

$\alpha$ - $\beta$  alloys are such that at equilibrium, usually at room temperature, they support a mixture of  $\alpha$  and  $\beta$  phases (10 to 50% of  $\beta$ ) [3,10]. Although many binary  $\beta$ -stabilized alloys in thermodynamic equilibrium are two-phase, in practice  $\alpha$ - $\beta$  alloys usually contain mixtures of both  $\alpha$  and  $\beta$  stabilizers [1-3,10,16,21]. They retain more  $\beta$  phase after the final heat treatment than do near- $\alpha$  alloys (specific amount depending on quantity of  $\beta$  stabilizers present and on heat treatment) [10]. It can be strengthened by solution treating and aging. Solution treating usually is done at a temperature high in the two-phase  $\alpha$ + $\beta$  field and followed by quenching. As a result of it, the  $\beta$  phase present at the solution treating temperature may be retained or partly transformed during cooling by either martensitic transformation or nucleation and growth. The specific response depends on the alloy composition, section size, cooling rate and solution-treating temperature. It is followed by aging to precipitate  $\alpha$  and produce a fine mixture of  $\alpha$  and  $\beta$  in retained or transformed  $\beta$ . Examples of  $\alpha$ - $\beta$  alloys are Ti6Al4V and Ti6Al6V2Sn.

### 2.2.4 Beta Alloys

Titanium can be made to exist entirely in the  $\beta$  phase at room temperature. Alloy additions inhibit the  $\beta$ -to- $\alpha$  transformation ( $\beta$  stabilizers) with the  $\beta$  phase completely retained. They are characterized by high hardenability, excellent forgeability and good cold formability in the solution treated condition. The disadvantages of the  $\beta$  alloys in comparison with the  $\alpha$ - $\beta$  alloys are higher density, lower creep strength and lower ductility in the aged condition. Although the ductility is lower, the fracture toughness of an aged  $\beta$  alloy generally is higher than that of an aged  $\alpha$ - $\beta$  alloy of comparable yield strength. In the solution treated condition (100% retained  $\beta$ ), the  $\beta$  alloys have good ductility and toughness, relatively low strength and excellent formability. They are prone to ductile-brittle transformation; therefore unsuitable for low-temperature applications. Some examples of  $\beta$  alloys are Ti10V2Fe3Al and Ti15V3Cr3Al3Sn [1-3].

### 2.3 Alpha + Beta Alloy Ti6Al4V

The  $\alpha+\beta$  Ti6Al4V alloy is the most widely used titanium alloy among all others. It contains 6% of aluminium and 4% of vanadium (weight percentage) and it has an excellent combination of specific strength and toughness as well as good stability at temperatures up to 400°C. The Ti6Al4V modulus (100 to 130 GPa) is about midrange for the titanium alloys but relatively low compared to other high-strength materials. In general, it has been found that the  $\alpha$ -stabilizing solutes increase modulus, whereas the  $\beta$ -stabilizing solutes decrease it [23,26].

Room-temperature tensile properties are affected by heat treatment, composition and texture. It is well established that the fracture toughness of titanium alloys strongly depends on microstructural parameters, which depend on both processing history and heat treatment [27]. The microstructural parameters can strongly affect the fracture toughness behaviour in two different ways: through direct influence on the material fracture properties and through influence on the crack front geometry [27,28]. In general, the fracture toughness increases as amount of transformed  $\beta$  structure increases, with  $\beta$  annealing providing the highest fracture toughness [29]. The best combination of microstructural parameters to improve the fracture toughness value ( $K_{IC}$ ) is coarse grain size and lamellar microstructure, low age-hardening and low oxygen content [28]. Murthy and Sundaresan [30] affirm that it is clear the superiority of microstructures that contain large acicular  $\alpha$  percentage due to their high aspect ratio that provides extended  $\alpha$ - $\beta$  interfaces for preferential crack propagation resulting in greater energy consumption. The grain size also plays an important role (increasing the grain size increases the  $K_{IC}$ ) since the crack front is much smoother for the fine grained compared to the coarse grained material [28]. The smoother the crack path is; the lower is the  $K_{IC}$  value since a more irregular fracture path (crack direction changes) leads to a greater dissipation of work per unit crack extension distance in the direction normal to the loading direction resulting in higher  $K_{IC}$  [27]. The geometry of  $\alpha+\beta$  structures also plays an important role in the  $K_{IC}$  behaviour; fine lamellar structure exhibits a much smoother crack path compared to serrated crack growth in coarse lamellar structure (higher  $K_{IC}$ ). When comparing equiaxed and lamellar structures, the equiaxed structure exhibits a smoother crack path than their lamellar counterparts. Also, the  $K_{IC}$  of bimodal structures decreased with decreasing primary  $\alpha$  volume fraction approaching the  $K_{IC}$  of fine lamellar structure. Table 2.1 presents the mechanical properties of Ti6Al4V according to various microstructural condition resulted from different heat treatments and mechanical processing [26].

**Table 2.1 - Tensile data for various microstructural conditions [26].**

Condition	Yield Strength (MPa)	Tensile Strength (MPa)	Elongation (%)	Reduction in area (%)
10% equiaxed primary $\alpha$ + ann. <sup>(a)</sup>	971	1068	14	35
40% equiaxed primary $\alpha$ + ann.	930	1013	15	41
10% equiaxed primary $\alpha$ + STOA. <sup>(b)</sup>	978	1061	15	41
10% equiaxed primary $\alpha$ + ann. <sup>(c)</sup>	958	1040	14	37
50% equiaxed primary $\alpha$ + ann. <sup>(c)</sup>	923	1020	13	32
$\beta$ forge + ann	882	992	11	20
$\beta$ forge/water quench + ann	951	1054	10	21
$\beta$ forge + STOA	978	1075	10	20
10% equiaxed primary $\alpha$ + ann. <sup>(d)</sup>	882	985	13	33

<sup>(a)</sup> Annealing = 705°C/2h/air cooling. <sup>(b)</sup> Solution treated and overaged (STOA) = 955°C/1h/water quenched + 705°C/2h/ air cooling. <sup>(c)</sup> Water quenched off forging press. <sup>(d)</sup> Low-oxygen material.

Compared to most structural titanium alloys, the Ti6Al4V alloy is considered to be highly weldable. This weldability can be attributed to two principal factors: firstly, the needle-like  $\alpha'$  martensite that forms in Ti6Al4V is not as hard and brittle as that exhibited by the more heavily  $\beta$ -stabilized  $\alpha$ - $\beta$  alloys; and secondly, Ti6Al4V exhibits relatively poor hardenability allowing the formation of higher proportions of Widmanstätten  $\alpha$  plus retained  $\beta$  microstructure even at relatively high weld cooling rates. Despite of its good weldability, Ti6Al4V has been welded by solid-state joining processes, particularly for complex components such as honeycomb panels and sandwich structures for aerospace applications [16,26]. Solid-state joining processes avoid postweld heat treatments and use of expensive electrodes, fluxes or shielding gases as well as many defects found in fusion welding, such as, hydrogen embrittlement, solidification segregation and cracking producing welds free of discontinuities with a good combination metallurgical and mechanical properties [16].

## 2.4 Advanced Titanium Alloys

Since the monolithic alloys have inherent performance limitations, the development of materials independent of equilibrium or metastable structures have been investigated leading to the development of MMCs where a metal or alloy is combined with a nonequilibrium-dispersed phase - generally nonmetallic. Due to their unique properties, titanium alloys were among this initial MMC development, leading to the obtention of TMCs with boron fibres and later on with other kind of reinforcements (whisker or particulate).

During the past decade, an extensive effort has been devoted in order to develop and increase the performance of advanced titanium alloys such as TMCs. These alloys have unique properties such as excellent high temperature performance (oxidation, fatigue and

creep resistances) as a result of their high specific modulus, high recrystallisation temperature and low self diffusion. Much effort is currently being made to use TMCs for high performance industrial applications such as automotive and aeronautic components.

### 2.4.1 Metal Matrix Composites (MMCs)

A composite is described as a macroscopic combination of two or more distinct materials having a recognizable interface between them. Composites are commonly classified with respect to the matrix constituent and can be divided according to the following classes: organic-matrix composites, ceramic-matrix composites and MMCs [31]. MMCs can be defined as a material consisting of two or more physically and/or chemically distinct, suitably arranged or distributed phases. It has characteristics that are not depicted by any of the components in isolation [12]. Generally, one component acts as a matrix (continuous phase) in which the reinforcing phase is distributed. It is a quasi-homogeneous structure that produces synergistic mechanical and physical properties better than those of the matrix material that can be tailored to a specific application, usually at less weight than unreinforced metallic materials. Because most of the metallic materials and reinforcements have relatively high operating temperatures, MMCs maintain these advantages at much higher temperatures. Additionally, electrical and thermal conductivity can be substantially improved along with better resistance to environmental and thermal instability [13]. Apart from the advantages described above MMCs have also improved wear resistance, higher modulus and specific strength. Because of these attributes, MMCs are under consideration for a wide range of application that includes aerospace and automotive industries among other minor applications [32]. One of the drawbacks is the difficulty of joining (similar or dissimilar welding) - it has become evident, that the joining process can impair the properties of the MMC to the level of the matrix or even lower [33]. Wider application of this material will require performance improvements coupled with novel welding process to drastically lower overall costs [34].

There are two distinct composite systems depending on the reinforcement length-to-diameter (see Fig. 2.1). Continuously reinforced MMCs have reinforcements with a very large length-to-diameter ratio (i.e., nonbroken filament or fibres). Discontinuously reinforced MMCs have reinforcements with a small length-to-diameter ratio (i.e., particulate or whisker) [12,13]. Nowadays discontinuously reinforced MMCs have assumed special importance for the following reasons: (1) it is inexpensive vis a vis continuous fiber reinforced composite; (2) conventional metallurgical processing techniques like casting or powder metallurgy, followed by conventional secondary processing (forging or extrusion) can be used; (3) higher

use temperatures than the unreinforced metal; (4) enhanced modulus and strength; (5) increased thermal stability; (6) better wear resistance; (7) relatively isotropic properties compared to the fiber reinforced composites [12].

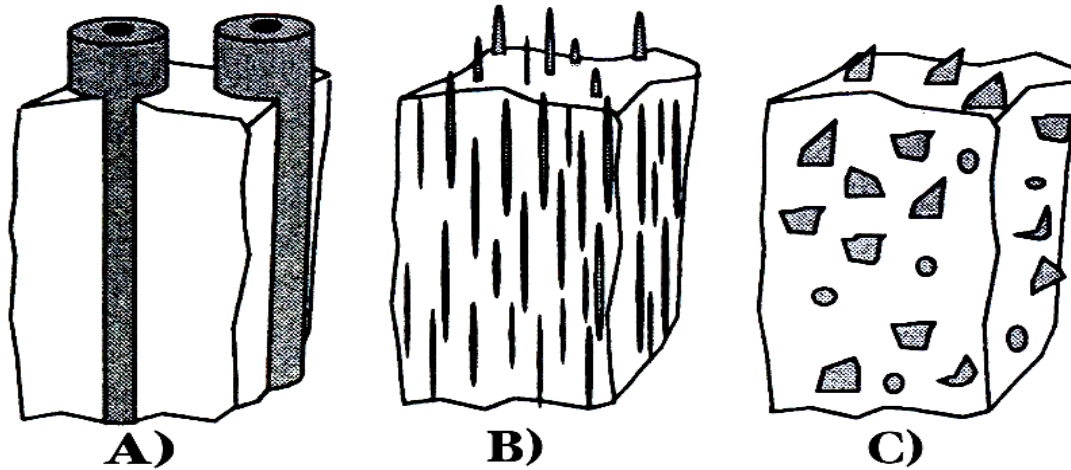


**Figure 2.1 - Examples of reinforcements in composites. (a) Continuous reinforcement (fibres). (b) Discontinuous reinforcement (whiskers). (c) Discontinuous reinforcement (particulate) [35].**

There are three entities that determine the characteristics of the composite: matrix, reinforcement and interface. Earlier on, the role of the matrix was considered to be that of a binder to hold strong and stiff fibres or other types of reinforcements. Over the years, however, it has been realized that the matrix microstructure and consequently its mechanical properties have a considerable influence on the composite overall performance. This is particularly true of MMCs because the very act of incorporating the reinforcement can result on changes in the matrix microstructure and consequently in their structure-sensitive properties such as strength and toughness [12].

The choice of the MMCs matrix alloy is dictated by several considerations, and of particular importance is whether the composite is to be continuously or discontinuously reinforced. In the case of continuous fibres, matrix serves to hold the fibres together, to fixate them in the desired stress direction and to transfer the applied load to fibres. The mechanical properties of MMCs are dependent upon matrix efficiency in transferring load to the reinforcing fibres and are therefore related to the bonding between fibres and matrix. Providing fiber/matrix bond is good, many of the MMC properties are related to those of the reinforcement while the matrix properties are of secondary importance. In addition the matrix serves to protect the fibres from mechanical damage providing environmental protection against external agents. The matrix alloy in a continuous MMC may be chosen more for toughness than for strength (to blunt cracks in the event that fiber failure occurs and to

provide load transfer to the fibres). On this basis, more ductile and tougher matrix alloys may be utilized in continuous MMCs. For discontinuously reinforced MMCs, the matrix may govern the composite strength; however both matrix and reinforcement bear substantial proportions of the load. Then, the matrix choice will be influenced by consideration of required composite strength and higher strength matrix alloys may be required [35,36].

Reinforcement materials in MMCs are second phase additions to a metallic matrix that result in some property improvement such as strength, stiffness and temperature capability. Generally, reinforcement materials for MMCs are ceramics (SiC, Al<sub>2</sub>O<sub>3</sub> and TiC among others) which are characterized by their high strength and stiffness at room and elevated temperatures. In discontinuously reinforced MMCs, the matrix is the major load-bearing constituent, therefore, the reinforcement role is to strengthen and stiffen the composite by preventing matrix deformation by mechanical restraint (generally a function of particle spacing-to-diameter ratio). When combined with a higher density matrix, the reinforcement also serves to reduce density, thus enhancing properties such as specific strength [36].

The interface region has a great deal of importance in determining the composite ultimate properties. An interface is, by definition, a bidimensional region through which there occurs a discontinuity in one or more material parameters. Its importance in MMCs stems from two main reasons: it occupies a large area, and in general, the reinforcement and the matrix form a system that is not in thermodynamic equilibrium. Among important discontinuities that can be found in the interface are elastic moduli and thermodynamic parameters (chemical potential and thermal expansion coefficient). Discontinuity in the chemical potential is likely to cause chemical interaction leading to an interdiffusion zone or a chemical compound formation. Discontinuity in the thermal expansion coefficient means that the interface will be in equilibrium only at the temperature that the reinforcement and the matrix were brought into contact; at any other temperature there will be present biaxial or triaxial stress fields due to thermal mismatch between the components [12].

#### **2.4.2 Titanium Matrix Composites (TMCs)**

TMCs are a class of MMCs consisting of a titanium alloy matrix and a reinforcement, such as fiber, whisker or particulate [13]. Nowadays, there is considerable interest in the development of MMCs based on titanium alloys and particulate reinforcements due to the unique properties of titanium and its alloys as well as the low-cost and stiffness of the particulate. Due to the high reactivity of titanium and its alloys, both in the liquid and solid state, the reinforcement phase processing conditions must be carefully chosen to minimize the

formation of reaction products at the reinforcement/matrix interface. Titanium alloys reinforcement is seen to directly address the relatively poor creep performance of these materials and may arrest the rather rapid fall off in modulus with temperature. In addition, general increases in strength and stiffness of these materials, coupled with a possible density dilution, are clearly attractive [37].

Much effort has been made during the past few years to produce discontinuous TMCs due to its low cost (compared to continuously reinforced) and avoidance of existing problems in continuous TMCs, such as mechanical properties difference according to the direction of the reinforcement. Among all possible routes to produce particle reinforced TMCs, such as, ingot metallurgy and powder atomisation [38] one has provided the key to a new class of low-cost and high-performance TMCs: Cold and Hot Isostatic Pressing (CHIP). It is an advanced powder metallurgy (P/M) technology based on the blended elemental (BE) method that has been recognized in recent years as a practical and economical method for fabricating fully dense titanium-alloy components to a near-net shape. It comprises cold and hot isostatic compressing without the need for additional expensive tooling. The process consists of blending elemental powders in a proper proportion producing uniform distribution of the desired alloy composition. After proper blending time, the material is cold isostatically pressed (CIP) in which a "green" preform shape is produced utilizing elastomeric tooling under hydrostatic pressure achieving densities of about 80 to 85%. Pressure is applied hydrostatically; thus compacting forces are applied in all directions unlike conventional powder metal consolidation (uniaxial). By this technique, higher and more uniform density is achieved. On removal from the CIP press, the sample undergoes vacuum sintering where the cold consolidated preform is sintered to high density (95% minimum). The sintering temperature, time and atmosphere conditions are carefully controlled to produce diffusion necessary for high density without introducing contaminating elements and to maintain the specified alloy composition. The titanium matrix is formed during sintering by diffusion-driven solid-state alloying, typically at temperatures less than 250°C above the  $\beta$ -transus (1230°C for Ti6Al4V). The sintering operation produces a closed porosity (94 to 98%) that eliminates need for canning of the P/M preform prior to hot isostatic pressing (HIP). Full density is achieved by HIP that is applied to the as-sintered preform under high pressure (103 MPa) and at elevated temperature (899°C) in protective atmosphere for 2 hours. [5,14,39,40]. Figure 2.2 shows a schematic representation of the CHIP process [5,39,40].



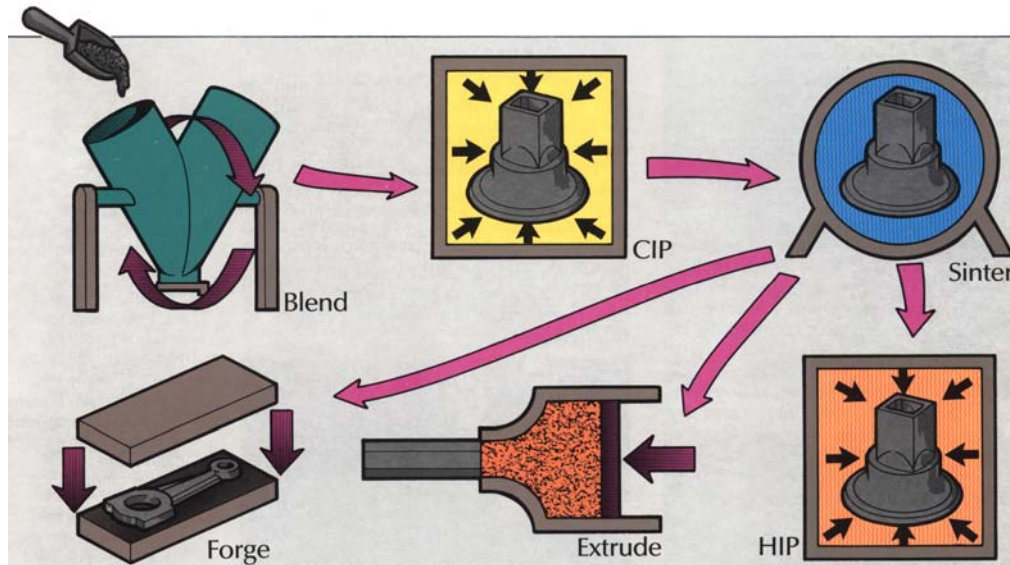


**Figure 2.2 – Schematic representation of the different stages in the CHIP process [5,39].**

Unlike direct HIPing, which involves expensive, non-cold-compactable, prealloyed powders and shaped, non-reusable container, the CHIP process employs low-cost, reusable, polymer tooling. CIPing component shape from cold-compactable powder allows near-net shape fabrication of complex shapes, including those with cored or hollow sections as well as undercuts. Important cost savings result from reducing the amount of input material needed to manufacture a preform as compared to the quantity requiring in machining from a mill-product form or from an oversized forging [5,14,40].

In order to achieve improved properties, TMCs were developed using particulate TiC as an addition to the P/M titanium-alloy matrix. The use of a particulate permitted the same low-cost CHIP manufacturing technology to be used. The result was a fabrication process employing less expensive materials as compared to specialty fibres such as SiC. The SiC fiber-reinforced TMCs are highly anisotropic in properties and their fabrication is complex and expensive [41]. Besides this, the desired mechanical properties are achieved in only one direction while inferior properties take place in other directions as well as detrimental interreactions that occur between titanium and stiffeners such as SiC, generating brittle intermetallic materials in the interface ( $Ti_5Si_3$ ) [42]. The properties of the TiC-particulate reinforcement are uniform in all directions and besides, the TiC particulate is thermodynamically stable in the titanium matrix at CHIP-processing temperatures resulting in a stable particle-matrix interface [5,14]. Indeed, as opposed to melt processing, the thermal decomposition of the TiC reinforcing particulate (melting point – 3065°C) can be limited to a practical extent during the sintering cycle. Another advantage is that the extent of composite stiffening and hardening can be tailored with the TiC content.

### 2.4.2.1 Discontinuously Reinforced Titanium Matrix Composite (Ti6Al4V+TiC particles)

Among all the discontinuously reinforced TMCs one has been intensively studied during the past few years [5,14,39-58]: TiC/particulate plus Ti6Al4V. This material seeks to combine the high strength and stiffness of a ceramic with the damage tolerance and toughness provided by a titanium matrix. The resultant composite exhibits high specific strength and specific modulus as well as good elevated-temperature properties [5,14,40,41,43,46]. A comparison of the tensile properties of this composite with those of the matrix-alloy indicates that elevated-temperature yield and tensile strength ( $R_{p0.2}$  and  $R_m$ , respectively) increase 10-15% to about 650°C. As expected, strength increases and ductility decreases with increased particle loading. The stiffness of the composite is dramatically improved from room temperature to 650°C. The ductility is impaired, but reasonable ductility is retained throughout the temperature range; the ductility of the composite and the monolithic alloy do not differ significantly at 650°C. The results of the creep- and stress-rupture tests from the Ti6Al4V+15%TiC and forged matrix-alloy specimens show that the TiC-reinforced materials typically have an order of magnitude increase in time-to-rupture compared to the unreinforced titanium alloy at temperatures up to 540°C [5,14,40]. According to Abkowitz et al [5], the creep testing results of the Ti6Al4V+10%TiC alloy fabricated by the CHIP process and hot working displayed 100°C creep strength enhancement compared to the wrought Ti6Al4V alloy, suggesting a further benefit from combining hot working with particle reinforcement.

As can be observed from Table 2.2 the incorporation of TiC particles into the Ti6Al4V matrix leads to the strengthening of the material formed. The strengthening mechanisms in particulate-reinforced materials can be of several ways such as, quench strengthening, Orowan strengthening, grain strengthening, and substructure strengthening as well as work hardening. According to Miller and Humphreys [59] the strengthening often occurs as a result of the simultaneous operation of the aforementioned mechanisms.

**Table 2.2 - High- and room-temperature tensile tests results for the Ti6Al4V matrix alloy and the reinforced Ti6Al4V + 10% TiC alloy [40].**

Material	Test Temperature (°C)	$R_m$ (MPa)	$R_{p0.2}$ (MPa)	Strain-to-failure (%)
Ti6Al4V+10%TiC	25	999	-	-
	425	517 - 530	469 - 476	1.63 - 1.80
	535	448 - 462	407 - 420	2.15 - 2.66
	650	303 - 324	262 - 276	2.90
Ti6Al4V	25	896	-	-
	425	503 - 517	379 - 400	11.1 - 12.1
	535	434 - 448	351 - 358	7.6 - 9.4
	650	303 - 310	207 - 228	3.9 - 4.5

Johnson et al [60] as well as Zhu et al [49] have suggested that the dominant strengthening mechanism is work hardening in the Ti6Al4V/TiC system. The increase in the yield strength of the composite over the unreinforced alloy is due to the more rapid work hardening of the composite, which is a result of the elastic restraint imposed on the matrix by the particulates due to their elastic modulus difference. Such difference between the constituents in the Ti6Al4V/TiC system is significant, i.e., 100-130 GPa and 345 GPa (462 GPa [49] or 451 GPa [50]) for Ti6Al4V and TiC respectively [61,62], and such elastic incompatibilities will contribute to the strengthening of the composite material.

Compared to the matrix there are several factors that will increase the work hardening rate in the composite. In the early stages of deformation there will be a load transfer between the matrix and the reinforcement by means of Orowan loops or some equivalent mechanism. The expected contribution to strength in the early stages of deformation is simply dependent on the volume fraction ( $F_v$ ) according to the Equation 2.1 [59]:

$$\sigma_{WH} = 4.5 * G * F_v * \varepsilon \quad \text{Equation 2.1}$$

where  $G$  is the shear modulus of the material,  $F_v$  is the volume fraction and  $\varepsilon$  is the true strain.

As deformation proceeds the stress induced at the particle/matrix interface leads to the relaxation of the Orowan loops at strains as low as  $10^{-4}$ . At higher strains the particle will contribute to work hardening due to the creation of geometrically necessary dislocations. This contribution to strength has been estimated by the following equation, see Equation 2.2 [59]:

$$\sigma_{WH} = 5 * G * \left( \frac{2 * F_v * b}{d} \right)^{\frac{1}{2}} * \varepsilon^{\frac{1}{2}} \quad \text{Equation 2.2}$$

where  $b$  is the Burger's vector and  $d$  is the particle size.

The coefficients of thermal expansion of the Ti6Al4V matrix and the TiC are  $9.0 \times 10^{-6}/K$  and  $7.4 \times 10^{-6}/K$  respectively [49,62,63]. Such difference is small indicating that the strengthening due to thermal incompatibilities is less significant. According to Zhu et al [49] comparing the unreinforced and the 10 wt.% TiC particle reinforced Ti6Al4V alloys (both produced by the CHIP process) the strengthening via modification of the matrix microstructure should also be considered for the Ti6Al4V/TiC system since the addition of the TiC reinforcement changes the matrix microstructure from one consisting of aligned laths colonies (unreinforced material) to one with a more random laths orientation. Additionally, the lath aspect ratio has been significantly reduced in the composite.

Overall, the TiC reinforced composites provide higher modulus and better high-

temperature performance than the monolithic titanium alloys without compromising titanium weight advantage (Table 2.3). For example, the modulus improvement is about 15% at room temperature and this advantage is maintained up to 650°C. Improvement in the high temperature strength and stiffness increases the use-temperature limit of Ti6Al4V by approximately 110°C. In addition, the composite alloy, even with limited room-temperature ductility (>1%) has a satisfactory level of fracture toughness. The fatigue properties of the composite are comparable to HIPed Ti6Al4V alloy castings. Besides, the properties can be tailored to meet specific applications by increasing or decreasing the level of reinforcement. Figure 2.3 compares the elastic modulus behaviour of Ti6Al4V to Ti6Al4V+10%TiC at different temperatures.

**Table 2.3 - Mechanical properties comparison of Ti6Al4V, Ti6Al4V+10%TiC and Ti6Al4V+20%TiC alloys [5,14,39,40].**

Properties	Ti6Al4V	Ti6Al4V+10%TiC	Ti6Al4V+20%TiC
Density (g/cm <sup>3</sup> )	4.43	4.45	4.52
R <sub>m</sub> (MPa) RT	896	999	1055
R <sub>m</sub> (MPa) 540°C	448	551	620
E (GPa) RT	113	133	144
E (GPa) 540°C	89	105	110
Fracture Toughness (MPa*m <sup>1/2</sup> )	55	44	32
Fatigue Limit (MPa)	517	275	--
Hardness (HRC)	34	40	44

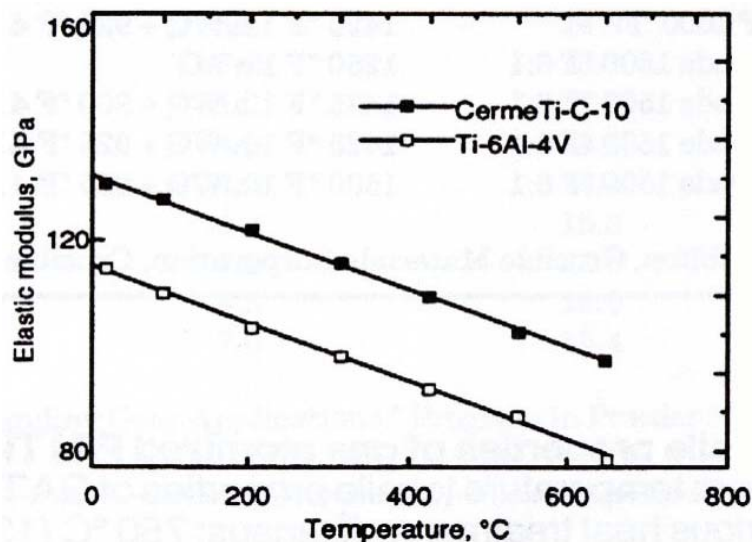


**Figure 2.3 - Ti6Al4V and Ti6Al4V+10%TiC elastic modulus vs. temperature [14].**

According to Shang and Ritchie [44] crack-growth rates for Ti6Al4V+20%TiC show a sigmoidal relationship with  $\Delta K$ ; threshold stress-intensity and  $K_{IC}$  values of 4 MPa\*m<sup>1/2</sup> and 18 MPa\*m<sup>1/2</sup>, respectively, have been found. Compared to the unreinforced P/M matrix alloy,

composite displays similar fatigue crack-growth behaviour over mid-range growth rates ( $\sim 10^{-9}$  to  $10^{-7}$  m/cycle). However, above  $10^{-7}$  m/cycle, the growth rates are far higher in the composite due to an earlier onset of fast fracture resulting from the much lower composite  $K_{IC}$ . Liu et al [48] studying fatigue crack growth at elevated temperature (450°C) in Ti6Al4V+20%TiC have shown that the composite fatigue threshold was 50% higher at 450°C than at room temperature. Such behaviour was shown to result from extensive microcracking of reinforcing particles, which promotes fatigue crack closure at elevated temperatures.

Another important characteristic of titanium and its alloys - corrosion resistance - can be improved due to the addition of the TiC particulate reinforcement. For example the addition of TiC particles to a P/M Ti6Al4V0.2Ru alloy significantly reduced the corrosion rate in room temperature and boiling hydrochloric acid. At room temperature, the corrosion rates of the Ti6Al4V0.2Ru+5%TiC alloy were negligible in up to 25% HCl and comparable to unalloyed Ti0.2Ru alloy [5].

Research efforts have been made in order to identify and establish the application field of TiC particulate reinforced TMCs (particularly the alloy Ti6Al4V+10%TiC). It has been proposed a wide spectrum of application ranging from aircraft and aerospace vehicles to sporting goods and high performance components. Abkowitz et al [5,14] as well as Abkowitz and Weihrauch [40] have suggested that TMCs produced by the CHIP process are being used in the production of high performance sporting goods such as baseball bats, ice hockey skate blades as well as golf clubs due to the weight advantages, good fracture toughness and high strength. It is also in investigation for using in missile components (fins) by the US Department of Defense. The alloy has also been used as shot sleeves and related tooling applications in the aluminium die casting industry replacing current commercial steel shot sleeve (H13) [55,56]. According to a study conducted by EHKTechnology [57] the Ti6Al4V+10%TiC alloy is also being considered as an alternative solution for both automotive and heavy vehicle valve train components. A study performed by NASA has shown that this material has demonstrated promising results for space propulsion applications as well as others aerospace applications [58].

#### ***2.4.2.2 Extent of Reaction between TiC Particles and Ti6Al4V Matrix***

Two closely-linked and important aspects of composite are the bonding nature and the extent of any reaction zone between the particles and the matrix, since the properties of this interface region determine, to a large extent, the composite properties. This reaction zone can lead to a disastrous degradation in the properties of the composite, especially the fracture

behaviour and damage mechanisms that can be intimately related to the matrix-reinforcement reaction during elevated-temperature, long-term processing and/or loading [49]. Because of the high reactivity of titanium, both in the liquid and solid state, there are major problems in finding reinforcement materials that are stable both during composite processing and service [47]. The reactions between the Ti6Al4V matrix and the TiC reinforcement have been studied and it is well known that it results in a nonstoichiometric annulus of  $Ti_2C$  growing around each TiC particle with the two phases separated by a wall of dislocations and that such layer does not lead to the particulate/matrix interface debonding. The reaction zone is thought to form through titanium diffusion into the particle and/or diffusion of carbon out of the particle. The evidence for this transformation was the presence of additional diffraction spots from the particles, which is consistent with a change from the rock-salt structure of TiC to a diamond-cubic structure [46]. Wagoner Johnson et al [51] affirm that additions of TiC provide a significant increase in the strength of the composite with no obvious reaction zone at the particle-matrix interface; however, it appears that this strength increase may result from the carbon that diffuses into the matrix from the carbides rather than from the presence of the carbides themselves. According to Gu et al [52], after heat treating samples of IMI829 with 10% of TiC particulate at 800°C and 1000°C, a composition gradient (from 37 at.% at the interface to about 50 at.%, which is the composition of stoichiometric TiC) has been found at the surface of the TiC particles concluding that no new reaction product exists on the interface. However a dissolution-type reaction occurred between titanium and TiC resulting in a continuous carbon-deficient zone in accordance with the equilibrium C-Ti phase diagram. Moreover, the phase diagram (see Fig. 2.4 [53]) suggests that the TiC would dissolve in the titanium matrix until either all the carbon is in solution or there is an equilibrium between a saturated solution of carbon in titanium and some remaining TiC, which would then be non-stoichiometric (i.e.  $TiC_x$ ). The carbon-deficient zone thickness depends on both the processing and heat-treatment parameters. The interdiffusion of carbon and titanium between the matrix and the reinforcement establishes a desirable dissolution-type bonding between them that renders good mechanical properties to the composite material. Loretto and Konitzer [42] have also observed that no interaction zone has been found in the matrix associated with the presence of the TiC particles in composites treated over temperatures up to 1050°C and for times up to 50 h. However, there is evidence of a reaction zone within the TiC particles which is separated from the centre of the particle by an array of dislocations and that such reaction zone is believed to be the non-stoichiometric TiC.

Wanjara et al [54] investigating the interface reactions in a Ti6Al4V+20%TiC alloy have shown that there is evidence for the formation of a stable stoichiometric Ti<sub>2</sub>C layer at the particle/matrix interface. The nature of the interfacial reaction has revealed that the lattice parameter of the matrix phase initially increased with holding time at the various isothermal temperatures investigation that suggests carbon diffusion from the reinforcement to the titanium alloy. Further reaction of the matrix alloy with the reinforcement resulted in the formation of a stable stoichiometric phase which was later identified as Ti<sub>2</sub>C and that remained stable up to temperatures of at least 1500°C.

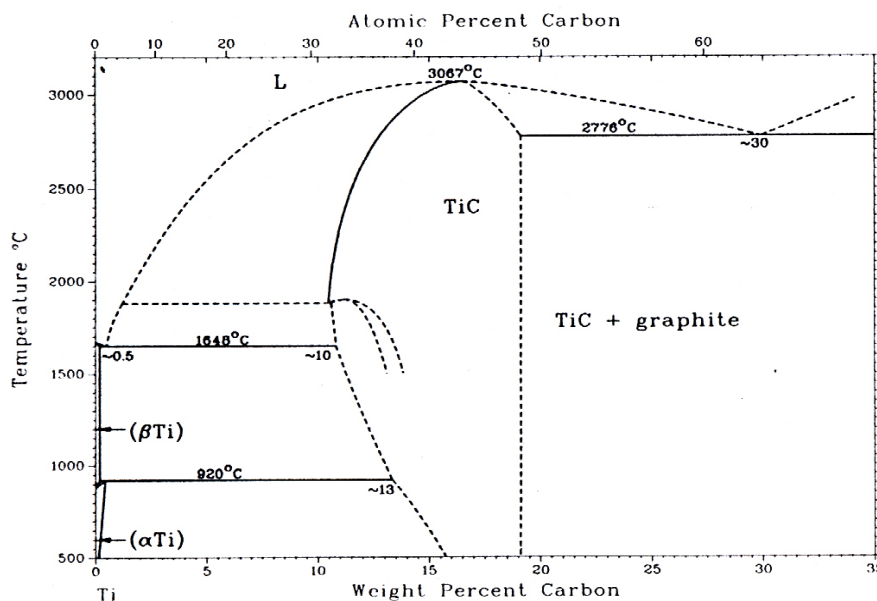
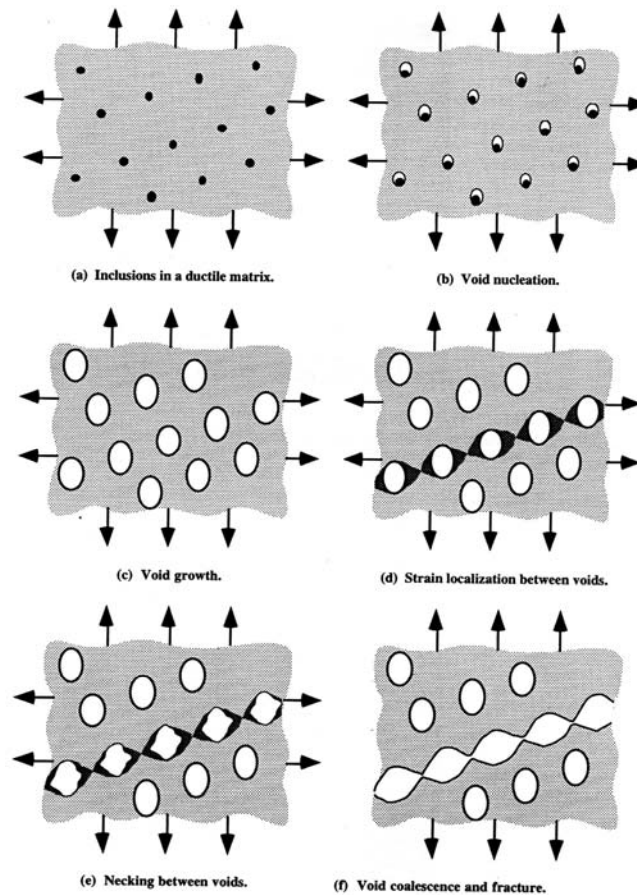


Figure 2.4 – Equilibrium Ti-C binary phase diagram [53].

### 2.4.2.3 Fracture Behaviour and Failure Mechanisms of Particle Reinforced MMCs

The presence of brittle ceramic phases in a ductile matrix has effects on the failure mechanism. The fracture is macroscopically brittle, but on a microscopic scale, local ductility of the matrix is frequently observed [35,64]. Early investigations in fracture behaviour of particle reinforced composites have considered weakly bonded particles showing fracture dominated by interfacial failure [65]. However, nowadays, composites have good bonding behaviour between particle and matrix, thus, the main concern is fracture of the reinforcing particle (however interfacial failure is still observed), especially in the case of Ti6Al4V alloys reinforced with titanium carbides. When studying failure in particulate MMCs it is useful to separate the total event of fracture in several steps, being void initiation, growth and followed by failure in the matrix by void coalescence [35]. Figure 2.5 exemplifies the fracture process in ductile metals as well as its several steps until the final failure.



**Figure 2.5 – Fracture process in ductile metals. (a) Inclusions in a ductile matrix (like ceramic reinforcements in a ductile matrix). (b) Void nucleation according to the correspondent void initiation mechanism. (c) Void growth. (d) Strain localization between the voids. (e) Necking between the voids. (f) Void coalescence and fracture. [66]**

According to Lloyd [67] the fracture initiation in particulate composites is associated with particle fracture, interfacial-matrix failure and inclusion fracture, depending on the particular composite and matrix condition. You et al [68] stated that the initial step of fracture initiation also occurs in the matrix, but as a consequence of the reinforcing particles that contribute to the failure process by imposing high levels of constraint on matrix deformation and by raising the stress in the matrix. According to Mussert [35] another mechanism for void initiation is that voids initiate near the reinforcing particle as a result of fracture of the reinforcing particle itself or debonding of the particle-matrix interface.

Clyne and Withers [69] have suggested a series of models to consider crack propagation in discontinuously reinforced MMCs including Evansen and Verk [70], Brown and Embury [71], Thomason [72] as well as Whitehouse and Clyne [73]. The most comprehensive is the one presented by Evansen and Verk [70] which consider crack propagation to arise from particle fracture. The matrix ligaments between two cracked particles are treated as notched bars, the fracture of which is predicted to occur when the



length of the two plastic zones is equal to the interparticle spacing. Taking the plastic zone to be the region surrounding the crack strained more than approximately 0.3, the crack opening displacement,  $\delta$ , has a value approximately 1.2 times the dimension of the plastic zone and this leads to Equation 2.3:

$$2.4\delta = r_0 \left( \sqrt{\frac{2\pi}{3f} - \sqrt{\frac{8}{3}}} \right) \quad \text{Equation 2.3}$$

where the particle separation is written in terms of the particle radius and volume fraction. Assuming  $\delta$  to increase directly in proportion to the overall composite strain, the strain  $\varepsilon_g$  needed for the void to grow sufficiently for fracture to occur is given by Equation 2.4:

$$\varepsilon_g = \left( \sqrt{\frac{2\pi}{3f} - \sqrt{\frac{8}{3}}} \right) \quad \text{Equation 2.4}$$

The total elongation ( $\varepsilon_T$ ) according to the Evanson and Verk model is calculated by Equation 2.5 taking into account the nucleation strain ( $\varepsilon_n$ ):

$$\varepsilon_T = \ln(1 + \varepsilon_g + \varepsilon_n) \quad \text{Equation 2.5}$$

However, Majumdar and Pandey [74] modelling the deformation and fracture of a particle-reinforced aluminium alloy composite have affirmed that such models have been found to be unsatisfactory for predicting the elongation of composites. They have presented a model which is essentially based on matrix failure since it is assumed that particles cracks are already present, so that the strain prior to the particle cracking is neglected in the elongation prediction. Figure 2.6 presents a schematic representation of this fracture mechanics model [74]. The length and width of the unit cell is 1, and the composite failure strain is identified with the overall strain on the cell EFGH to cause matrix rupture to proceed from location A to location B. Initially it is calculated the plastic strain at B (Eq. 2.6). After that it is assumed that the work hardening ( $N$ ) is equal to the tensile failure strain of the matrix ( $\varepsilon_m^f$ ) and due to this simplification flow localization is also incorporated into the matrix rupture conditions, since  $N$  may be considered to be a measure of flow localization.

$$\varepsilon_B = \left( \frac{\varepsilon_m^f}{(2.2 + 7N)(N + 1)} \right) \left( \frac{\varepsilon_m^f}{0.002} \right)^N \quad \text{Equation 2.6}$$

where  $\varepsilon_B$  is the plastic strain at B (Fig. 2.6);  $N$  is the work hardening exponent and  $\varepsilon_m^f$  is the tensile failure strain of the matrix material which is assumed to represent the strain of the

matrix up to void nucleation and some growth, i.e., void coalescence contributes very little to the measured strain to failure of the monolithic matrix, since that strain is extremely localized.

After calculating the plastic strain at B ( $\epsilon_B$ ) it is possible to calculate the  $\lambda$  value which is equal to  $R/\delta$  (distance from the crack tip) according to Equation 2.7:

$$\lambda = \frac{9.4 + 3.5\epsilon_B}{0.3 + 100\epsilon_B} \tag{Equation 2.7}$$

Finally, the Equation 2.8 presents the formula to predict the failure strain of the composite according to Majumdar and Pandey [74]:

$$\epsilon_c^f = \left( \frac{1}{\lambda\sqrt{2}} \right) \left( 1 - \frac{6v_p}{\pi} \right)^{\frac{1}{3}} \left( 1.285 - 4.403v_p + 4.122v_p^2 \right) \tag{Equation 2.8}$$

where  $\epsilon_c^f$  is the failure strain,  $\lambda$  is the value of  $R/\delta$  corresponding to the local failure strain and  $v_p$  is the volume fraction of the particles.

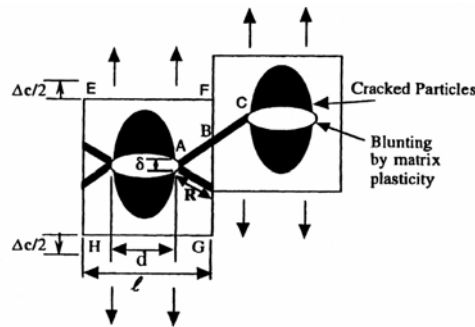


**Figure 2.6 – Schematic representation illustrating the fracture mechanics model for estimating the strain to failure of a composite.**

Clyne and Withers [69] have also shown that it is possible for cavities to form in high hydrostatic stress locations and when a certain condition is established, such voids link up by a ductile tearing mechanism which is thought to cause failure. Indeed, according to Mummery and Derby [75] the fracture of such materials has been shown to proceed by a ductile rupture (tearing) mechanism (Fig. 2.7).

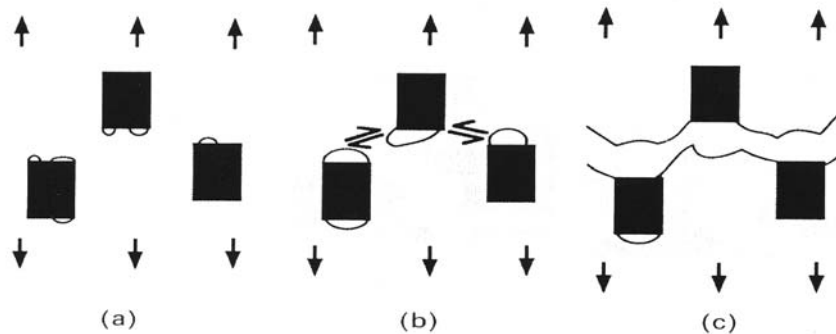


**Figure 2.7 –Crack initiation/propagation during tensile failure of MMCs. (a) Void formation in high hydrostatic tension regions. (b) Void coalescence by ductile tearing. (c) Failure. [69]**

When cracked particles act as void nucleation sites and initiate microcracks, these microcracks can be linked to each other causing macroscopic fracture. If this mechanism is responsible for failure, the crack path followed is the one that contains the highest area density of broken particles, whereby a relatively large percentage of broken particles should be seen at the fracture surfaces. If particle-matrix debonding precedes matrix failure, few or no broken particles should be seen at the fracture surfaces.

According to Mussert [35], independent of void nucleation, a third failure mechanism can be found when microcracks (in particles as well as in the matrix) in front of the main crack are linked to this crack by void growth [76,77]. These microcracks can arise as a result of the high local stresses caused by inhomogeneous deformation due to the fact that ceramic particles within the plastic zone of a growing crack reduce the amount of plastic deformation of the material. Figure 2.8 shows an example of such mechanism (sequence until final failure) [76]. Preferential sites have been observed in regions of high local volume fraction of particulate (clustering) suggesting that local plastic constraints is important [67].

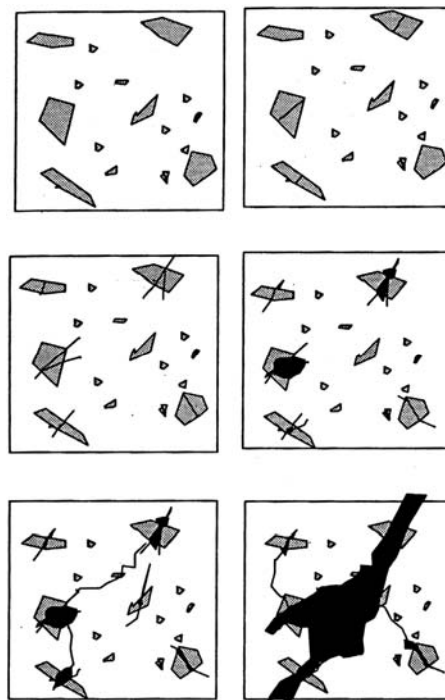


**Figure 2.8 – Mechanism of microcracks linking in front of the main crack by void growth [76].**

#### **2.4.2.4 Fracture Toughness Behaviour of Particle Reinforced MMCs**

The presence of the TiC particles causes significant changes and plays an important role in the fracture toughness behaviour since its addition into the titanium matrix results in an improvement in modulus and strength but it is accompanied by a drastic loss in the final  $K_{IC}$  values. Indeed, the incorporation of discontinuous reinforcements generally decreases the

fracture toughness of the composite (when compared to the matrix alloy) due to the brittle nature of the ceramic particle. Shang and Ritchie [44] observed that adding 20% of TiC to a Ti6Al4V matrix resulted in a decrease in  $K_{IC}$  from  $77 \text{ MPa}\cdot\text{m}^{1/2}$  (P/M matrix alloy) to  $18 \text{ MPa}\cdot\text{m}^{1/2}$  (matrix alloy+20%TiC). However, Liu et al [43] applying an annealing treatment (holding at  $1065^\circ\text{C}$  for 2 hours and furnace cooling) could produce a tougher Ti6Al4V+20%TiC achieving  $K_{IC}$  values up to  $30 \text{ MPa}\cdot\text{m}^{1/2}$ . The Ti6Al4V+10%TiC  $K_{IC}$  value is about  $28 \text{ MPa}\cdot\text{m}^{1/2}$ , which is comparable to the widely used aerospace aluminium alloy 2014-T6 [40]. The Ti6Al4V+20%TiC  $K_{IC}$  temperature dependence is shown in Figure 2.9. It consists of three regions: a low temperature regime, where  $K_{IC}$  increases with the temperature; an intermediate temperature regime, where  $K_{IC}$  is relatively constant; and a high temperature regime, where  $K_{IC}$  decreases with the temperature. The low and high temperature regimes apparently are associated with matrix brittle fracture at low temperature and matrix ductile stretching at high temperatures. The relatively constant toughness over the intermediate temperature region can be considered as a transitional region where the fracture mechanism gradually changes from cleavage to ductile stretching [43].

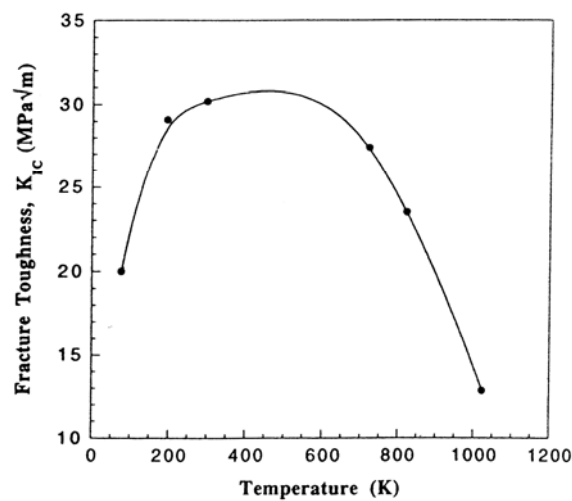


**Figure 2.9 - Ti6Al4V+20% TiC fracture toughness temperature dependence [43].**

The MMCs fracture toughness behaviour can be compared to the fracture toughness behaviour in ductile materials that is strongly affected by the presence of second-phase particles, which induce dimple formation, by void initiation and propagation. In the case of discontinuously reinforced MMCs the fracture toughness can be quite sensitive to microstructural details [35]. Such sensitivity covers the reinforcement size, shape and distribution, the volume fraction of reinforcing particles, the interfacial bond strength and the matrix ageing condition in the case of heat treatable alloys. The reinforcement size has an influence on the fracture toughness since the failure stress of a ceramic is reduced with its

size. A larger ceramic reinforcement fails sooner, thereby transferring the void nucleation mode from interfacial debonding to particle fracture. In populations with a larger scatter in particles sizes, it is the largest particles that tend to fracture. Flom and Arsenault [78] have shown that particle size has no effect on the fracture toughness behaviour while Manahoran and Lewandowski [79] as well as Lewandowski et al [80] have demonstrated the opposite behaviour, i.e., composite reinforced with larger particles possessed greater toughness than those containing smaller particles. According to Alman [50], generally there is a slight tendency for fracture toughness to increase with increasing particle size. This can be explained by considering that interparticle spacing increases with particle size and a greater volume of matrix material is available for unconstrained plastic flow in the wake of the propagating crack, resulting in higher fracture toughness. The geometry of the reinforcement has also a marked influence since a spherical particle reinforced composite exhibits a slightly lower yield strength and work hardening rate, but a considerably higher ductility than an angular particle reinforced composite. Therefore the spherical composite fails through void nucleation and linking in the matrix near the particle/matrix interface, whereas the angular composite fails through particle fracture and matrix ligament rupture. Reinforcement distribution is also important since particulate clustered areas are dominant sites for crack nucleation and propagation. Indeed, according to Lloyd [67] the fracture process is controlled by large triaxial stresses intensification occurring in a cluster.

The reinforcement volume fraction has also an influence on the fracture toughness properties, increasing it, the local strain in the matrix between the particles becomes higher, resulting in premature matrix fracture. This is caused by the fact that, when strain is the dominating factor for failure, the distance over which this strain should be accomplished, i.e. the interparticle spacing becomes shorter with increasing particle volume fraction. Since the constraint imposed on the matrix determines the plastic zone size, which on its turn influences the overall fracture behaviour, it is assumed that an increase in the reinforcement volume fraction leads to a decrease in the plastic zone size and thus in the  $K_{IC}$  value.

The interfacial strength has also an important influence on the  $K_{IC}$  because of the larger total interface surface, the chemical instabilities and their incoherence. Stiffening and strengthening rely on load transfer across the interface and ductility is affected by relaxation of peak stresses near the interface. Since particle fracture and interfacial debonding may occur in the same MMC alloy depending on subtle changes in the microstructure, it might be concluded that the difference in strength between the interface and the particle is small [35].

## 2.5 Solid State Welding Processes

Joining of any material with another has always been a necessity in engineering applications. Welding or bonding of two materials always caused changes or deterioration of the original material microstructural and mechanical properties at the joining region. Among the modern joining techniques used in engineering today, the solid state processes are widely used particularly in the advanced materials. Bonding is achieved by the introduction of mechanical, electrical or thermal energy and/or diffusion. These processes differ in times, pressures and temperatures used as well as methods of applying heat [11].

Solid state welding is a group of processes which produce coalescence at temperatures below the melting temperature of the base metal without the addition of brazing or solder filler metal; pressure may or may not be applied. These processes involve either the use of deformation or, diffusion and limited deformation in order to produce high-quality joints [81]. Solid state welding in its simplest form requires only that the atoms of one workpiece be brought sufficiently close to the atoms of another workpiece to permit interatomic forces to bridge interface; however, there are major difficulties in occurring that: first, metal surfaces are rough on an atomic scale; even a finely ground surface, presents hills and valleys that are thousands of atoms deep. Under light pressure, only a few opposing peaks of the metal surfaces actually touch. Second, the number of contacting surfaces can be increased by applying more pressure; but a layer of oxides and occluded gas which is present on all metal surfaces under normal atmospheric conditions (Fig. 2.10) is encountered, and for welding to occur, these layers must be removed [82].

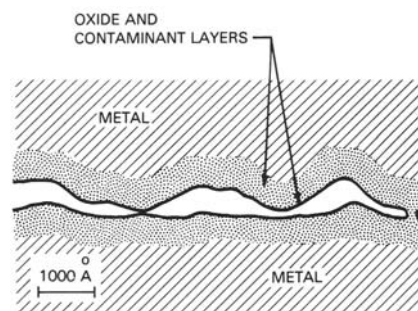


**Figure 2.10 – Metal surface under normal atmospheric conditions [82].**

Temperature, pressure and time to achieve solid state welding are adjusted to suit the materials involved, the workpieces nature as well as the facility and the technique being employed. In general, an effective temperature for solid state welding is at least 0.7 of the melting temperature of the metal to be joined. The pressure applied will depend on the workpieces nature, the surface conditions and the overall deformation that can be tolerated

[82]. The welding time varies over a wide range depending on which process is going to be used, but it is kept in a predetermined range in order to ensure the required intimacy at the faying surfaces, development of interatomic bonding and disappearance of interfacial oxide particle and voids.

### 2.5.1 Friction Welding (FW)

Friction Welding is a solid state welding process that produces a weld under compressive force contact of workpieces rotating relative to one another to produce heat and plastically displace material from the friction surfaces. This method relies on the direct conversion of mechanical energy to thermal energy to form a weld, without the application of heat from any other source. In its simplest form (see Fig. 2.11), it involves two axially aligned parts; while one is rotated and advanced to make pressure contact, the other part remains stationary (Fig. 2.11a and 2.11b). The axial force then increases to generate the necessary frictional heat for welding the surfaces in order to form a joint (2.11c and 2.11d) [83-89].

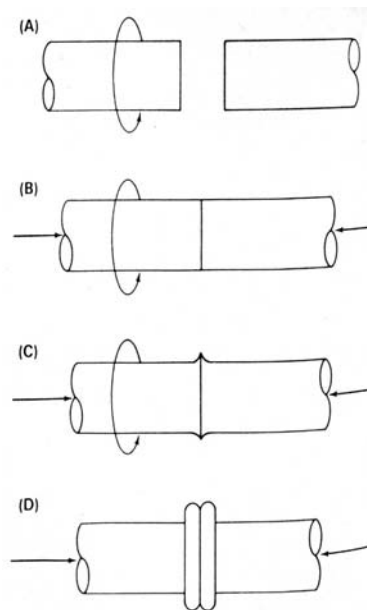


**Figure 2.11 - Basic steps in the friction welding process [84,86].**

While considered a solid state welding process, under some circumstances a molten film may be produced at the interface. However, even then the final weld should not exhibit evidence of a molten state because of the extensive hot working during the final stage of the process. The two general requirements for producing good friction welds are, first, that the materials to be joined can be forged and, second, that friction can be generated at the weld interface. Friction weld quality depends on the proper selection of material, joint design, welding variables and postweld treatment, if necessary.

There are two methods of supplying energy in the friction welding process: inertia friction welding, also known as flywheel friction welding, as well as direct drive friction welding, also called conventional friction welding [81-94,100]. In conventional friction welding, one of the workpieces is attached to a motor driven unit, while the other is restrained from rotation remaining stationary. The motor driven workpiece is rotated at a predetermined speed during the heating period; the workpieces to be welded are moved together and then a friction welding force is applied. Heat is generated as the friction surfaces rub together. Such process continues for a predetermined time, or until a preset amount of axial shortening takes place. The rotational driving force is discontinued and the rotating workpiece is made to stop (either by the application of a braking force or by its own resistance to rotation). The friction welding force can be either increased or not; if increased, it is denominated forging force and maintained for a predetermined time after rotation ceases to increase the upset of the heated metal at the joint. The friction weld is then completed [81,85,86,88,91,94,100]. Figure 2.12 shows the relationship of the direct drive friction welding parameters [87].

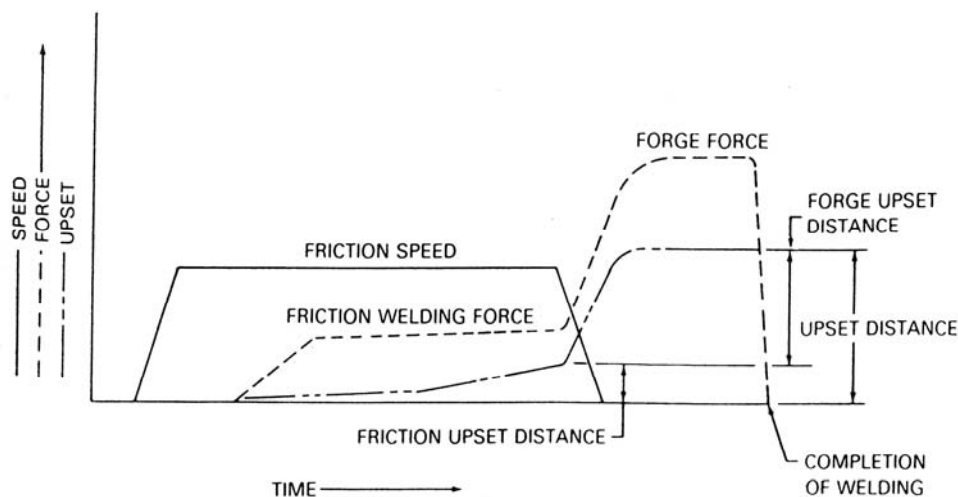


**Figure 2.12 – Characteristics of the direct drive friction welding parameters [87].**

In inertia friction welding, one workpiece is connected to a flywheel and the other is restrained from rotation remaining stationary. The flywheel is accelerated to a predetermined rotational speed, storing the required energy which is going to be converted into heat. The drive motor is disengaged and the workpieces are brought together by a friction welding force. This causes the faying surfaces to rub together under pressure. The kinetic (mechanical) energy stored in the rotating flywheel is dissipated as heat, through friction at the weld interface, as the flywheel speed decreases. The friction force is maintained for a predetermined time after the rotation ceases or increased (forging force) increasing the amount of upset and flash, which usually improves the weld quality and the mechanical



properties [88]. If the frictional heating has brought the interfacial area to a welding temperature, the rising torque causes the flywheel rotation to suddenly stop and the friction weld is formed. The energy made available for this particular welding operation will depend on the flywheel size, shape, weight and rotating speed [81,85,87,88,91,94,100]. Figure 2.13 shows the relationship of the inertia friction welding parameters [87].

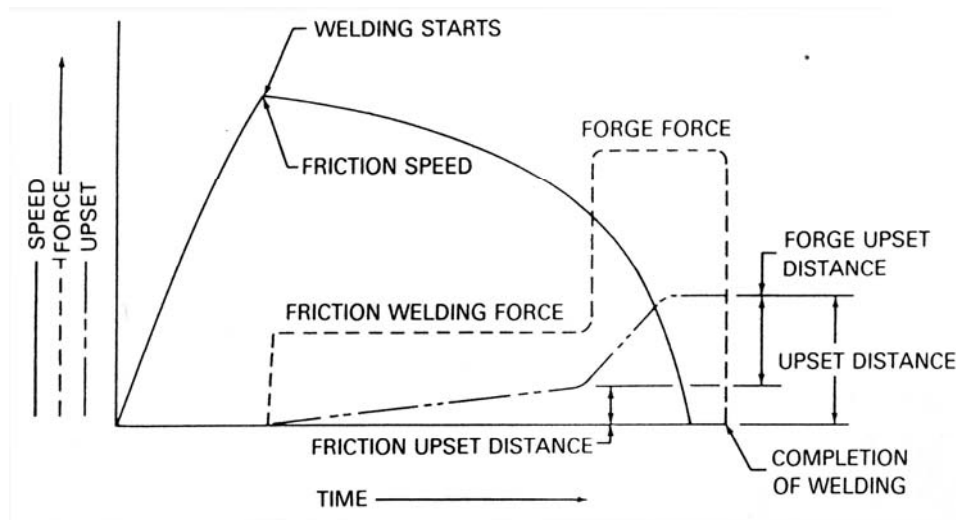


Figure 2.13 - Characteristics of the inertia friction welding parameters [87].

A brief comparison of the process parameters of the two methods of supplying energy in friction welding is presented in Table 2.4 [84,91].

Table 2.4 – Comparison between the process parameters of the direct drive friction welding system relative to the inertia friction welding system [84,91].

Process Parameters	Direct Drive FW	Inertia FW
Welding Parameters	Rotational Speed	Rotational Speed
	Axial force	Axial force
	Burn off	Flywheel moment of inertia
Energy conversion to frictional heat	Constant energy in a preset duration of rotation	Fixed energy in flywheel Rotational time determined by welding parameter
Energy input	Low	High
Heat generation rate	Low	High
HAZ width	Wide	Narrow
Cycle time	Similar	Similar
Machine system spindle rigidity	Less rigidity	Greater rigidity

The friction welding process can be divided in different phases and this division varies from author to author. AWS [87] as well as Elmer and Kautz [83] divide the process in two steps: (1) the friction stage, when the workpieces make contact, rubbing takes place between the friction surfaces and strong adhesion takes place at various contact points; and (2) the

forging stage, during the end of the heating process when forging pressure is applied to the workpieces causing axial shortening. Vill [86] divides the process into three phases, the first one is characterized by the predominance of exterior (dry or marginal) friction, the second phase starts with the appearance of seizures and is characterized by a vigorous increase in the number of unit seizure centres and the last stage is characterized by high temperatures during which the process has a tendency to become stationary. Crossland [89] has separated the process into 4 stages; during the first step predominantly dry friction exists; in the second phase seizure takes place and there is a very large rise in the torque before it reaches a limiting value due to the removal of the initial contaminant film; in the third phase there is a temperature increase resulting from the shearing of the increased areas of seizure; the last step is when the relative rotation is reduced to zero and the load is increased or kept constant. Any very plastic or fluid metal will finally be extruded out of interface, especially if load is increased, consolidating the weld. Ellis [92] has divided the friction welding process into 5 steps: the initial step is contact and initial friction; the second step is the viscous interface start; the third stage is when equilibrium conditions are achieved; the fourth stage is when a torque plateau takes place while the last step is weld completion.

Several other researchers [95-98] divide the process into three stages (but in a different way explained by Vill [86]). Stage I is characterized by rapid heating caused by dry friction and seizure. It starts when substrates are brought into contact at low applied load. Deformation process is dominated by frictional wear. In stage II, applied load is substantially increased and considerable frictional heating occurs at the bondline and a balance of strain hardening as well as a softening process is attained. It is characterized as a steady-state period where torque, temperature distribution and axial shortening rate become essentially constant. During stage III, the frictional heat generation is terminated and the applied stress is substantially increased to forge the heated material on either side of the bondline.

Duffin and Bahrani [99] have divided the friction welding process into two distinct phases: friction and forging stages. The former was further divided into 4 phases. In phase I two components start rubbing against each other, transferring material from one surface to the other. The material temperature rises and the size of the individual adhesion junctions increases leading to an increase in the torque which continues until the initial peak torque value is reached. In this phase decreasing rotational speed produce an increase in the torque while increasing the axial pressure increases the torque. Phase II is a transition in which the initial peak torque is reached and axial shortening begins. The temperature reaches a value at

which the material recovery rate exceeds the work hardening rate. The material then becomes "plastified" and starts to behave like a viscous fluid. In phase III, torque and axial shortening rate remain constant. In phase IV, the rotational speed decreases and the torque increases until a peak value is reached, then it drops to zero.

The most suitable division was presented by Pinheiro et al [91] and by Meyer [100] dividing the process into four stages. The stage I (rubbing) can be divided into two steps, the first one is the initial contact resulting in smoothening of the friction surfaces; the remaining part is characterized by seizing and microbonding processes [86,91,100]. Initially, only a small part of the welding surface actually makes contact; thus, the surface pressure reaches locally very high values promoting plastic deformation and hence, friction surfaces flattening. Apart from this, the outer regions of the joint are subjected to the highest relative rotational speed between the friction surfaces. By rubbing, the surface roughness is partly smoothened (starting in the outer regions) by elastic and plastic deformation. The region between 0.3 and 0.7 of the radius is subjected to severe deformation and heating, while the rest of the surface remains almost unaffected. Heating and plastification at the beginning of the process is mainly in the rotating specimen, which leads to an uneven HAZ and degree of deformation. Isolated local microbonding eventually taking place simultaneously across the contact surface is almost immediately sheared off inducing additional heating in the surrounding material. Owing to the high radial forces, isolated particles (particularly from the outer parts) are transported out of the rubbing zone (hydro-extraction effect). When the smoothening in the outer regions is completed it starts to develop towards the rotational centre. In the outer regions almost no heat is produced during this intermediate phase due to the reduced friction contact (surfaces are smoothened) and the presence of oxide layers generated in the first part of rubbing. Lower radial forces and restricted material flow closer to the rotational centre obstruct the hydro-extraction effect of the surface contamination particles; therefore material concentration on a circular ring area can be observed, its distance from the rotation centre is about 0.5 to 0.7 of the friction surface radius (Fig. 2.14 – green areas), causing local heating forming a thin plastified film of sheared off material. Such ring area increases in size, an increased amount of the friction surfaces make contact and more isolated microbonding is produced. Owing to heat conduction the temperature also rises in the axial adjacent material. The rubbing phase is completed when the friction moment reaches its maximum caused by the removal of the contaminant film and by the additional friction caused by the rough surfaces produced by seizure [100].

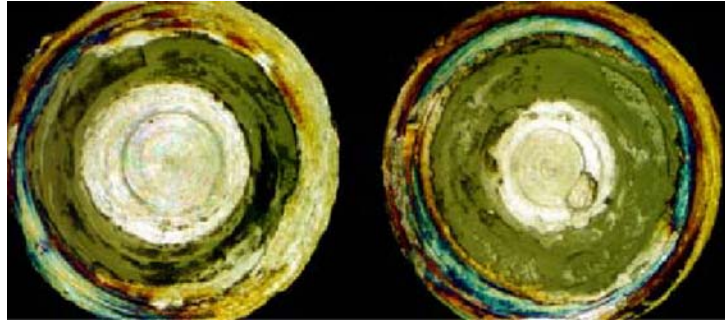


**Figure 2.14 - Schematic illustration of plastified material concentration (green areas indicate concentration – 0.5 to 0.7 of the radius) during rubbing stage after different rubbing durations [100]. Outer part shows oxidation due to heating; while the inner region shows unaffected surface (machining marks).**

In stage II (heating), the increasing temperature in the plastified ring causes the squeezing of highly plastified material to cooler zones of the friction area. Due to the immediate cooling of the plastified material intense friction is produced again in these particular zones and the plastified ring area is extended towards the rotational centre and outer regions (Fig. 2.15). In the outer regions of the weld, the material is easily pressed out of the friction surfaces due to the high plastification and low deformation constrain. As material temperature and plastified zone height increases, the resistance to axial force reduces and the material is pressed out of the friction area forming the flash. The plastified zone height decreases and cooler areas make friction contact, heat up and become plastified. Such process is kept as long as the temperature and the plastified zone height can be kept in equilibrium result more flash is formed. A stationary temperature field is achieved at the friction surfaces and the friction moment decreases. From this point on an almost constant burn-off rate is established. With increasing workpieces thermal saturation the energy required for plastification reduces leading to a lower friction moment [100]. However, the growing flash increases the friction surface and hence the friction moment. Wang and Nagappan [101] affirm that these phenomena balance each other resulting in an almost constant friction moment. The heating phase is finished when the process reaches the limiting control parameter (predetermined temperature, burn-off or time).

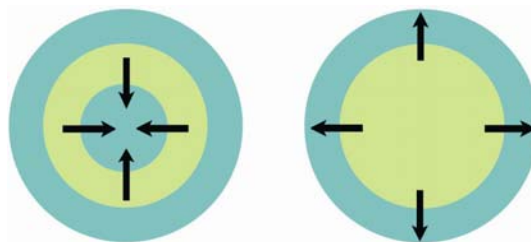


**Figure 2.15 - Schematic illustration of the friction surfaces during heating phase [100]. Plastified ring area extends initially towards the rotational centre and then to the outer regions.**

The stage III (breaking) is also divided into two steps, starting with a controlled rotational speed decrease. Due to the processes described in the heating phase there is a temperature drop. Additionally, the shear resistance increases owing to the lower deformation rate and hence the friction moment reaches its second peak. Such increase in the friction moment causes additional deformation in the adjacent material, which had so far not been subjected to any deformation. The lower rotational speed also results in a higher burn-off rate. The last step of the breaking stage is characterized by a rotational speed reduction to such a low level that the temperature of the friction surfaces can no longer be maintained; therefore the shear resistance of the material increases and torsional deformation takes place in a larger region along the workpieces. The friction moment increases substantially, staying constant for some milliseconds (see Fig. 2.16 – phase 3-2) [100].

The last stage (bonding) is when a homogeneous bonding is achieved by the application of a forging pressure. The increased force results in an increase of the upset rate. The welding surfaces make closer contact and the material is brought together within atomic distances to produce metallic bonding. After the rotation has stopped, deformation is completed, but diffusion process still occurs (static recrystallisation, crystal regeneration and creeping process [100]). Figure 2.16 presents the friction welding parameters and process phase division [91].

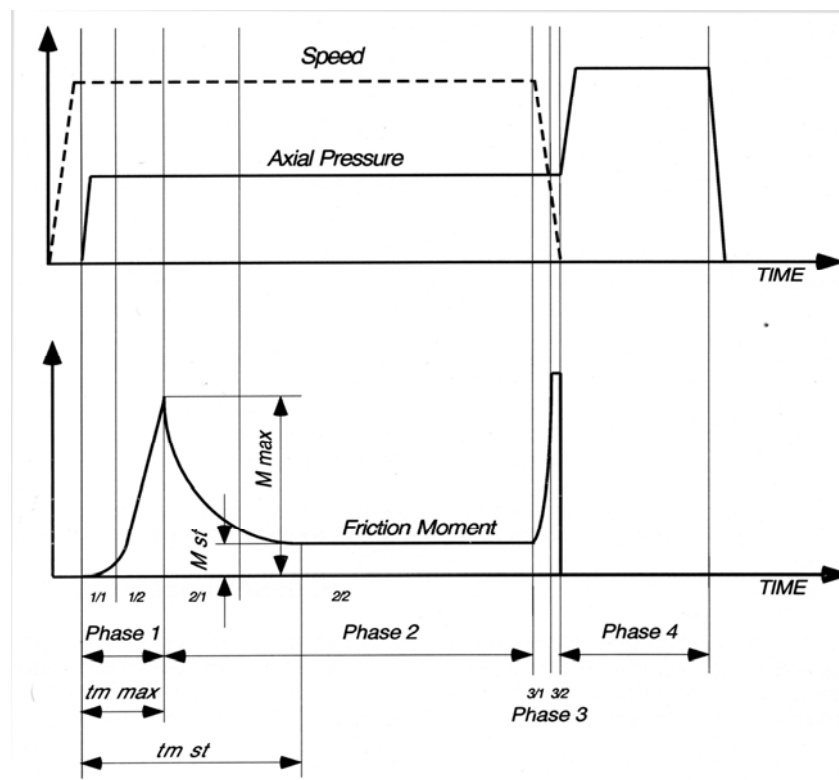


Figure 2.16 - Friction welding parameters and phase division [91].

There are several relevant process parameters, however only four are going to be considered in more details due to its relative importance to the process regarding the amount of weld energy input and the rate of heat generation at the interface when using direct drive friction welding [81-86,91,93,94,100].

### ***2.5.1.1 Rotational Speed***

According to Vill [86], the rotational speed is the least sensitive process parameter and it may vary over a rather wide range without influencing the weld joint quality. However, there are certain optimum speeds for each individual material combination and application [100]. The main function of rotation is to produce a relative velocity at the friction surfaces. From the standpoint of process intensification and quality improvement of the welded connection (especially metals sensitive to overheating), it is desirable to use relatively low rotational speeds since process efficiency is improved as a result of reduced heat losses, which reduce the amount of energy used for welding. According to Pinheiro et al [91], at high rotational speeds deep tearing is replaced by a polishing action. As a result, to achieve the conditions for plastification at the friction surfaces, longer heating times are required allowing thermal energy propagation along workpieces axial direction and as a consequence a greater volume of material is heated. Therefore, high rotational speeds lead to lower cooling rates, wider heat affected zone (HAZ) and hence lower hardness at the bonding line vicinity. On the other hand, low rotational speeds produce a thinner HAZ with a profile that is much more pinched in comparison with welds produced at higher rotational speeds. Therefore, low rotational speeds lead to higher cooling rates and higher heating times resulting in higher hardness. Generally speaking, an increase in the rotational speed reduces significantly the ultimate tensile strength [91,92,102]. However, Nessler et al [103] studying parameters influence in two titanium alloys (Ti6Al4V and Ti6Al2Sn4Zr2Mo) showed that neither ultimate tensile strength nor yield strength were affected by any of the parameters analysed (normal pressure, rotational speed, concentricity, squareness and surface finish). Zhou et al [104] analysing aluminium MMCs and AISI304 friction joints showed that when rotational speed is increased, the tensile strength initially increased and then levelled out.

### ***2.5.1.2 Pressure (Forging and Friction)***

The pressure may vary in wide range and controls the weld zone temperature gradient, the required drive power and the axial shortening. The specific pressure depends upon metals being joined as well as joint geometry and can be used to compensate for heat loss to a large mass. The heating pressure must be high enough to hold the friction surfaces in intimate

contact to avoid oxidation. For a set rotational speed, low pressure limits heating with little or no axial shortening. High pressure causes local heating to high temperature and rapid axial shortening (high burn-off rate). After the heating stage, two different methods of varying axial pressure are usually utilised: keep pressure constant or increase it. The ultimate and the notch tensile strength generally increases when pressure is increased [91,92,102,104,105]. Such behaviour is explained in terms of frictional energy per unit volume since this value is maximized when a high frictional pressure is used producing joints with high notch tensile strength [105]; which is confirmed by Shinoda et al [106] reporting high notch tensile strength when a high energy input (in terms of pressure) was applied. It is generally recommended that the forging pressure should be at least twice the frictional pressure for production of joints free of unbonded regions [107]. Additionally, increasing the pressure causes an increase in the upset rate and as a consequence the heat input amount is low resulting in higher cooling rates and hardness. For a given burn off, the time from the initial contact of the surfaces to the end of the welding procedure decreases as the normal force increases. The higher the pressure, the faster the material is consumed and the shorter the welding time will be [100].

The axial pressure also influences the HAZ width and shape changing from an almost parallel sided boundary at low pressures to a more "pinched" or double-cone profile at the stud centre at high pressures [85]. In the latter, the heat liberated is totally used to plastify the material and hence does not propagate in the axial direction. According to Ellis [92], the welds made at higher forces show a narrower region where the hardness values are lower than in the parent material. It means that the higher the force is, the more pinched the hardness profile will be in the interface region [100]. Figure 2.17 presents the effect of the axial pressure and the rotational speed over the HAZ width and shape [84].

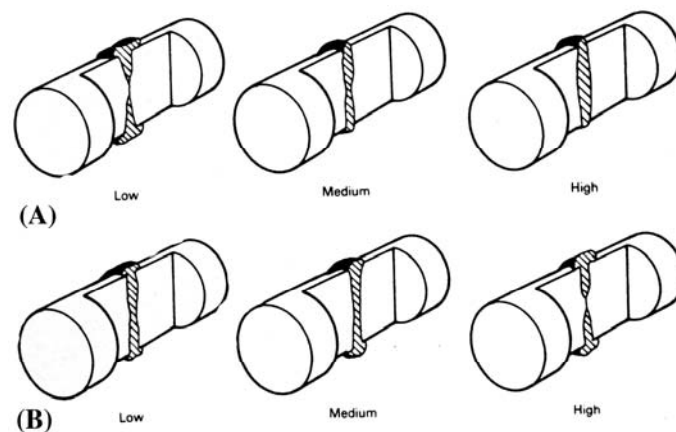


**Figure 2.17 - Schematic representation showing the effect of the welding parameters on the HAZ shape and width. (A) Rotational speed and (B) pressure [84].**

### **2.5.1.3 Heating Time**

According to Lebedev and Chernenko [108], the friction welding process may be regulated either by the heating time or the upsetting during heating. Regulation in time is recommended in those cases where the workpiece linear dimensions have large tolerances and joining surfaces are not machined or are machined roughly or inaccurately. Regulation by upsetting value is used in those cases where parts dimensions have to satisfy strict requirements. However, Vill [86] suggested that it would be better to select the heating period duration rather than the upset as the third basic parameter based on the fact that for a given power of the process (the speed and pressure are given) the duration fully determines the energy to be utilised for welding. The heating time determines the temperature conditions of the process and the plastic deformation of the specimen is derived from the temperature conditions [100]. The heating time is defined as the period from the initial contact of the friction surfaces to the end of the breaking phase. It is significantly influenced by the axial pressure and rotational speed [91] as well as the material properties and joint diameter [108]. It is reduced as pressure is increased and decreases with rotational speed [91]. It is important especially for a low upset rate because it not only defines the interface microstructure but also controls the depth of heating by conduction and therefore the HAZ width [92]. The cooling rate is affected by the surrounding media and the welding time combined with the total amount of flash formed around the weld interface. If the flash has a large mass, then the heat stored within the flash will be conducted back into the weld thereby reducing the cooling rate of the metal within the HAZ. Short heating times naturally result in a high heat generation rate which also involves a relatively high upset rate forming a big flash where most of the heat is stored as sensible energy. In comparison, when using longer heating times, not all of the heat generated at the weld interface is stored in the flash, but much of it has time to conduct into the welded parts. It is desirable, in order to improve the weld joint quality, to have short heating times without flash formed. Thus, the cooling rate will be higher and mechanical properties will be improved. On the other hand, if it is desirable to preserve the toughness behaviour it is better to have longer heating time and lower cooling rate [91].

### **2.5.1.4 Burn-Off**

The burn-off describes the amount of plastified material and is usually measured as the axial shortening of the rotating workpiece. It can be also described in terms of the burn-off rate (amount of burn-off per second) and can be considered as a representation of the welding speed. It has also a significant influence on the weldment properties and not only controls the welding cycle. The applied force and rotational speed will influence the time needed to reach



the preset amount of burn-off. The time from surfaces initial contact to the end of the burn-off becomes shorter as the force increases and a lower speed results in a higher burn-off rate for the same nominal pressure [92,100]. According to Vill [86], controlling the process by the burn-off has its disadvantages since it can occur large burrs (central projections remaining on specimen surface) as well as surface defects affecting negatively the weld quality.

### 2.5.2 Diffusion Bonding

Diffusion bonding is a solid state welding process that produces solid-state coalescence between two materials under the following conditions [109]:

- Joining occurs at a temperature below melting point ( $T_m$ ) of the materials to be joined (usually  $> 0.5 T_m$ ).
- Coalescence of the contacting surfaces is produced with loads below those that would cause macroscopic deformation to the part.
- A bonding aid can be used (i.e. intermetallic foil) to either facilitate bonding or prevent the creation of brittle phases between dissimilar materials, but the material should not produce a low-temperature liquid eutectic upon reaction with the materials to be joined.

According to the AWS definition, diffusion welding "is a solid state welding process that produces a weld by application of pressure at elevated temperature with no macroscopic deformation or relative motion of workpieces". Thus, it facilitates joining of materials to produce components with no abrupt discontinuity in the microstructure and with a minimum of distortion [110]. Kazakov [111] described the process as: "a monolithic joint is due to the formation of metallic bonds as a result of local plastic deformation at elevated temperature, closest approach of the surfaces and interdiffusion in the surface layers of the metals brought in contact". It can be divided into three main groups, depending on type of pressurization, use of interlayers and liquid phase formation [11,112]: solid state diffusion bonding; liquid state diffusion bonding (diffusion brazing) and superplastic forming-diffusion bonding (SPF-DB).

The specific advantages of the process include its ability to join most of the metals and some non-metals in similar or dissimilar combinations, minimal amount of deformation and the fact that the weld area is mostly independent of the welding time. These advantages are offset by the need to machine parts to fairly tight tolerances on the component fit-up, as well as surfaces finish. Other disadvantages include, the longer thermal cycle (normally longer than that of conventional welding and brazing processes), equipment costs and non-adaptation to high production rate [110]. In addition, diffusion bonding avoids undesirable structural transformations since temperatures involved in the process are rather low. Messler [88] has

described more advantages, such as no presence of HAZ since the entire assembly in which diffusion bonding is being made is virtually heated to the same temperature, use of filler to permit increased microdeformation to provide more contact for bond formation and/or promote more rapid diffusion by providing faster diffusing species. According to Pilling [113] the major reasons for using diffusion bonding as opposed to adhesive bonding are as follows: first, since no melting or additional materials are involved there is no discontinuity in properties at the bond; second, since the pressure required to form the bond is very low with respect to the yield strength, there is virtually no distortion of the component during bonding, nor any temperature gradients developed which could lead to distortion following bonding.

These prime advantages have led to the extensive use of diffusion bonding in a wide range of industries extending from electronic to nuclear fields and manufacturing of various engineering components. According to Çam and Koçak [11], another driving force extending the use of diffusion bonding is the increasing development of advanced materials, such as MMCs and intermetallics where fusion processes are not generally applicable or are of limited use. Another important area is dissimilar bonding of ceramics to metals. Despite reports of dissimilar combinations, more demanding applications are expected especially in engine parts from automotive and aerospace components. In such applications, the joints that can withstand much more severe operating conditions than the previously considered will be required. The widest application area is in the aerospace industry, often used in combination with superplastic forming for the production of aircraft and aerospace components.

Holding times at elevated temperature can exceed 60 minutes, but this depends on the material types being bonded, the joint properties required and the remaining bonding parameters [11]. It should be understood that the parent metal strength is only approached for materials with surface conditions that do not have barriers to impede atomic bonding, such as the absence of surface oxides or absorbed gases. In practice, oxide-free conditions exist only for a limited number of materials [109]. Accordingly, real surfaces properties limit and impede extent of the diffusion bonding. Most notable exception is the titanium and its alloys, which at bonding temperatures higher than 850°C, can readily dissolve minor amounts of adsorbed gases and thin surface oxide films and diffuse them away from the bonding surfaces, so that they will not impede formation of required metallic bonds across the interface. A second class of material, that is, metals and alloys that exhibit very low solubility for interstitial elements (such as aluminium alloys) are not readily diffusion bonded. Special consideration must be given to remove the surface barriers to atomic diffusion prior to joining

and prevent their reformation during the bonding process. The surfaces of the metals have several general characteristics such as, roughness, oxidized or chemically reacted and adherent layer as well as other solid or liquid products (oil, grease) or adsorbed gas (Fig. 2.10). Two necessary conditions must be met before a satisfactory diffusion weld can be made [110]: mechanical intimacy of the faying surfaces; and disruption and dispersion of interfering surface contaminant to allow metallic bonding.

The nature of the process is essentially the coalescence of two atomic clean solid surfaces [106,111], and it comes about through a three-stage metallurgical sequence of events, namely, microasperity deformation, diffusion-controlled mass transport and interface migration. Other authors divide the process into two stages: stage I is when plastic flow disrupts oxide film to expose clean metallic surface and produce intimate contact; stage II is when bonding is established by atomic interdiffusion and recrystallisation and/or grain growth across bond interface [11,114]. However the most suitable division is when each stage is associated with a particular metallurgical mechanism that makes a dominant contribution to the process. Consequently, the stages are not discretely defined, but begin and end gradually, because the metallurgical mechanisms overlap in time (Fig. 2.18) [88,109].

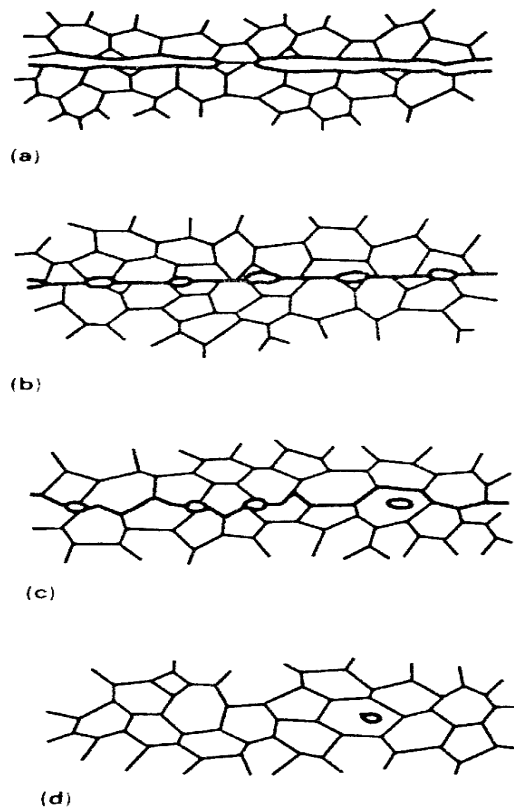


**Figure 2.18 - Metallurgical stages sequence in the bonding process. (a) Initial contact: limited to a few asperities. (b) Stage I: deformation of surface asperities by plastic flow and creep, a thinner oxide layer with large voids results. (c) Stage II: grain boundary diffusion of atoms to voids and grain boundary migration. (d) Stage III: volume diffusion of atoms to the voids [109].**

### 2.5.2.1 *Microasperity Deformation*

The stage I is denominated microasperity deformation (Fig. 2.18b) and the nature of the starting surface is of considerable importance because of the small macroscopic deformation allowed during diffusion bonding. The metal-to-metal contact area between the surfaces is a very small fraction of the joint contact area therefore contact is limited to a relatively few microasperities. At room temperature and under load, these asperities deform as long as the surface contact area is such that material yield strength is exceeded. As temperature increases to the bonding temperature, the material flow stress decreases and additional asperity deformation occurs through plastic flow. Again flow occurs until the contact area increases to an extent that the material yield strength is exceeded. With time at temperature, creep mechanisms now control the asperity deformation rate and the contact area continues to grow. As it grows the stress acting on the surface asperities decreases. Consequently, creep deformation progressively slows and diminishes in significance.

The temperature and pressure contributions to both plastic and creep deformation during stage I are synergistic, i.e., at higher temperatures, less pressure are required and vice versa. For example, for a distinct material, at lower pressures (using the same temperatures), where surface deformation is lower during stage I, large voids remain at the interface, even after a reasonable time at the temperature. However when higher pressures are applied and a corresponding greater initial interface deformation, the interface becomes indistinguishable from the matrix alloy. Ideally, at the completion of stage I, the asperity collapse extent should result in a planar area of contacting surfaces with individually dispersed voids.

The surface roughness plays an important role in time dependency for completion of the different stages. Surfaces that are mated at the bond line are usually rather irregular as a result of machining or other surface preparation steps. It is expected that during the stage I, a more uneven initial surface that is due to either roughness or waviness would produce more large voids than would a smooth initial surface. For example, as the load is applied, asperities on rough surfaces will experience higher stresses on contact points. Plastic flow will occur at a lower load and greater interface shear will occur. Although the first-stage plastic flow and creep will create more localized interface deformation for a rough surface, fewer but larger voids will remain at the interface. In addition to size, the void shape and curvature would be different, with higher aspect ratio voids for rougher starting surfaces. For diffusion-controlled collapse of the interface voids during stage II, an initially rough surface will require a longer time or higher temperatures for mass-transport processes to shrink and eliminate voids [109].

### 2.5.2.2 Diffusion-Controlled Mass Transport

The densification or collapse of the interface cavities during stage II (diffusion-controlled mass transport - Fig. 2.18c) is attributable to the lowering of the surface free energy by the decrease in surface area. This takes place with the formation of new, but lower-energy, solid state interfaces. A number of mass-transport processes are operative simultaneously, including time-dependent plastic flow, diffusion from the interface to the cavity via lattice, interface and grain boundaries as well as diffusive flow around the void surface via lattice and vapour phase. These different paths of mass transfer are shown in Fig. 2.19 according to the following list: (1) plastic yielding that deforms an original contacting asperity, (2) surface diffusion from a surface source to a neck, (3) volume diffusion from a surface source to a neck, (4) evaporation from a surface source to condensation at a neck, (5) grain boundary diffusion from an interfacial source to a neck, (6) volume diffusion from an interfacial source to a neck and (7) power-law creep [109,115].

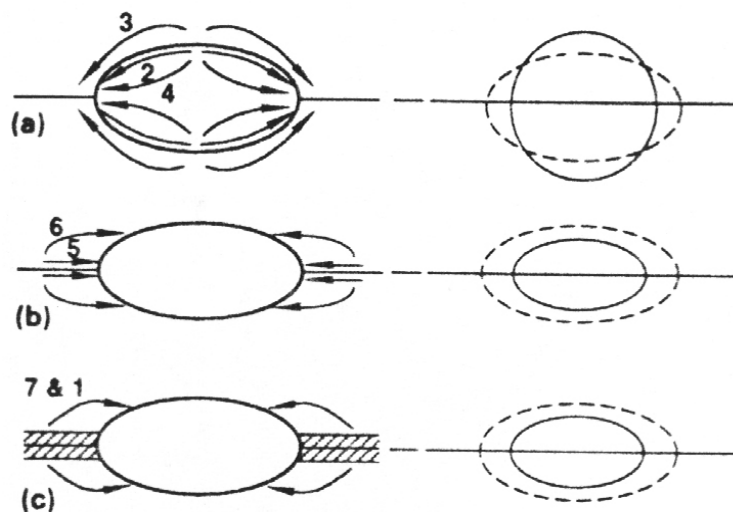


**Figure 2.19 - Paths of material transfer generated during the bonding process. (a) Surface mechanisms. (b) Interface mechanisms. (c) Bulk deformation mechanisms [109,115].**

Some transport paths such as, the vapour transport and the matter surface transport, have only secondary influence on the void collapse rate since they do not alter void volume. Only the transfer of matter from the matrix volume or grain boundaries cause shrinkage and pore elimination; thus, only plastic flow and interface diffusion actually reduce the interfacial voids volume. The dominance of either of these processes is dependent on many inseparable factors, including material system, voids geometry, microstructure and diffusion bonding parameters. When considering diffusion, evidence seems to suggest that the most efficient path for atom flow and counterdiffusing vacancies is along the interfacial grain boundary and grain boundaries that intersect the void when the grain size is smaller than the pore size.

Diffusion is, at times, the rate-controlling factor for void coalescence. Maintaining temperature while removing the pressure following stage I was shown to not significantly impede the joining process. The void elimination rate was only slightly slower without the applied pressure. However, this rate change could be due to either the lost contribution that deformation makes to void coalescence or the reduction in the stress-enhanced grain boundary efficiency contribution [109].

### ***2.5.2.3 Interface Migration***

During the stage II, voids become much smaller and many are eliminated. Their grain boundary pinning influence decreases, so that the interfacial grain boundary migrates toward an equilibrium configuration which is indistinguishable from the other grain boundaries in the microstructure. The boundary migration driving force is the reduction of the grain boundary area. Initially the straight interfacial bond line becomes distorted with local penetrations of a few microns of one material to the other at triple points. As the boundary moves, any remaining void becomes enclosed within the grains where they are no longer in contact with the grain boundary. Diffusional processes continue to shrink and eliminate these cavities, but the diffusion path is now restricted to volume diffusion through the matrix lattice. Accordingly, the elimination of this final porosity small volume would be likely to contribute an inordinate time to process for any interface strength benefits that might be achieved [109].

### ***2.5.2.4 Influence of the Diffusion Bonding Parameters on the Process***

Among three bonding key parameters, two are of significant importance: temperature and pressure. The former helps to promote weld formation by driving off the volatile absorbed layers of gases or organic contaminants, by breaking down brittle oxides through differential thermal expansion or thermal decomposition or, by disrupting the continuity of these layers and finally by lowering the yield strength of the base material allowing plastic deformation under pressure to bring more atoms into intimate contact across the interface. The pressure helps welding to take place by disrupting absorbed layers of gases by macro- or microscopic deformation, by fracturing brittle oxides or tarnish layers to expose the clean base material atoms as well as plastically deforming the asperities to increase the number of atoms, and thus, the intimate contact area [109].

According to Kazakov [111] the three bonding variables play different roles during the bonding process. The bonding temperature should be anywhere between 50% to 70% of the most fusible metal melting point. Elevated temperature aids interdiffusion of atoms across the weld interface assisting surface deformation. The bonding pressure should ensure contact

between the edges of the pieces and it must be sufficient to aid surface asperities deformation as well as to fill the voids in the weld zone. If pressure is not enough, some of the voids will be left unfilled, and the joint strength will be impaired. Importantly, the pressure load disperses the oxide films leaving a clean surface and aiding diffusion and coalescence. The holding time at the specific bonding temperature and pressure must in some cases be kept to a minimum from physical and economic considerations. It should be just sufficient for an intimate contact to be formed and for diffusion to take place. Excessive diffusion time might leave voids in the weld zone or even change the metal chemical composition or lead to the formation of brittle intermetallic phases.

Temperature is the most influential variable since together with pressure determines the contact area extent during the stage I and alone determines the diffusion rate that governs the void elimination during stages II and III. Pressure is necessary only during the stage I to produce a large contact area at the welding temperature. Pressure removal after this stage does not significantly affect the joint formation; however, premature pressure removal before stage I completion is detrimental to the process. Time required to form a joint depends upon the temperature and pressure used which means that time is not an independent variable [110].

According to Kazakov [111], the joint quality heavily depends on the temperature at any bonding pressure. Messler [88] affirms that among the three key process parameters, temperature is by far the most important, provided there is enough pressure to cause contact between the joint elements since diffusion occurs by an Arrhenius type relationship (see Eq. 2.9) that varies exponentially with the temperature:

$$D = D_0 e^{\frac{-Q}{kT}} \quad \text{Equation 2.9}$$

where  $D$  is the coefficient of diffusion (of the diffusing species) at the temperature  $T$ ,  $D_0$  is a constant of proportionality (dependent on the particular diffusing species and host),  $Q$  is the activation energy for the type of diffusion to occur,  $k$  is the Boltzmann's constant and  $T$  is the temperature (in Kelvin).

According to Messler [88], time is also important because diffusion takes time to occur (atoms jumping from site to site takes time); thus, the distance over which diffusion occurs depends on time according to the Equation 2.10:

$$x = C(D * t)^{\frac{1}{2}} \quad \text{Equation 2.10}$$

where  $x$  is the diffusion distance,  $D$  is the coefficient of diffusion (of the diffusing species),  $t$  is the time and  $C$  is a constant for the system.

### 2.5.3 Joining of MMCs and TMCs

The high inherent thermal conductivity and serviceability as well as other important metal properties and their strength extension to higher temperatures through reinforcement by appropriate materials often dominate property requirements when MMCs are selected and used. Therefore, when MMCs need to be joined, the joining process must result in bonding that can tolerate high temperatures and preserve reinforcement across the joint as much as possible. Joining of such materials is clearly an important manufacture feature and attractive method for making complex products since these materials usually have high strength and moduli retaining their strength to high temperatures. However there are a number of problems peculiar to MMCs [116,117]:

- In the particulate reinforcement case, the particles may have different densities from those of the matrix leading to pronounced segregation effects. The higher the reinforcement volume fraction, the less likely for standard metal joining techniques to adapt to the MMC. The discontinuously reinforced MMCs are easier to join than the continuously reinforced.
- Prolongated contact between the molten metal matrix and the reinforcement can lead to undesirable chemical reactions which are accelerated as the molten metal temperature is increased; therefore, matrix-reinforcement chemical compatibility is a temperature and material dependent factor. For this the higher the metal matrix melting temperature, the less likely fusion welding techniques will be applicable.
- Although high thermal energy is required for many conventional joining processes, excessive thermal energy input is undesirable. Therefore, the automated or special joining process use that can offer well controlled thermal energy input in minimum process time will likely improve MMCs joining adaptability.
- Materials ductility is very low compared with that of the matrix material, and thus the risk of cracking in the weldment, particularly in fusion processes, is higher.



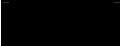
Solid state diffusion bonding and friction welding can be considered an attractive alternative to fusion welding processes since both processes do not involve melting of the parent base metal. The key problem in joining TMCs by fusion joining processes is the particulate rejection by the solidifying interface. Most of the MMCs are reasonably homogeneous, but following fusion welding, ceramic particles agglomerate in the interdendritic regions, reducing their efficiency as reinforcement. The magnitude of this effect and its significance are clearly influenced by the particle size and cooling rate, which



determines the dendritic cell size. In large weld pools, gravitational effects may also lead to enhanced macrosegregation [117]. Indeed, TMCs have proved to be quite sensitive to fusion joining processes due to the high chemical reactivity of titanium that leads to a chemical interaction with the reinforcing material having a deleterious effect on the mechanical properties of the joint. Besides this, the solid state welding processes for TMCs offer several advantages over the fusion processes such as low heat involved, minimal disrupt in the microstructure of the material as well as the avoidance of many defects, such as solidification segregation and cracking, porosity as well as hydrogen embrittlement. However the most significant advantage is the possibility of joining dissimilar materials which can lead to several improvements. Table 2.5 shows the joining process applicability of fusion and solid state welding compared to joint applications.

**Table 2.5 - Qualitative rating for joining adaptability, applications and selection of different joining processes (solid state welding and fusion welding processes) [36].**

Joining Methods	Strength driven	Stiffness driven	High temperature	Dimensional stable	Complex shapes	Dissimilar materials	Applicability for MMCs
<i>Inertia Friction Welding</i>				Medium	Low	Low	
<i>Friction Stir Welding</i>					Low	Low	
<i>Diffusion Bonding</i>	Medium					Low	Medium
<i>Laser Beam Welding</i>				Medium	Low	Low	Low
<i>Electron Beam Welding</i>				Medium	Low	Low	Low
<i>Gas Metal Arc Welding</i>				Medium		Low	Low
<i>Gas Tungsten Arc Welding</i>				Medium		Low	Low
<i>Brazing</i>	Medium		Medium	Medium		Low	Medium
<i>Soldering</i>	Medium		Low			Low	Low

Joint Performance Rating: High  Medium  Low 

Fusion welding, brazing as well as resistance spot welding processes have already been used to join TMCs. Hirose et al [118] and Fukomoto et al [119] have carried out studies in laser-beam welded Ti6Al4V reinforced with SiC fibres. Although there was no significant physical damage to the fibres from the process, temperatures involved have led to reactions between the reinforcement and the matrix degrading the mechanical properties. Hirose et al [118] have observed that the high heat input resulted in SiC decomposition and subsequent TiC formation causing joint strength degradation. Fukomoto et al [119] have concluded that dissimilar laser-beam welding of Ti6Al4V SiC fibre-reinforced and Ti6Al4V can be achieved without serious fibre damage by directing the laser beam onto the Ti6Al4V plate. Brazing of

TMCs is also possible and Blue et al [120,121] have used infrared energy heating to braze SCS-6/Beta 21S TMCs using a Ti15Cu15Ni filler metal. Very rapid cooling and short dwell at the brazing temperature (60s at 1100°C) is possible resulting in strong bonds with a high temperature capability when compared with diffusion bonding. The Welding Institute has also reported the use of a variation of the resistance spot welding process (resistance heating) to weld SiC fibre reinforced Ti6Al4V MMCs by using relatively low welding currents and longer welding times to avoid fusion and promotes solid phase bonding [122].

### **2.5.3.1 Friction Welding of MMCs and TMCs**

Similar and dissimilar titanium alloys friction welding have been extensively studied, primarily because of their application in the aerospace and chemical industry [22,91,100,123-137]. However, a literature survey has indicated a limited amount of information available on similar and dissimilar friction welding of TiC particulate reinforced Ti6Al4V alloys.

The fabrication of structural components often requires welding and as explained above the fusion welding processes, especially in particulate-reinforced titanium alloys, are not recommended, primarily due to high heat input and fast cooling rate that frequently lead to local microstructural changes which, in turn, change the mechanical behaviour of the local welded joint and, thereby, the welded component overall performance. Besides that, problems related to porosity and clustering of reinforcing particles have also been found [11].

Friction welding in MMCs using similar and dissimilar combinations have been extensively studied [95,97,98,104,105,107,138-145]. Midling et al [138] have demonstrated the possibility of joining A357 aluminium alloys reinforced with 10 vol.% SiC particles without promoting segregation of SiC particulate at the joint centreline (the HAZ on either side of the bondline contained an uniform distribution of precipitates). Cola and Baeslack [139] have examined the relationship between the joining parameter settings and the tensile and torsional strength properties of friction welded Al 6061+10 vol.% Al<sub>2</sub>O<sub>3</sub>. However, the presence of unbonded regions, excessive joint misalignment and failure to remove external an internal flash from completed joints severely compromised the analysis of the results. Maldonado and North [95] have studied the influence of welding parameters, reinforcing particle chemistry and shape as well as matrix condition on particle fracture in similar and dissimilar friction welding combination (MMC to MMC, MMC to Al 6061, MMC to AISI 304 and MMC to 1020). Results have shown that smaller particles were produced when the friction and forging pressures were increased during dissimilar friction joining. The particle fracture tendency markedly increased when the MMC (6061+16.8 vol.% Al<sub>2</sub>O<sub>3</sub> and also

6061+20vol.% of  $\text{Al}_2\text{O}_3/\text{Fe}_2\text{O}_3/\text{SiO}_2/\text{TiO}_2$ ) material contained blocky alumina particles. However there was negligible particle fracture when the MMC material contained spherical-shaped  $\text{Al}_2\text{O}_3\text{-Fe}_2\text{O}_3\text{-SiO}_2\text{-TiO}_2$  particles.

Zhou et al [105] studying the mechanical properties of Al-based MMCs (6061+10 vol.%  $\text{Al}_2\text{O}_3$ ) and Al 6061 alloys in similar and dissimilar combination have shown that the frictional pressure has a statistically-significant effect on the notch tensile strength of the joints produced in all base material combinations. It was also demonstrated that the fatigue strength of MMC/MMC joints and 6061/6061 joints are poorer than the base materials. Midling and Grong [97] have developed a process model for the microstructure and strength evolution during continuous drive friction welding of Al-Mg-Si alloys and Al-MMCs alloys. North et al [98] studying Al 6061+10 vol.%  $\text{Al}_2\text{O}_3$  and AISI 304 stainless steel in similar and dissimilar combination suggested that small-diameter particles formed due to fracture early in the friction joining operation are retained at the bondline of MMC/MMC joints as a direct consequence of the flow of plastified material and reinforcing particles in the contact zone.

Li et al [107] studying different joint combinations using MMCs (Al 6061+10 vol.%  $\text{Al}_2\text{O}_3$ ), Al 6061 alloy and AISI 304 stainless steel have demonstrated the successful application of friction welding process when using correct parameters (high friction pressure) which has produced good notch tensile strength properties. Zhou et al [104] have demonstrated the influence of joining parameters (rotational speed, frictional time and pressure) in dissimilar welding of a particulate MMC (Al 6061+10 vol.%  $\text{Al}_2\text{O}_3$ ) and a AISI 304 stainless steel showing that the frictional pressure and the rotational speed had a statistically-significant effect on the notch tensile strength values. North [140] has studied the metallurgical and mechanical properties of friction joints in particle-reinforced Fe-based and Al-based MMCs showing the influence of the joining parameters over particle fracture that is retained at the joint interface as a direct result of the fluid flow in the weld zone. Pan et al [141] have investigated the microstructural characteristics of dissimilar welds between 6061+10% vol.%  $\text{Al}_2\text{O}_3$  and AISI 304 stainless steel showing that a interlayer was formed at the dissimilar joint interface comprising a mixture of oxides and intermetallic phases.

#### **2.5.3.1.1 Particle Fracture Phenomenon in Particulate-Reinforced Friction Welding**

Particle fracture is an important issue while friction welding particulate-reinforced composites since the reinforcing particles can provide information concerning detailed features of friction-joining process. The particle fracture process occurs early in the

deformation process and increases at high strain levels [95,96,98]. Particle cracking extent depends on particle size distribution and aspect ratio and on the matrix microstructure [98].

When two substrates are brought together, the contact occurs between the protruding asperities and the reinforcing particles in a composite material. The magnitude of the pressure contact will depend on the contacting substrates nature, elastic moduli, coefficient of friction and surface topography. High stresses will be produced at contact points and will facilitate particle fracture and matrix deformation. Maldonado and North [95] have calculated the required stress to fracture an alumina particle (approximately 217 MPa) and the range of normal pressure necessary to reach the radial stress required to fracture alumina particles during the initial stage of the joining process (between 0.5 to 17.5 MPa) concluding that particle fracture will occur very early in the joining operation (immediately following the contact between the adjoining substrates) since the minimum value of normal pressure used in their investigation was 30 MPa, therefore higher than the normal pressure calculated values. Accordingly, North et al [98] have affirmed that the initial stage of joining is the critical one for the particle fracture phenomenon. The following stage is characterized by low torque and high peak temperatures values; consequently, there will be little likelihood of particle fracture during this particular phase of the welding process, since lower stresses can be transferred to the reinforcing particles. Such behaviour can be compared to a high temperature shear testing of particle reinforced materials since when the temperature increases, the particle fracture likelihood diminishes because the matrix flow decreases and local stresses are not high enough to fracture the reinforcing particle.

It is also important to point out that the matrix microstructure condition may play an important role in the modifications of the particles characteristics caused by the friction welding operation. When the matrix exhibits low tensile strength and high work hardening coefficient, the operating strengthening mechanism leads to the load being transferred from the particles to the matrix as a result of plastic straining. On the other hand, for a high tensile strength matrix and low strain-hardening coefficient, most of the load is transferred from the matrix to the reinforcing particles. As a result, particles are subjected to loads which could produce failure and when one particle cracks, neighbouring particle(s) will be subjected to a similar loading process which can also create the ideal conditions for cracking. The particle shape condition will also affect the particle fracture phenomenon since the load which can be supported by a composite material will depend on the particle volume fraction and on the

aspect ratio of the reinforcing particles. Increasing the aspect ratio increases the load carried by the reinforcing particle; therefore in spherical particles the local stresses are lower [95].

### 2.5.3.1.2 Dynamic Recrystallisation

It is well established that when pressure is used to join materials by plastic deformation to produce welds without fusion, there is a localized effect on the microstructure. Such effect depends on the temperature at which the pressure is applied and under which plastic deformation is caused to take place. If the temperature at which the pressure is applied, or to which the material raises as a result of work converted to heat, exceeds  $0.4 T_{MP\ absolute}$  for sufficient time, the material in the interface vicinity will undergo plastic deformation and immediate recrystallisation which means that recrystallisation and plastic deformation happen at the same time. Such process is called dynamic recrystallisation and is caused by the movement of the dislocations which pile up or entangle and multiply by generation, therefore increasing the crystal lattice strain energy (which is the driving force for recrystallisation). The recrystallisation process occurs almost at once in a rather rapid sequence [88]. Figure 2.20 exemplifies the dynamic recrystallisation process.

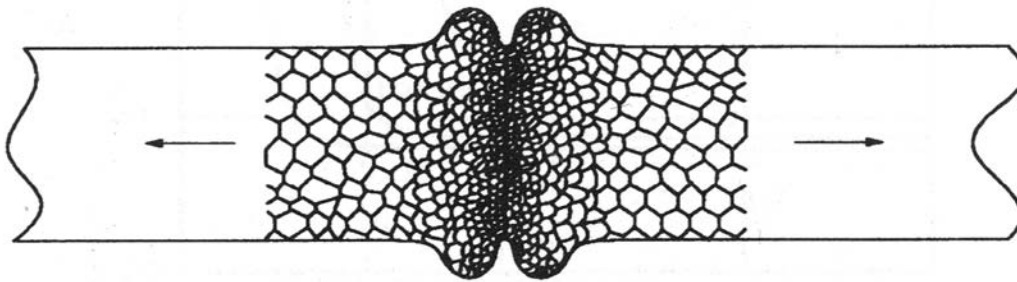


**Figure 2.20 - Dynamic recrystallisation process in the vicinity of the original interface between two materials being welded using pressure at temperatures above  $0.4 T_{MP\ absolute}$ . Grain refinement is observed at the centre region. [88]**

### 2.5.3.2 Diffusion Bonding of MMCs and TMCs

Many diffusion bonding applications involve titanium and its alloys components being the majority of that the Ti6Al4V alloy. The popularity of the diffusion bonding process with titanium and its alloys stems from the following factors [110]:

- It is readily joined without any special surface preparation or unusual process control.
- Diffusion bonding joints may have better properties for some applications than fusion welded joints.
- Most titanium structures or components are used principally in aerospace applications where weight savings or advanced designs are more important than manufacturing costs.

Several investigations have been conducted using diffusion bonding in titanium alloys as well as TMCs since the surface oxides dissolution in the titanium matrix promotes bonding which can be carried out at temperatures below those at which the reinforcement particles will start reacting with titanium [40,146-152]. Furthermore, the titanium yield and creep strengths are low at the bonding temperatures enhancing stages I and II [10]. Most of the available literature is about the intermetallic  $\gamma$ -TiAl [153-163] as well as other titanium alloys (in similar and dissimilar combination) [164-170].

Diffusion bonding process in MMCs using similar and dissimilar combinations have been extensively studied [145-152,171-174]. Ureña et al [171] studying diffusion bonding of an aluminium MMC alloy (AA2014 with 13% SiC) have reported the importance of using a silver interlayer (3 $\mu$ m) on the final metallurgical characteristics since it has avoided the formation of continuous intermetallic layers in the bond interfaces. However the presence of another constituent (needles of  $\delta$  phase) has limited the maximum strength that can be reached. Lee et al [172,173] have studied diffusion bonding of Al 6061+20% Al<sub>2</sub>O<sub>3</sub> particles showing that it was possible to form joints with up to 90.5% of joint efficiency. Zhang et al [174] have investigated similar and dissimilar diffusion bonding characteristics of SiC particulate reinforced aluminium MMCs (AA2024+10%SiC particles and AA6061+20%SiC particles). The vacuum diffusion bonding on dissimilar Al/SiC<sub>p</sub>-MMC is more difficult than that of similar Al/SiC<sub>p</sub>-MMC therefore the use of a soft insert alloy layer to improve diffusion bonding quality has been suggested. Dissimilar diffusion bonding between SiC-fiber reinforced Ti6Al4V and Ti6Al4V has been performed with good results [146]. The void ratio decreased as bonding time increased and it was accelerated (void elimination) for lower fibre volume fraction and higher bonding pressure, similar to the trend found for the joint strength.

The most successful diffusion bonding application using TMCs (Ti6Al4V+10 wt.% TiC) and Ti6Al4V has been reported by Abkowitz and Weihrauch [40]. A material denominated commom-matrix micro-macrocomposite (CM<sup>3</sup>C) can be obtained joining such materials to a multilayer approach. Materials having up to eight alternating micro-macrocomposite layers have been successfully fabricated. Typical applications for these dual-property (hardness, ductility and fracture toughness) macrocomposite include, among others: (a) wear parts (gears, bearings and shafts) having abrasion-resistance surface layer and tough, load-bearing body, (b) erosion-corrosion resistant tubing for chemical service, (c) creep/fatigue-resistant engine components for elevated-temperature service. The CM<sup>3</sup>C materials can be used for any structural component where the macrocomposite properties

would be beneficial, but where the component also would benefit from having a ductile monolithic alloy cladding or containment construction.

The TMCs components and structures, such as particulate or fiber reinforced, commonly have problems during fusion welding (fiber damage, brittle intermetallics formation, segregation, among other minor problems), therefore the joining process selection is critical, making the solid state welding process (diffusion bonding or friction welding) an alternative solution to minimize, or even eliminate such defects [175]. However, even reducing temperature and pressure, the composite can be still subjected to several problems like degradation of the mechanical properties due to an interfacial reaction between the fibre and the matrix as well as fiber misalignment due to the high applied pressure. Therefore the selection of optimum parameters must be done applying preferably as low a pressure and temperature and as short a time as possible. Hirose et al [147] studying diffusion bonding of SiC fibre reinforced Ti6Al4V alloy have demonstrated the difficulties in welding the composite due to surface roughness and differences in stiffness of the microconstituents (SiC fibres and Ti6Al4V alloy) which have led to unbonded regions, especially in the areas with fiber/fiber contact. Therefore it has been used a deformable interlayer of Ti6Al4V that has high compatibility with both the matrix and the fibre as well as an etching treatment to reduce the surface roughness in order to improve the bonding capability. Onzawa et al [152] studying SiC fibre reinforced Ti6Al4V affirm that increasing pressure and temperature is possible to increase the joint tensile strength, however there is an optimum condition for both parameters as shown in Fig. 2.21a and 2.21b and increasing such optimum values considerably reduce the final joint strength (in the case of bonding pressure).

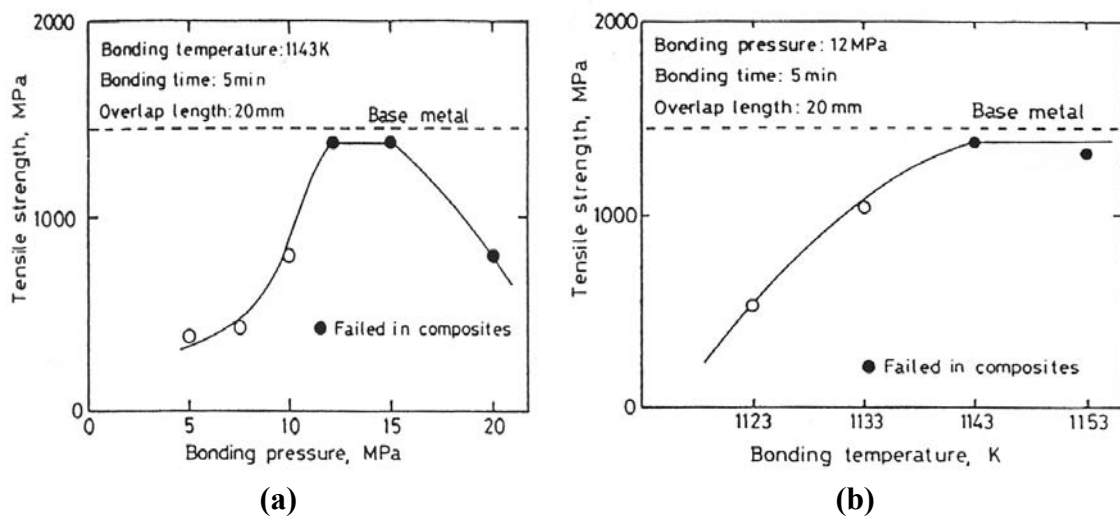


**Figure 2.21 - Relation between bonding conditions and joint tensile properties. (a) Bonding pressure ( $T = 1143^{\circ}\text{C}$  and  $t = 5\text{minutes}$ ). (b) Bonding temperature ( $P = 12\text{MPa}$ ,  $t = 5\text{minutes}$ ) [152].**

### 3 EXPERIMENTAL PROCEDURE

#### 3.1 Methodology

A flow chart showing schematically the methodology devised for this study is presented in Figure 3.1. It has been done in order to clarify all procedures used in this investigation. Further details are given in the subsequent subsections of this chapter.

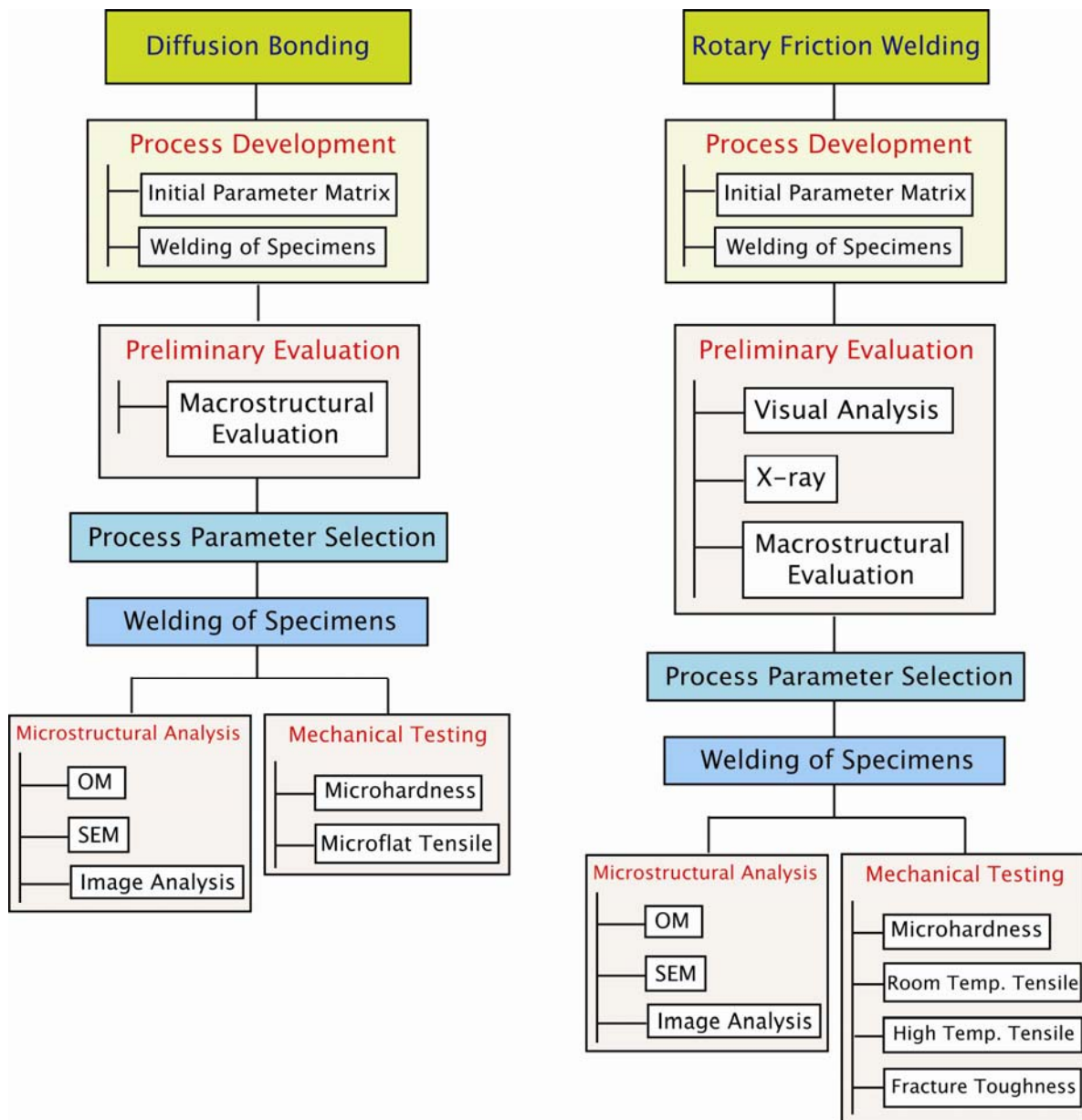


Figure 3.1 - Experimental procedure flow chart.

#### 3.2 Titanium Matrix Composite - TMC (Ti6Al4V+10 wt.% of TiC)

The material used in this investigation was a TiC-particulate reinforced Ti6Al4V composite. It was produced by the CHIP process, which is a P/M technique (blended



elemental method – BE), comprising cold isostatic pressing of blended elemental powders (master alloy and TiC particles) in a reusable elastomeric mould, followed by vacuum sintering to achieve a closed porosity (94 to 98%) and hot isostatic pressing (HIP) at 899°C for 2 hours at 103 MPa without need for additional expensive tooling achieving a final density of 99 to 100%. With this technique proper proportion of master alloy powders and reinforcement particles are blended to obtain a uniform distribution of the required chemical composition. Further information on the CHIP Process is given in item 2.4.2 of Chapter 2. The Ti6Al4V+10 wt.% of TiC alloy was supplied by Dynamet Technology Inc. in the form of 50 mm diameter bars.

The reinforcement of the Ti6Al4V alloy leads to several modifications in the mechanical and metallurgical properties changing the matrix alloy original characteristics. Basically, the most dramatically improvements in the composite are stiffness and high temperature tensile properties (10 to 15% higher). The material properties can be tailored to meet specific applications by increasing or decreasing the reinforcement level. The material has not been heat treated after fabrication and it was furnace cooled inside the HIP chamber under protective atmosphere. Such procedure allowed the formation of platelike  $\alpha$  and intergranular  $\beta$  microstructures with TiC randomly distributed in the matrix alloy. Table 3.1 shows the as-received Ti6Al4V/TiC-particulate reinforced chemical composition. A detailed description of the microstructure and properties of the base material is presented in Chapter 4.

**Table 3.1 - As-received base material chemical composition.**

<b>Element</b>	<b>C</b>	<b>Cu</b>	<b>W</b>	<b>Al</b>	<b>V</b>	<b>Ti</b>
<b>Wt. %</b>	2.00	0.03	0.27	5.78	3.57	balance

### 3.3 Friction Welding Process

#### 3.3.1 Friction Welding Equipment

The friction welding system used is a purpose-build version of the HMS 3000 welder from Circle Technical Services which is a hydraulically driven 50kW power capable of applying 40 kN axial load at speeds up to 8000 rpm (see Fig. 3.2). The rotating workpiece is attached to the HMS 3000 via a connector. The weld cycle is electronically controlled, with the machine functions displayed on-line on a monitor. The HMS 3000 welding system can be classified as a direct drive system in which the friction welding process is controlled by the burn-off distance which is the amount of plastified stud material and pressed aside (distance that the hydraulic ram moves out).



**Figure 3.2 - HMS 3000 friction welding machine.**

The test rig used to perform the welds is a rigid stand with a bayonet-connector on the top and an adjustable vice for the fixed specimen at the base (see Fig. 3.3). The weld-head is attached to this rig via the bayonet-connector completing this vertical friction welding machine. Owing to the high forces applied during the friction welding process, the test rig is designed for maximum stiffness to minimise bending deflection. Besides the standard equipment a data recording system with additional sensors has been especially developed and built at GKSS to monitor on-line the complete process (described in detail in [100]).

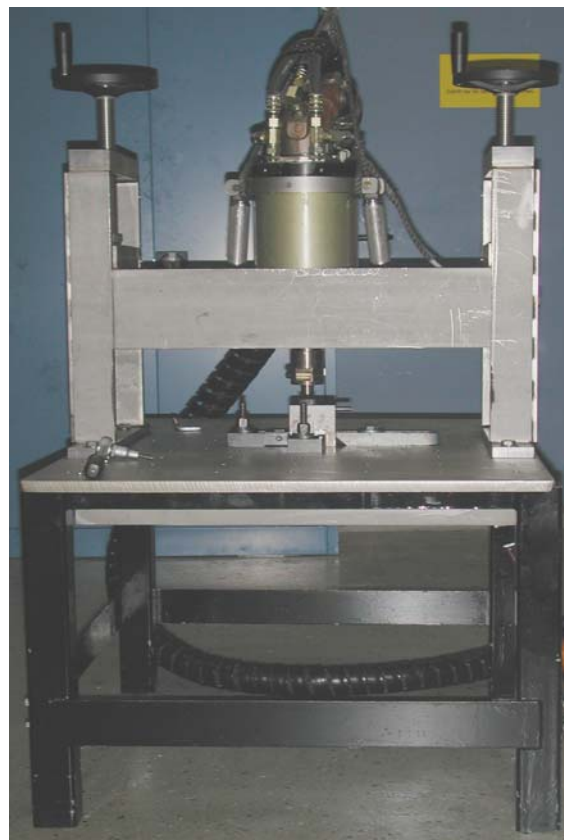


**Figure 3.3 - Friction welding system used to perform the friction welding process.**

### 3.3.2 Friction Welding Studs Configuration

Figure 3.4 shows the stud configuration for the friction welding process. All dimensions have been empirically developed based on previous tests and investigations on friction welding at GKSS Research Centre. The static workpiece has 25 mm diameter and 30 mm length while the rotating part has a different geometry, with 60 mm length and 20 mm diameter. In the lower part there is an angle of  $45^\circ$  and the contact area has 8 mm diameter. In the upper part there is an undercutting of 4 mm depth and 15 mm length in order to attach the workpiece to the friction welding machine.

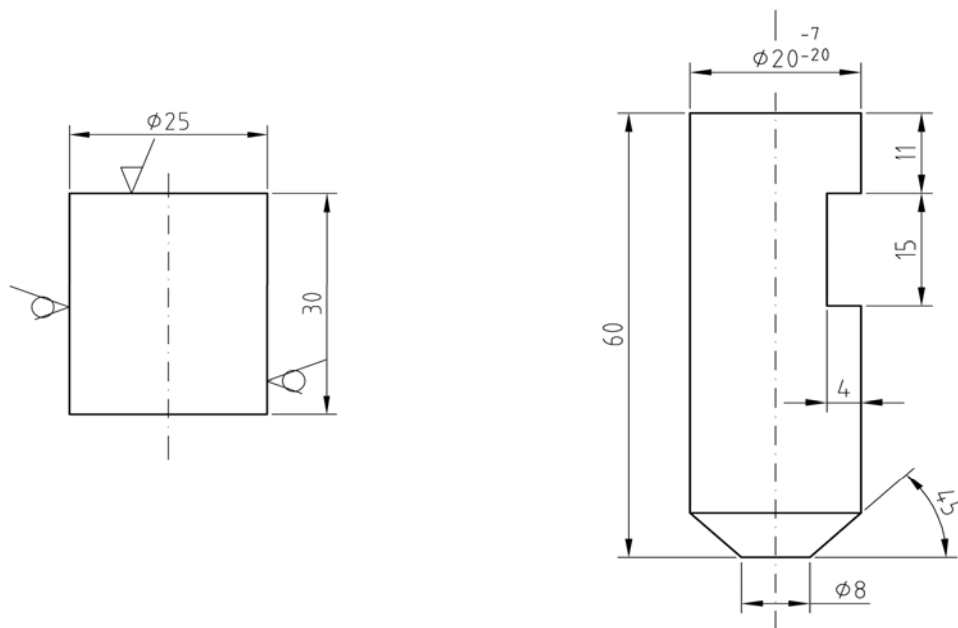


**Figure 3.4 - Configuration of the studs (dimensions in mm) for the friction welding process.**

### 3.3.3 Friction Welding Parameter Matrices

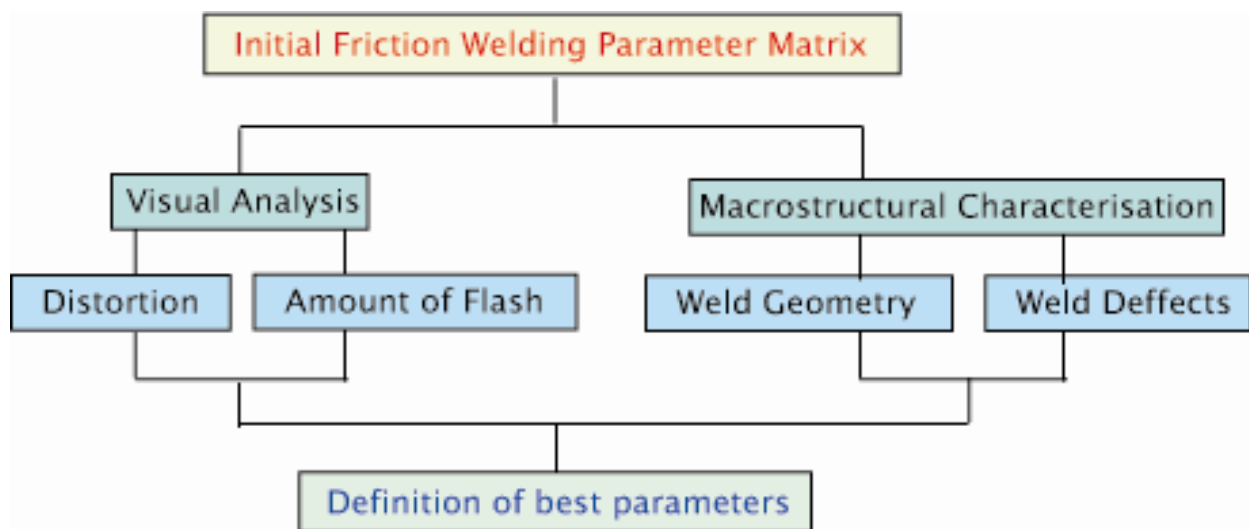
Friction welding process development has been performed by means of testing a selection of appropriate welding parameters for producing satisfactory Ti6Al4V + 10 wt.% of TiC welding. In this part of the investigation, the process parameters have been evaluated viewing the definition of parametric fields leading to suitable weldment quality. Initially, the weldment quality has been established only based on visual examination and a macrostructural evaluation. An optimized parameter matrix has been established and further investigated for the friction welding process. Figure 3.5 shows the initial parameter matrix investigated for the friction welding of the Ti6Al4V + 10 wt.% of TiC alloy with the following parameters: forging and friction pressure, rotational speed and burn-off distance.

Table 3.2 shows the friction welding parameters utilised in the initial characterisation. All friction welding parameters have been varied in order to check the material response over the different friction welding conditions and heat inputs.

**Table 3.2 - Friction welding parameters of initial matrix.**

Condition	Forging Pressure (MPa)	Friction Pressure (MPa)	Rotational Speed (rpm)	Burn-Off (mm)
DM01	884	136	1500	4
DM02	884	136	3000	6
DM03	544	136	4500	4
DM04	544	272	1500	2
DM05	544	272	3000	2
DM06	544	272	4500	2
DM07	544	136	3000	3
DM08	544	136	4500	3
DM11	408	136	1500	2
DM12	408	136	3000	2
DM13	408	136	4500	2
DM14	408	272	1500	2
DM15	408	272	3000	2
DM16	408	272	4500	2

Six conditions have been chosen for further investigation (metallurgical and mechanical evaluation) after the visual examination and macrostructural evaluation of all specimens. The evaluated factors were weld distortion (component deformation), presence of melted products, amount and formation of flash, weld geometry as well as weld defects (presence of brittle phases or contaminants, lack of bonding and cracks). Figure 3.6 shows the procedure flowchart to analyse the first parameter matrix.



**Figure 3.5 - Flowchart showing the procedure used to investigate the initial parameter matrix.**

The conditions selected after this initial investigation were DM 11, DM 12, DM 13, DM 14, DM 15 and DM 16. In this second attempt two friction welding parameters (rotational speed and friction pressure) have been varied while two others (burn-off distance and forging pressure) have been held constant. Table 3.3 shows the secondary parameter matrix of the friction welding process used in the investigation.

**Table 3.3 - Secondary matrix of the friction welding parameters. All conditions have been welded with a forging pressure of 408 MPa and a burn-off of 2 mm.**

Condition	Friction Pressure (MPa)	Rotational Speed (rpm)
DM11	136	1500
DM12	136	3000
DM13	136	4500
DM14	272	1500
DM15	272	3000
DM16	272	4500

### 3.4 Diffusion Bonding Process

#### 3.4.1 Diffusion Bonding Equipment and Specimens Configuration

The diffusion bonding equipment used in this investigation (Fig. 3.6) has an electronic control of temperature, pressure and time applied during the process and can be adjusted by the operator in a computer connected to the control system.

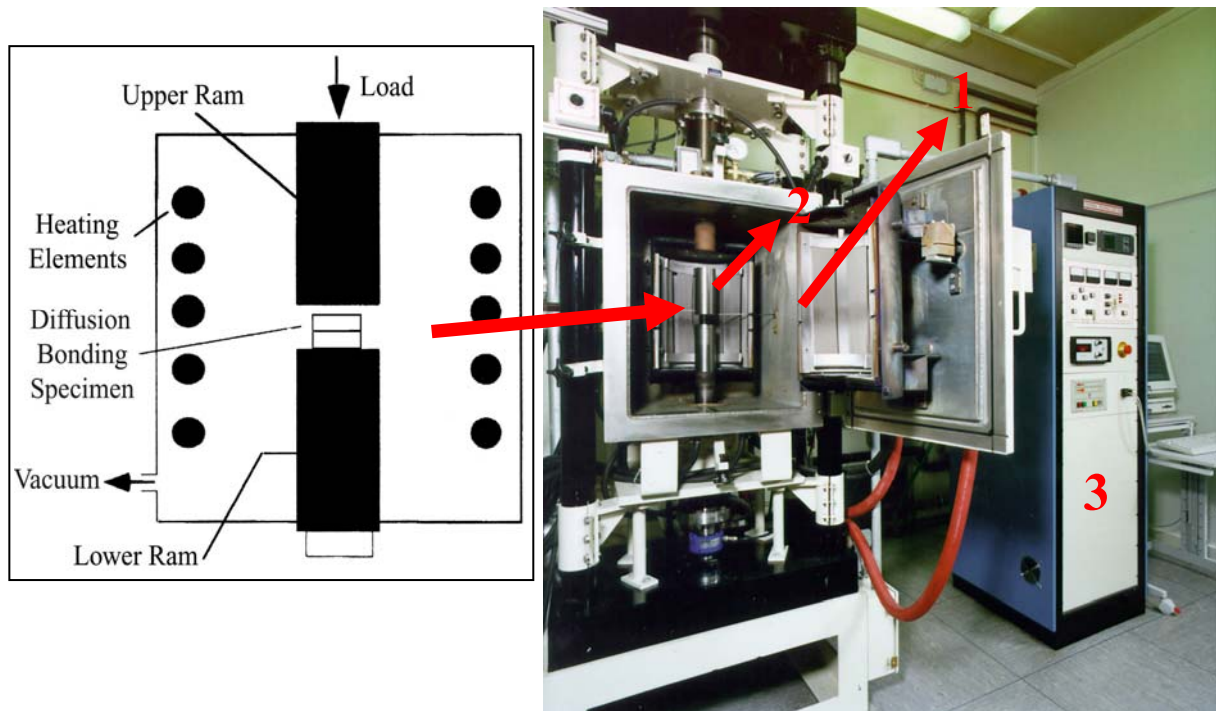


**Figure 3.6 - Diffusion bonding equipment and experimental setup of the diffusion bonding process used in this investigation.**

As it can be seen in Figure 3.6, there is a furnace (1 in Fig. 3.6) where the samples are placed. The upper piston (2 in Fig. 3.6) moves down and applies the required pressure for completing bonding. The data acquisition system and controller are located beside the machine (3 in Fig. 3.6) and both are connected to a computer from where the results can be visualised and recorded. Fig. 3.6 also presents a schematic representation of the experimental setup inside the furnace chamber. A series of diffusion bonded joints with different parameters have been made using round specimens measuring approximately  $50 \times 15 \text{ mm}^2$  (see Fig. 3.7). The maximum temperature utilized in this investigation was  $1000^\circ\text{C}$  (maximum temperature that can be obtained in industrial diffusion bonding equipments used for titanium). The maximum pressure used was 7 MPa and the bonding time has been varied between 35 and 60 minutes. For the diffusion bonding trials the mating surfaces have been machined and ground with 1200 SiC paper and then polished with a  $\text{Al}_2\text{O}_3$   $0,05\mu\text{m}$  solution followed by rinsing with acetone before bonding. The pressure (vacuum) was lower than  $3.0 \times 10^{-4}$  torr ( $4.0 \times 10^{-4}$  mbar).

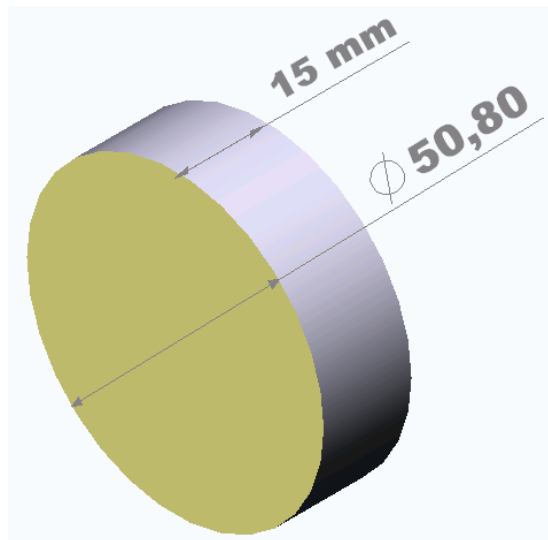


**Figure 3.7 – Configuration of the diffusion bonding specimens.**

### 3.4.2 Diffusion Bonding Parameter Matrix

The diffusion bonding process development has been done by means of testing and selection of appropriate bonding parameters for producing satisfactory Ti6Al4V + 10 wt.% of TiC joints. In this part of the investigation the process parameters have been evaluated viewing the definition of parametric fields leading to suitable weldment quality and the definition of a secondary parameter matrix for further investigation. The weldment quality has been evaluated on basis of a microstructural evaluation. The best conditions were established and further investigated. Table 3.4 shows the bonding parameters used in this investigation.

**Table 3.4 - Diffusion bonding parameters.**

<b>Condition</b>	<b>Temperature (°C)</b>	<b>Pressure (MPa)</b>	<b>Time (min.)</b>
<b>DB1</b>	875	5	60
<b>DB2</b>	900	5	35
<b>DB3</b>	900	6	35
<b>DB4</b>	900	7	60
<b>DB5</b>	1000	5	35
<b>DB6</b>	1000	5	60

After the initial microstructural evaluation, three conditions have been selected for further characterization: DB4, DB5 and DB6. The purpose of this evaluation is to establish an optimised condition after an investigation in the chosen conditions with suitable selection of the bonding parameters in which good metallurgical and mechanical properties can be achieved. The selection was based on the results obtained during the metallurgical characterisation and microflat tensile tests.

### **3.5 Non-Destructive Tests (NDT)**

Non-destructive tests, such as, X-ray and visual control have been performed in order to identify weld defects assisting the determination of the optimised welding parameters. The visual analysis was carried out to determine common welding defects such as: component deformation, in which undesirable changes occur in the component geometry caused by inadequate welding parameters selection (high forging and friction pressure), insufficient bonding, such as marginal notches which occur in the vicinity of the plasticized area caused by inadequate preparation of the friction surfaces and wrong selection of the welding parameters, cracks or partial joint faces separation that can occur due to high forging pressures, structural defects as well as unusual weld flash formation such as spirally extruding from between friction surfaces caused by insufficient heating time. The main objective of the X-ray procedure was to determine and identify insufficient bonding, such as bonding defects such as lack of bonding in the friction surfaces caused by inappropriate selection of welding parameters and inappropriate preparation of the friction surfaces as well as cracks due to high forging pressure [85].

### **3.6 Metallurgical Characterization**

#### **3.6.1 Macrostructural Characterization**

After being friction-welded or diffusion-bonded, one sample of each condition has been selected randomly in order to evaluate its macrostructure and the presence of weld defects or any other problem regarding solid state welding processes. Samples were cut

perpendicularly to the welded joint and prepared according to standard metallographic procedures following ASTM E3-95 [176] and ASTM E340-95 standards [177]. Initially, the samples have been ground on a Buehler Motopol 2000 mechanical grinding and polishing automatic machine using emery paper (220 and 1200 grit) for 10 minutes with a rotational speed of 300 rpm and pressure of 7 kN and later polished using a cloth Struers MD-Dur with a diamond suspension P-2000 3  $\mu\text{m}$  solution for 10 to 12 minutes with a rotational speed of 150 rpm and pressure of 5 kN. The final polishing step has been made in a cloth Struers MD-Chem with a FS-3 0.05  $\mu\text{m}$   $\text{SiO}_2$  alkaline solution using the same parameters of the first polishing step. After the metallographic preparation, samples have been etched using Kroll's reagent (2% HF + 8%  $\text{HNO}_3$  and water balance) and then analysed in an optical microscopy Reichert-Jung MEF-3 coupled with a Polaroid system and a CCD camera.

### **3.6.2 Microstructural Characterization**

Following friction welding and diffusion bonding processes a microstructural evaluation has been carried out in order to evaluate the metallurgical transformations that have taken place within the joints as well as a base material microstructure evaluation. With this in mind several evaluation techniques have been used to analyse the joints and the base material such as Optical Microscopy (OM), Scanning Electron Microscopy (SEM), Energy-Dispersive Spectrometry (EDS) as well as Image Analysis.

### **3.6.3 Optical Microscopy (OM)**

Basically the metallographic techniques that have been used to prepare samples for the OM were the same used during the macrostructural characterization. The only difference was that the samples have been mounted in order to improve handling. The same etching solution has been used to reveal the microstructural features across the specimens during the OM analysis. The samples have been extracted from different areas along the friction-welded and diffusion-bonded joints to evaluate the microstructural changes taking place after processes. All micrographs were taken perpendicularly to the joints.

### **3.6.4 Scanning Electron Microscopy (SEM)**

SEM has been used in this investigation when high resolution and high depth of field images were necessary. Since the depth of field is much greater than in OM, the ability to observe details spread along samples is better. The microstructural and fracture surface analysis have been performed using two types of imaging signals - back-scattered electrons (BSE) and secondary electrons (SE).



Specimen's preparation was identical to that used for macrostructural characterization. The only exception was the need to use a conductive mounting resin (DemoTec 70) in order to have the appropriate electric contact between the sample (cathode) and the SEM table (anode). Two SEMs have been used during the analysis: a Philips XL-20 and a Zeiss DSM 962. Energy-Dispersive Spectrometry was used in order to investigate and determine the chemical constituents qualitatively.

### 3.6.5 Image Analysis

The image analyses have been performed on specimens without etching in order to determine the particle characteristics. The evaluation has been carried out utilising the software ImageC for Windows [178] and also Leica QWin [179]. The particle characteristics (mean Ferret diameter, shape factor, interparticle spacing and area of particles) were examined and documented with the OM as well as the SEM and later transferred to the softwares. It involved examining particle distribution at the joint centerline and in the base material using 200 times magnification comprising 0.77 mm<sup>2</sup> area fields.

The mean Ferret diameter (particle size) is related to the perimeter of the particle convex hull (Fig. 3.8) and has been calculated using the following formula [180]:

$$F_{av} = \frac{P_{CH}}{\pi} \quad \text{Equation 3.1}$$

where  $F_{av}$  is the mean Ferret diameter and  $P_{CH}$  is the perimeter of the convex hull.



**Figure 3.8 - Convex hull perimeter used during the mean Ferret diameter measurements [180].**

The interparticle spacing has been measured using the software function Nearest Neighbour Distance (NND), which enables the determination of the frequency of occurrence as a function of the distance between the closest particles. The shape factor, which is the relation that determines the particle sphericity (the closest the value to 1, the more "round" is the particle), has also been determined.

### 3.6.6 Determination of $\beta$ Grain Size

The  $\beta$  grain size determination has been performed according to the ASTM E 112-96 standard [181]. Two different positions for the  $\beta$  grain size determination have been analysed.

It is important to emphasize that all the measurements have been done inside the joint; thus results are from the recrystallised  $\beta$  grains formed due to the friction welding process.

### 3.7 Mechanical Characterization

Besides the metallurgical characterization, a mechanical assessment has been performed in the friction welded and diffusion bonded joints as well as in the base material in order to determine the mechanical properties and correlate them with the microstructural features across the joints. Several testing methods, at room and high temperature, have been used to study the mechanical features of the joints and base material, such as hardness, tensile, microflat tensile and fracture toughness. These are presented in detail below.

#### 3.7.1 Microhardness

Microhardness testing using conventional Vickers hardness measurements has been performed across the joints at specific locations and has followed the ASTM E384-99 standard [182]. Problems have arisen due to the presence of TiC particles since such particles disturbed the hardness values when the indentation is exactly on or close to them. To minimize such effect testing was performed on 5 lines across the joints and with the resulting values a statistical analysis was performed. The indentation lines had a distance of 2 mm from each other beginning from the weld centre (2 on each side of the centreline).

The hardness testing machine used in this study was a Shimadzu HVM 2000 with a computer controlled displacement and indentation coupled with the software Duramin for Windows NT to analyse the data results. The load used was 300 p corresponding to a force of 2.94 N (HV0.3). The spacing between the indentations was 0.2 mm along 8 mm of each weld centre side corresponding to 80 points.

#### 3.7.2 Tensile Test

The specimens were precision machined from the friction welding joints as well as from the base material by spark erosion (EDM – electric discharge method) with the specimen centre located exactly at the interface between the two workpieces (see Fig. 3.9). In order to minimize the effects of surface irregularities and finish all the specimens have been polished to eliminate scratches and surface machining marks. The specimen (threaded ends) used to investigate the composite tensile properties of the joints and base material in both room and high temperatures is shown in Figure 3.10. All tests have been carried out in laboratory air at room temperature as well as at 200°C and 375°C. The equipment utilized for testing at room temperature was a screw-driven tensile testing machine Zwick 1484 (see Fig.

3.11) with 200 kN load capacity. All tensile specimens have been tested with a traverse speed of 0.2 mm/min and the displacement was recorded by a MTS extensometer (gauge length of 30 mm). All data has been recorded and analyzed by the software TestXpert connected to the testing machine. The equipment utilized to accomplish the high temperature tests was a Schenck Trebel RM100 (see Fig. 3.12) with 100 kN load capacity and a high temperature chamber coupled to it. The temperature has been monitored using a type K thermocouple with an Eurotherm<sup>®</sup> controller. All data has been recorded and analysed using the software TestXpert coupled to the testing machine. The room temperature tests have been performed according to the ASTM E8-00 [183] and EN 10002-1 [184] standards while the elevated temperatures tests have been performed according to the ASTM E21-98 [185] and EN 10002-5 [186] standards. Three specimens have been tested for each friction welding condition (secondary matrix) as well as for the composite base material at both room and high temperatures.

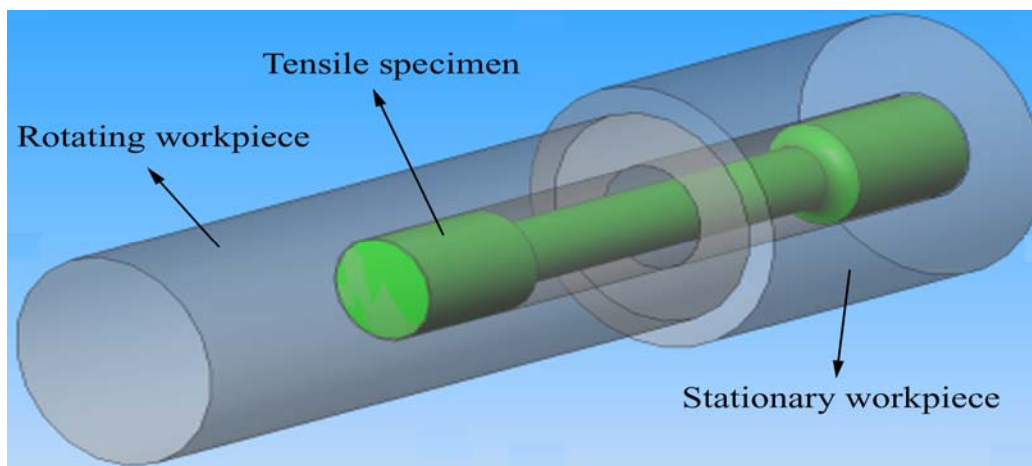


Figure 3.9 – Location of the tensile specimen in the friction welding specimens.

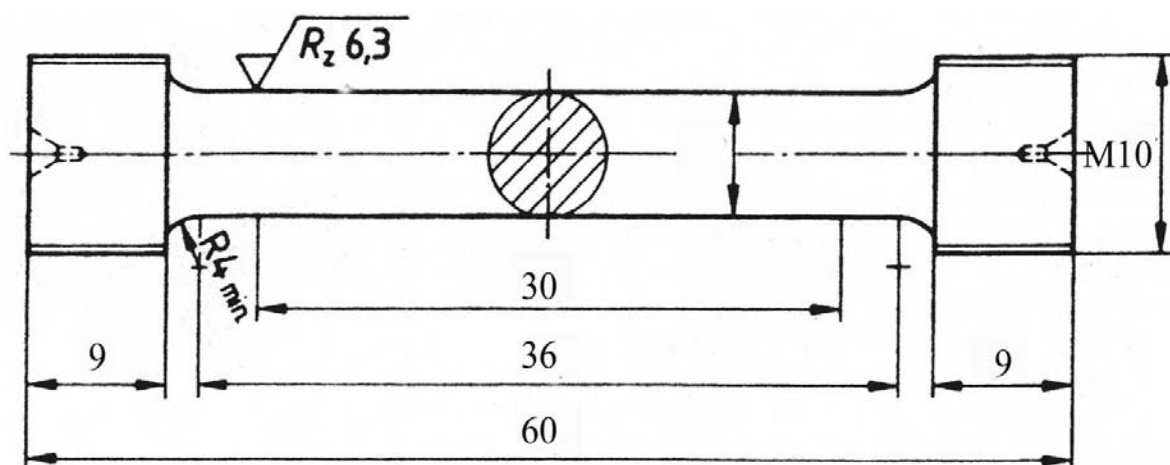


Figure 3.10 - Geometry of the tensile specimens used to investigate the tensile properties for the friction welding process (dimensions in mm).

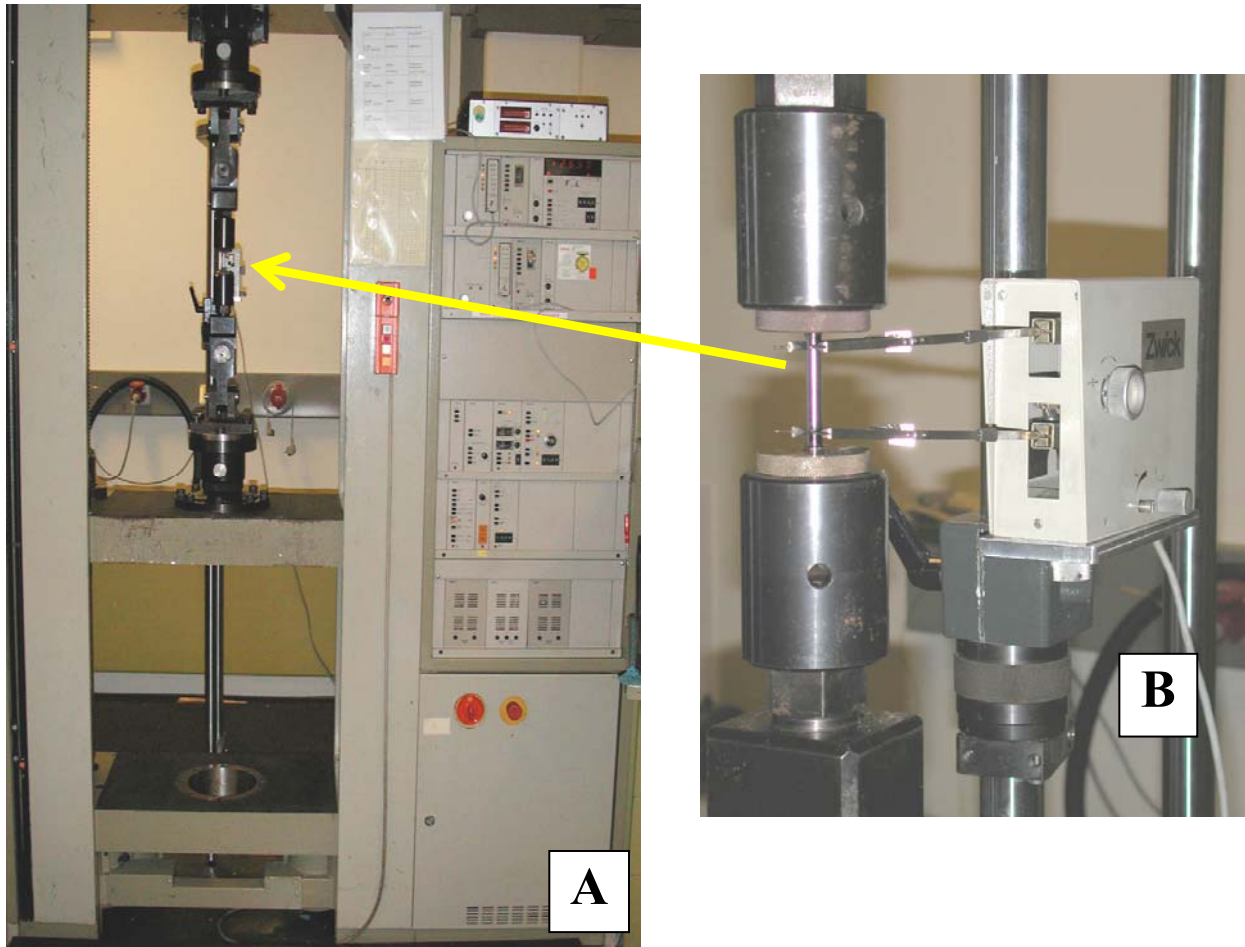


Figure 3.11 - Equipment utilized to perform the tensile tests at room temperature. (a) General view. (b) Detail of specimen positioning and extensometer.

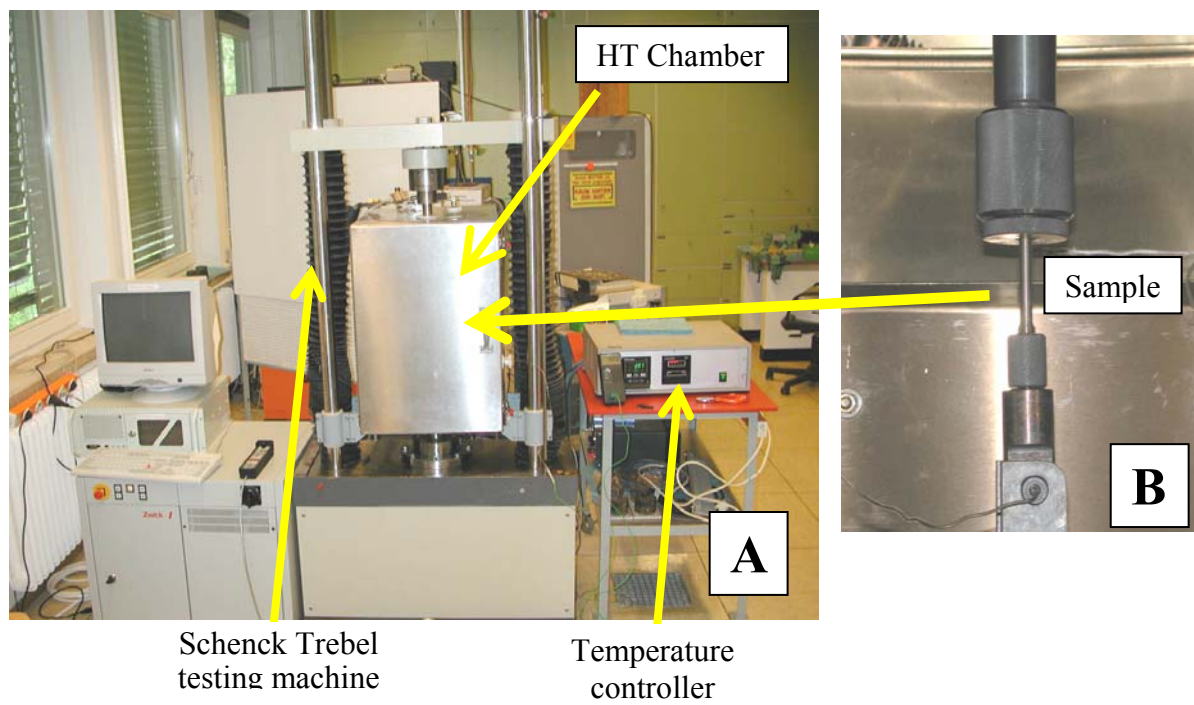


Figure 3.12 - Equipment utilized to perform the tensile tests at high temperature. (a) General view. (b) Detail of specimen positioning.

### 3.7.3 Microflat Tensile Test

Microflat tensile tests have been carried out in the base material as well as in the different diffusion bonding conditions. Such test enables a detailed characterisation of the tensile properties along the material and it was first suggested by Çam et al [187]. The specimen has 28x2x0.5 mm in size with 9 mm gauge length and radius of 1.5 mm (see Fig. 3.13). The specimens have been machined using spark erosion. Five specimens from each condition have been tested. The tests have been conducted in a screw-driven Instron 1195 testing machine (see Fig. 3.14) at 0.1 mm/min cross-head speed. It has a FOEPS 50 mm laser extensometer coupled with a data monitoring system to record the displacement. All data was recorded and analysed by the LQ/CFG1.8 software.

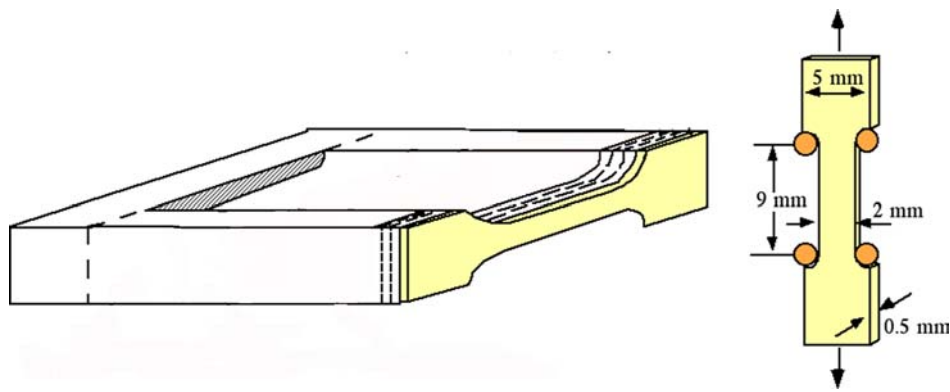


Figure 3.13 - Schematic representation of the extraction of the microflat tensile specimens.

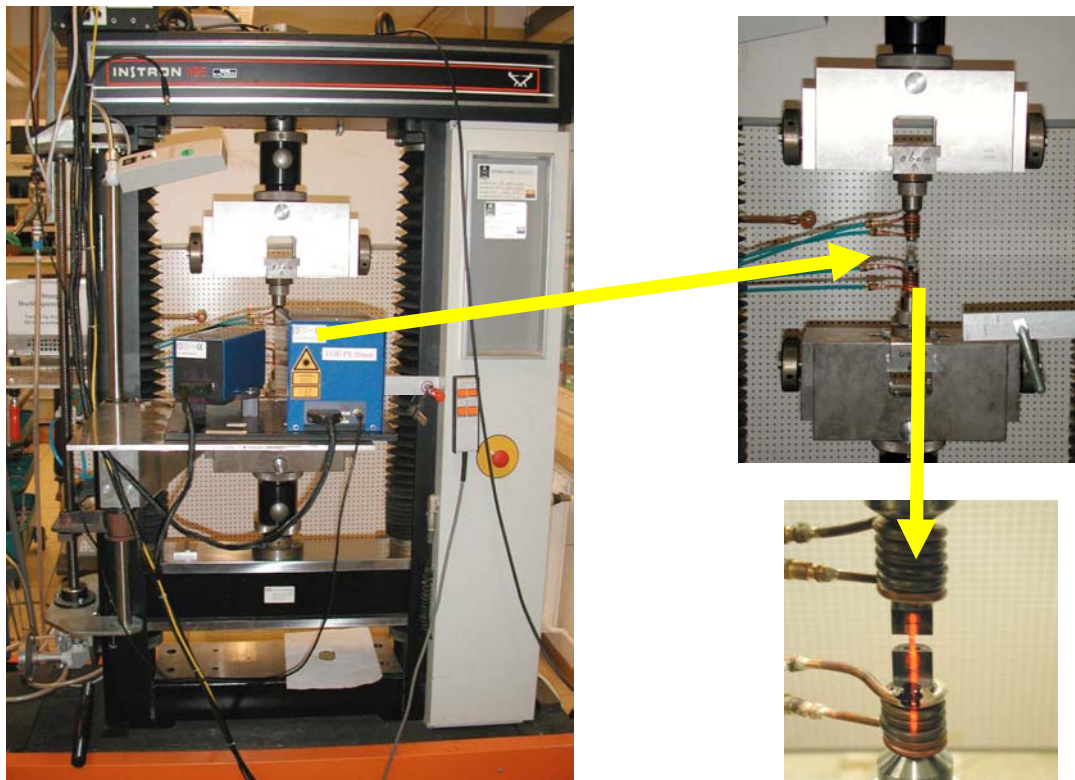
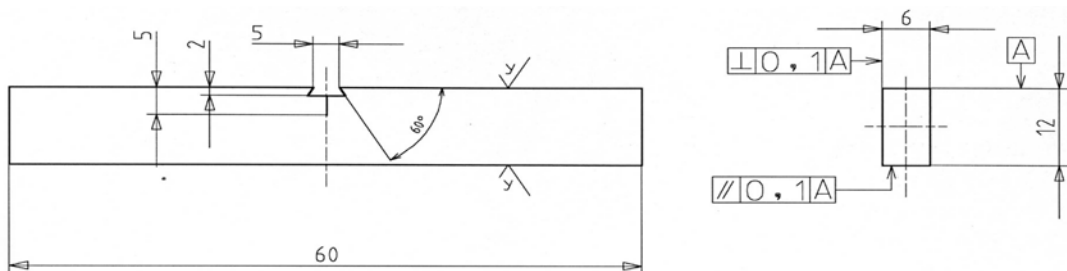


Figure 3.14 - Microflat tensile testing machine and laser extensometer.



### 3.7.4 Fracture Toughness Testing ( $K_{IC}$ )

Single Edge Notch Bend – SE(B) - specimens have been extracted for the  $K_{IC}$  tests with 6 mm thickness (B), 12 mm width (W) and 5 mm notch length (Fig. 3.15). The specimens were machined using EDM and an undercut was machined to accommodate the CMOD (Crack Mouth Opening Displacement) clip gauge with 5 mm width and 2 mm depth. The fracture toughness tests have been determined according to the ASTM E399-90 [188] and the EFAM GTP94 [189] Standards. The  $a/W$  ratio after fatigue precracking was approximately 0.5, where "a" is the crack length.



**Figure 3.15 - SENB specimens for fracture toughness testing (dimensions in mm).**

Two different weld positions have been tested - base material and joint centre (TRZ) – (Fig. 3.16). The most critical point was to ensure the notch machining at an exactly position in the weld centre. For this purpose the surface of the specimens were polished and etched using Kroll's and then the notch position was marked on the specimen surface for final machining.

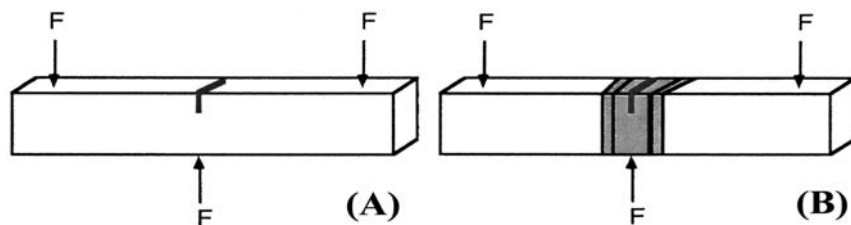


**Figure 3.16 – Fracture toughness testing notch positions. (a) Base material. (b) FW joint centre.**

The fracture toughness evaluation procedure has started with the fatigue precracking of the machined notch to produce a sharp crack. The specimens have been metallographically prepared on both faces in order to monitor the crack growth. The procedure to calculate the forces used during fatigue precracking have followed the EFAM GTP 94 Standard [189], where the maximum fatigue force must not exceed the lower of  $0.6 F_y$  or the force corresponding to a maximum stress intensity factor to Young's modulus ratio ( $K_{MAX}/E$ ) equal or less than  $1.5 \times 10^{-4} \text{ m}^{1/2}$ .  $F_y$  is determined for SE(B) specimens by the following equation:

$$F_y = \frac{4 * B(W - a)^2}{3 * S} * R_{p0.2} \quad \text{Equation 3.2}$$

where  $F_y$  is the fatigue precracking force;  $B$  is the specimen's thickness;  $W$  is the specimen's width;  $a$  is the crack length;  $S$  is the span ( $4*W$ , distance between the rolls) and  $R_{p0.2}$  is the yield strength of the material to be tested.

Therefore, the  $F_y$  value was determined to be 5.72 kN. Due to material brittleness it was used a minimum force of  $0.2*F_y$  for fatigue precracking resulting in a force value of 1.14 kN. Using a load ratio  $R$  ( $F_{MIN}/F_{MAX}$ ) value of 0.1, the resulted  $F_y$  values to open the precracks were:  $F_{MAX}=1.14$  kN and  $F_{MIN}=0.11$  kN. The precracks have been controlled and monitored using two OMs coupled to a servohydraulic structural test machine (Schenk Hydropuls PSA) equipped with a 4 t (40 kN) load cell (see Fig. 3.17). The frequency utilized to open the fatigue precracks was between 30 and 50 Hz.

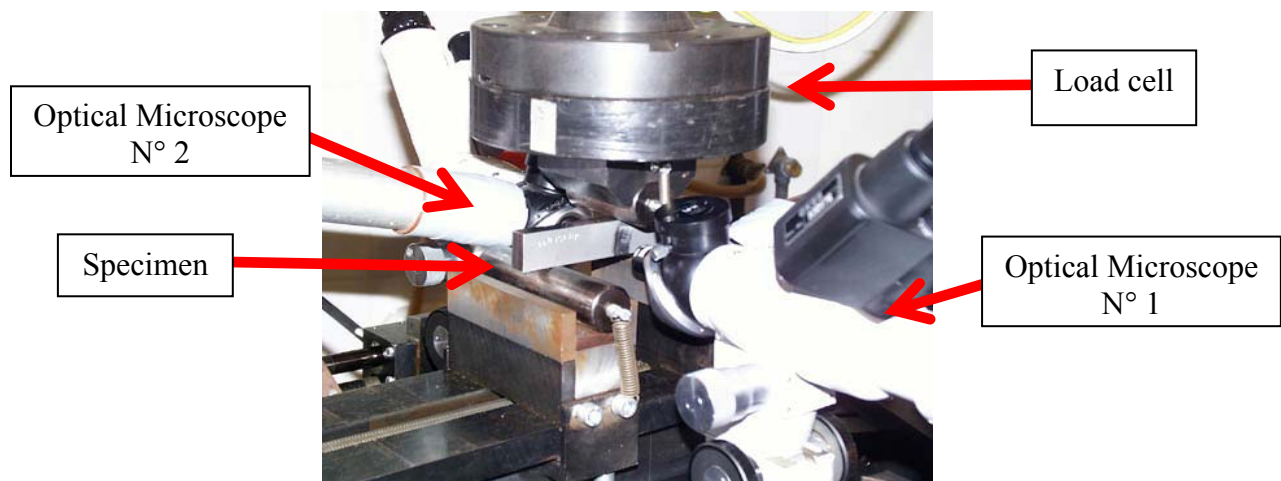


**Figure 3.17 - Optical microscopes utilized to monitor fatigue precrack growth and experimental setup to open the fatigue precracks.**

Following fatigue precracking, the specimens have been monotonically loaded using the Zwick 1484 with a displacement rate of 0.1 mm/min. Two parameters have been recorded for the  $K_{IC}$  calculation: force and CMOD. The crack length measurements have been performed using a low magnification stereoscope coupled with a computer controlled table according to the item 4.2.2 of the EFAM GTP94 Standard [189] in which the measurements are made at 9 equispaced points where the outer points are located at  $0.01B$  from the reference lines. The  $K_{IC}$  has been determined according to the item A3.5.3 of ASTM E399-90 Standard [188]:

$$K_{IC} = \frac{P_Q * S}{B * W^{3/2}} * f(a/W) \quad \text{Equation 3.3}$$

where  $K_{IC}$  is the fracture toughness value;  $P_Q$  is the load as determined in the item 9.1.1 (ASTM E399-90 Standard [188]);  $S$  is the span ( $4*W$ );  $B$  is the specimen's thickness;  $W$  is the specimen's width; and  $f(a/W)$  is the  $a/W$  ratio function.

## 4 RESULTS AND DISCUSSION

### 4.1 Metallurgical and Mechanical Characterisation of the Ti6Al4V+10 wt.% TiC Base Material Composite Alloy

#### 4.1.1 Metallurgical Characterisation - Ti6Al4V+10 wt.% TiC

The Ti6Al4V+10 wt.% TiC alloy used in this investigation was produced by the CHIP (Cold and Hot Isostatic Pressing) process. The utilisation of this process allows low temperature processing routes (approximately 1250°C, see section 2.4.2); however, even using such low temperatures, compared to other P/M processes, the  $\beta$  transus temperature for this alloy has been probably reached. The distribution of the TiC particles throughout the specimen is shown in Figure 4.1. It can be observed by analysing the reinforcing particles, an inhomogeneous distribution with some regions having fewer particles than others showing some degree of TiC clustering throughout sample (such concentration is located mainly in the prior  $\beta$  grain boundaries). Indeed, Ranganath [190] has affirmed that particles clustering and porosity in such composites (CHIP-processed) have proved to be problematic.

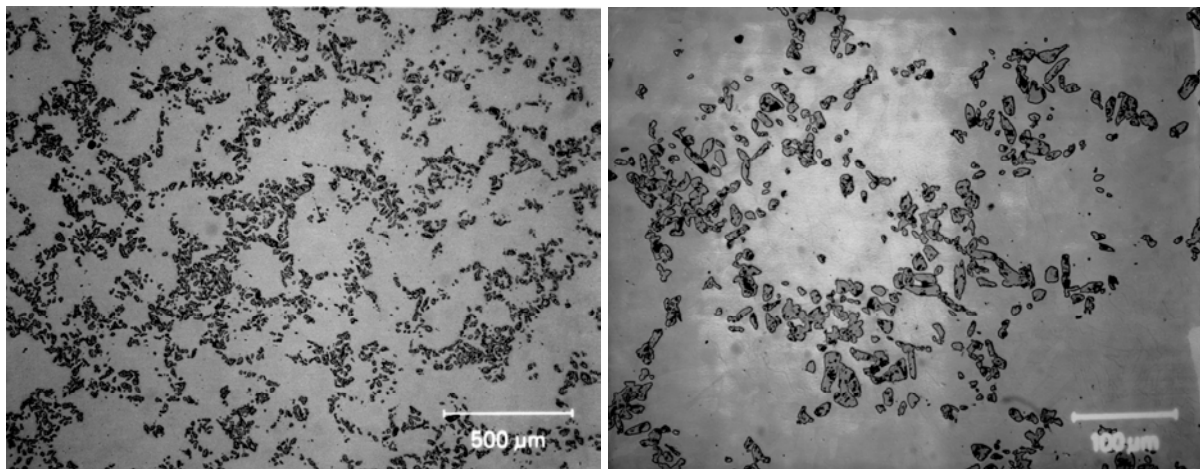


**Figure 4.1 – Particle distribution of the CHIP-processed Ti6Al4V+10 wt.% TiC composite. OM.**

Figure 4.2 shows the microstructure of the Ti6Al4V+10wt.% TiC alloy which consists of platelike elongated and equiaxed (in some regions)  $\alpha$  grains as well as intergranular  $\beta$  produced by alloying between titanium, aluminium and vanadium, with TiC particles randomly distributed in the matrix. The microstructure is typical of  $\alpha+\beta$  titanium-base alloys, particularly Ti6Al4V, that have been furnace cooled from above the  $\beta$  transus temperature. Indeed, the titanium alloy matrix is formed during the sintering process by diffusion-driven solid-state alloying, typically at temperatures less than 250°C above  $\beta$  transus temperature (1230°C for Ti6Al4V). It is also possible to observe from Figure 4.2 that in some regions the



composite matrix contains not-elongated grains, with  $\beta$  crystals at the grain boundaries. The quasi-equiaxed morphology of  $\alpha$  grains in the composite suggests that the growth of this phase from the  $\beta$  crystals occurs in a different way with respect to the other regions. Very likely, the presence of the TiC particles (which means the appearance of matrix/TiC interfaces) hinders the growth of  $\alpha$  crystals parallel to specific crystallographic planes and, as a consequence, the formation of elongated crystals (see Fig. 4.3) [191]. The final properties of the composite are improved as well since as opposed to melt processing, the thermal decomposition of the TiC reinforcing particulate (melting point of approximately 3065°C) can be limited to a practical extent during the sintering cycle [192]. The last step of the process is HIP at 899°C for 2 hours at 103 MPa which has allowed slow cooling rates (furnace cooled) and the formation of such microstructure with large plates of  $\alpha$  separated by the semi-continuous  $\beta$  phase ribs between them; however the presence of equiaxed  $\alpha$  has also been observed in some regions (indicated by E in Fig. 4.2), particularly close to the TiC particles. The platelike  $\alpha$  is the dark grey phase (indicated by P in Fig. 4.2); while the intergranular  $\beta$  is the bright grey phase at the grain boundary (indicated by I in Fig. 4.2). Porosities could be observed in some areas, particularly in between TiC particulate indicating that full density has not been achieved; however, the presence of such defects can result from problems occurred during metallographic preparation, when TiC parts were knocked off as a result of excessive force during polishing and/or grinding.

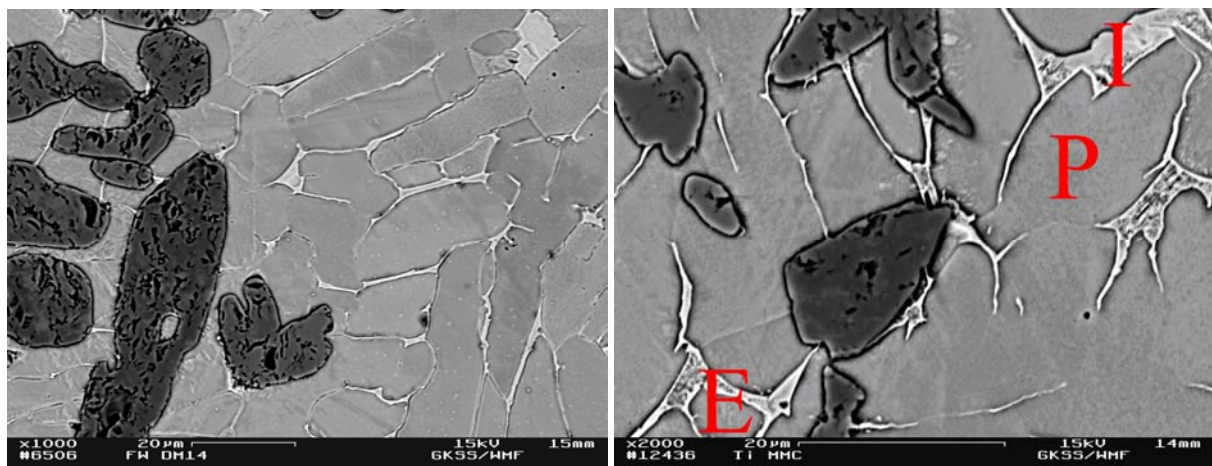


**Figure 4.2- Base material (Ti6Al4V+10 wt.% of TiC) microstructure. SEM.**

The presence of platelike  $\alpha$  is explained as a result of the slow cooling from the  $\beta$  region by a diffusion-controlled process (nucleation and growth) along one or several sets of preferred crystallographic planes of the prior  $\beta$  matrix (see Fig. 4.3). Upon slow cooling, a nucleus of  $\alpha$  forms and, because of the close atomic matching along this common plane, the  $\alpha$

phase thickens relatively slowly perpendicular to this plane but grows faster along the plane; thus, plates are developed and the microstructure consists of  $\alpha$  plates delineated by  $\beta$  phase between them. The platelet width depends on the cooling rate; higher cooling rates resulting in finer microstructures while slower cooling rates result in coarsened microstructures [23].

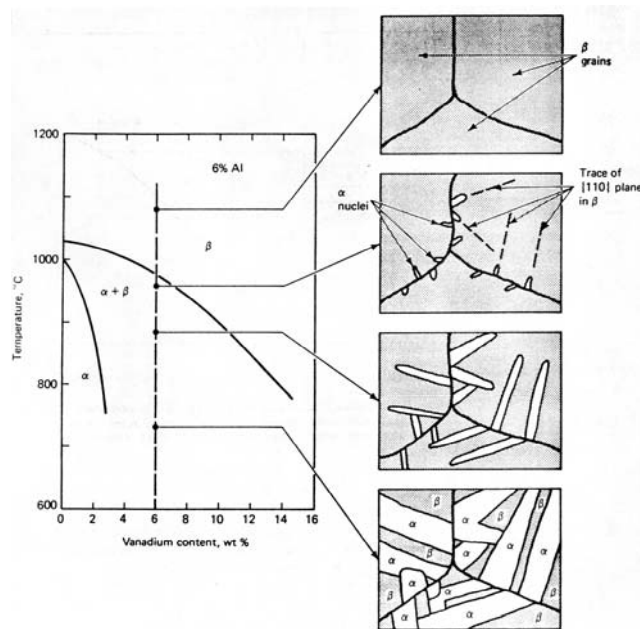


**Figure 4.3 - Schematic representation of platelike  $\alpha$  and intergranular  $\beta$  formation in a Ti6Al4V alloy by slow cooling from above the  $\beta$  transus temperature [23].**

Energy-Dispersive Spectrometry (EDS) has been used in this investigation in order to identify and quantify the chemical elements present in the Ti6Al4V+10 wt.% TiC base material. Figure 4.4 and Table 4.1 show the typical element distribution for the Ti6Al4V+10%TiC alloy presenting four different elements - carbon, aluminium, titanium and vanadium. Six different positions have been analysed in order to determine the compositional analysis of the individual phases providing information concerning the specimen composition on a microscopic scale. As it is possible to observe, the body-centered cubic (bcc) vanadium segregates in the  $\beta$  phase (points 1 and 2) which is also bcc; while the face-centered cubic (fcc) aluminium segregates in the  $\alpha$  phase which is close-packed hexagonal - points 3 and 4 – According to Brooks [23], in ternary Ti-Al-V alloys, it is not apparent what the stabilizing effect will be with both Al and V present; however, one would expect that if both phases are present, the Al will tend to segregate in the  $\alpha$ , and the V in the  $\beta$ . Points 5 and 6 shows the chemical composition of the TiC particles. Figure 4.5 shows the element distribution (C, Ti, V, Al) along a predetermined line and is also possible to observe the aluminium and vanadium segregation in the  $\alpha$  and  $\beta$  phases, respectively, and the different carbon distribution along the sample. Badini et al [191] have found carbon content values of 34.15 %

at. in an as-received Ti6Al4V/TiC<sub>p</sub> (10 % vol.) which is very different from the ones found in this investigation mainly due to the qualitative character of the test. However, the carbon content values in weight percent in the matrix (2.0 % wt. – inductively coupled plasma optical emission spectroscopy) are much higher than the ones found by Badini et al [191] (0.45 % wt – wavelength dispersive spectroscopy method) which means that there is much more carbon available in the matrix for the composite investigated.

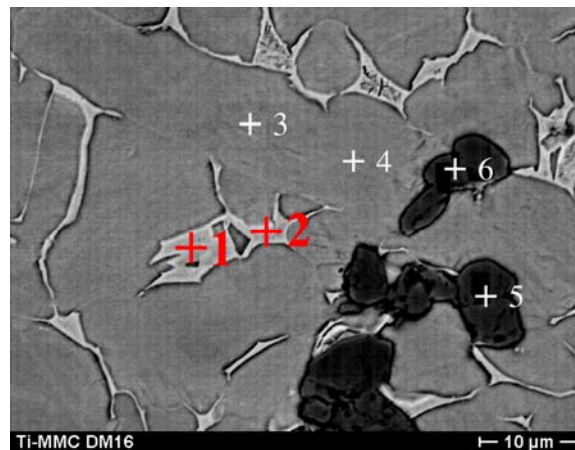


Figure 4.4 - Position of the different points at the composite for the EDS analysis. SEM.

Table 4.1 - Results of the EDS analysis in six different points of the composite.

	C (% at.)	Al (% at.)	Ti (% at.)	V (% at.)
<b>Point 1</b>	4.26	2.93	77.97	14.85
<b>Point 2</b>	4.34	2.59	72.82	20.25
<b>Point 3</b>	3.68	6.57	85.21	4.551
<b>Point 4</b>	3.71	6.60	85.16	4.53
<b>Point 5</b>	14.09	0.24	82.36	3.31
<b>Point 6</b>	14.59	0.07	82.64	2.70

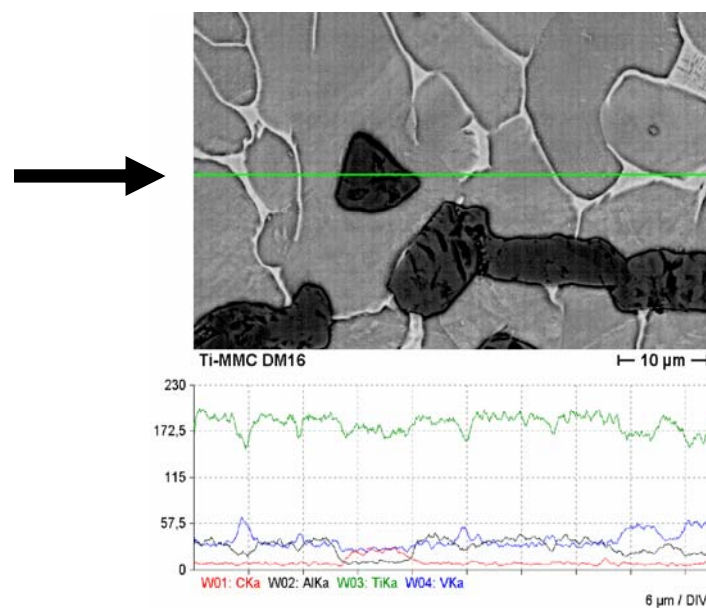
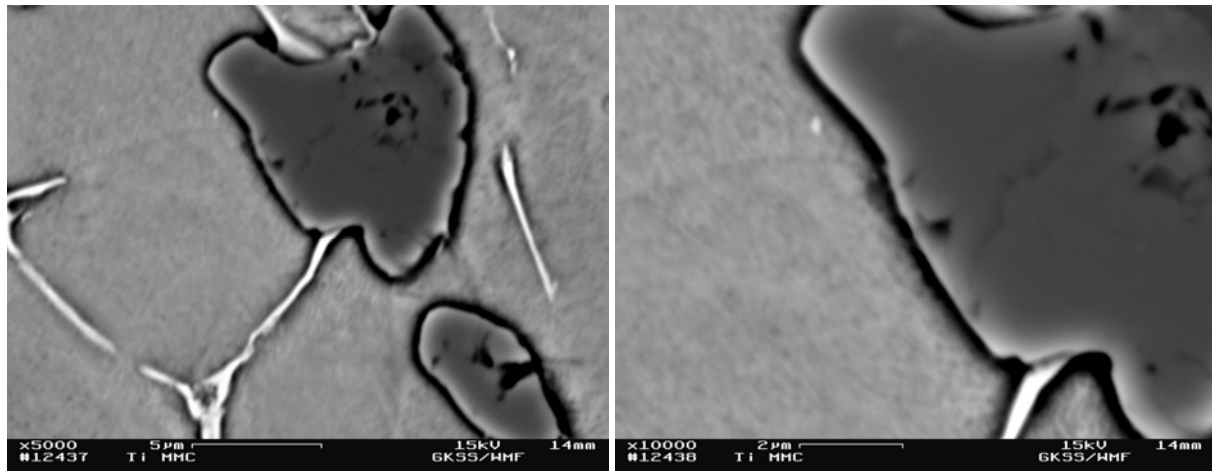


Figure 4.5 –Chemical composition profile analysed by EDS (line indicated by the arrow). SEM.

Another important feature is that the TiC particulate is thermodynamically stable in the titanium alloy matrix at CHIP-processing temperatures resulting in a stable particle-matrix interface [39,40]. It is assumed that the Ti6Al4V/TiC matrix/particulate interface system is stable because no interface cracking or any kind of intermetallic phase has been observed (Fig. 4.6) showing no evidence of interaction between the components of the system.



**Figure 4.6 – SEM high magnification micrograph showing no evidence of interaction between the TiC particle and the Ti6Al4V matrix.**

#### **4.1.1.1 Image Analysis of the Base Material**

The particle characteristics of the base material, such as shape factor, mean Ferret diameter, particle area as well as the nearest neighbour distance (NND, i.e., the frequency distribution of the interparticle spacing) have been determined with the aid of an image analyser and an optical microscope. The image analysis technique consisted of analysing the particle distribution using a magnification of 200 times comprising a total area field of approximately  $0.77 \text{ mm}^2$  (for each of the ten micrograph analysed). Figure 4.7 shows examples of micrographs used to analyse the base material particle distribution.

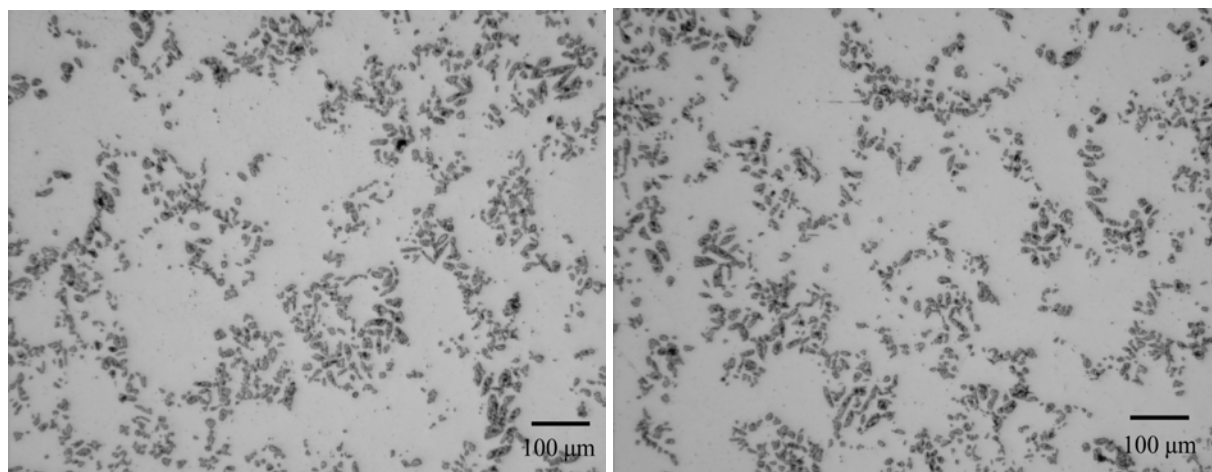


**Figure 4.7 - Micrographs used to investigate the base material particle characteristics.**

The shape factor of the base material was determined to be 0.68 with a STD of 0.22. Table 4.2 shows the results for the determination of the base material mean Ferret diameter and Figure 4.8 shows the particulate mean Ferret diameter distribution. One can observe that more than 50% of the particles are in the range of 0.01 to 10  $\mu\text{m}$  indicating a very fine distribution, however more than 5% of particles are larger than 50  $\mu\text{m}$  indicating problems in controlling the manufacturing process since such large particles are not expected. Indeed, Ranganath [190] has suggested that particle distribution is critical in CHIP-processed composites. Doel and Bowen [64] have observed that the presence of larger ceramic particles (even though the specimen has a fine particle distribution) may have a detrimental influence on the mechanical properties (reduction in strength and ductility) affecting the overall performance of the material by initiating localised damage since they are more prone to fracture at a given applied stress than smaller particles (larger particles are more likely to contain a flaw of a critical size). Therefore a 50  $\mu\text{m}$  particle is more likely to fail at a low applied stress than a small particle (10  $\mu\text{m}$  or less).

**Table 4.2 - Mean Ferret diameter results of the base material.**

Mean Ferret diameter ( $\mu\text{m}$ )	
Average	14.7
STD	20.1

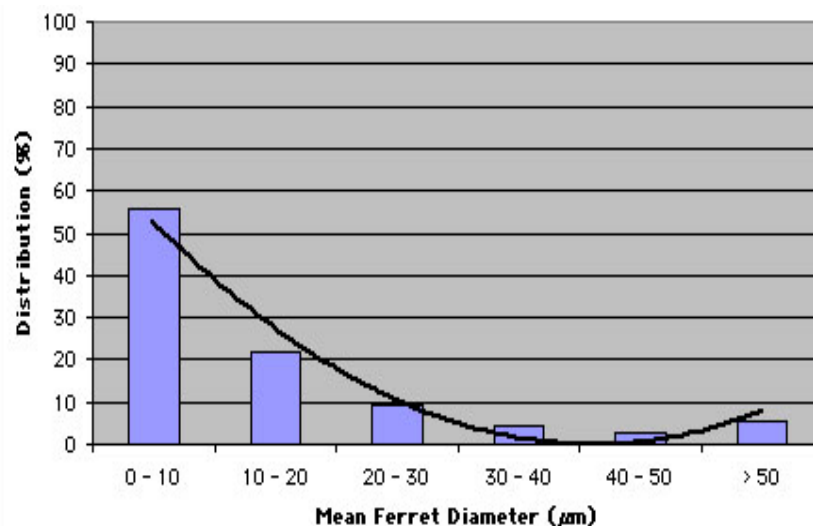


**Figure 4.8 –Mean Ferret diameter distribution of the base material condition.**

The TiC particles area in a 0.77  $\text{mm}^2$  area field was 20.5% with a STD of 2.2%. The remaining average area (79.5%) comprises platelike  $\alpha$  and intergranular  $\beta$  (Ti6Al4V matrix microstructure). It was not possible to determine the platelike  $\alpha$  and intergranular  $\beta$  area separately due to difficulties in establishing an appropriate threshold to ensure a correct evaluation. The individual particle area average was determined to be 231.8  $\mu\text{m}^2$  (STD of

641.7  $\mu\text{m}^2$ ). Another particle feature analysed was the NND which determines the interparticle spacing frequency analysing the distances between each particle. Such feature allows the observation of how close one particle is from the other and the subsequently indication of particle clustering or inefficient distribution along the specimen. It can be observed from Fig. 4.9 that there is an inhomogeneous distribution with some areas having fewer particles than others indicating particle clustering since there is a wide distance distribution ranging from very small to very large distances (up to 70  $\mu\text{m}$ ). Composites with homogeneous distribution would have a NND versus frequency curve with a peak-like behaviour in which an ideal value of NND has a high frequency value. The interparticle spacing was determined performing an interpolation in the NND values and for the base material the value was 18.11  $\mu\text{m}$ .

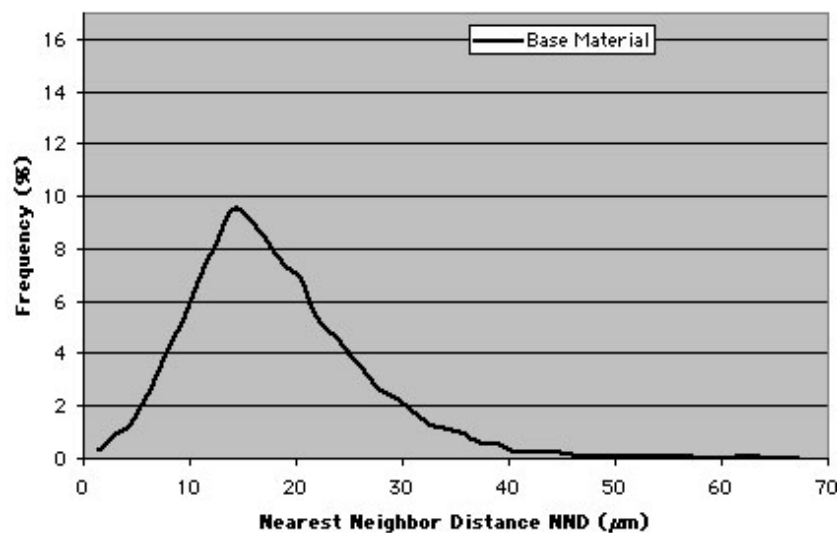


Figure 4.9 –Nearest neighbour distance distribution of the base material condition.

## 4.1.2 Mechanical Characterisation - Ti6Al4V+10 wt.% TiC

### 4.1.2.1 Microhardness

Microhardness profiles were performed across the base material using 300 p (2.94N) load with 0.2 mm spacing between each indentation. The presence of the TiC particles have influenced the hardness final results since whenever an indentation was exactly at the particle, the hardness value was much higher than the expected one for the base material; differences of up to 400 HV0.3 have been reported during the test. Figure 4.10 shows the variation in the values of three different indentations. In order to minimize such effect it has been performed five indentation lines across the material and with the resulting values a statistical analysis (average and STD) has been performed (two on each side of the centreline, see 3.7.1 of the Experimental Procedure), see Fig. 4.11. Base material microhardness results evaluation carried out by this investigation are in perfect accordance to the literature [193].



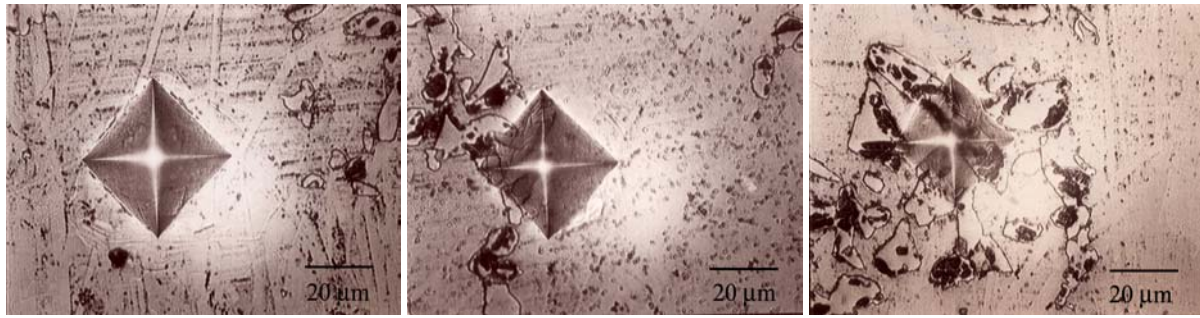


Figure 4.10 - Hardness variation due to the TiC particles presence. (a) base material, 352 HV0.3; (b) base material + TiC particles, 413 HV0.3 and (c) TiC particle, 551 HV0.3.

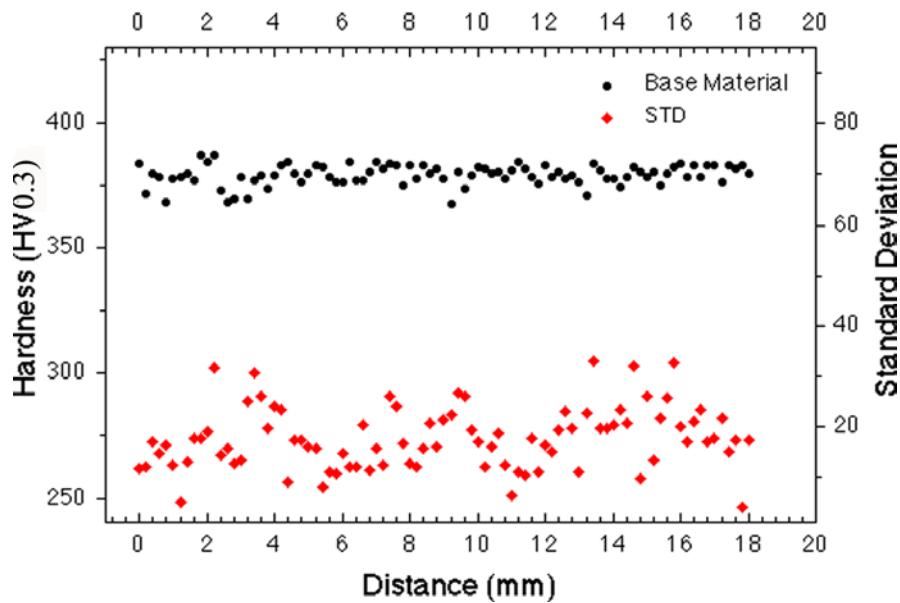


Figure 4.11 – Hardness distribution of the base material (Ti6Al4V+10 wt.% TiC).

#### 4.1.2.2 Tensile Tests

##### 4.1.2.2.1 Room Temperature Tensile Tests

The base material room temperature tensile results are presented in Table 4.3 in terms of yield strength ( $R_{p0.2}$ ), tensile strength ( $R_m$ ) and elongation. The increase in the strength values of the base material compared to the monolithic matrix is a result of the much higher work-hardening rate at lower strains resulting from the constraint exerted by the elastic reinforcing particles on the plastic flow of the matrix. Since the particles can only deform elastically, considerably higher local matrix strain is required to accommodate any plastic deformation in the composite than in the unreinforced monolithic alloy [194]. The low values of elongation (less than 1%) results from the elastic restraint imposed on the matrix by the particles and the subsequent stress concentration around the particulate [49]. The presence of clustering (see Fig. 4.1) was also crucial for the final elongation behaviour. Indeed, when the material is being subjected to loading the presence of clusters and defects (higher local reinforcement volume fraction than the mean value) reduce the ductility because these areas

are more sensitive to premature damage since the elastic reinforcing particles constrain the matrix plastic flow producing increased stress levels in the particles and high stress triaxiality in the matrix between the particles [49,65]. The homogeneity of the material is also important since it can affect the degree of strengthening. Indeed, the base material composite has a certain degree of inhomogeneity (see Fig. 4.1) that could have reduced the degree of strengthening that is caused by two factors that act in opposition to the elastic restraint and decrease the rate of work hardening; first, there is the plastic relaxation of the elastic restraint caused by lattice rotation in the vicinity of the larger particles; second, the presence of particle cracking since in the areas with high volume fraction a crack that forms in one particle easily “jump” to neighbouring particles [60]. Segurado et al [195] have affirmed that the presence of particle clustering in the microstructure of a composite greatly reduces the flow stress of the composite (due to the rapid fracture of the reinforcement). In addition a marked drop in the strain hardening capacity happens, and the onset of plastic instability (which controls the tensile ductility of the composites) occurs at very low strains. Therefore, the presence of even a small degree of clustering has very negative effects on the onset of damage by particle fracture, and consequently on the overall mechanical properties.

**Table 4.3 – Tensile properties of the base material.**

<b>Condition</b>	<b>R<sub>p0,2</sub> (MPa)</b>	<b>R<sub>m</sub> (MPa)</b>	<b>Elongation (%)</b>
<b>BM</b>	954 ± 10	967 ± 17	0.31 ± 0.15

#### **4.1.2.2.1.1 Fracture Surface Analysis of the Tensile Specimens**

The fracture investigation of particle reinforced materials in the past has always considered a weak bonding interface between the matrix and the particles resulting in fracture dominated by interfacial failure. However, nowadays, due to the improvements in the processing and manufacturing technologies, the composites have good bonding between the matrix and the particles, and the BE-CHIP-processed Ti6Al4V+10%TiC has demonstrated such behaviour (see Fig. 4.6). Therefore, the composite fracture is controlled by fracture of the reinforcing particle which occurs very early in deformation, and continues with increasing strain. The extent of particle cracking is dependent on the reinforcing particles size distribution, their aspect ratio and volume fraction, particle distribution homogeneity and matrix microstructure. Therefore, particle clustering and particle size play an important role in controlling the crack growth and composite failure [196]. Also, the failure strain of the composite with clustered particle arrangement is significantly lower than that for the composite with uniform distribution [197]. Indeed, the presence of such clustered particles in the base material must have significantly decreased the final elongation of the base material.



It is possible to observe from Fig. 4.1 that there is an inhomogeneous distribution with the particles concentrated in some areas (especially in the prior beta grain boundaries) confirming such tendency for low strain to failure behaviour.

The fracture surface analysis performed in the SEM has indicated, as expected, brittle fracture of the TiC particles and ductile fracture of the matrix. The important features of the base material fracture behaviour are local matrix microvoid coalescence (ductile fracture, indicated by DF in Fig. 4.12) as well as flat facets of fractured particles (particle fracture, PF in Fig. 4.12). Indeed, there has been found a high amount of fractured particles in the crack path of the tensile fracture surfaces indicating the presence of such behaviour. Secondary cracking has also been observed (SC in Fig. 4.12) showing the brittle nature of the reinforcing particles (the particles have been shattered before rupture).

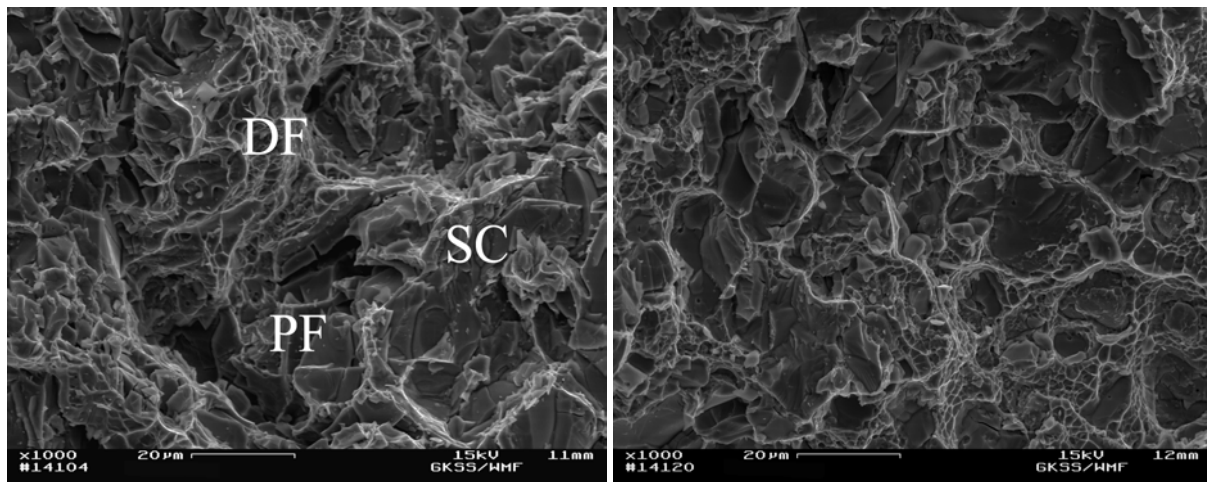


**Figure 4.12 – SEM micrographs taken from the base material fracture surface.**

The failure mechanism of the composite involves stress being transferred to the particles when the composite is loaded [77]. When the stress build up around a particle reaches a critical value, particle fracture or interface decohesion takes place. Particle fracture has been considered the responsible for initiating the fracture since there has been found a large amount of fractured particles in the fracture surface of the base material (see Fig. 4.12). Therefore as the applied tensile load increases more particles reach their critical stress and fracture accumulating internal damages. This phenomenon leads to the introduction of internal defects (voids) and consequently the fractured particle no longer supports the applied load leading to the expansion of these damaged regions which introduce more voids that eventually grow leading to failure and reduced ductility of the composite. The fracture of the base material has occurred by the same mechanism explained above, i.e., void initiation as a result of particle reinforcement fracture (due to the high amount of fractured particles in the

crack path), growth and linking of these damaged areas and finally ductile fracture of the matrix (confirmed by the presence of coalescence of microvoids).

The fracture of MMCs has been shown to proceed by a ductile rupture (tearing) mechanism [75]. Indeed, the fracture mechanism of MMCs can be depicted into three stages: nucleation, growth and finally coalescence of the voids to give total failure of the material. Additionally, in ductile materials reinforced with a high volume fraction of hard second phase particles it has been suggested that the fracture nucleation events may dominate the ductility since the subsequent stages of void growth and coalescence may be extremely rapid once fracture initiation has occurred [80]. Brechet et al [198] affirm that one can consider damage events occurring either due to the load transfer and elastic loading of the particles or the development of critical stresses levels due to local work hardening of the adjacent matrix. Llorca and Gonzalez [199] have suggested that during deformation (monotonic tensile loading) the stress on intact particles increases owing to two mechanisms: the progressive strain hardening of the matrix as well as the fracture of neighbour particles. The increase in the load carried by the reinforcements was mainly due to the former mechanism at the initial stages of plastic deformation leading to a homogeneous distribution of the broken particles throughout the specimen as the load relaxed by the broken particles is mainly taken up by the surrounding matrix. However, as the matrix strain hardening capacity saturates, the stresses relaxed by the fracture of the reinforcements are transferred to the neighbour particles, because the matrix cannot harden more. The load carried by the neighbour particles is thus increased, which leads to more particle fracture. This chain reaction is self-sustained and tends to localize very quickly in a given section of the specimen. The final fracture of the specimen takes place by a ductile mechanism involving the nucleation and growth of voids in the matrix around the particles of the reinforcement material, which contribute to the final coalescence of the larger voids originated around the broken reinforcements.

#### 4.1.2.2.2 High Temperature Tensile Tests

The TiC reinforced Ti6Al4V composite tensile behaviour at elevated temperatures (200°C and 375°C) was the expected i.e., increasing the temperature reduces the tensile strength ( $R_m$ ) as well as the yield strength ( $R_{p0.2}$ ). Tables 4.4 and 4.5 present the high temperature tests results. The high temperature tensile behaviour is explained by the fact that increasing the testing temperature the density and the multiplication rate of dislocations decrease therefore resulting in a loss of resistance to plastic flow with the material becoming more ductile. Loretto and Konitzer [46] have also shown that ductility increases at

intermediate temperatures (200°C), decreases at higher temperature (375°C) and once again increases at high temperatures; however Badini et al [191] have not observed such effect since elongation has always increased with increasing temperature. Figure 4.13 shows the difference in the mechanical behaviour according to the temperatures tested. It can also be observed that the  $R_m$  and the  $R_{p0,2}$  decrease approximately 38% and 34%, respectively. Secondary electron micrographs taken from the fracture surfaces of the conditions tested have indicated the same failure mechanism to that found at room temperature, i.e, the TiC particles fracture (identified by PF in Figs. 4.14 and 4.15) prior to failure of the surrounding matrix and ductile failure through matrix (presence of microscoalescence of microvoids, identified by DF in Figs. 4.14 and 4.15). Figure 4.14 presents the fracture surfaces of the specimens tested at 200°C while Figure 4.15 presents the ones tested at 375°C. Due to the secondary cracking (represented by SC in Figs. 4.14 and 4.15) and TiC particles cracking it can be clearly observed from these figures that the fracture of the composite is controlled by failure in the reinforcing particle (no formation of interaction zones between the reinforcement and the matrix which could have led to particle debonding). The only difference that has been found when comparing room and high temperature fracture surfaces is the size of the dimples, with the higher temperature condition presenting, as expected, larger dimples as well as a slightly larger amount of dimples in the fracture surface with increasing temperature.

**Table 4.4 - Tensile test results at high temperature (200°C) for the base material composite.**

	$R_{p0,2}$ (MPa)	$R_m$ (MPa)	Elongation (%)
<b>Average</b>	$695 \pm 10$	$732 \pm 2$	$2.32 \pm 0.38$

**Table 4.5 – Tensile test results at high temperature (375°C) for the base material composite.**

	$R_{p0,2}$ (MPa)	$R_m$ (MPa)	Elongation (%)
<b>Average</b>	$589 \pm 2$	$636 \pm 19$	$1.41 \pm 0.50$

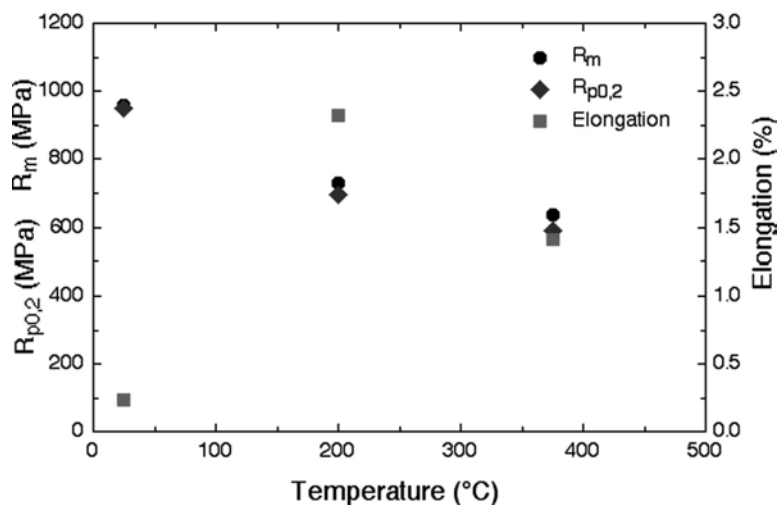


**Figure 4.13 - Tensile behaviour according to different testing temperatures (base material zone).**

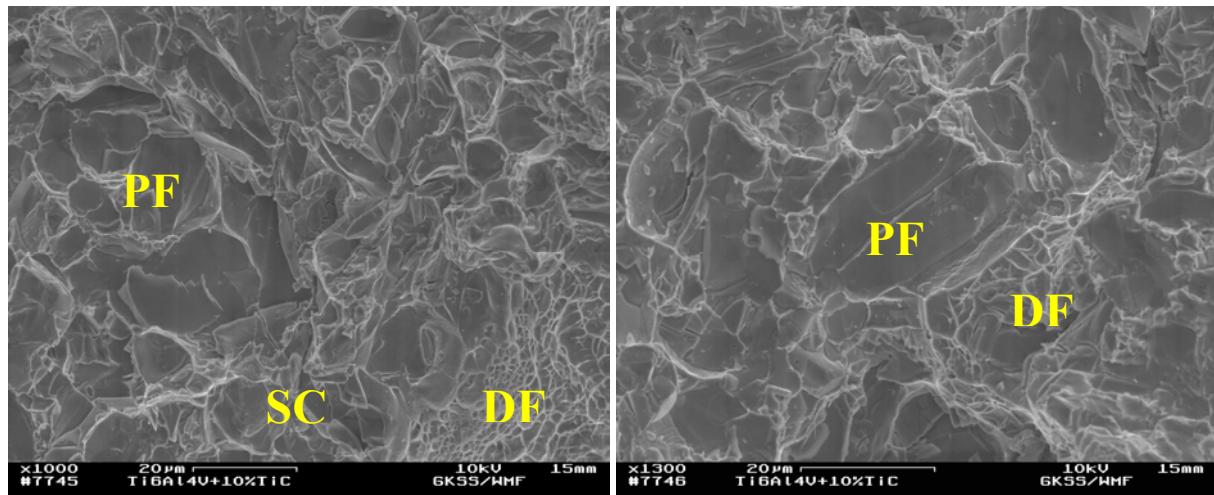


Figure 4.14 - SEM micrographs taken from the fracture surfaces of the tensile specimens tested at 200°C. PF: Particle fracture. SC: Secondary cracking. DF: Ductile fracture.

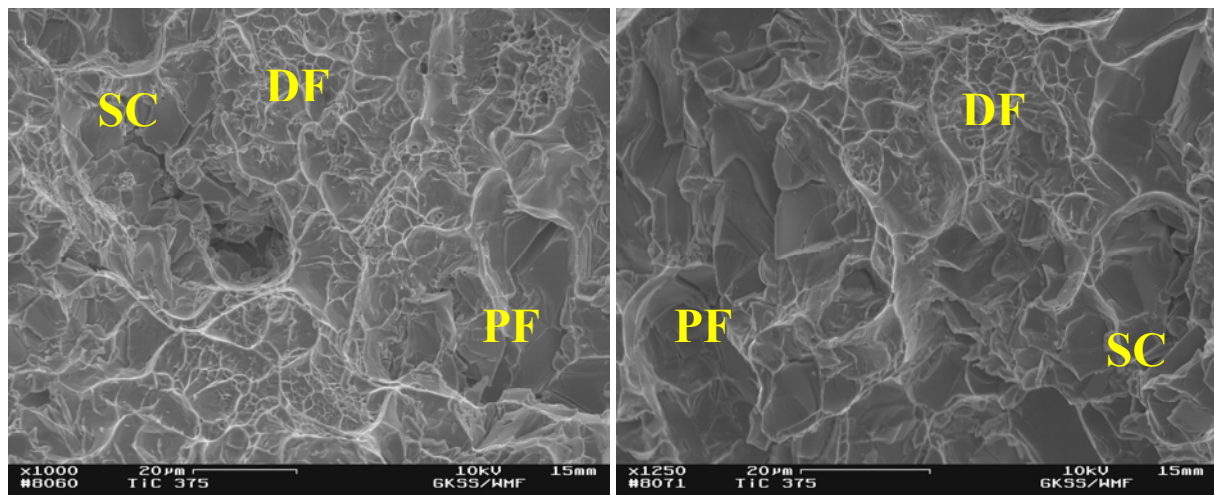
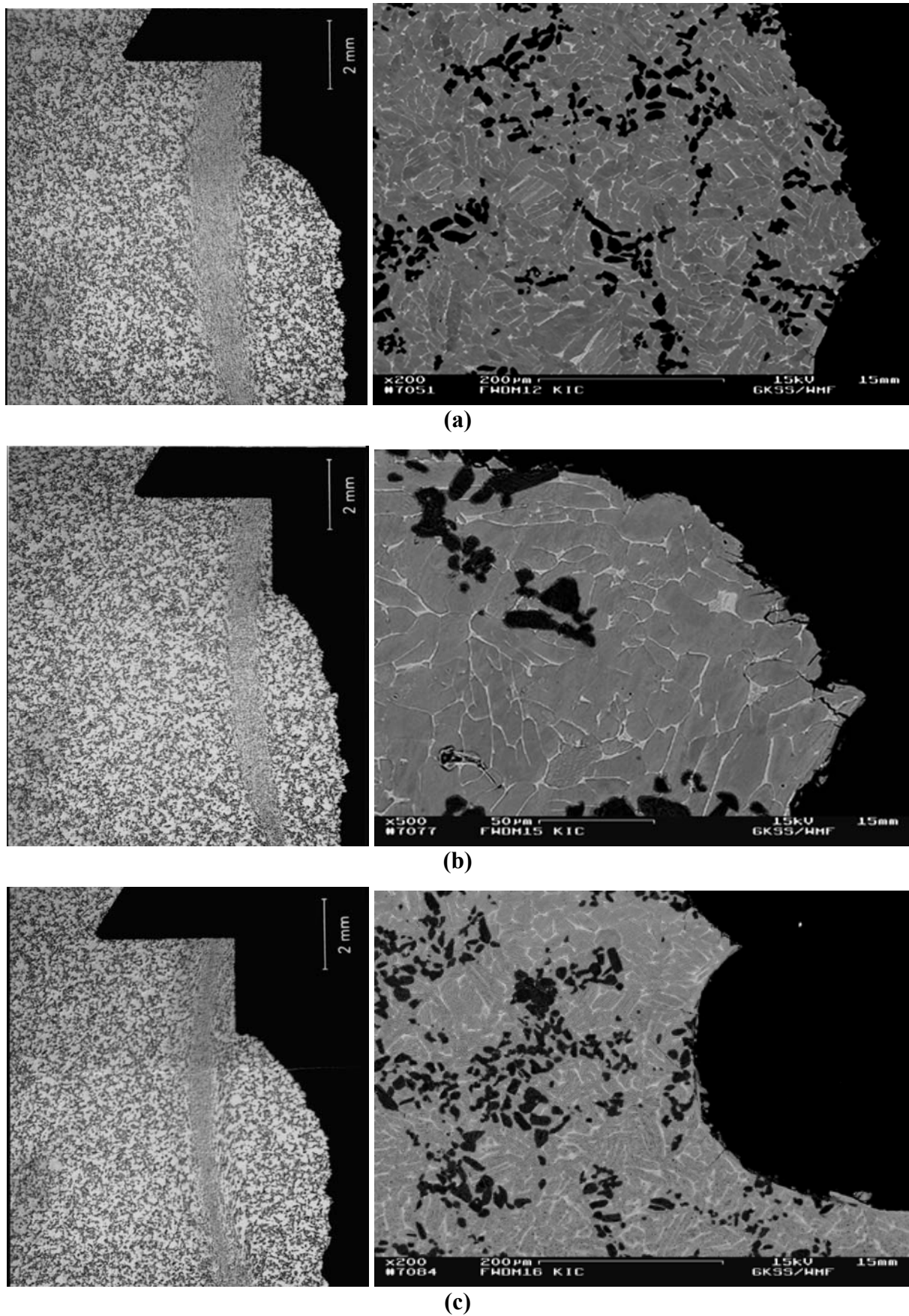


Figure 4.15 - SEM micrographs taken from the fracture surfaces of the tensile specimens tested at 375°C. PF: Particle fracture. SC: Secondary cracking. DF: Ductile fracture.

#### 4.1.2.3 Fracture Toughness Tests

The fracture toughness tests performed in the Ti6Al4V+10 wt.% TiC friction welded joints are masked due to problems during machining of the notches (see Fig. 4.16). Most of the notches have been spark eroded in the base material (see Table 4.6 for the exact location of all notches and  $K_{IC}$  values), which represents an unreal situation, i.e., instead of testing the welded condition (transformed regions – TRZ and HAZ) the base material condition was tested and as a consequence the “apparent” fracture toughness of the material was determined and not the representative value. Therefore the specimens that had the notch located in the base material are going to be evaluated as base material condition; and the specimens that had the notch located in the transformed regions are going to be evaluated separately.



**Figure 4.16 – SEM micrographs showing the location of the notches in the fracture toughness specimens of the friction welding conditions. (a) DM12-6 (3000 rpm/136 MPa). (b) DM 15-7 (3000 rpm/272 MPa). (c) DM16-4 (4500 rpm/272 MPa).**

**Table 4.6 - Notch location according to the different friction welding zones in the fracture toughness specimens.**

Specimen	Location of the notch	$K_{IC}$ (MPa*m <sup>1/2</sup> )
DM11-4	BM	37.66
DM11-5	BM+HAZ	36.98
DM11-6	BM	36.96
DM11-7	BM	35.96
DM12-4	BM	36.33
DM12-5	BM	34.10
DM12-6	BM	39.88
DM12-7	TRZ+HAZ	38.42
DM13-4	TRZ	32.62
DM13-5	TRZ	33.24
DM13-6	TRZ	32.08
DM13-7	TRZ	34.59
DM14-4	BM	32.40
DM14-5	BM	34.30
DM14-6	BM	34.92
DM14-7	TRZ+HAZ	35.82
DM15-4	BM	34.23
DM15-5	BM	33.14
DM15-6	BM	35.41
DM15-7	BM	36.60
DM16-4	TRZ+HAZ	33.34
DM16-51	TRZ+HAZ	41.03
DM16-52	BM	40.78
DM16-7	BM	33.09

Table 4.7 presents the results of the fracture toughness tests (average and STD) performed in the base material (values from the welded joints which had the notch located in the base material have also been considered). It can be observed that there is a relatively large scatter of the  $K_{IC}$  values. Such behaviour can be justified by the presence of the TiC particles and their distribution as well as the local interparticle spacing, particle diameter and aspect ratio. Figure 4.17 presents the fracture toughness behaviour of all conditions tested where it is possible to observe the large scatter of the  $K_{IC}$  values.

**Table 4.7 – Results of fracture toughness of the base material (Ti6Al4V + 10 wt.% TiC).**

Condition	$K_{IC}$ (MPa*m <sup>1/2</sup> )	STD
BM	35.04	2.73



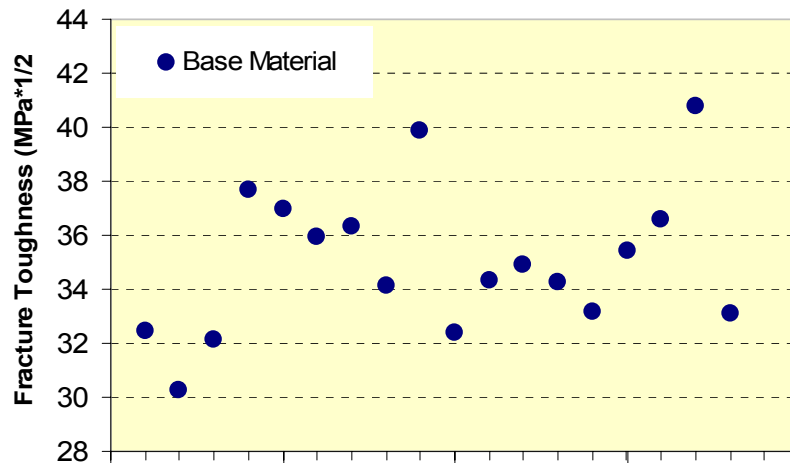


Figure 4.17 – Fracture toughness behaviour of the Ti6Al4V+10 wt.% TiC base material.

The crack path of the fracture toughness specimens in the base material is strongly influenced by the TiC particles (particle fracture), but it has also surrounded the particle (particle debonding); however the latter has not been as often observed as the former, Fig. 4.18.

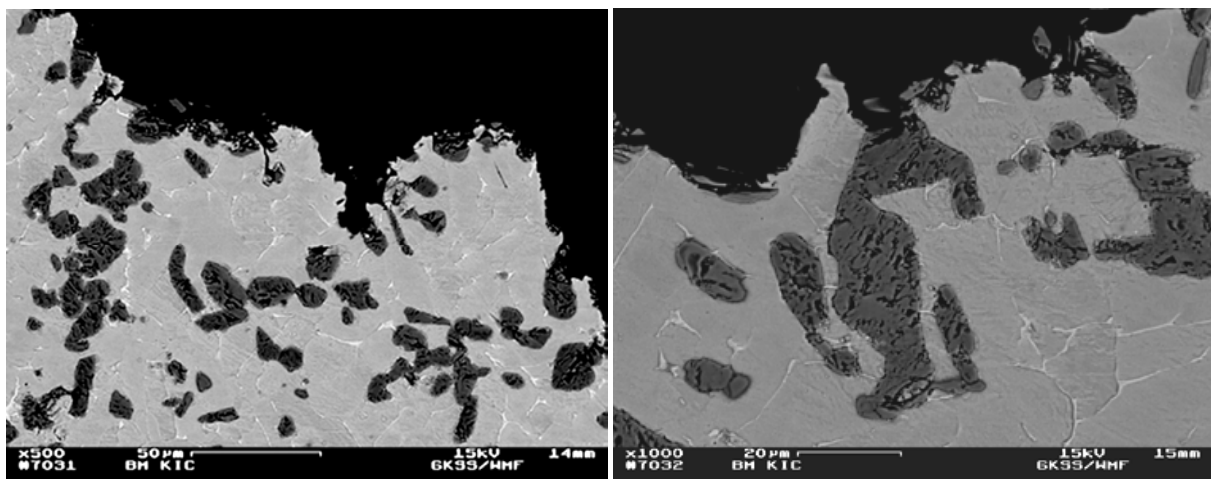
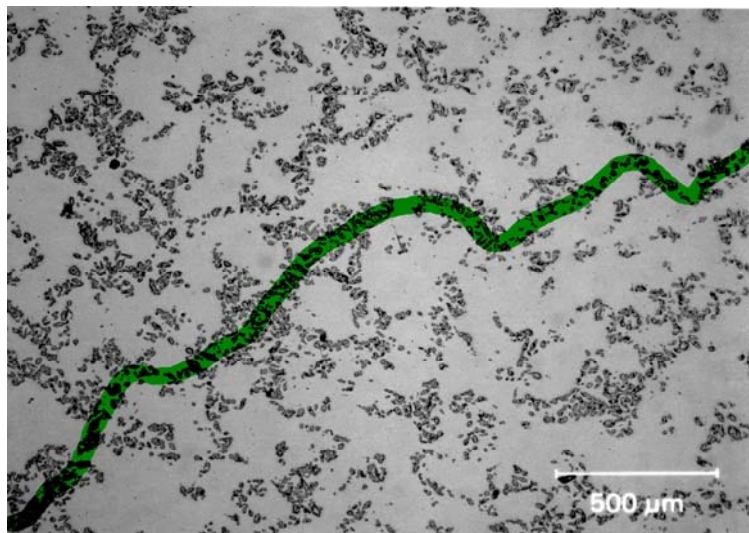


Figure 4.18 – SEM micrographs showing the crack path geometry of the base material. Etched.

The TiC particle resistance to crack propagation is considerably smaller and crack easily initiates in such locations. Since the TiC particles provide a crack propagation path, the crack deflection degree is small; however such behaviour is found when there is a homogeneous particle distribution; when inhomogeneity or clustering is present, such as in the base material, the crack path is deflected due to the different particle distribution across the base material. Berns et al [200] have also suggested that crack deflection leads to an increase of the crack area; therefore a deflected crack needs more surface energy to propagate than a straight crack path leading to an improvement of the fracture toughness behaviour.

The fracture toughness of the composite alloy can be quite sensitive to microstructural features. This sensitivity covers, among others, the reinforcement size and distribution, the volume fraction of reinforcing particles as well as the interfacial bond strength. However, according to Clyne [201] there is still a certain degree of uncertainty on the effects of these features but it is clear that relatively fine particle size, uniform spatial distribution and strong interfacial bonding all lead to enhanced fracture toughness. The reinforcement size has a great influence since the failure stress of a ceramic particle reduces with its size. A larger ceramic reinforcement fails sooner, thereby transferring the void nucleation mode from interfacial debonding to particle fracture. The largest particles in populations with a larger scatter in particles sizes tend to fracture. Reinforcement distribution is also important since clustered areas are dominant sites for crack nucleation and propagation as well as the fact that the fracture process is controlled by large triaxial stress intensification occurring in a cluster. According to Boyd and Lloyd [202] when particle distribution is nonuniform, damage is concentrated in particle clusters (or large reinforcements) and fracture occurs by linking of the “damage clusters”. Lewandowski [203] has also affirmed that macroscopic extension crack occurred via linkage of the crack tip with the damage present in the clustered regions ahead of the crack tip. Indeed, an influence of the particle distribution on the fracture toughness behaviour of the base material was found since the particles are concentrated in the prior  $\beta$  grain boundaries (see Fig. 4.19) creating a preferable crack path along the specimen reducing the fracture toughness.



**Figure 4.19 – Example of preferable crack path due to poor reinforcement distribution.**

Another important feature concerning the interpretation of the  $K_{IC}$  results is the determination of the plane strain plastic zone size at the crack tip ( $2r_p$ ) since the plastic zone



size represents the upper limit to the extent over which damaging stresses may exist as well as represents the area in which there is a high possibility of finding broken particles. The plastic zone size has been calculated according to Equation 4.1 [35,61,204] and the value found for the base material condition is 143.1  $\mu\text{m}$  (interparticle spacing of 18.11  $\mu\text{m}$ ).

$$2r_p \approx \frac{1}{3\pi} * \left( \frac{K}{\sigma_{YS}} \right)^2 \quad \text{Equation 4.1}$$

According to Doel and Bowen [204] it is expected that the stress levels close to the crack tip are very high and maintained at these high levels over distances of the same order as the interparticle spacing. Under such high levels of stress it is very likely that all the particles in the region of the crack tip will fail (inside the plastic zone and also close to it). Hence, all internal damage would be expected to occur very quickly in the early stages of loading. Voids can grow from these damaged particles, and thus the presence of cracked particles is expected to reduce the fracture toughness. In the base material condition the plastic zone size envelopes many particles extending over a distance much greater than the calculated interparticle spacing. This means that many more particles lie within this highly stressed region making the particle cracking phenomena more important in the final failure process. Figure 4.20 presents the influence of the size of the plastic zone in the fracture toughness behaviour of a particulate reinforced composite where it is possible to observe that the larger the plastic zone size, the higher is the possibility of causing more damage reducing the final fracture toughness value. This can be understood by considering different sampling volumes involved in crack propagation at different stress intensities (i.e., the volume of microstructure where crack-tip stresses and displacements are sufficient to induce local cracking processes associated with the crack advance). During fatigue pre-cracking of the specimens (low  $\Delta K$  levels) the sampling volumes (which can be approximated by the maximum plastic-zone size) are of the order of the interparticle spacing, accordingly, the probability of the crack "seeing" a particle cluster, associated voids or large particles is small. Conversely, with larger stress-intensity levels involved in monotonic crack extension, the sampling crack is attracted to them. It is reasoned that this interaction between the crack front and the voids from the TiC-particle clusters as well as the large particles is responsible for the non-uniform crack extension which in turn results in the poor fracture toughness behaviour of the composite.

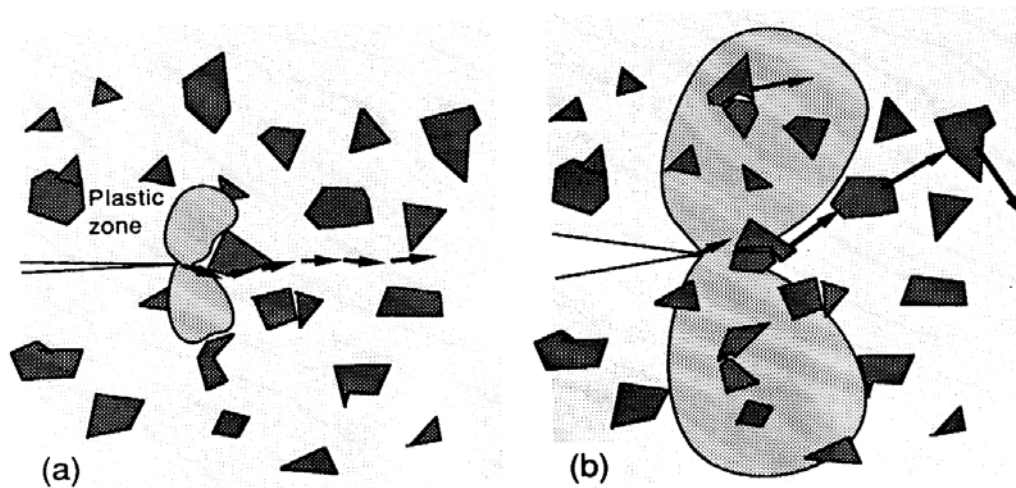


**Figure 4.20 – Influence of the plastic zone size on the fracture toughness behaviour of particulate reinforced composites. (a) Small plastic zone size (few or no particles inside). (b) Large plastic zone size (large amount of particles inside) [69].**

#### 4.1.2.3.1 Fracture Surface Analysis of the Fracture Toughness Specimens

According to the fractography performed in the fracture surfaces of the base material there are two types of damage modes: TiC particle cracking and matrix/particle interface debonding; however the latter has not been often observed as the former. According to Clyne and Withers [69] there are two types of mechanisms by which damage can initiate at a microscopic level: (1) reinforcement cracking, (2) matrix cavitation and interfacial debonding. The former occurs as a result of the local stress transfer from the matrix to the reinforcement particularly the ones in the upper range of size. The second failure mechanism normally takes place in immediate reinforcement vicinity, promoted by high levels of triaxial constraint and increased matrix work hardening degree resulting from both localisation of applied plastic strain and from differential thermal contraction effects. A series of factors tend to favour voids formation and it includes: large reinforcement size, high matrix flow stress, large imposed plastic strain, reinforcement on grain boundaries, particle clustering and others.

Basically, the fracture mechanism of the fracture toughness specimens is the same one observed in tensile testing), i.e., nucleation at the TiC particles, growth followed by ductile fracture of the matrix by coalescence of microvoids. However it has also been found extensive microcracking at and near the crack tip indicating that another fracture mechanism may be present. Such micromechanism of fracture is associated with the size of the plastic zone since high local stresses are associated with this specific site resulting in extensive microcracking at and near the crack tip. Also, the reinforcement size is an important feature strongly influencing the fracture toughness since larger particles have a higher probability of fracturing than the smaller ones. Such feature can be observed in Figure 4.21 where a high

amount of fractured particles can be observed and especially the larger ones (representing a preferable crack path). Figure 4.21 presents the fracture surface of the base material where it is possible to observe the same features presented by the fracture surfaces of the microflat tensile and tensile specimens such as coalescence of microvoids (DF in Fig. 4.21), particle fracture (PF in Fig. 4.21) as well as secondary cracking (SC in Figs. 4.21).

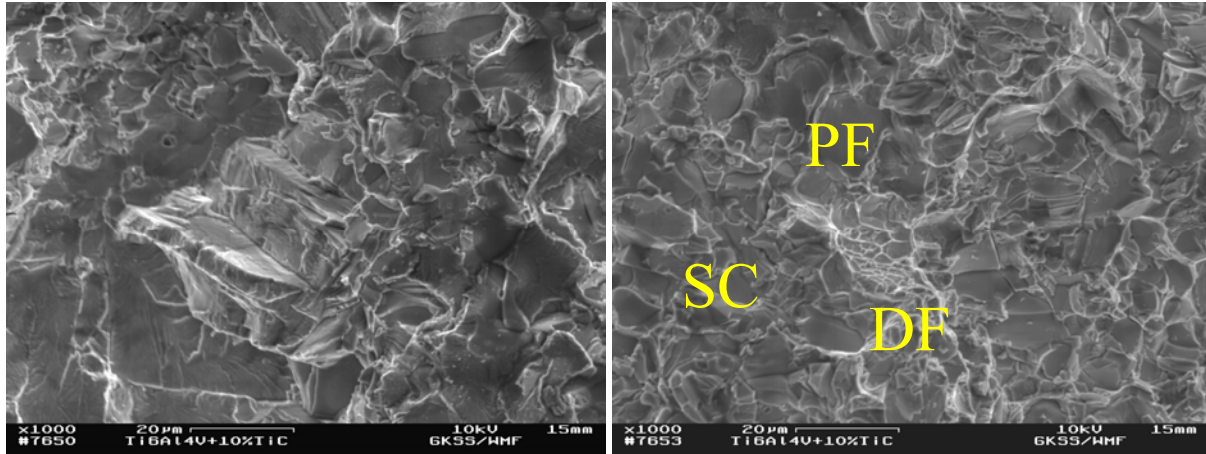
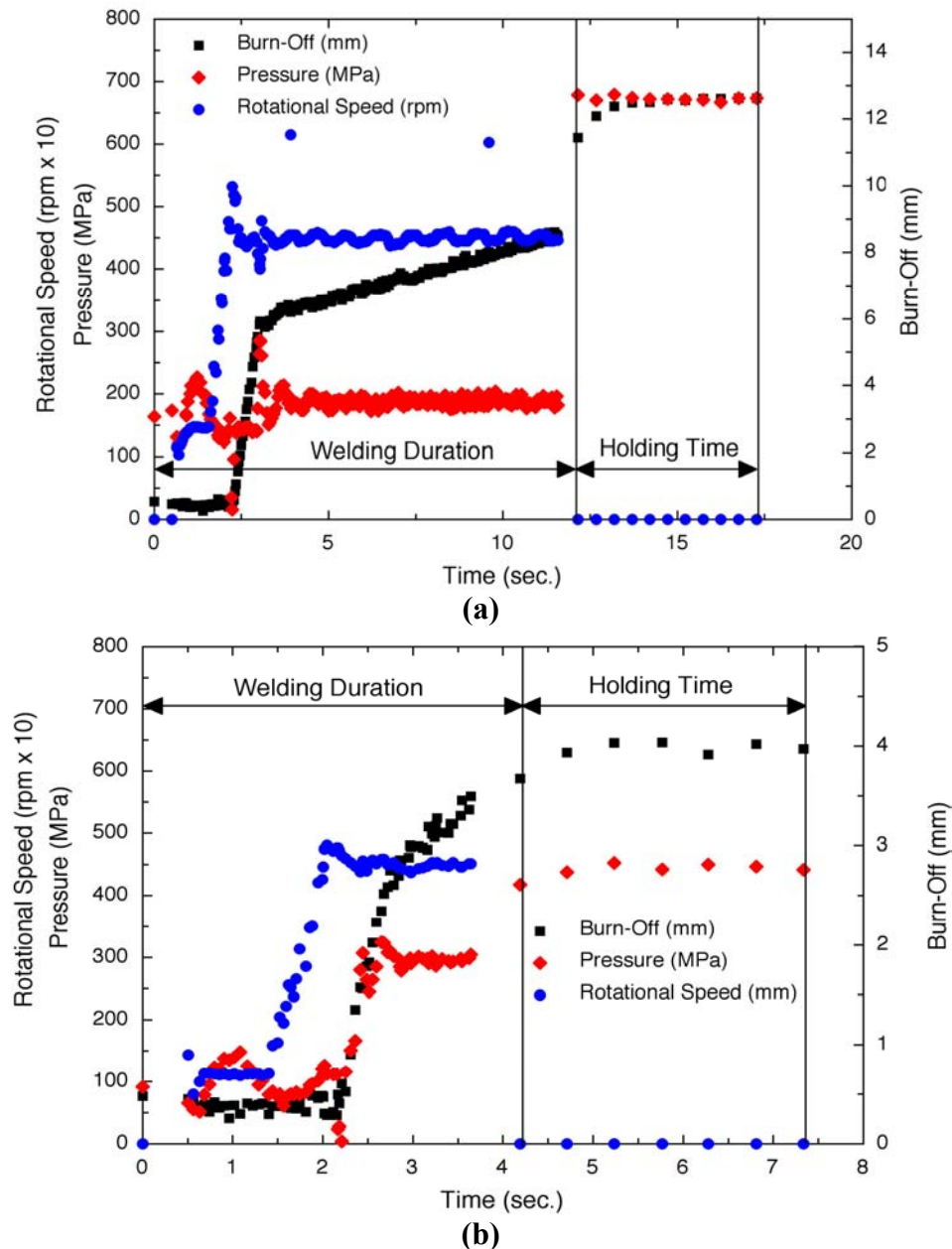


Figure 4.21 - SEM micrographs taken from the fracture surfaces of the base material.

## 4.2 Metallurgical and Mechanical Characterisation of the Ti6Al4V+10 wt.% TiC Friction Welded Joints

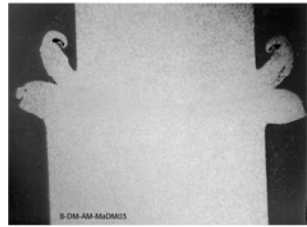
### 4.2.1 Friction Welding Process

The friction welding process has been initially performed varying four different parameters: rotational speed, burn-off and friction and forging pressure. Data information for every weld produced in this investigation has been stored for further processing and evaluation. Figure 4.22 presents the process diagram including the most important process parameters and also some information about the process, such as the welding duration and the holding time (3 seconds for every weld). As one can see, the rotational speed is started first and after the required speed is reached, the rotational stud is moved down making contact with the stationary stud. At this point the axial downward movement is measured as burn-off. The rotational speed and the pressure may vary during the welding process due to instabilities of the welding system (variation in the oil pressure). When the set burn off distance is reached, the rotational speed is stopped, but the pressure is kept for another three seconds.

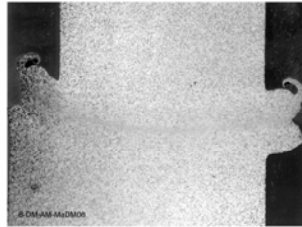


**Figure 4.22 – Welding process diagrams. (a) Condition DM 08: friction pressure 136MPa; forging pressure 544MPa; rotational speed 4500rpm; burn-off 3mm. (b) Condition DM 16-2: friction pressure 272MPa; forging pressure 408MPa; rotational speed 4500rpm; burn-off 2mm.**

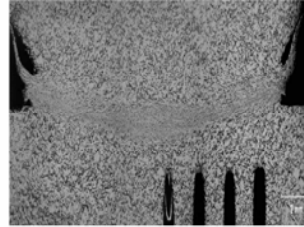
Among all the welded joints of the primary parameter matrix (14 initial conditions varying all the investigated welding parameters - rotational speed, burn-off, forging and friction pressure – Fig. 4.23), 6 have been selected, after a previous evaluation, resulting in the secondary parameter matrix (only 2 welding parameters have been varied – rotational speed and friction pressure, Fig. 4.24) in order to investigate the metallurgical changes that have taken place after the welding process. Such selection has been made in terms of a visual examination (presence of weld distortion and defects as well as the amount and formation of flash) and an initial macrostructural evaluation (presence of melted products and brittle intermetallic phases as well as the presence of weld defects - cracks, lack of bonding).



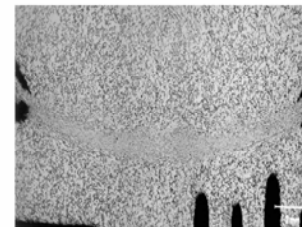
**DM 03**  
136 MPa 4 mm 4500 rpm  
544 MPa



**DM 08**  
136 MPa 3 mm 4500 rpm  
544 MPa



**DM 13**  
136 MPa 2 mm 4500 rpm  
408 MPa



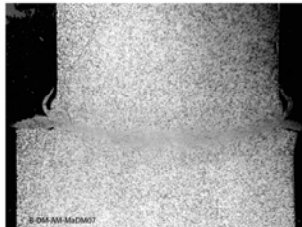
**DM 16**  
272 MPa 2 mm 4500 rpm  
408 MPa



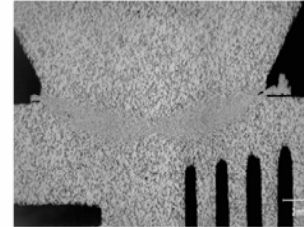
**DM 06**  
272 MPa 2 mm 4500 rpm  
544 MPa



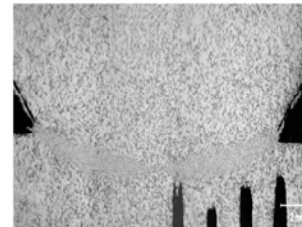
**DM 02**  
136 MPa 6 mm 3000 rpm  
748 MPa



**DM 07**  
136 MPa 3 mm 3000 rpm  
544 MPa



**DM 12**  
136 MPa 2 mm 3000 rpm  
408 MPa



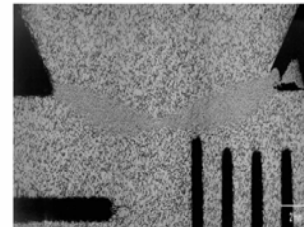
**DM 15**  
272 MPa 2 mm 3000 rpm  
408 MPa



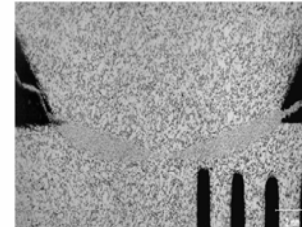
**DM 05**  
272 MPa 2 mm 3000 rpm  
544 MPa



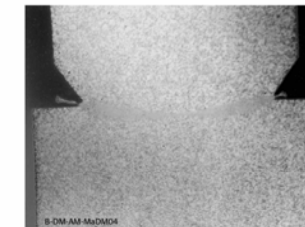
**DM 01**  
136 MPa 4 mm 1500 rpm  
748 MPa



**DM 11**  
136 MPa 2 mm 1500 rpm  
408 MPa

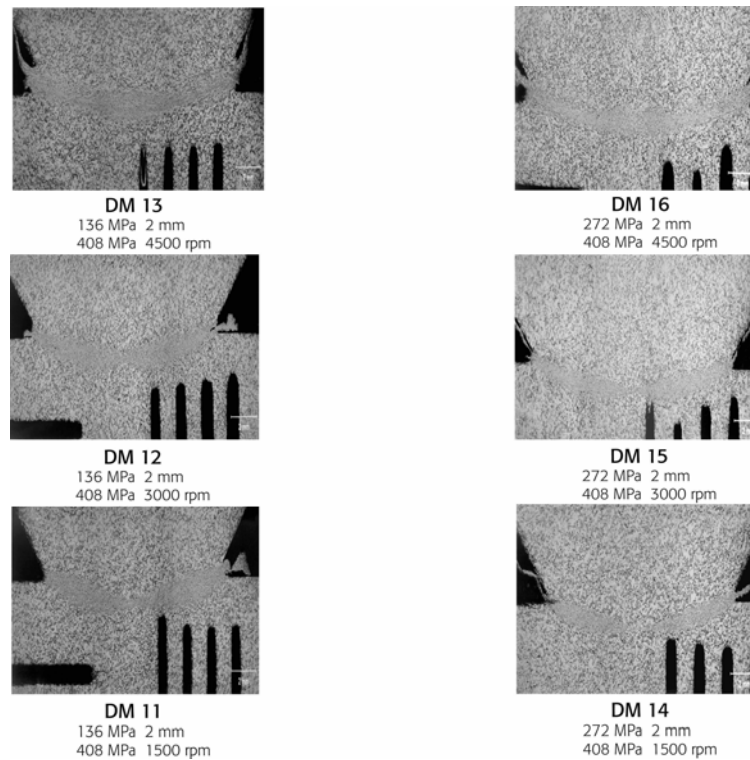


**DM 14**  
272 MPa 2 mm 1500 rpm  
408 MPa



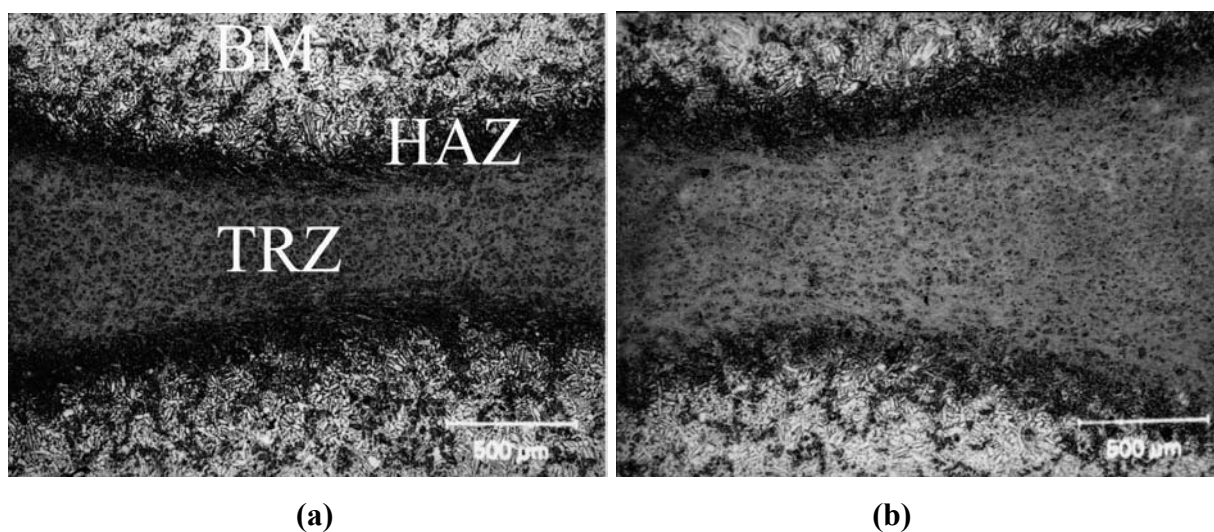
**DM 04**  
272 MPa 2 mm 1500 rpm  
544 MPa

**Figure 4.23 - Initial parameter matrix of the Ti6Al4V + 10 wt.% of TiC alloy friction welding.**



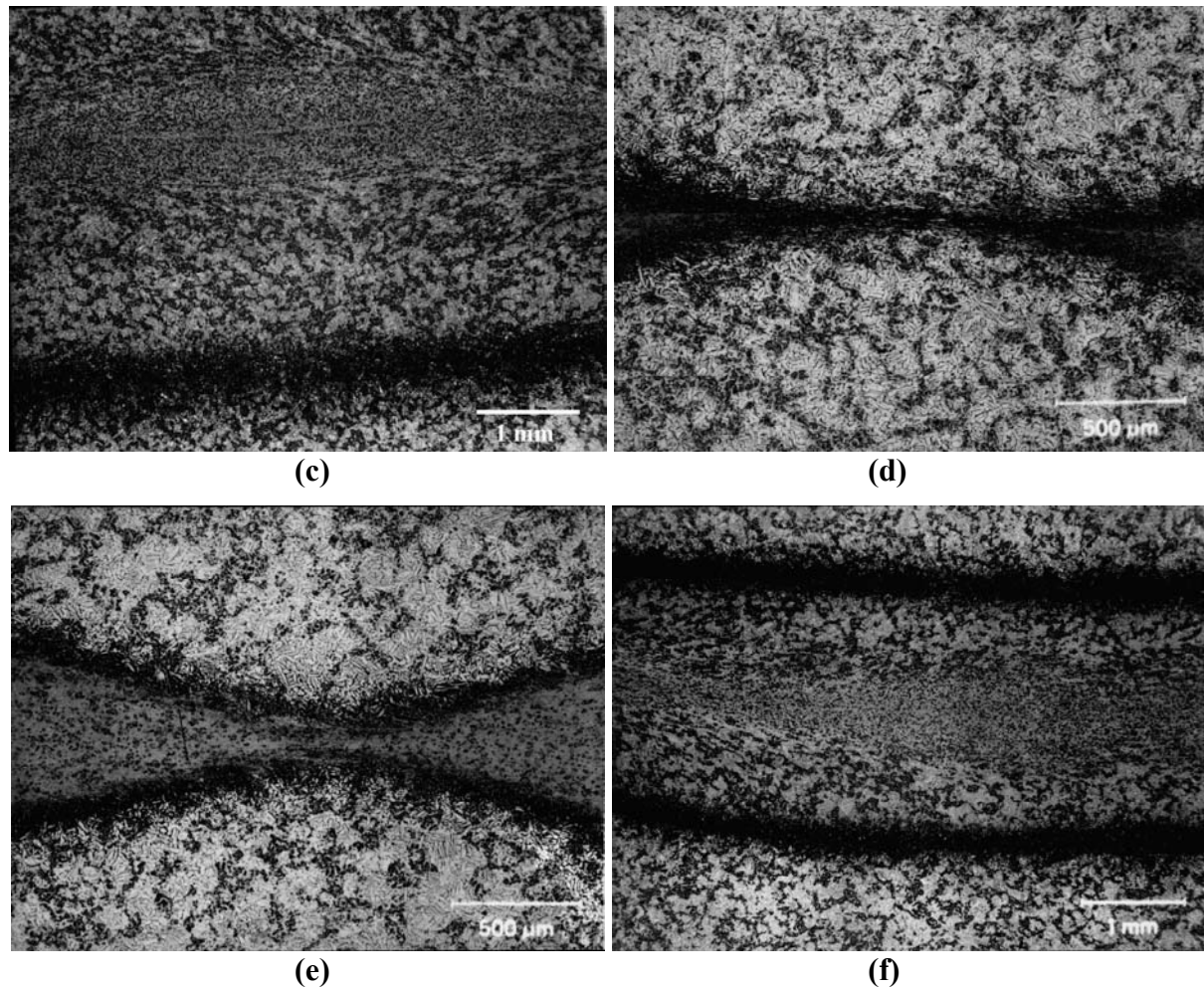
**Figure 4.24 – Secondary parameter matrix of the Ti6Al4V + 10 wt.% of TiC friction welding. Two friction welding parameters have been held constant (forging pressure 408 MPa and burn-off 2mm), while two have been varied (friction pressure and rotational speed).**

Figure 4.25 shows the macrostructural characterization and the respective features of the friction welded joints according to the parameters selected (rotational speed and friction pressure). One can clearly observe that it is possible to divide the microstructure of the friction welded joints into two zones (apart from the base material), namely: Heat Affected Zone (HAZ) as well as Transformed and Recrystallized Zone (TRZ) – as shown in Fig. 4.25a.



**Figure 4.25 – Friction welding macrostructure (BM, HAZ and TRZ). (a) DM11 (1500 rpm/136 MPa), (b) DM12 (3000 rpm/136 MPa), (c) DM13 (4500 rpm/136 MPa), (d) DM14 (1500 rpm/272 MPa), (e) DM15 (3000 rpm/272 MPa) and (f) DM16 (4500 rpm/272 MPa). Etch. OM.**





**Figure 4.25 – Friction welding macrostructure (BM, HAZ and TRZ). (a) DM11 (1500 rpm/136 MPa), (b) DM12 (3000 rpm/136 MPa), (c) DM13 (4500 rpm/136 MPa), (d) DM14 (1500 rpm/272 MPa), (e) DM15 (3000 rpm/272 MPa) and (f) DM16 (4500 rpm/272 MPa). Etch. OM.**

The size of these zones varies according to two basic parameters - rotational speed and pressure. The rotational speed has a great influence on the final characteristics of the joint as well as on the mechanisms of plastification since at high rotational speeds deep tearing mechanisms at the friction surfaces are replaced by a polishing action accompanied by a greatly reduced upsetting. As a result, to achieve the conditions for plastification at the friction surfaces, longer heating times are required. Such longer heating times allow the propagation of thermal energy along the axial direction of the workpieces and as consequence a greater volume of material is heated; therefore high rotational speed values lead to lower cooling rates and, consequently, wider transformed regions (HAZ and TRZ) [91,100]. Voinov [205] has postulated that the changeover in the mechanisms of plastification from deep tearing to a polishing action with increasing rotational speed is caused by strain localization in the thin sub-superficial layer, itself resulting from the high temperature gradient from the joint interface inwards. It is possible to observe from Fig. 4.25 that increasing the rotational speed

values (DM11/Fig. 4.25a, DM12/Fig. 4.25b and DM13/Fig. 4.25c), the geometry of the weld region changes from a double cone profile to a parallel-sided boundary profile. The influence of the pressure on the geometry of the weld region can be explained by the total amount of heat that is liberated since at higher pressure values heat is totally used to plastify the material and consequently does not propagate at the axial direction. Hence, high pressures lead to thinner transformed regions (HAZ and TRZ) since the heat does not propagate at the axial direction leading to a weld geometry shape of a double cone [91,100]. Additionally, higher axial pressure change the heating conditions of the friction surfaces, as the plastified material that “carries” the heat is immediately pressed out into the flash, see Figs. 4.25a (DM11/136 MPa) and 4.25d (DM14/272 MPa).

In order to verify the influence of the welding parameters over the size and shape of the welded joints it has been calculated the area of the joints (see Table 4.8). It can be observed the same behaviour described before, i.e., high rotational speeds lead to higher transformed areas (Fig. 4.26) and high pressures lead to thinner transformed areas (Fig. 4.27). It can be clearly observed that there is a good correlation in both trend lines ( $R^2$  equal to 0.76 and 0.84, respectively) from Fig. 4.26.

**Table 4.8 – Area of the friction welded joints**

Condition	Area (mm <sup>2</sup> )	STD
DM11	18.72	0.296
DM12	19.25	1.216
DM13	51.61	3.719
DM14	8.09	0.141
DM15	11.30	0.770
DM16	34.00	0.346

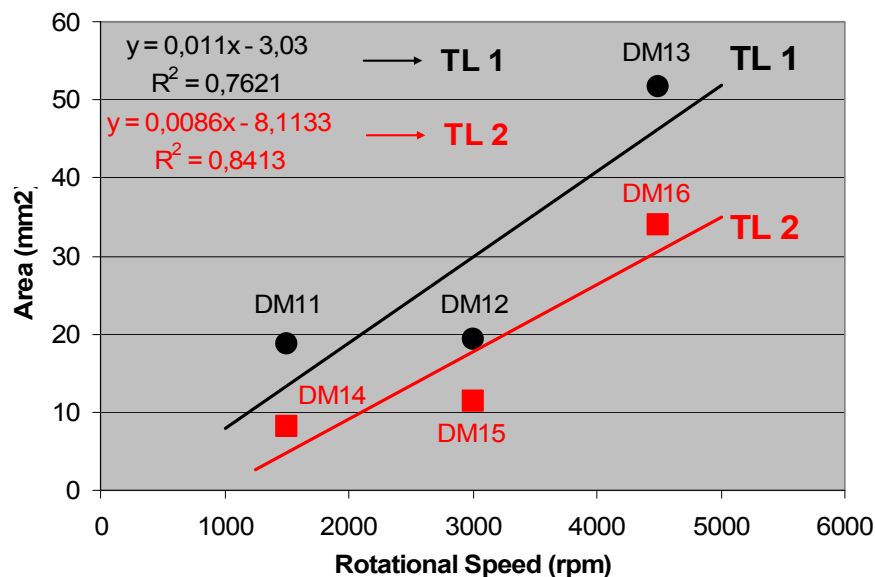


**Figure 4.26 – Influence of rotational speed over the friction welded area.**



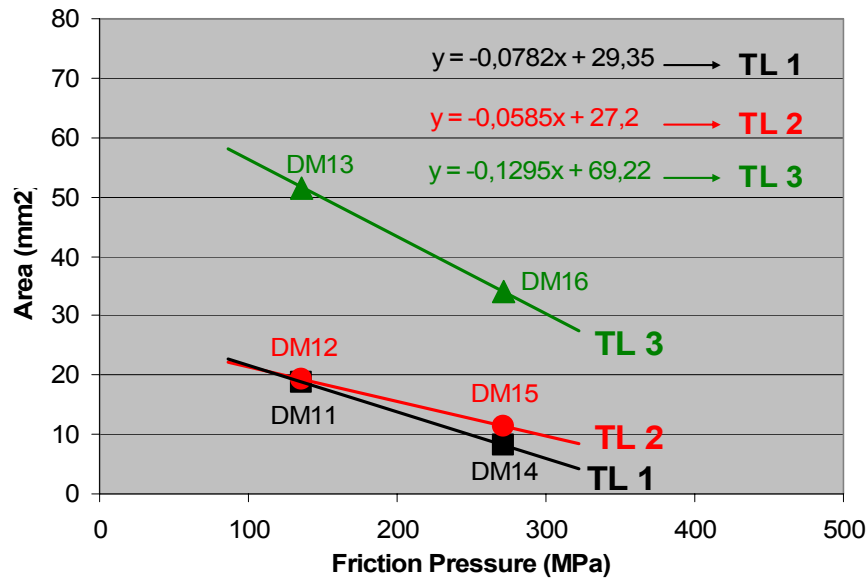


Figure 4.27 – Influence of friction pressure versus the friction welded area.

#### 4.2.2 Metallurgical Characterisation of the Friction Welded Joints

The base material metallurgical characteristics have been presented and discussed at the item 4.1.1. The subsequent layer is the HAZ which displays a typical  $\alpha$  Widmanstätten microstructure in regions close to the base material and also acicular  $\alpha$  in regions close to the TRZ (Figs. 4.28 and 4.29). Since the specimens have been cooled in air, the slower cooling rate from the friction welding temperature (above  $\beta$  transus temperature) has avoided martensitic transformation; therefore, the transformation from  $\beta$  to  $\alpha$  was a diffusion-controlled process (nucleation and growth). The  $\alpha$  plates in this condition are parallel to each other delineated by the  $\beta$ -phase ribs between them; however it is possible to observe in some parts the existence of acicular  $\alpha$ . The explanation of such microstructural transformation is the same as in the base material but since in the HAZ the cooling rate is higher, the platelet width is reduced resulting in the microstructure shown in Fig. 4.28. Another important feature of the HAZ is that it has suffered severe deformation due to the high forces applied during the process; therefore, in some regions, the microstructure is aligned and the original platelike (or equiaxed)  $\alpha$  grains have been reoriented resulting in aligned grains. A detailed view of the transition zone between HAZ and BM (Fig. 4.29) shows the elongated grains and the change in the  $\alpha$  platelet width as the transformation advances into HAZ. It is also possible to observe that the transformation from  $\beta$  to  $\alpha$  was not complete (only part of this region has reached and exceeded  $\beta$  transus temperature) since in regions close to the base material intergranular  $\beta$  can be observed; however as the temperature increases (transition zone between HAZ and TRZ) such microstructure disappears indicating complete transformation from  $\beta$  to  $\alpha$ .

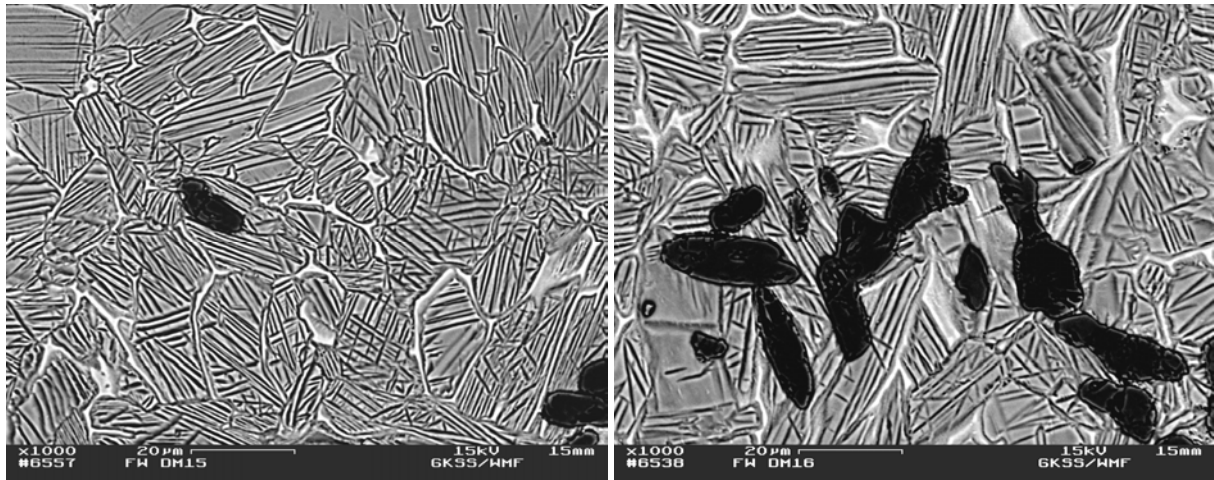


Figure 4.28 – SEM micrographs of the HAZ microstructure – Widmanstätten  $\alpha$  (acicular  $\alpha$ ) and intergranular  $\beta$  with TiC particles.

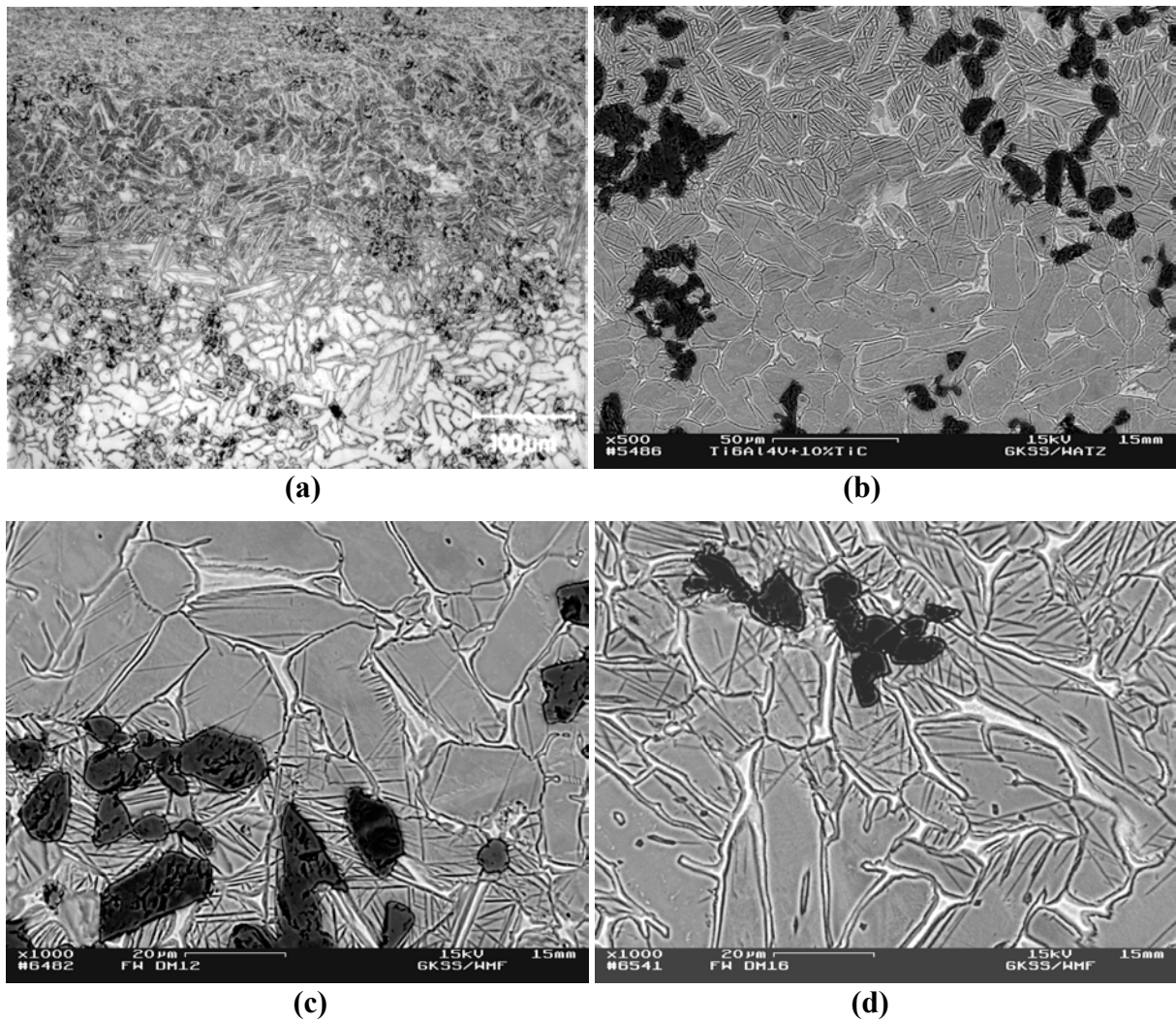
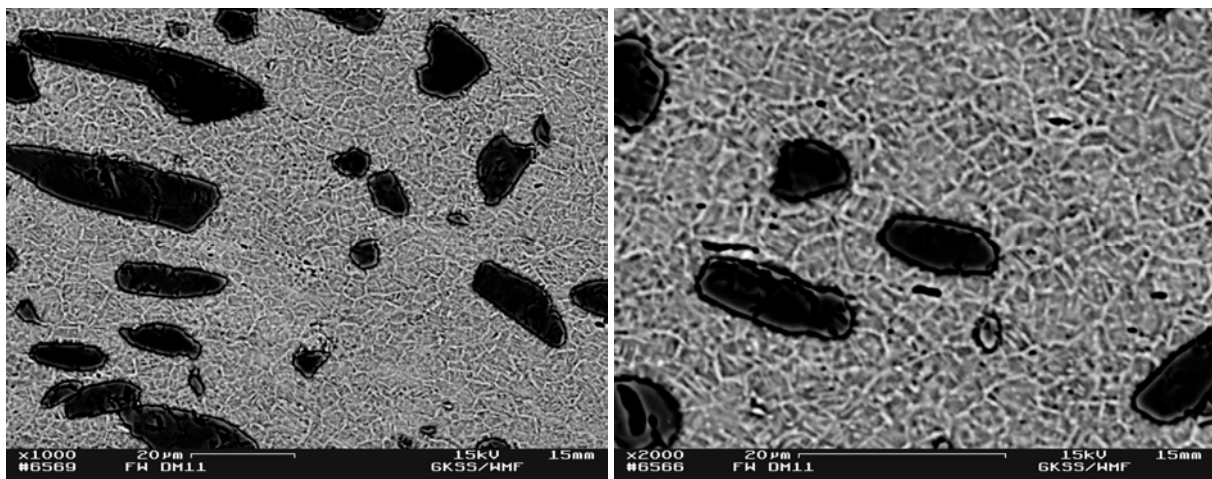


Figure 4.29 – Transition zone between HAZ and BM. Widmanstätten  $\alpha$  and intergranular  $\beta$  (HAZ) as well as platelike  $\alpha$  and intergranular  $\beta$  (BM) with TiC particles. (a) DM12 (3000 rpm/136 MPa). (b) DM11 (1500 rpm/136 MPa). (c) DM12. (d) DM16 (4500 rpm/272 MPa).

The inner region has been identified as the transformed and recrystallized zone (TRZ – Fig. 4.30). The size of this region in the centre of the weld is also very small having approximately, according to the welding condition, between a few microns (DM14) to a few millimetres (approximately 3 mm – DM13). The TRZ microstructure consists of acicular  $\alpha$  with redistributed TiC particles (different distribution from that of the base material due to the particle fracture phenomenon that occurs during the welding process). The TRZ has been entirely transformed to  $\beta$  (friction welding temperature has reached and exceeded the  $\beta$  transus temperature for the composite) and then air cooled with an intermediate cooling rate (higher cooling rate than the HAZ). Indeed, such cooling rate has avoided a martensitic transformation and the transformation from  $\beta$  to  $\alpha$  was a nucleation and growth process. According to Mehl et al [206], the acicular  $\alpha$  microstructure is often difficult to distinguish from the  $\alpha'$  (martensite), although acicular  $\alpha$  usually is less well-defined and has curved rather than straight sides; however due to the intermediate cooling rate (air cooled) it is believed that the microstructure formed is acicular  $\alpha$  (lamellar) that nucleated in the prior  $\beta$  grain boundary vicinity and grew into the prior  $\beta$  grain along several sets of preferred prior  $\beta$  grain crystallographic planes; however it is believed that due to the presence of the TiC particles randomly distributed in the matrix the nucleation of acicular  $\alpha$  in such preferred crystallographic planes is changed but without influence on the final microstructure and mechanical properties of this zone. The lamellae packets size and the fineness depend on the prior  $\beta$  grain size and the cooling rate.



(a)

**Figure 4.30 – SEM micrographs taken from TRZ. (a) DM11 (1500 rpm/136 MPa); (b) DM12 (3000 rpm/136 MPa); (c) DM13 (4500 rpm/136 MPa), (d) DM14 (1500 rpm/272 MPa); (e) DM15 (3000 rpm/272 MPa); (f) DM16 (4500 rpm/272 MPa).**

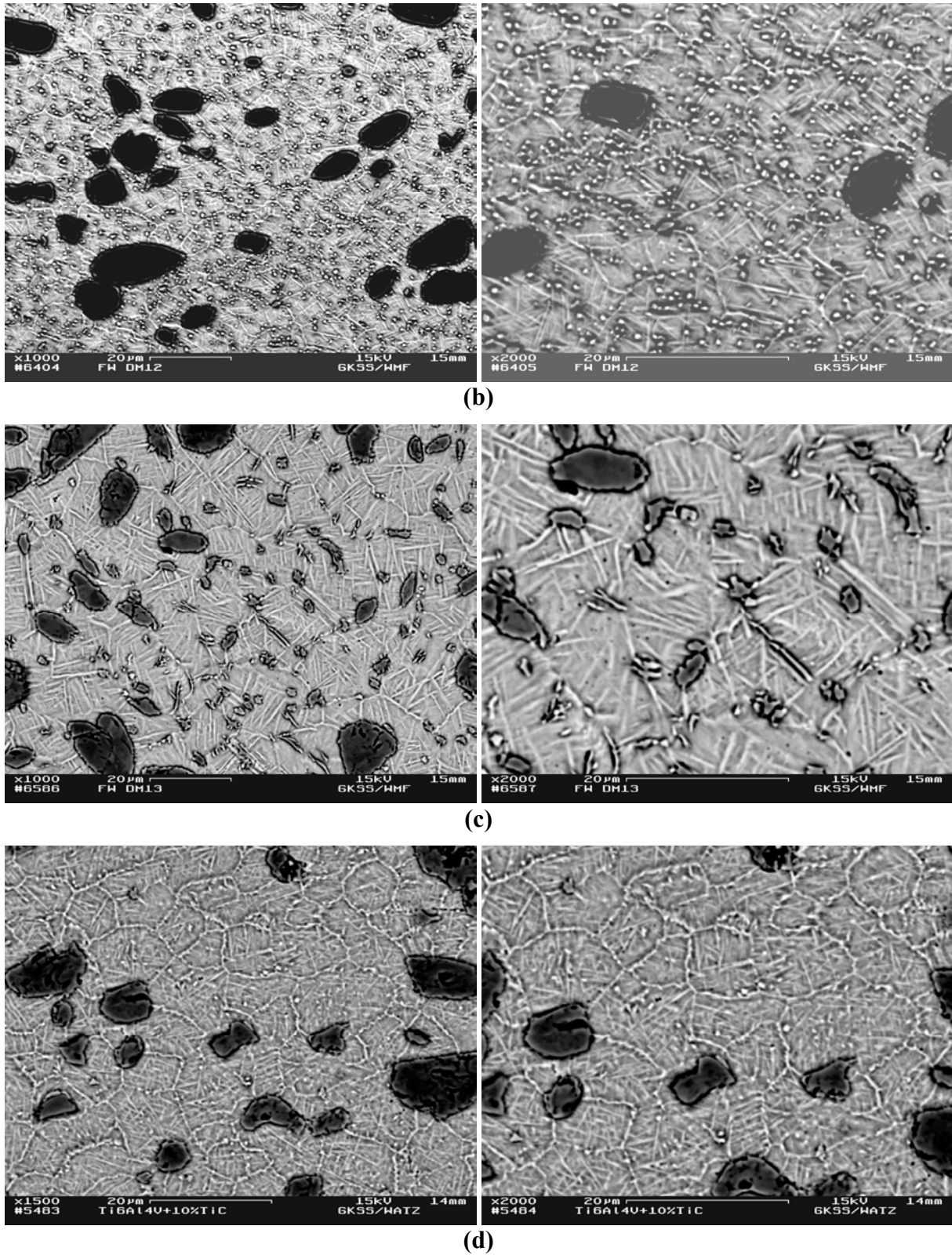
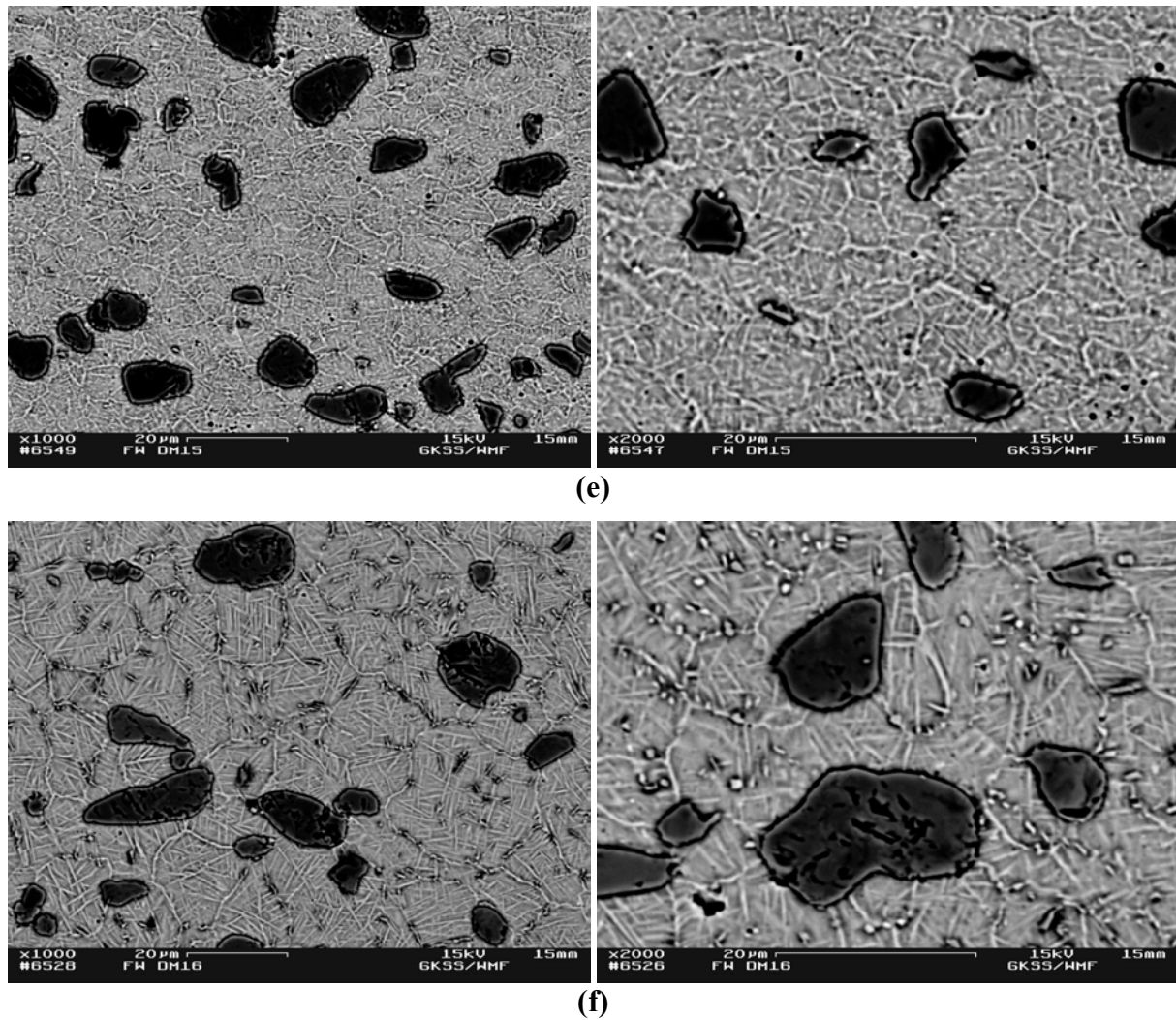


Figure 4.30 – SEM micrographs taken from TRZ. (a) DM11 (1500 rpm/136 MPa); (b) DM12 (3000 rpm/136 MPa); (c) DM13 (4500 rpm/136 MPa), (d) DM14 (1500 rpm/272 MPa); (e) DM15 (3000 rpm/272 MPa); (f) DM16 (4500 rpm/272 MPa).





**Figure 4.30 – SEM micrographs taken from TRZ. (a) DM11 (1500 rpm/136 MPa); (b) DM12 (3000 rpm/136 MPa); (c) DM13 (4500 rpm/136 MPa); (d) DM14 (1500 rpm/272 MPa); (e) DM15 (3000 rpm/272 MPa); (f) DM16 (4500 rpm/272 MPa).**

Two important features of TRZ can be clearly seen from, for example, in Fig. 4.30f: a continuous phase network at the prior  $\beta$  grain boundary as well as the presence of small particles along the  $\beta$ -grains and prior  $\beta$  grain boundary. All friction welded joints (see Fig. 4.31, DM13) presented these small particles which are expected to be TiC particles due to reprecipitation (metallurgical interaction) or particle fracture (mechanical interaction) along the  $\beta$ -grains and prior  $\beta$ -grain boundary. The presence of the original TiC particles at the composite combined with high temperatures and plastic deformation must have given ideal conditions for a TiC secondary precipitation along this zone and in all friction welded joints.

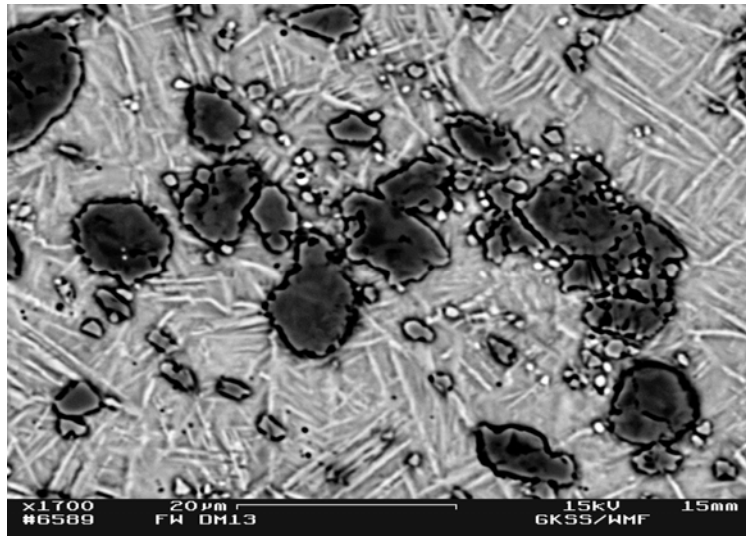


**Figure 4.31 – SEM micrograph showing small TiC particles. DM13 (4500 rpm/136 MPa). Etch.**

Such interaction between the TiC particles and the Ti6Al4V matrix has been extensively studied [42,47,51,52,54]; however, until now the diffusion of TiC into the matrix to reprecipitate small TiC particles or mechanical interaction has not been reported. The only interaction that has already been documented is the formation of a layer around the TiC particle and the diffusion of carbon from this layer either to the particle or to the matrix. A dissolution-type reaction can occur between the matrix and the reinforcement forming a continuous carbon deficient region between the titanium matrix and the TiC particle [52]. Wanjara et al [54] have shown that the initial reaction between the reinforcement and matrix phases is carbon dissolution into the  $\beta$ -Ti6Al4V alloy. The Ti-C binary phase diagram shows that carbide composition in equilibrium with  $\alpha$ -Ti at high temperatures is significantly more carbon deficient than at room temperature, and the  $\alpha$ -Ti exhibits an increased solubility for carbon with increasing temperature. Therefore, there exists a thermodynamic driving force for TiC to lose carbon as temperature increases which could explain the presence of TiC particles due to the high temperatures used in the welding process associated with high pressures.

Several EDS analysis have been performed in this region in order to identify these particles. According to the obtained results (Fig. 4.32 and Table 4.9) it can be concluded that such particles are TiC with unknown stoichiometry resulted from an interaction (particle fracture phenomenon or precipitation due to carbon low solubility in titanium) between the matrix and the TiC particles. Such behaviour has not been found in Ti6Al4V+10 vol.% TiC [42], since there has been no interaction between the constituents even when the samples have been heat treated at 1050°C for times up to 50 hours. The only visible interaction was confined to the TiC phase where an annulus of non-stoichiometric TiC is formed around the

original TiC. A state of quasi-equilibrium between the TiC particle stoichiometric centre and the annulus; and between this non-stoichiometric annulus and the matrix (which would be expected to be saturated with carbon) was found since the true equilibrium would consist of a uniform non-stoichiometric TiC particle and a saturated solution of carbon in the titanium matrix; but, for this condition to be achieved it would be necessary for the carbon from the centre to diffuse through the annulus and this would take a very long time to occur. Instead, the composite remains in this metastable state and, if it is cooled slowly, much of the carbon apparently redeposits on the TiC, reducing the non stoichiometric annulus width [42]. One of the main differences between this situation and friction welding is that the welded joint has a higher cooling and heating rate as well as a much shorter time at temperature and probably there would be no time for the carbon to diffuse back to the particle thus combining with the titanium from the matrix resulting in these small TiC particles.

Badini et al [191] have affirmed that the carbon percentage in the reinforcement is scarcely affected by the composite thermal treatments. Furthermore, the carbon content in the TiC particles is always well below the upper limit of 49 % at. Hence, it can be inferred that carbon diffusion occurs from the particles towards the matrix since composite processing. The reported carbon values (Table 4.9) are higher than the equilibrium one observed in the TiC phase diagram (see Fig. 3.7) at room temperature and they often are close to the maximum solubility of carbon in titanium (about 1.6 % at. achieved at 920°C). Therefore, very likely, following the rather rapid cooling (air cooled) of the composite from the processing temperatures (welding temperature, above  $\beta$  transus temperature) metastable supersaturated solid solutions of carbon in the titanium were obtained resulting in optimum conditions for the precipitation of these small TiC particles. Hirose et al [118] and Fukumoto et al [119] have also reported the presence of small particles in the fusion zone of laser beam welded SiC fibre reinforced Ti6Al4V concluding that such particles were TiC particles due to carbon low solubility in titanium giving ideal condition for such precipitation. Such particles were probably formed by a reaction of titanium with carbon which was produced by decomposition of SiC fibres due to the laser irradiation.

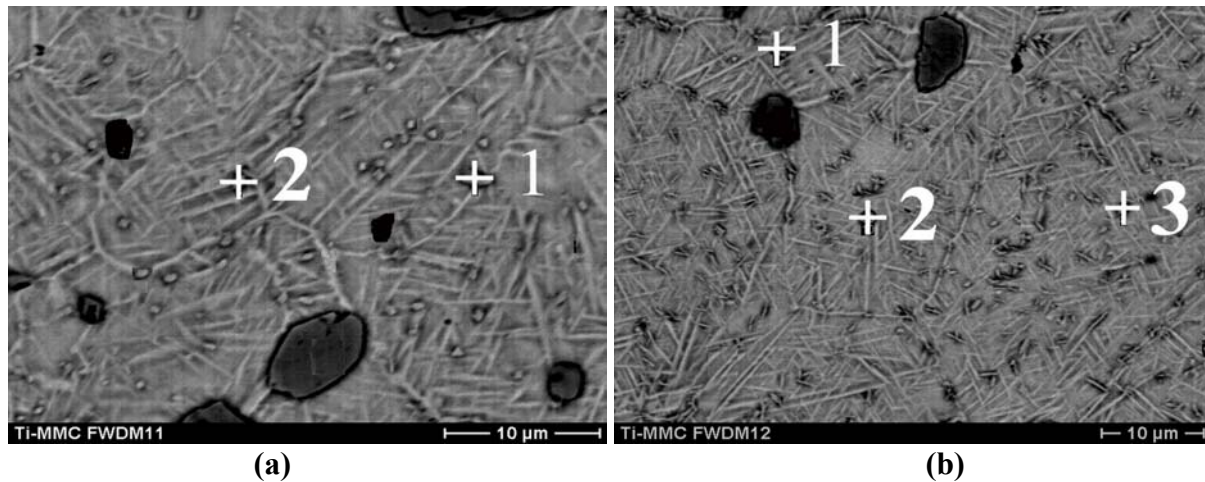


Figure 4.32 – EDS analysis at the particles found in the TRZ region. (a) DM11 (1500 rpm/136 MPa) and (b) DM12 (3000 rpm/136 MPa).

Table 4.9 – Results from the EDS analysis at the particles found in the TRZ region.

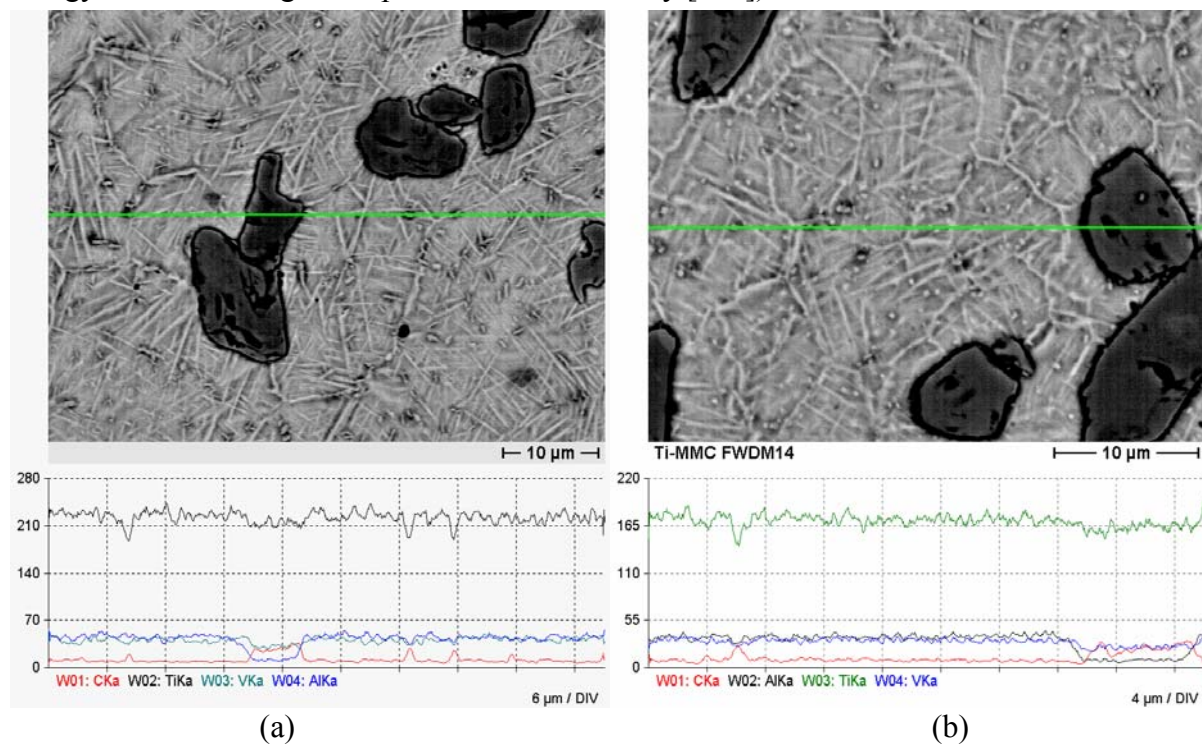
Figure 4.32a				
	Ti (wt. %)	Al (wt. %)	V (wt. %)	C (wt. %)
Point 1	85.01	3.57	3.74	<b>7.69</b>
Point 2	85.07	5.27	4.34	<b>5.32</b>
Figure 4.32b				
	Ti (wt. %)	Al (wt. %)	V (wt. %)	C (wt. %)
Point 1	82.59	4.30	4.17	<b>8.94</b>
Point 2	84.61	5.40	5.38	<b>4.60</b>
Point 3	83.11	4.41	5.06	<b>7.42</b>

Obs: Carbon results are just comparative and not quantitative.

The grain boundary phase network can be attributed to the presence of a continuous  $\alpha$  phase layer at the  $\beta$  grain boundary. Normally, the prior  $\beta$  grain boundaries are not well defined in titanium alloys, but in all welded conditions the presence of such grain boundary phase is clearly visible. Such formation is attributed to the fact that most of the titanium alloys (particularly  $\beta$ -rich-Ti6Al4V) when heated above the  $\beta$  transus and subsequent cooled down from this temperature develop such microstructure [16]. Thompson et al [27] have suggested that if the material is heated into the  $\beta$  phase field and cooled without simultaneous working or if the working operation is terminated above  $\beta$ -transus, then the prior  $\beta$  grain boundaries can serve as potent sites for heterogeneous nucleation of the  $\alpha$  phase. This is particularly true at low undercooling where there is a small driving force for uniform intergranular  $\alpha$  nucleation; in such circumstances, a nearly continuous  $\alpha$  phase layer can be formed along the prior  $\beta$  grain boundaries and this is referred to as grain boundary  $\alpha$ . Since the working operation is finished above  $\beta$ -transus in friction welding it should be expected the formation of this  $\alpha$  phase layer at the  $\beta$  grain boundary. In order to understand such phenomenon, EDS



line analysis has been performed along TRZ in all welded conditions. Since the aluminium stabilises the hcp  $\alpha$ , one would expect that if both phases ( $\alpha$  and  $\beta$ ) are present, the aluminium will tend to segregate in the  $\alpha$  phase. With this in mind, after performing the line analysis one should expect an aluminium peak whenever the beam passes through the grain boundary. It is possible to observe a small peak in the aluminium when it reaches the grain boundary, Fig. 4.33; however, there is a problem with interference from the surroundings since the depth of information is about 1 to 10  $\mu\text{m}$  (increasing with increasing electron beam energy and decreasing with specific element density [207]) which can mask the results.



(a) (b)  
**Figure 4.33 – EDS analysis in TRZ. (a) DM12. (b) DM14.**

Since the base material has a coarse lamellar microstructure, the  $\beta$  grain size could not be determined; however, the TRZ has been subjected to a prior  $\beta$  grain recrystallisation resulting in globular  $\beta$  grains. The  $\beta$  grain size in regions close to the HAZ is much larger than at the middle of the friction welding joint due to the dynamic recrystallisation that has taken place after/during the welding process as can be observed from the results in Table 4.10 where can be clearly seen that increasing the rotational speed has increased the  $\beta$  grain size since at high rotational speeds the heating times are higher (due to changes in the mechanisms of plastification) leading to lower cooling rates that result in coarser  $\beta$  grains. When comparing conditions with different pressure is possible to observe that pressure has no influence on the grain size since the total amount of heat is used to plastify the material (there is no heat propagation in the axial direction) with no direct influence on the final  $\beta$  grain size.

**Table 4.10 – ASTM Beta grain size determination for all the investigated friction welding conditions in the weld centre and close to the HAZ region.**

Condition	Grain Size	Average diameter	Grain Size	Average diameter
	(weld centre)	( $\mu\text{m}$ )	(close to HAZ)	( $\mu\text{m}$ )
DM11 (1500 rpm/136 MPa)	< 8	< 22.5	7	31.8
DM12 (3000 rpm/136 MPa)	8	22.5	7	31.8
DM13 (4500 rpm/136 MPa)	7	31.8	4	89.8
DM14 (1500 rpm/272 MPa)	< 8	< 22.5	8	22.5
DM15 (3000 rpm/272 MPa)	8	22.5	7	31.8
DM16 (4500 rpm/272 MPa)	7	31.8	4	89.8

#### 4.2.2.1 Image Analysis of the Friction Welded Joints

The particle characteristics resulting from the welding process such as shape factor, mean Ferret diameter, particle area as well as NND have been determined with the aid of an image analyser and an optical microscope. The image analysis consisted of analysing the distribution and size of the particles using a magnification of 200 times comprising an area field of approximately  $0.77 \text{ mm}^2$  (for each of the ten micrograph analysed). Figure 4.34 shows the micrographs utilised to analyse the particles characteristics of the welded joints.

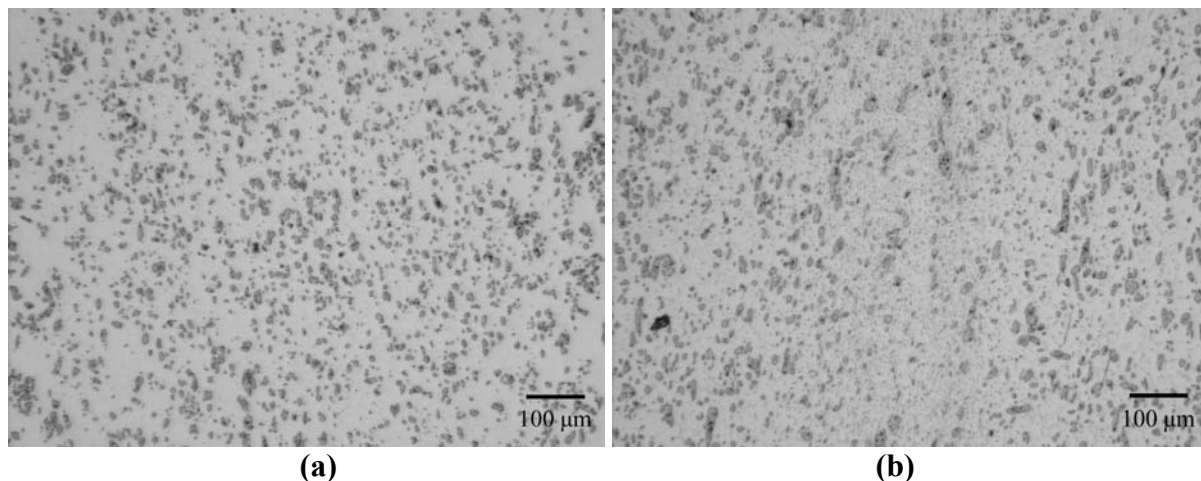


**Figure 4.34 Examples of micrographs used to investigate the particle characteristics of the friction welding joints. (a) DM12 (3000 rpm/136 Mpa). (b) DM13 (4500 rpm/136 Mpa). OM.**

It is well established that particle distribution as well as other particle characteristics in the TRZ and adjacent HAZ are quite different from those in the base material. The base material has a wide range of particle dimensions; however, as it will be explained later, a much narrower particle dimension distribution exists in the material close to the friction surface (i.e. joint line) because of the particle fracture process which occurs during joining operation. In fact, small-diameter reinforcing particles as well as particle fracture can be observed at the friction surfaces of all welded conditions. The retention of these fractured particles at the joint interface is promoted by limit cycles (singularities) embedded within the

flow and by the material flow, which favours the accumulation of the reinforcing particles at the joint rotating boundary. Material and reinforcing particle transfer is determined by plasticized material flow during welding operation [140].

As it is possible to observe from the results presented in Table 4.11 there is no significant difference between the welded joints concerning shape factor (particles are rounder after friction welding due to the particle fracture phenomenon). Table 4.12 shows the results of the mean Ferret diameter for the welding conditions where it can be observed that the particle size has reduced significantly when compared to the base material due to the particle fracture phenomenon. No particle clustering has been observed and the particle distribution is much more homogeneous than in the base material. It can be observed that the welding parameters play an important role on the particle size; increasing the rotational speed causes a decrease in the particle size; however increasing the pressure has not induced any important change. It seems that pressure has an optimum value above which particle fracture occurs and that the pressure used in this investigation is far above such value since no significant difference in particle diameter could be observed. A material rotational speed dependence can be observed concerning the particle fracture phenomenon since increasing rotational speed increases the temperature at the friction surface; therefore in such high temperatures the material (fluid) flow is increased favouring the retention of these particles in the joint rotating boundary and consequently reducing the particle size diameter. Figures 4.35 and 4.36 present the particle size distribution according to different welding parameters.

**Table 4.11 – Results for the shape factor of the friction welding conditions investigated.**

Condition	Shape Factor	STD
DM11 (1500 rpm/136 MPa)	0.75	0.16
DM12 (3000 rpm/136 MPa)	0.74	0.16
DM13 (4500 rpm/136 MPa)	0.74	0.15
DM14 (1500 rpm/272 MPa)	0.73	0.18
DM15 (3000 rpm/272 MPa)	0.73	0.17
DM16 (4500 rpm/272 MPa)	0.74	0.15

**Table 4.12 – Results for the mean Ferret diameter of the friction welding conditions.**

Condition	Mean Ferret diameter ( $\mu\text{m}$ )	STD
DM11 (1500 rpm/136 MPa)	9.9	8.6
DM12 (3000 rpm/136 MPa)	7.5	8.8
DM13 (4500 rpm/136 MPa)	5.8	9.1
DM14 (1500 rpm/272 MPa)	9.9	11.7
DM15 (3000 rpm/272 MPa)	7.9	7.2
DM16 (4500 rpm/272 MPa)	6.1	7.8

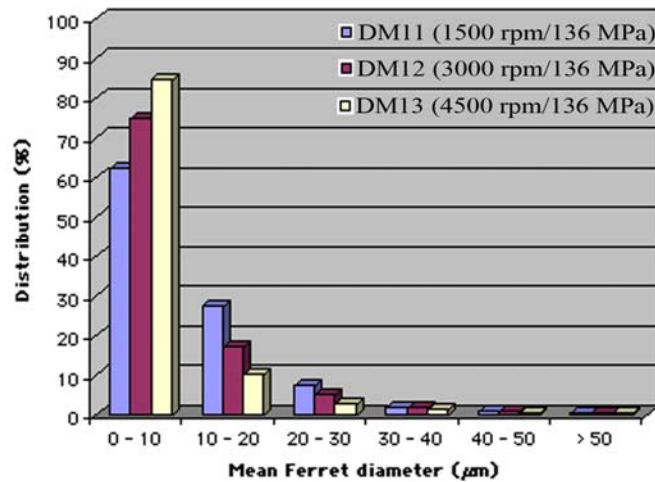


Figure 4.35 – Mean Ferret diameter distribution according to friction welding rotational speed.

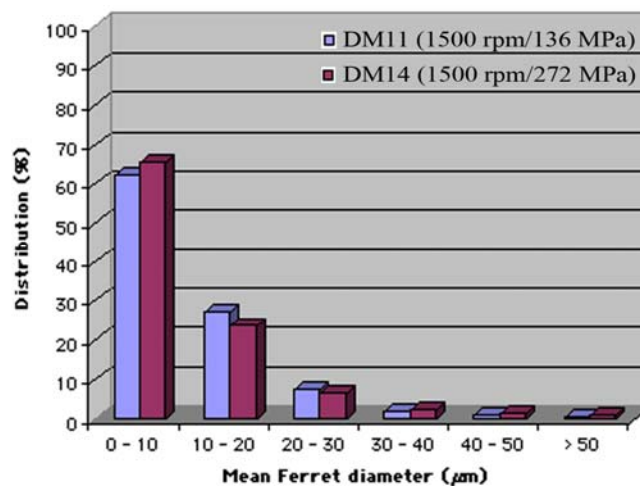


Figure 4.36 – Mean Ferret diameter distribution according to friction welding pressure.

The TiC particles area in a  $0.77 \text{ mm}^2$  area field is shown in Table 4.13 for all welded conditions. As for the shape factor analysis no significant changes could be observed; particle clustering throughout TRZ and HAZ has not been found, since such concentration is not expected due to the particle fracture phenomenon. The results of the area of an individual particle are shown in Table 4.14. It has been found the same behaviour presented by particle size, i.e., increasing the rotational speed decreases the individual particle area and increasing the pressure has almost no influence on the final average value.

Table 4.13 – Area fraction of the TiC particles after the friction welding process.

Condition	Area fraction (%)
DM11 (1500 rpm/136 MPa)	21.0
DM12 (3000 rpm/136 MPa)	21.9
DM13 (4500 rpm/136 MPa)	22.3
DM14 (1500 rpm/272 MPa)	22.9
DM15 (3000 rpm/272 MPa)	23.6
DM16 (4500 rpm/272 MPa)	23.9

**Table 4.14 – Individual particle area determination for all the welded conditions.**

Condition	Particle Area ( $\mu\text{m}^2$ )	STD
DM11 (1500 rpm/136 MPa)	87.0	156.90
DM12 (3000 rpm/136 MPa)	65.4	159.9
DM13 (4500 rpm/136 MPa)	42.8	180.2
DM14 (1500 rpm/272 MPa)	100.2	316.3
DM15 (3000 rpm/272 MPa)	93.8	197.8
DM16 (4500 rpm/272 MPa)	47.7	138.1

### 4.2.3 Mechanical Characterisation of the Friction Welded Joints

#### 4.2.3.1 Microhardness

Microhardness profiles were performed across the friction welded joints using the same procedure as for the base material microhardness characterisation (see Fig. 4.37). The same difficulties found in the base material has also been found here concerning the presence of the TiC particles. The hardness increase at TRZ and HAZ regions can be attributed to the microstructural transformations occurred during welding process. Mostly, the strengthening effect observed in this region is a direct result of the rather rapid cooling from the welding temperature, transforming the as-received microstructure into acicular  $\alpha$  or Widmanstätten  $\alpha$ .

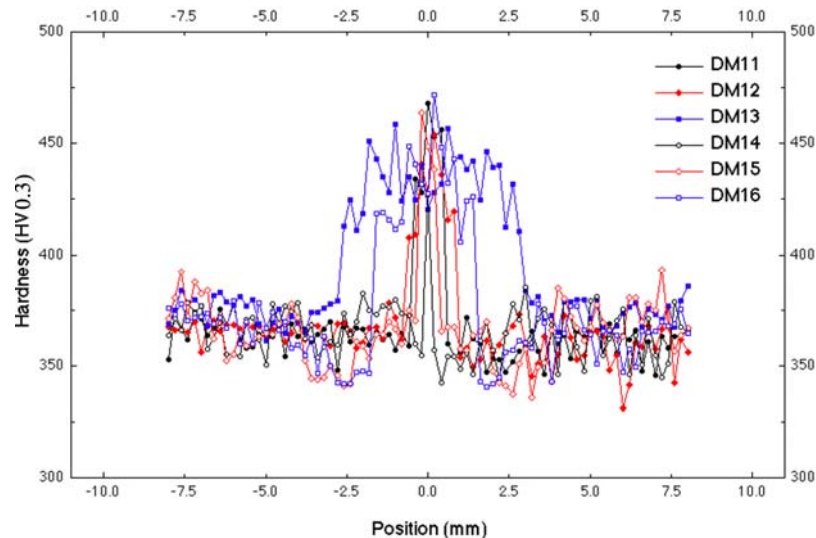


**Figure 4.37 – Hardness distribution of all the welded conditions investigated.**

All welded conditions have shown, as expected, the same behaviour, i.e. an increase in hardness at HAZ and TRZ (strength overmatching) due to the much higher cooling rates in such zones. However, the size of these zones varies according to two welding parameters – rotational speed and pressure (as presented in subsection 4.2.1). To achieve the conditions for plastification at the friction surfaces at high rotational speeds (DM13 or DM 16) longer heating times are required which allow thermal energy propagation along the axial direction of the samples. Hence, a greater volume of material is heated, leading to lower cooling rates

and wider transformed regions. On the other hand, at high pressures applied (DM14 or DM16), the heat generated is mainly used to plastify the material and consequently does not propagate in the axial direction; therefore high pressures lead to thinner transformed regions.

The difference between the hardness values from one zone to another in the welded joints is insignificant. Several individual hardness indentations have been performed in the different welded regions (avoiding TiC particles) and the BM average value is 359.8 HV0.3, HAZ value is 393.9 HV0.3, while TRZ value is 428.9 HV0.3. Such behaviour is in accordance with the literature [61] and the scattering is much lower when compared to the regular indentations performed in the composite and presented in Fig. 4.11. The main reason for such difference in hardness values between the welded zones is the  $\alpha$  platelet width which is influenced by the friction welding cooling rate since the higher the platelet width (low cooling rate) the lower the hardness value.

#### 4.2.3.2 Tensile Tests

Since the friction welding process is characterized by a fast applied thermal and stress/strain cycle causing microstructural changes, it would be expected that the mechanical properties of the welded joints would be quite different from those of the base material. The tensile results of the welded joints have not shown such behaviour as can be observed in Table 4.15. The  $R_m$  varies from 950 to 990 MPa, while the  $R_{p0,2}$  from 917 to 954 MPa and it can be seen that there was a slight reduction of  $R_{p0,2}$  and a slight increase of  $R_m$  after the welding process. The highest difference in  $R_m$  and  $R_{p0,2}$  values when comparing base material to the welded joints was 23 MPa (DM 12) and 37 MPa (DM 15), respectively, corresponding to less than 5% variation. From these results it can be affirmed that there is a wide operating window for production of satisfactory joints concerning tensile properties when Ti6Al4V+10wt.% TiC is joined. Nessler et al [103] studying friction welding of Ti6Al4V and Ti6Al2Sn4Zr2Mo alloys has observed the same behaviour, i.e. neither  $R_m$  nor  $R_{p0,2}$  were significantly affected by any of welding variables.

**Table 4.15 – Results of the tensile tests performed in the friction welded conditions.**

Condition	$R_{p0,2}$ (MPa)	$R_m$ (MPa)	Elongation (%)
DM11	938 ± 18	983 ± 15	0.61 ± 0.16
DM12	936 ± 10	990 ± 23	0.65 ± 0.23
DM13	934 ± 10	975 ± 22	0.62 ± 0.22
DM14	935 ± 12	973 ± 3	0.78 ± 0.06
DM15	917 ± 8	950 ± 27	0.57 ± 0.28
DM16	934 ± 16	969 ± 7	0.54 ± 0.12

The joint tensile strength was optimized when low rotational speed and pressure were employed during the friction welding of the composite (“cold” friction welds) – conditions DM11 and DM12 (1500 rpm/136 MPa and 3000 rpm/136 MPa, respectively). Figure 4.38 shows the tensile behaviour of all welded conditions under a displacement rate of 0.2 mm/min. Table 4.16 presents the joint efficiency based on  $R_m$  values. It can be observed that all welded joints exhibited almost the same base material tensile behaviour retaining between 98 and 102% of base material  $R_m$ . The worst tensile behaviour has been found for condition DM15 (3000 rpm/272 MPa) with 98% of base material  $R_m$ . The strength overmatching observed in the hardness behaviour (Fig. 4.37) in all welded joints is reflected on the tensile test results since in all cases (except in three of 24 specimens) failure has taken place in the base material. Figure 4.39 presents an overview of broken tensile specimens showing the fracture location.

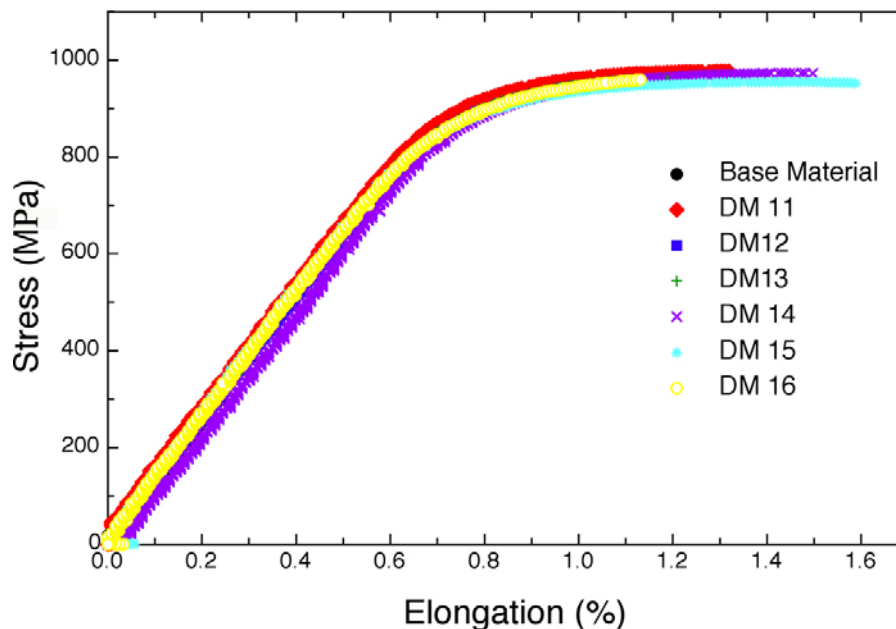


Figure 4.38 – Tensile behaviour of the friction welded joints and base material.

Table 4.16 – Joint efficiency (based on  $R_m$  values) presented by the friction welded joints.

Condition	Joint efficiency based on $R_m$ (%)
DM11	101.7
DM12	102.4
DM13	100.8
DM14	100.6
DM15	98.2
DM16	100.2



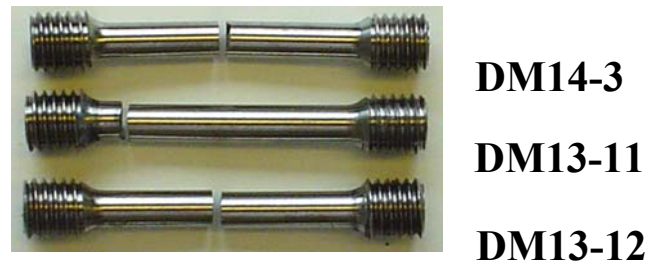


Figure 4.39 – Fracture position of the friction welded tensile specimens.

The  $R_m$  differences between welded conditions and base material in all tested specimens is shown in Fig. 4.40 where it is possible to observe that there is no significant difference. Scattering in testing composites is a major concern and differences of up to  $\pm 25\%$  (proportional limit) may be found while testing discontinuously reinforced MMCs at room temperature [208]. Indeed, the highest scattering while testing the welded joints has been found in elongation ( $\pm 1.92\%$  for  $R_{p0.2}$ ;  $\pm 2.31\%$  for  $R_m$  and  $\pm 49.12\%$  for elongation) but such behaviour was expected due to failure outside the gauge length (some specimens).

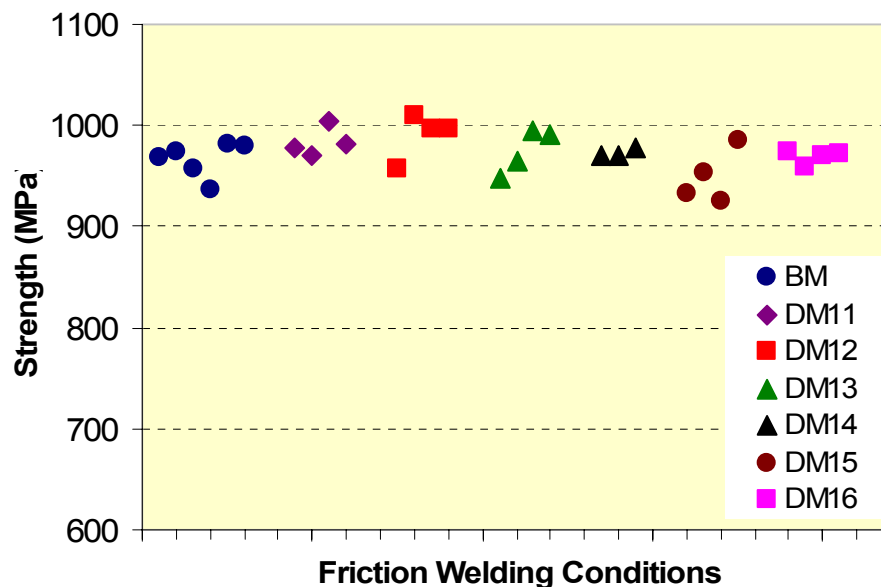


Figure 4.40 – Tensile strength behaviour of the friction welded joints and base material.

#### 4.2.3.2.1 Longitudinal Section Analysis of the Fracture Surface of the Tensile Specimens

Longitudinal sections taken from the fracture surfaces have indicated the exact fracture position (see Fig. 4.41 and Table 4.17) and as can be observed most of the fracture positions are located in the base material which was the expected behaviour since the base material hardness is lower than in the other zones (see, Fig. 4.35); however three specimens have fractured in other regions: DM11-2 and DM12-3 – HAZ; and DM14-3 – TRZ. It can be observed that the fracture path have followed the TiC particles (especially the particles along the prior  $\beta$  grain boundary, Fig. 4.1) since there is a large amount of fractured particles in the



crack path showing that the intrinsic strength of TiC particles is an important parameter in determining the composite tensile behaviour. It can also be observed that the particles most susceptible to fracture are in the larger size range of the population.

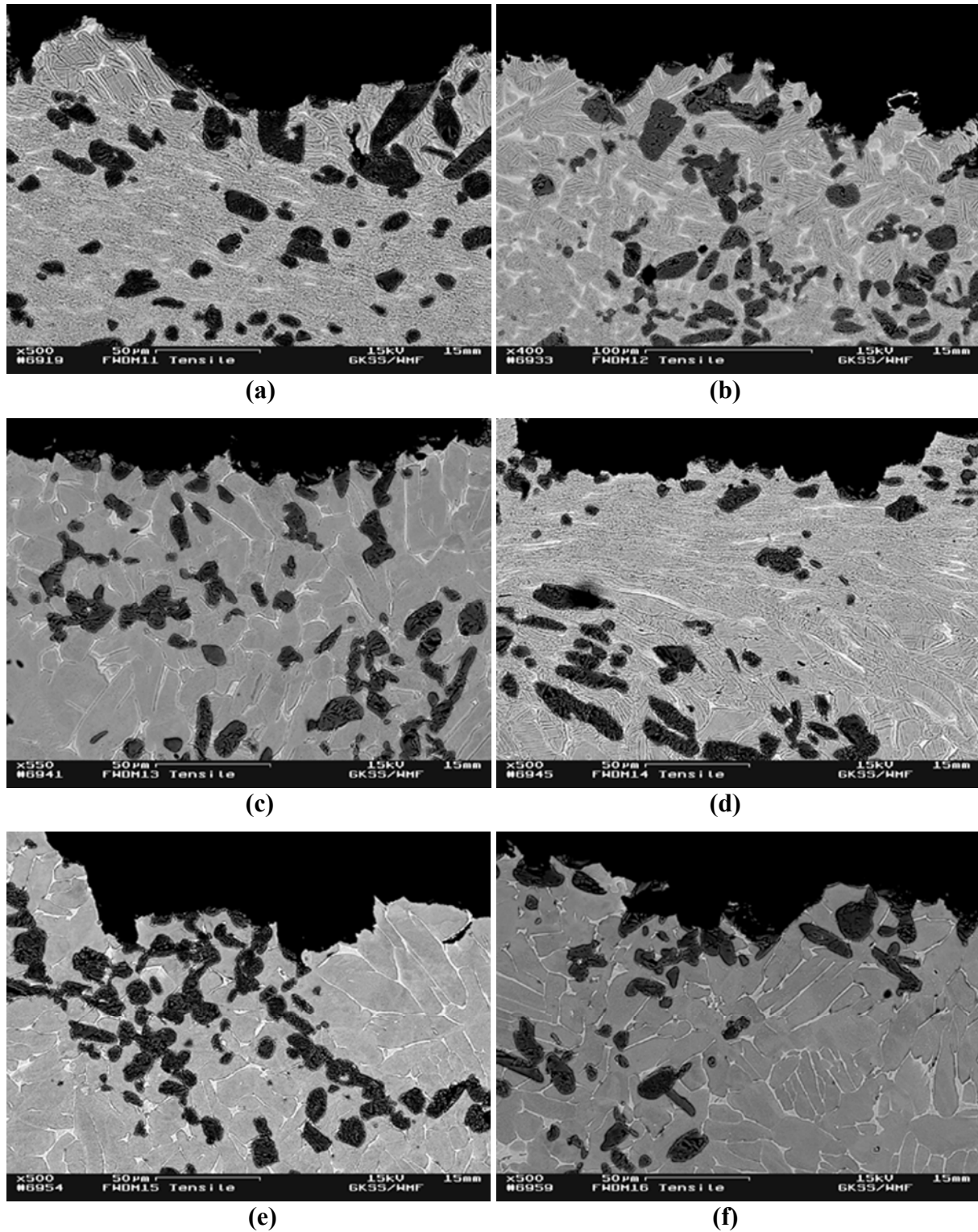


Figure 4.41 –SEM micrographs of the longitudinal sections of the fracture surfaces. (a) DM11-2 (1500rpm/136MPa), (b) DM12-3 (3000rpm/136MPa), (c) DM13-2 (4500rpm/136MPa), (d) DM14-3 (1500rpm/272MPa), (e) DM15-2 (3000rpm/272MPa), (f) DM16-2 (4500rpm/272MPa).

**Table 4.17 – Fracture location of the friction welded tensile specimens.**

<b>Specimen</b>	<b>Fracture location</b>
DM11-2	HAZ
DM11-3	BM
DM11-11	BM
DM11-12	BM
DM12-3	HAZ
DM12-11	BM
DM12-12	BM
DM12-13	BM
DM13-2	BM
DM13-3	BM
DM13-11	BM
DM13-12	BM
DM14-2	BM
DM14-3	TRZ + HAZ
DM14-12	BM
DM15-2	BM
DM15-3	BM
DM15-11	BM
DM15-12	BM
DM16-2	BM
DM16-3	BM
DM16-11	BM
DM16-12	BM

#### 4.2.3.2.2 Fracture Surface Analysis of the Tensile Specimens

It has been found the same fracture behaviour in the friction welded joints as in the base material condition, i.e., brittle fracture of the TiC particles and ductile fracture of the matrix. The important features of the friction joints fracture behaviour are local matrix microvoid coalescence (indicated by DF in Fig. 4.42a) as well as fractured particles (PF in Fig. 4.42a). Indeed, there has been found a high amount of fractured particles in the crack path of the fracture surfaces indicating the presence of such behaviour. Secondary cracking has also been observed (SC in Fig. 4.42b) showing the brittle nature of the reinforcing particles (the particles have been shattered before rupture).

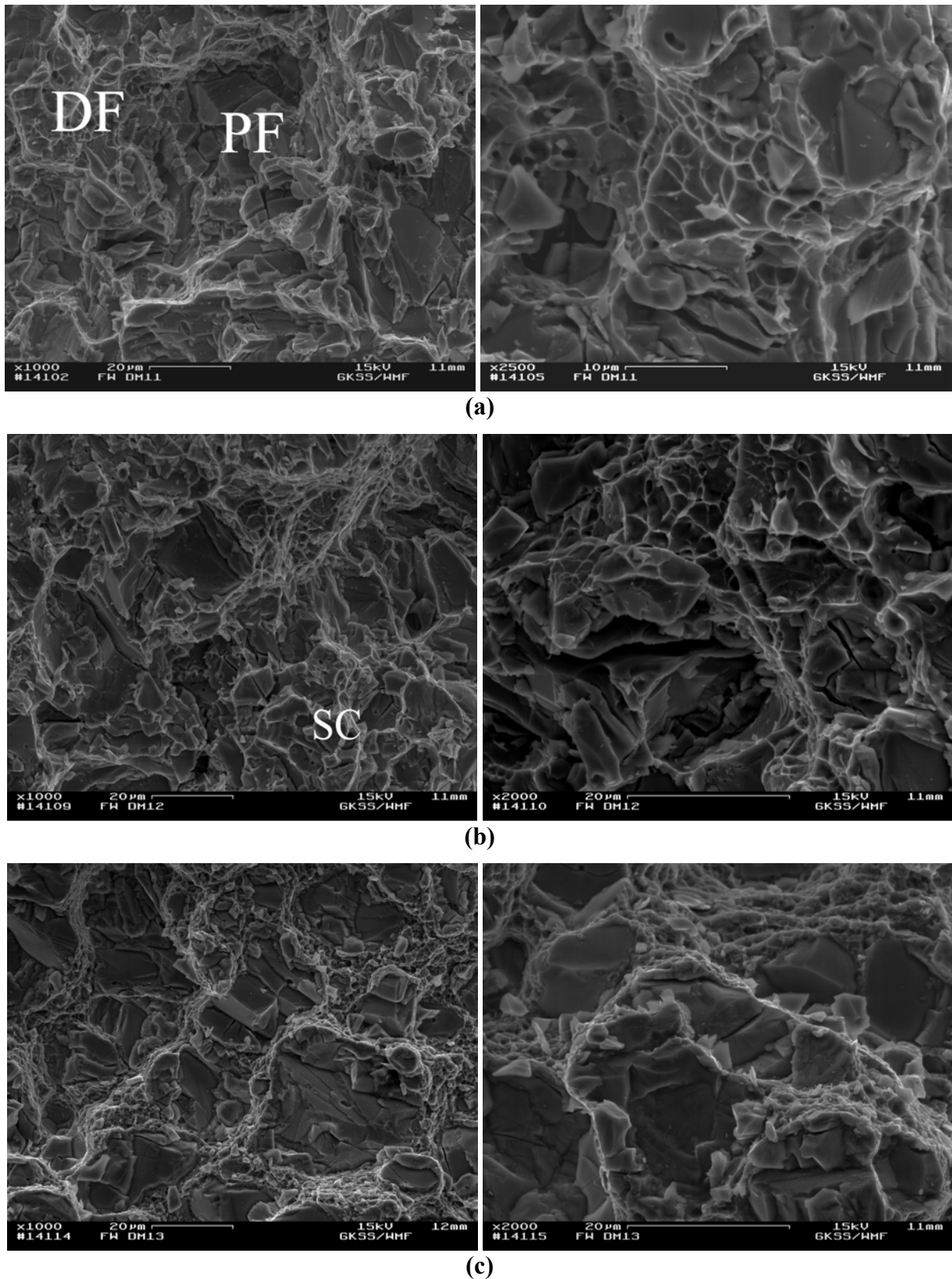


**Figure 4.42 – Secondary electron micrographs taken the friction welded joints fracture surfaces. (a) DM11 (1500 rpm/136 MPa), (b) DM12 (3000 rpm/136 MPa), (c) DM13 (4500 rpm/136 MPa), (d) DM14 (1500 rpm/272 MPa), (e) DM15 (3000 rpm/272 MPa), (f) DM16 (4500 rpm/272 MPa).**

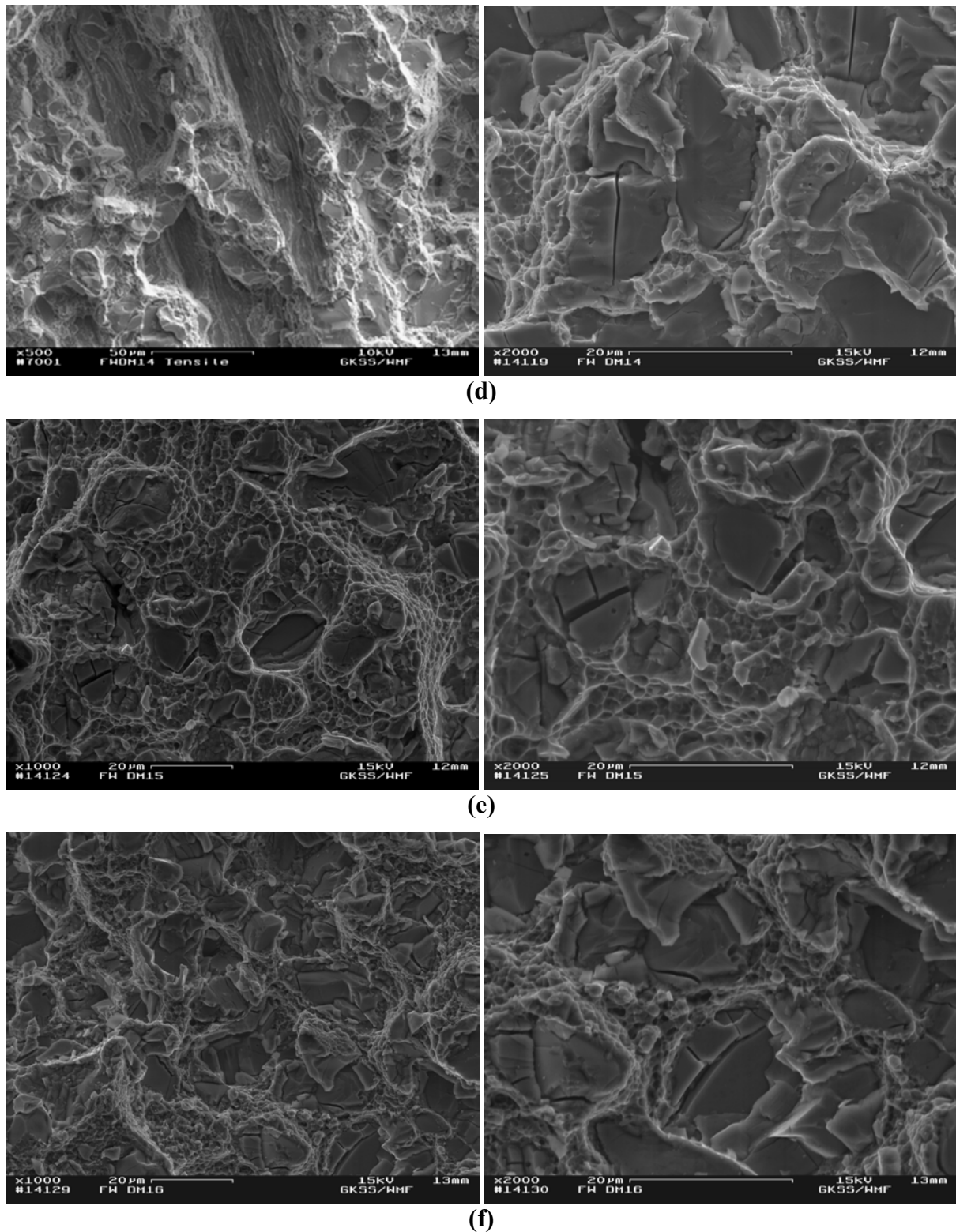


**Figure 4.42 – Secondary electron micrographs taken the friction welded joints fracture surfaces. (a) DM11 (1500 rpm/136 MPa), (b) DM12 (3000 rpm/136 MPa), (c) DM13 (4500 rpm/136 MPa), (d) DM14 (1500 rpm/272 MPa), (e) DM15 (3000 rpm/272 MPa), (f) DM16 (4500 rpm/272 MPa).**

It was not found any significant difference in the fracture surfaces of the welded joints due to the location of the fracture, see Fig. 4.43. When fracture was located in HAZ (Fig. 4.43b and 4.43c – conditions DM11-2 and DM12-3, respectively) particle distribution and

size played an important role in the fracture behaviour since the presence of clustered areas lowers strength and are more susceptible to fracture because the elastic reinforcing particles constrain the plastic flow of the matrix producing increased stress levels in the reinforcing particles and high triaxiality in the matrix between the particles. Since HAZ is not affected by the particle fracture phenomenon the particle distribution usually has the same characteristics as in the base material; therefore such region is affected by the same manner as in base material and particle clustering as well as particle size are dominant features in the fracture characteristics of the welded joint. Such behaviour overcomes the overmatching behaviour of the welded joints (HAZ has a slightly higher hardness value than the base material therefore fracture is expected to be located in base material); however, as explained above, particle features (plastic flow constraint and high triaxiality in the matrix) are dominant factors when it comes to analyse fracture behaviour of composite materials.

Another important feature of the fracture analysis of the welded tensile specimens is the presence of deformation bands in condition DM14-3 (resulted from high pressure and low rotational speed values) which have fractured in TRZ that could have contributed to the poor tensile behaviour found leading to matrix debonding; however in between these deformation bands it can be observed the same fracture behaviour of the base material, i.e., brittle fracture of the particles and ductile fracture of the matrix. It can be observed by the tensile results that such deformation bands have slightly influenced DM14 tensile behaviour (lower values than base material). The fracture mechanism in these three specimens is the same one presented by the base material tensile specimens, i.e., void nucleation as a result of particle fracture, growth and matrix ductile fracture.

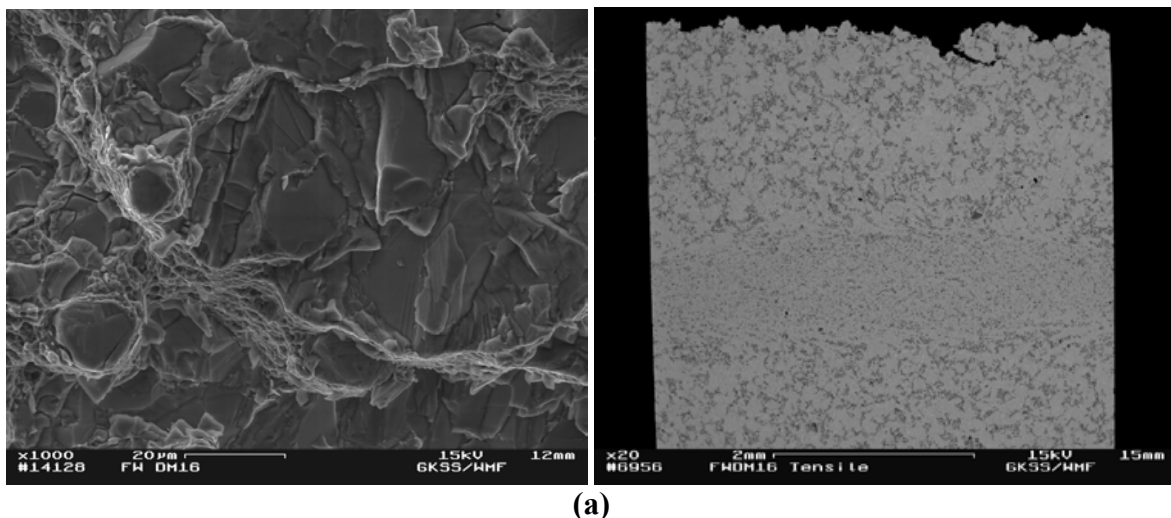


**Figure 4.43 – SEM micrographs showing the fracture surfaces and longitudinal sections from the different regions in the friction welded conditions. (a) Base material. (b) HAZ. (c) TRZ.**

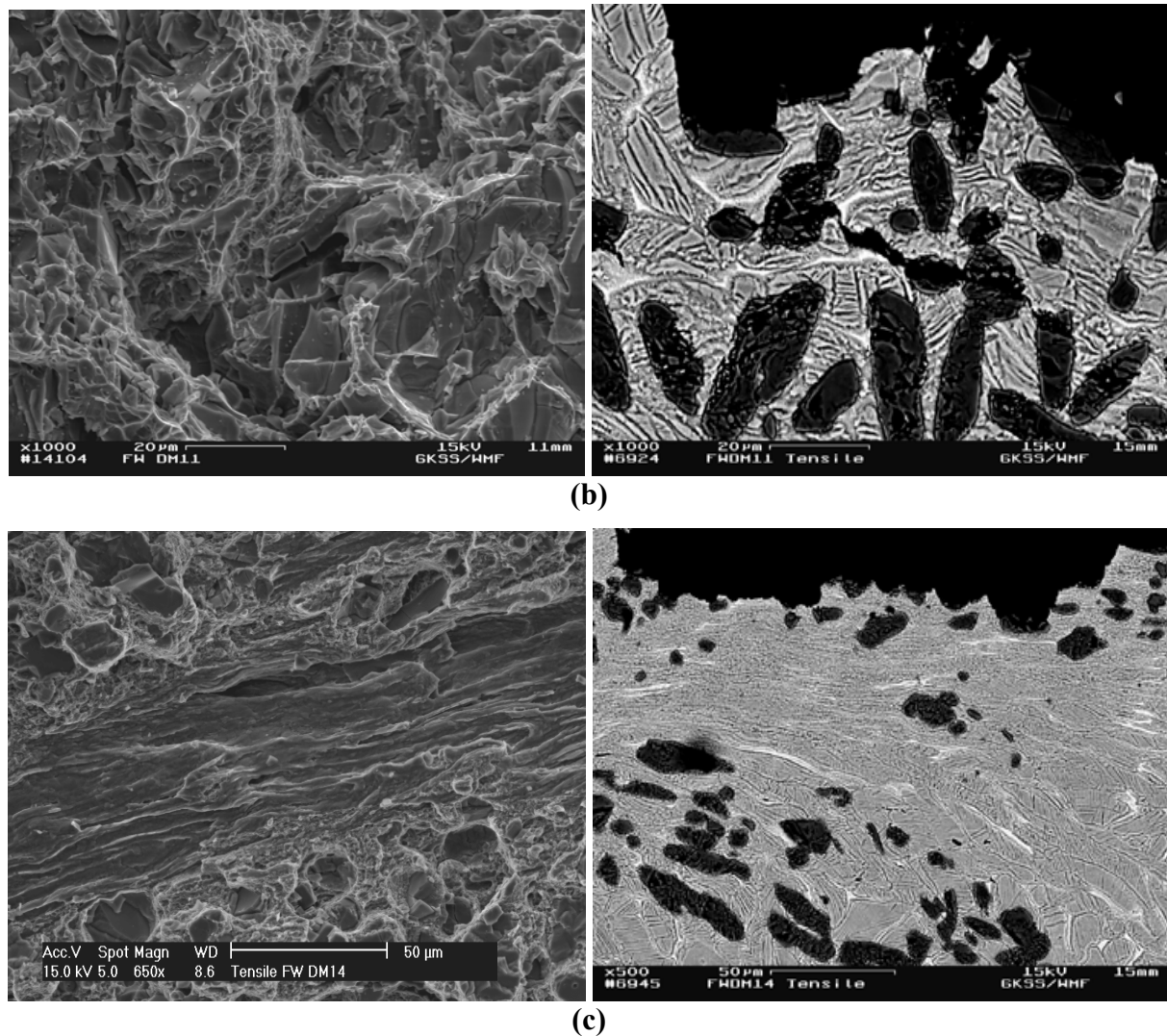


**Figure 4.43 – SEM micrographs showing the fracture surfaces and longitudinal sections from the different regions in the friction welded conditions. (a) Base material. (b) HAZ. (c) TRZ.**

#### 4.2.3.3 Fracture Toughness Tests

The fracture toughness behaviour of the welded joints is expected to be different from the one presented by the base material due to metallurgical and/or mechanical transformations induced by the welding process. Table 4.18 presents the results from the fracture toughness tests (average of 4 specimens) performed in the friction welded joints as well as the joint efficiency (based on base material  $K_{IC}$  average value). The  $K_{IC}$  values for the joints vary from 33.13 to 38.42  $\text{MPa}\cdot\text{m}^{1/2}$  representing only a 16% variation indicating that there is a wide operating welding parameter window for production of sound joints concerning the fracture toughness properties when the composite is joined. It can be observed the scatter of the  $K_{IC}$  values of the welded conditions justified by the presence of the TiC particles and their distribution as well as the local interparticle spacing, particle diameter and aspect ratio, see Fig. 4.44.



**Table 4.18 – Results of fracture toughness of the friction welding and base material conditions.**

Condition	$K_{IC}$ (MPa*m <sup>1/2</sup> )	STD	Joint Efficiency (%)
BM	35.04	2.73	*
DM 11 <sup>*2</sup>	36.98	*	105.54
DM 12 <sup>*2</sup>	38.42	*	109.65
DM 13	33.13	1.08	104.74
DM 14 <sup>*2</sup>	35.82	*	102.23
DM 15 <sup>*1</sup>	*	*	*
DM 16 <sup>*3</sup>	37.19	5.44	106.14

\*1 – In condition DM15 there was no specimen with the notch located in the weld region.

\*2 – Only 1 specimen with the notch located in the weld region.

\*3 – Only 2 specimens with the notch located in the weld region.

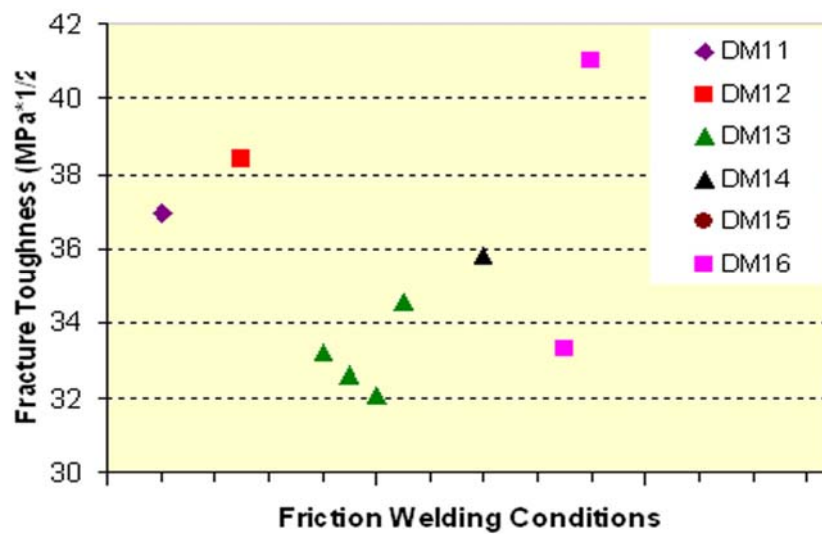


**Figure 4.44 – Fracture toughness behaviour of the friction welded joints.**

The crack path geometry of the welded joints has the same behaviour of the base material, i.e., strongly influenced by the TiC particles (particle fracture); however it has also surrounded the particles (particle debonding) in few occasions, see Fig. 4.45.

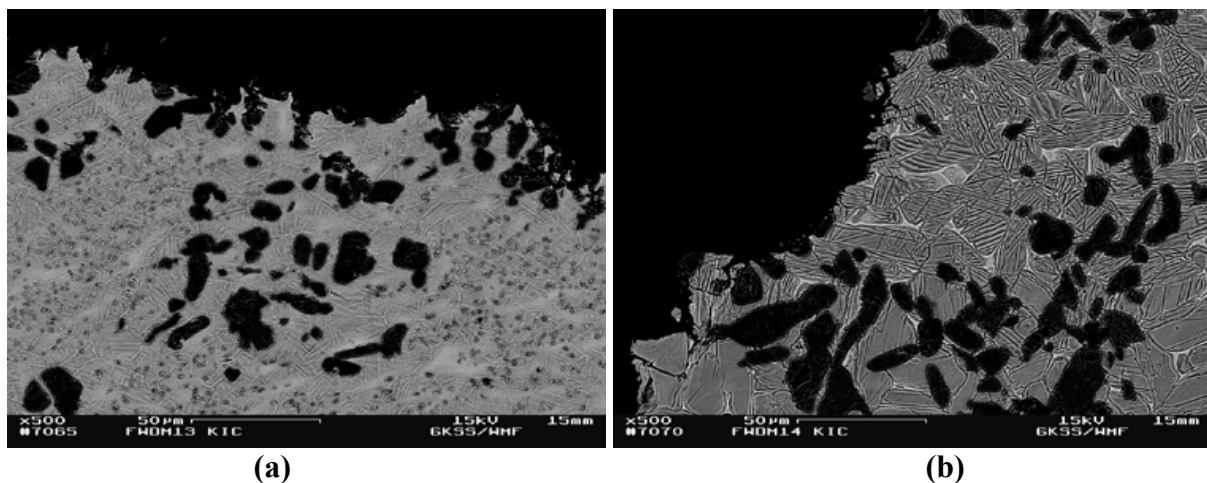


**Figure 4.45 – SEM micrographs showing the crack path geometry of the friction welded joints. (a) DM13 (4500 rpm/136 MPa). (b) DM14 (1500 rpm/272 MPa).**

The only condition among all the friction welded joints that has shown a different behaviour was DM 13 since it has exhibited a smoother crack path than the others (Fig. 4.45a) resulting in lower  $K_{IC}$  values (the lower the degree of deflection, the lower is the  $K_{IC}$  value since lower energy is required to propagate the crack). The transformed area has a different microstructure (acicular  $\alpha$ ) and it is well known that fine structures such as acicular  $\alpha$  exhibits a smoother crack path compared to coarse lamellar structures (platelike  $\alpha$  and intergranular  $\beta$ ). However the most important point in the crack path behaviour of DM13 specimens is the size of the plastic zone (the lower among the welded conditions,  $133.5 \mu\text{m}$ ) and the size of the welded area (the higher among the welded conditions,  $51.61 \text{ mm}^2$ ); since the plastic zone size (upper limit to the extent over which damaging stresses may exist) is inside the weld region (see Fig. 4.46a) the damage (particle fracture) after the initial fatigue precracking is concentrated within the friction welded region (see Fig. 4.46b). After starting the fracture toughness testing (see Fig 4.46c), damage continues in these “pre-damaged” regions with the crack running through the damaged particles (fracture micromechanism is void initiation by particle fracture, growth followed by ductile failure of the matrix); since the welded area has a homogeneous particle distribution and size the plastic zone and consequently the crack path are not deviated into the base material region (particle clustering and larger particles), see Figs 4.46d to 4.46f, until final failure of the specimen.

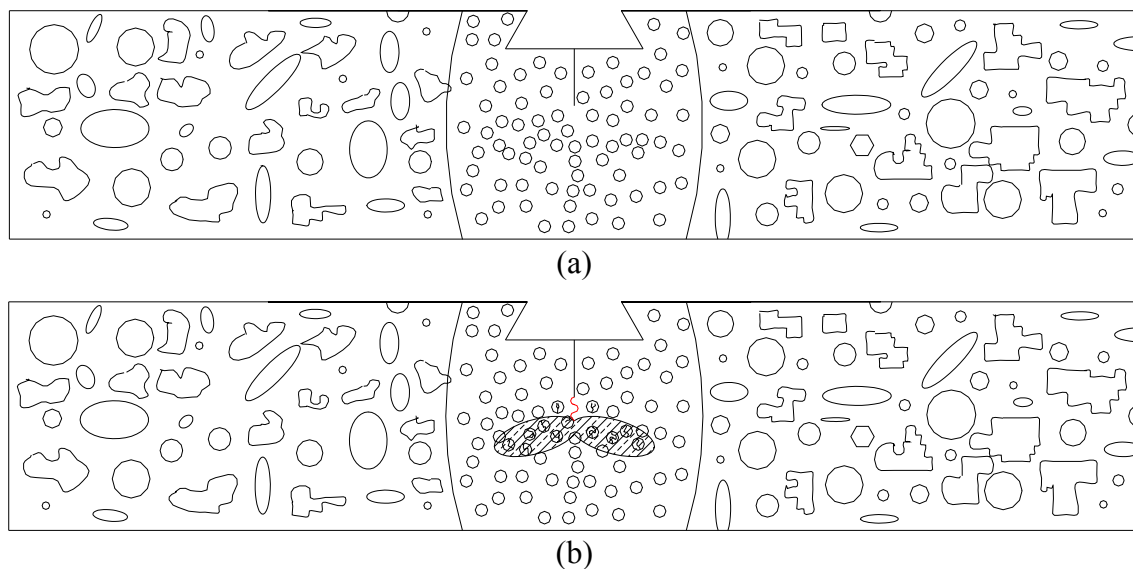


**Figure 4.46 – Crack path behaviour of condition DM13. (a) Before fatigue precracking. (b) After fatigue precracking. (c) to (f) After initiation of the fracture toughness testing. Plastic zone as well as crack path are inside the friction welded region.**



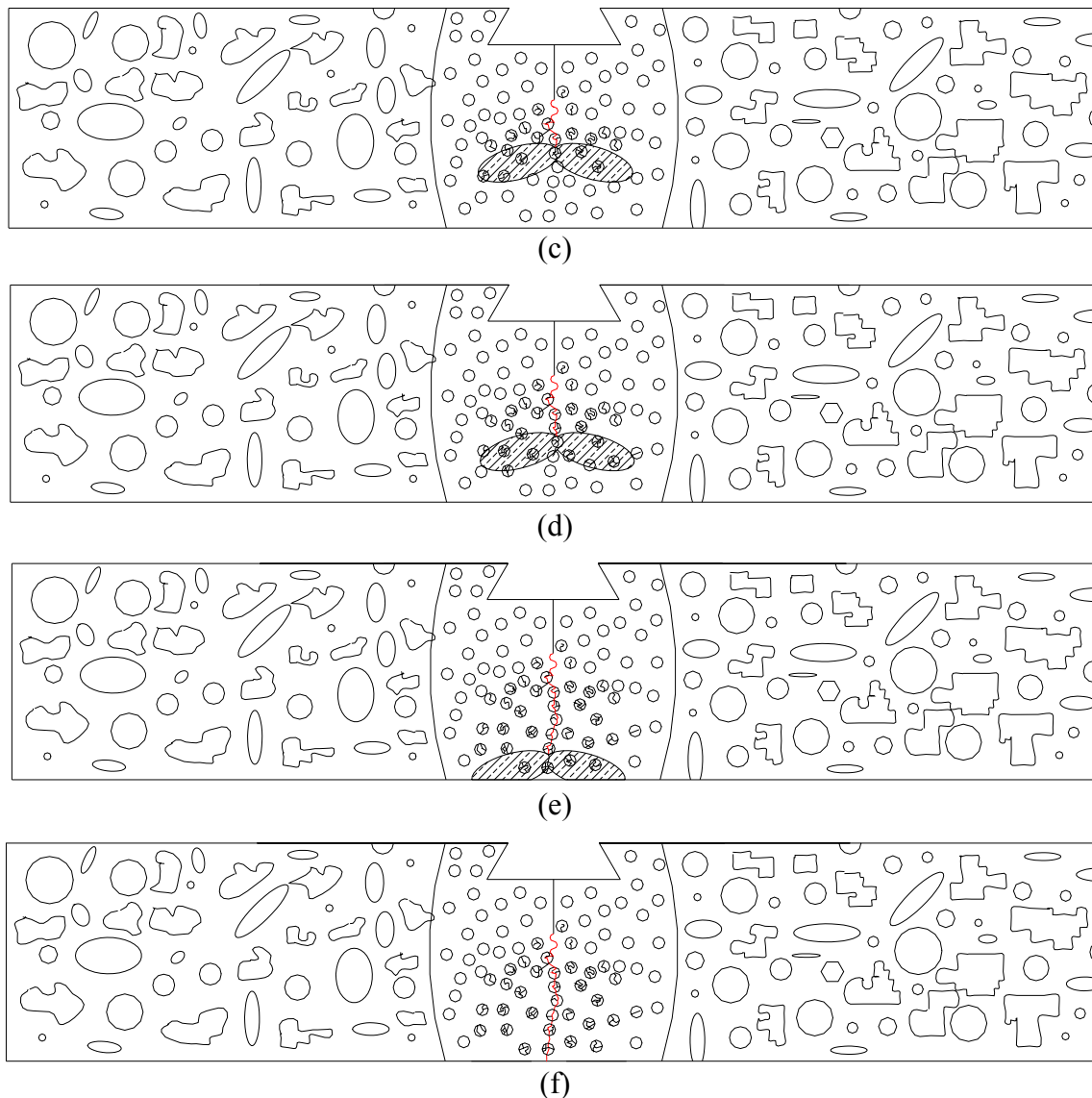


**Figure 4.46 – Crack path behaviour of condition DM13. (a) Before fatigue precracking. (b) After fatigue precracking. (c) to (f) After initiation of the fracture toughness testing. Plastic zone as well as crack path are inside the friction welded region.**

The other conditions (DM11-5, DM12-7, DM14-7, DM16-4 and DM16-52) have presented a deflected crack path (higher  $K_{IC}$ ) since the notch was located in the transition zone where interparticle spacing, particle distribution and size as well as microstructure is quite different than in TRZ, see Fig. 4.47. It is important to emphasize that in these conditions where the notch was located in the transition zone the crack has started and later deviated into the base material due to the plastic zone and welded area size phenomenon explained above; it is possible that the overmatching behaviour of the welded joints has also some degree of influence in this respect (mismatch effect, see Fig. 4.48 [209]).

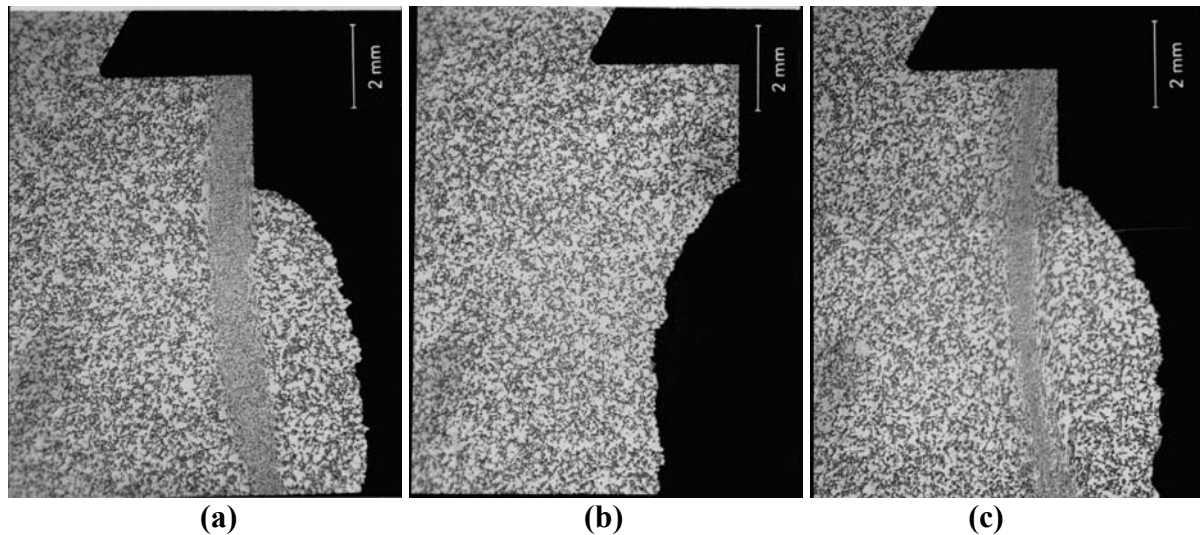


Figure 4.47 – Crack path deviation in the welded joints. (a) DM11-5. (b) DM14-7. (c) DM16-4.

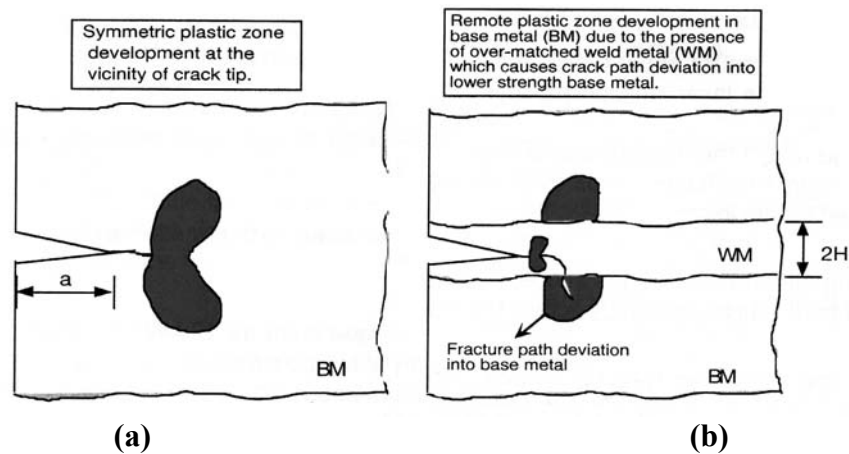
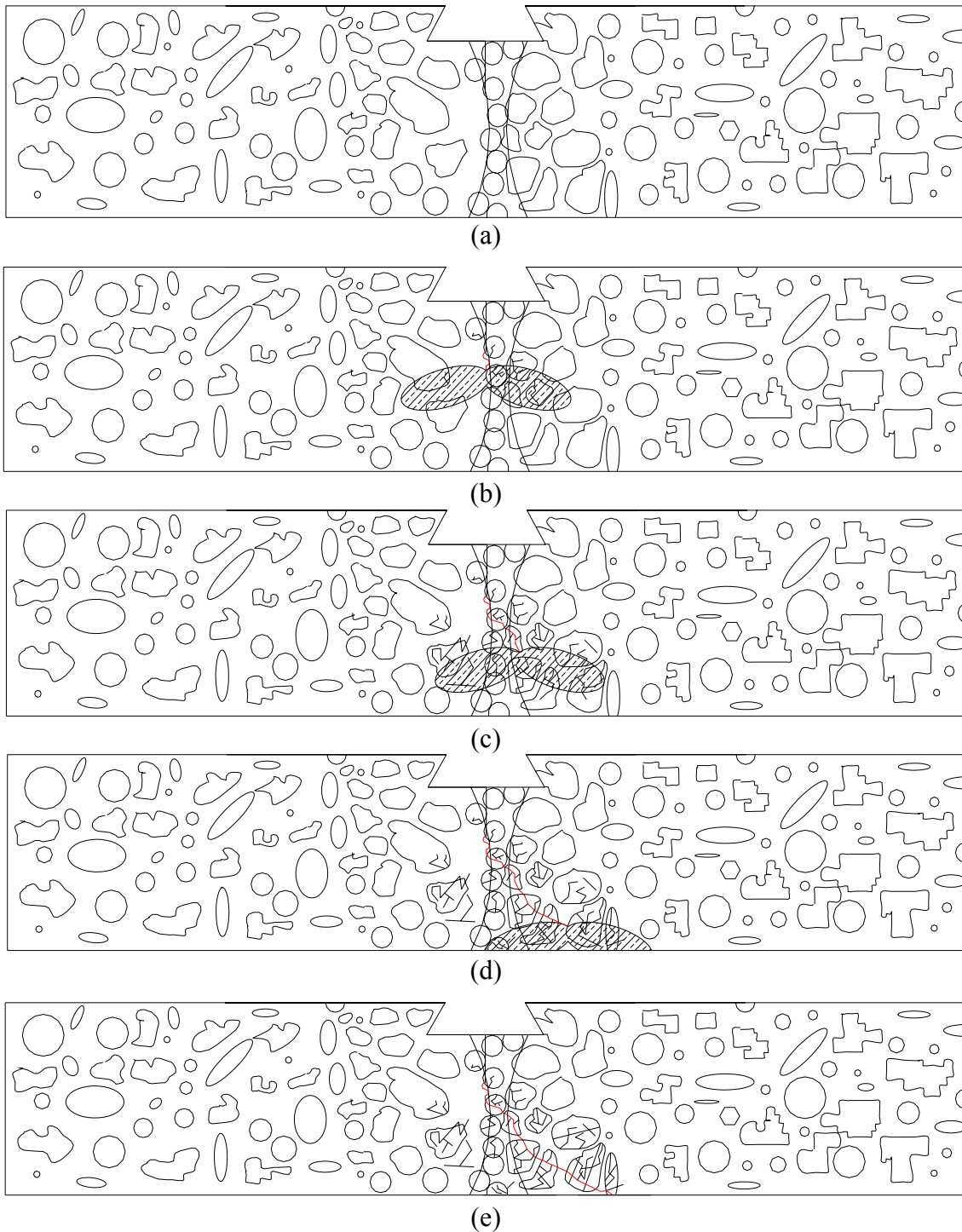


Figure 4.48 – Crack tip plasticity behaviour. (a) homogeneous and (b) mismatched materials.

Different from the behaviour found in condition DM13, the conditions DM11-5, DM12-7, DM14-7, DM16-4 and DM16-52 present much smaller friction welded areas as well as the notch placed in the transition zone either in between HAZ and BM or HAZ and TRZ (see Fig. 4.49a); therefore, while fatigue precracking the specimens, the plastic zone is located inside the different welded zones (see Fig 4.49b). Hence, when starting the fracture toughness test, this higher stressed region contains particles with different size (varying from  $6.1 \mu\text{m}$  to  $14.7 \mu\text{m}$ ) and distribution (presence or not of clustering) as well as different interparticle spacing. It is well known that in composite materials there is a strong tendency of fracturing the largest particles in populations with a larger scatter in particle size as well as that clustered areas are dominant sites for crack nucleation and propagation. Another important point is the fact that the fracture process is controlled by large triaxial stresses intensification occurring in a cluster. Therefore, since the probability of the crack “seeing” a damaged particle in the base material is much higher than in TRZ or HAZ the crack path deviates into the “more damaged”

base material (see Fig. 4.49c to 4.49e) before final failure. As explained in item 4.1.2.3, when particle distribution is nonuniform, damage is concentrated in particle clusters (or large reinforcements) with fracture occurring by linking of these “damage clusters” and macroscopic crack occurs via linkage of the crack tip with the damage present in the clustered regions ahead of the crack tip.



**Figure 4.49 – Crack path behaviour of condition DM14. (a) Before fatigue precracking. (b) After fatigue precracking. (c) to (f) After initiation of the fracture toughness testing. Plastic zone as well as crack path are inside different regions (TRZ, HAZ and base material).**

There is a slight tendency for fracture toughness to increase with increasing particle size since interparticle spacing increases with particle size and a greater volume of matrix material is available for unconstrained plastic flow in the wake of the propagating crack resulting in higher  $K_{IC}$  [50]. However there is no trend (see Table 4.19) in relating particle size, interparticle spacing and fracture toughness in the friction welded joints which may be explained either by a poor particle distribution of the TiC particles (clustering) or by an inhomogeneous particle size distribution since, apart from condition DM13, in all the other conditions the notches were located in the transition zone between HAZ and TRZ with the crack deviating into the base material region.

**Table 4.19 – Influence of the interparticle spacing on the fracture toughness behaviour.**

Condition	$K_{IC}$ (MPa*m <sup>1/2</sup> )	Interparticle spacing (μm)	Particle size (μm)
DM 11	36.98	13.41	9.9
DM 12	38.42	13.84	7.5
DM 13	33.13	9.67	5.8
DM 14	35.82	13.94	9.9
DM 15	*	13.96	7.9
DM 16	37.19	12.36	6.1

The plastic zone size of the friction welded joints has also been calculated according to Equation 4.1 [35,61,204]. Table 4.20 presents the results using the values from Tables 4.15 and 4.18 as well as the calculated interparticle spacing. In all the welded joints the plastic zone size envelopes many particles extending over a distance much greater than the calculated interparticle spacing (apart from the influence of the presence of clustered areas). This means that many more particles lie within this highly stressed region making the particle cracking phenomena more important in the final failure process (see Fig. 4.20) since the higher the plastic zone size, the higher is the possibility of cracked particles lie within this zone causing more damage reducing the  $K_{IC}$  value (as explained before).

**Table 4.20 – Plastic zone size and interparticle spacing of the friction welded joints.**

Condition	Plastic Zone Size (μm)	Interparticle spacing (μm)
DM 11	164.9	13.41
DM 12	178.8	13.84
DM 13	133.5	9.67
DM 14	155.7	13.94
DM 15	*	13.96
DM 16	168.2	12.36

#### 4.2.3.3.1 Modelling the Fracture Toughness of the Particulate-Reinforced Material (Base Material and Friction Welded joints)

Since problems in machining the notches of the fracture toughness specimens (the majority of the notches were located in the base material region) have been found resulting in a perturbation of the  $K_{IC}$  values, a fracture toughness prediction model has been used to determine the  $K_{IC}$  values of the base material and friction welded joints. This model was first proposed by Hahn and Rosenfield [210] according to Equation 4.2:

$$K_{IC} = f^{-\frac{1}{6}} * \sqrt{2 * R_{p0,2} * E * \left(\frac{\pi}{6}\right)^{\frac{1}{3}} * d} \quad \text{Equation 4.2}$$

where  $K_{IC}$  is the fracture toughness ( $\text{MPa}\cdot\text{m}^{1/2}$ );  $f$  is the volume fraction;  $R_{p0,2}$  is the yield strength (MPa);  $E$  is the elastic modulus (MPa) and  $d$  is the particle diameter (m).

This model is based on the assumption that the crack opening displacement ( $\delta = (0.5 * K^2)/(R_{p0,2} * E)$ ) is equal to  $\lambda_V$  (where  $\lambda_V$  is the distance between microcracks in front of the crack tip). According to this assumption crack growth will occur if the extent of the heavily deformed zone ahead of the crack tip becomes comparable to the width of the unbroken ligaments separating the cracked particles. The model also assumes that a microcrack is associated with every reinforcing particle. It is clear that the Hahn and Rosenfield model is valid over a restricted range of particle volume fractions, i.e. it fails in the limit  $f = 0$ , leading to infinitely large  $K_{IC}$  values. However the main problem with this model is that it shows an increasing toughness with the yield strength whereas the reverse is normally observed. From a microstructural perspective, a higher strength is usually accompanied by concentrated and localized slip bands, which accelerates the initiation of microvoids in these bands. Mechanically, a higher strength is accompanied with a reduction in the work hardening exponent. The Hahn and Rosenfield model does not take into account such observations and apart from that there is another problem since the model is valid only for material with homogeneous particle distribution and also with elastic-plastic behaviour.

Table 4.21 presents the values used in the calculation of  $K_{IC}$  of both base material and friction welded conditions. It is important to emphasize that the area fraction was used instead of the volume fraction since the composite is reinforced with 10 wt.% of TiC particles instead of 10 vol.% (see Table 4.13) and also the elastic modulus has been determined from only one sample for each condition, therefore the values may not represent the actual elastic modulus of the welded joints. Replacing these values into Equation 4.2 gives the  $K_{IC}$  values according to the Hahn and Rosenfield model.

**Table 4.21 – Parameters used to calculate the fracture toughness of the base material and friction welded joints according to the Hahn and Rosenfield model.**

Specimen	Volume fraction (f)	R <sub>p0.2</sub> (MPa)	E (GPa)	Particle size (µm)
BM	0.205	954	134	14.7
DM 11	0.210	938	127	9.9
DM 12	0.219	936	126	7.5
DM 13	0.223	934	128	5.8
DM 14	0.229	935	129	9.9
DM 15	0.236	917	130	7.9
DM 16	0.239	934	127	6.1

It can be observed that the calculated  $K_{IC}$  values are higher than the ones obtained during fracture toughness testing (see Table 4.22), since the Hahn and Rosenfield model calculates the  $K_{IC}$  of materials with homogeneous particle distribution which is not the case presented in this investigation (particle clustering and inhomogeneous particle size). Another problem is that the amount of particles in the crack plane varies a lot; if the crack is deflected towards the particles, the volume fraction is higher in the crack plane causing a drop in the calculated  $K_{IC}$  value. Other problems associated with this model are that it fails for large particles since there is a direct evidence that these particles crack easily and there are problems associated with plastic instability in the highly strained region adjacent to the crack tip accelerating the linking of voids which seems to be the composite behaviour due to the presence of large TiC particles and clustering.

**Table 4.22 – Comparison (in % values) of measured and calculated  $K_{IC}$  values.**

Specimen	Measured $K_{IC}$ (MPa*m <sup>1/2</sup> )	Calculated $K_{IC}$ (MPa*m <sup>1/2</sup> )	Difference (%)
BM	35.04	71.68	204.55
DM 11	36.98	56.55	152.93
DM 12	38.42	48.64	126.59
DM 13	33.13	42.93	129.58
DM 14	35.82	56.09	156.59
DM 15	*	49.25	*
DM 16	37.19	43.35	116.57

Figure 4.50 presents a comparison between the calculated and measured  $K_{IC}$  values where it can be clearly seen that the model has a strong dependence on particle size since the  $K_{IC}$  values sharply increase with an increase in the particle size, while the other parameters do not have a significant influence on the final  $K_{IC}$  value. Changing the particle diameter value from 14.7 µm (base material) to 5.8 µm (DM 13) causes a drop in the  $K_{IC}$  value from 71.56 MPa\*m<sup>1/2</sup> to 43.11 MPa\*m<sup>1/2</sup>. Table 4.23 presents the difference (% values) between the calculated and tested  $K_{IC}$  values.

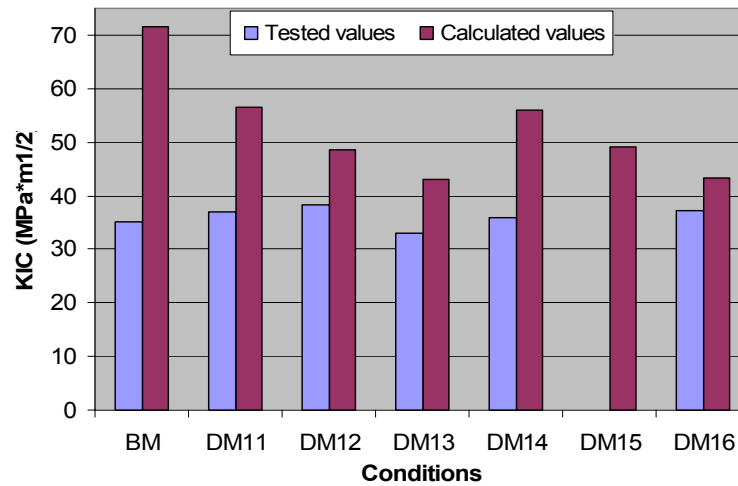


**Figure 4.50 – Comparison between tested and calculated  $K_{IC}$  values.**

With this problem of having different local volume fraction as well as local particle distribution and size a local image analysis was performed in order to determine the size and distribution of the particles as well as the volume fraction (in terms of area fraction) of the particles close to the crack front (in an area approximately 300  $\mu\text{m}$  away from the crack front) representing the “local” TiC particle characteristics for one specimen from each welded joint. Table 4.23 presents the results of this evaluation performed in ten micrographs for each condition for the volume fraction and particle size. Figure 4.51 shows the micrographs used to perform this investigation in specimen DM12-4 where it is possible to observe that there is a measure frame (blue frame – Fig. 4.51b) which has varied according to each individual micrograph and only the particles inside this frame have been measured (see Fig. 4.51c).

**Table 4.23 – Parameters used to calculate the  $K_{IC}$  of the base material and welded joints by the Hahn and Rosenfield model according to the image analysis performed close to the crack front.**

Specimen	Volume fraction (f)	$R_{p0.2}$ (MPa)	E (GPa)	Particle size ( $\mu\text{m}$ )
BM	0.210	954	134	14.70
DM11-6	0.168	938	127	13.64
DM12-4	0.110	936	126	14.94
DM13-4	0.105	934	128	13.44
DM14-4	0.119	935	129	13.66
DM15-5	0.150	917	130	15.34
DM16-52	0.130	934	127	14.92

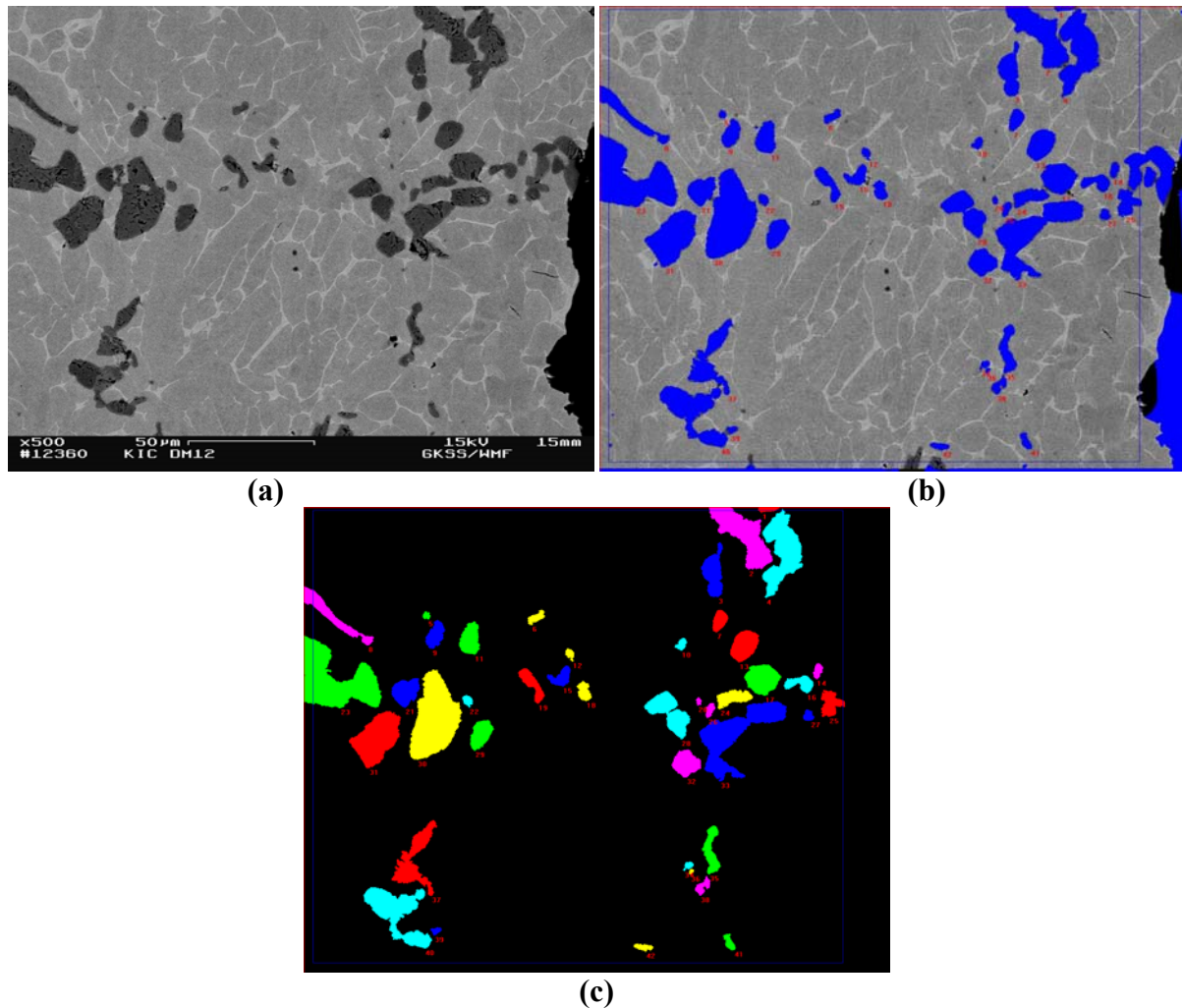


**Figure 4.51 – Micrographs showing the sequence of the image analysis performed in condition DM12-4 (3000 rpm/136 MPa and  $K_{IC}$  value of  $36.33 \text{ MPa}\cdot\text{m}^{1/2}$ ). (a) SEM micrograph showing the area analysed. (b) and (c) Micrographs presenting the particles identified by the software.**

The reinforcement volume fraction has also a great deal of importance on the fracture toughness properties because when increasing its value the local strain in the matrix between the particles becomes higher resulting in premature matrix fracture. This is caused by the fact that when strain is the dominating factor for failure, the distance over which this strain should be accomplished (interparticle spacing) becomes shorter with increasing particle volume fraction. Since the constraint imposed on the matrix determines the plastic zone size, which in turn influences the overall fracture behaviour, it is assumed that an increase in the reinforcement volume fraction leads to a decrease in the plastic zone size and thus in the  $K_{IC}$  value. The toughness decreases sharply with the addition of reinforcement at low volume fraction although relatively smaller losses in toughness accompany increasing reinforcement levels. The values from Table 4.13 represent the global “volume fraction”; however the most important volume fraction is the one close to the crack front since it indicates the real



influence of the TiC particles features (especially the local interparticle spacing and particle size) in the crack tip. However, when using the Hahn and Rosenfield model, the local volume fraction does not strongly influence the final calculated values since a great variation (comparing BM and DM12-4 with almost the same particle diameter, 14.7 and 14.9  $\mu\text{m}$ , and different volume fraction, 0.20 and 0.11, respectively) has not induced any significant difference in the  $K_{IC}$  value (Table 4.24). It can be observed that the differences were even higher than the former analysis (with global volume fraction and particle size). Such problems derive from the fact that the analysis has been performed in the base material region (in all specimens investigated the notch was located in the base material) and that the model fails in predicting the fracture toughness of materials with inhomogeneous particle distribution leading to an overestimation of the  $K_{IC}$  values. Table 4.25 presents a comparison between the tested values and the calculated values (global and local analysis).

**Table 4.24 – Calculated fracture toughness values of the base material and friction welded joints (Hahn and Rosenfield model) after the image analysis performed close to the crack front.**

Condition	Calculated $K_{IC}$ ( $\text{MPa}\cdot\text{m}^{1/2}$ )
BM	71.68
DM 11	69.47
DM 12	77.01
DM 13	74.07
DM 14	73.48
DM 15	75.12
DM 16	75.14

**Table 4.25 – Comparison between measured and calculated  $K_{IC}$  (global and local analysis) values according to the Hahn and Rosenfield model.**

Specimen	$K_{IC}$ ( $\text{MPa}\cdot\text{m}^{1/2}$ )	Calculated $K_{IC}$ ( $\text{MPa}\cdot\text{m}^{1/2}$ ) <sup>*global</sup>	Calculated $K_{IC}$ ( $\text{MPa}\cdot\text{m}^{1/2}$ ) <sup>*local</sup>
BM	35.04	71.68	71.68
DM 11	36.98	56.55	69.47
DM 12	38.42	48.64	77.01
DM 13	33.13	42.93	74.07
DM 14	35.82	56.09	73.48
DM 15	*	49.25	75.12
DM 16	37.19	43.35	75.14

#### 4.2.3.4 Fracture Surface Analysis of the Fracture Toughness Specimens

According to the fractography performed in the fracture surfaces of the welded joints there are two types of damage modes: TiC particle cracking and matrix/particle interface

debonding; however the latter has not been often observed as the former. The fracture mechanism of the welded joints is the same one presented by the base material specimens, i.e., nucleation at the TiC particles, growth followed by ductile fracture of the matrix by coalescence of microvoids. It has also been found extensive microcracking at and near the crack tip indicating the same behaviour found in base material. A high amount of fractured particles can be also observed representing a preferable crack path. Figure 4.52 presents the fracture surface of the welded joints where it is possible to observe the same features presented by the base material such as coalescence of microvoids (DF in Fig. 4.52c), particle fracture (PF in Figs. 4.50b) as well as secondary cracking (SC in Fig. 4.52e). There is no evidence of a different fracture behaviour due to the position of the notch since it was found the same fracture characteristics of the base material specimens.

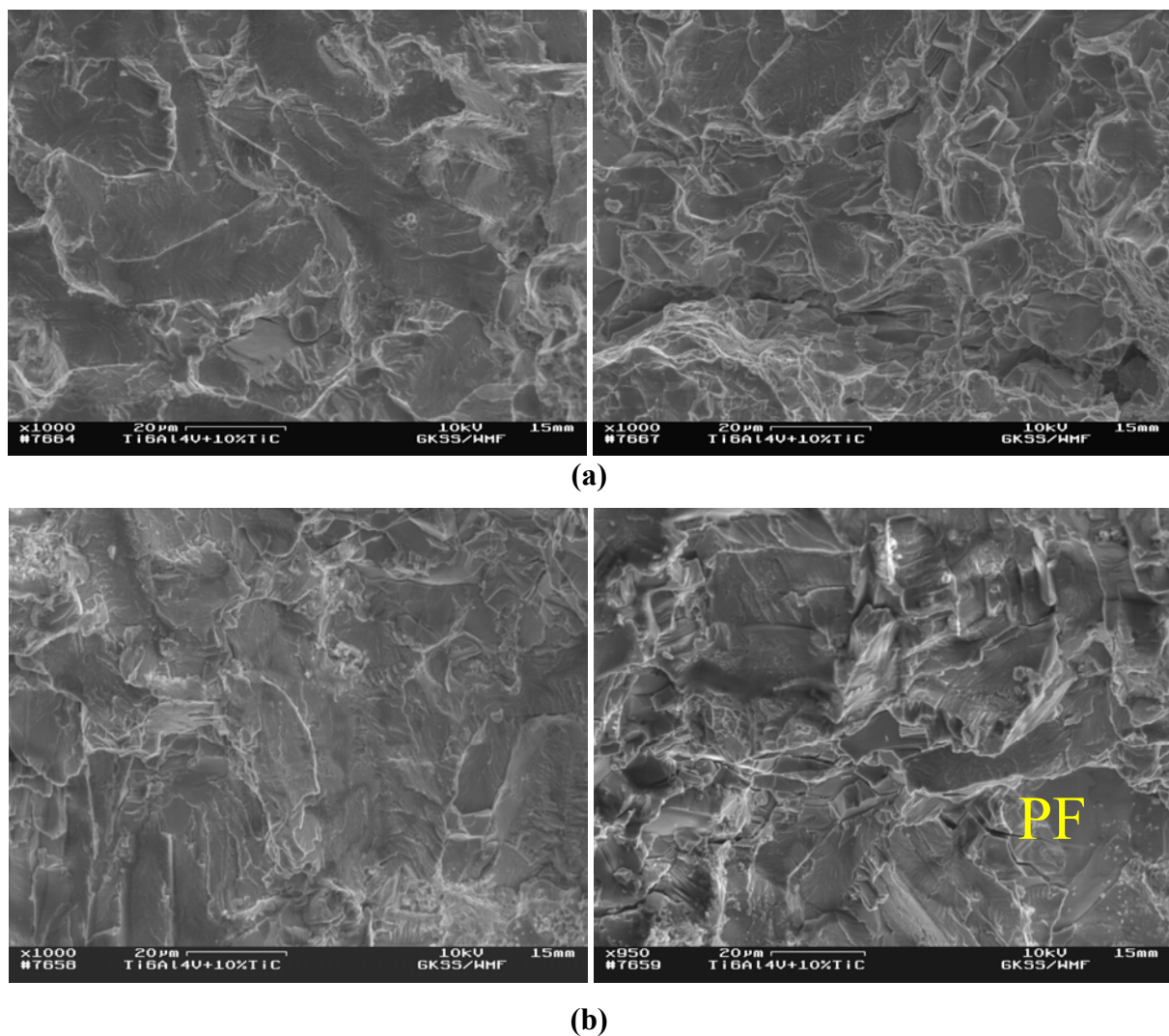
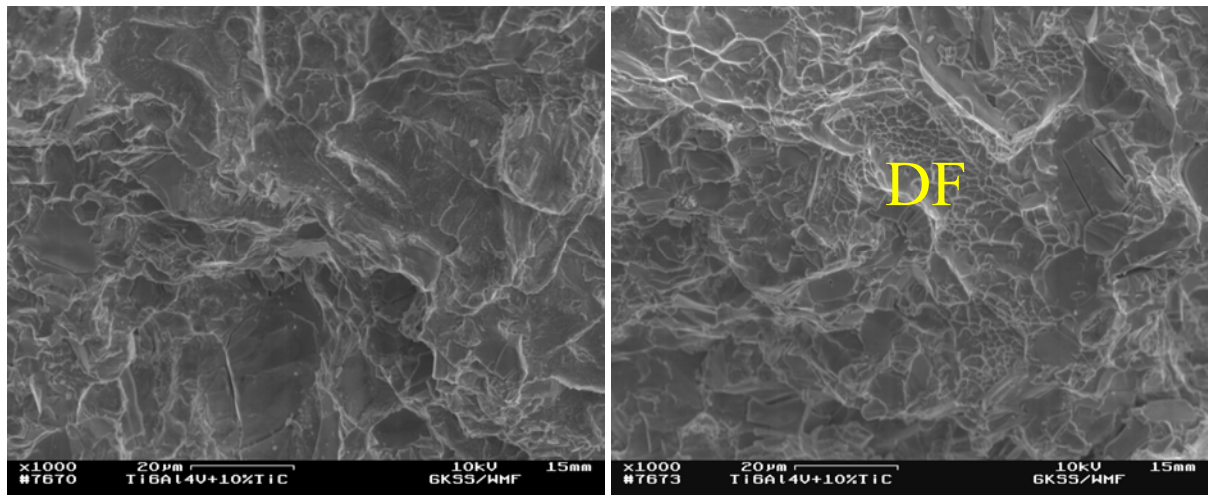
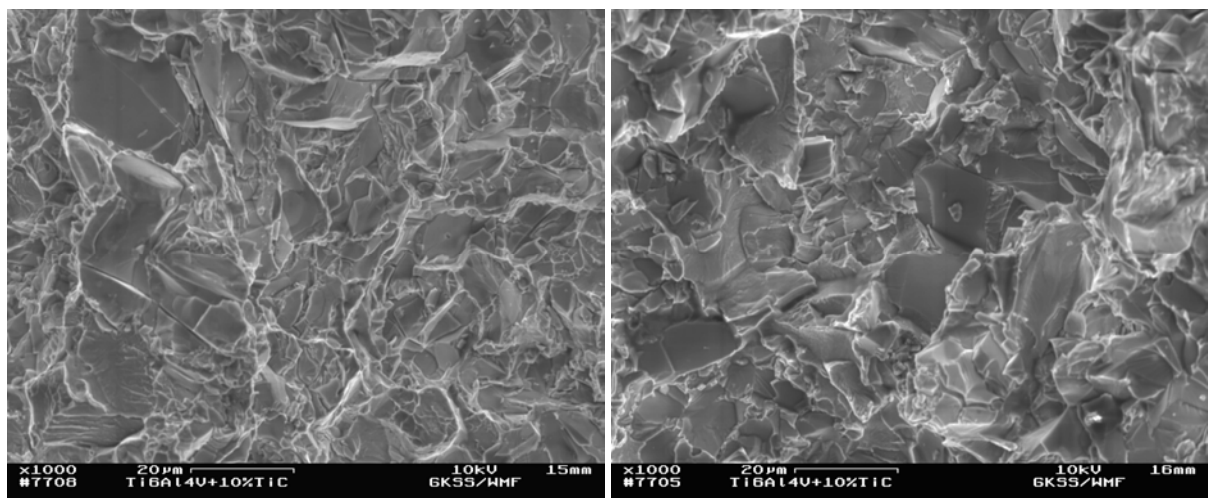


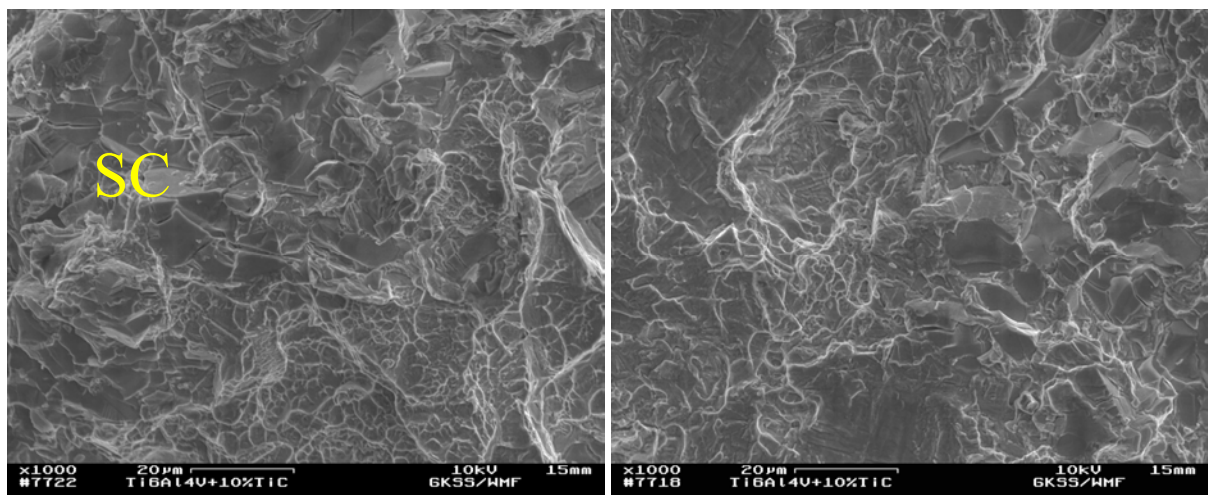
**Figure 4.52** – SEM micrographs from the fracture surfaces of the welded joints. (a) DM11 (1500 rpm/136MPa). (b) DM12 (3000rpm/136MPa). (c) DM13 (4500rpm/136MPa). (d) DM14 (1500 rpm/272MPa). (e) DM16 (4500rpm/272MPa). DM15 is not shown (notches in base material).



(c)



(d)



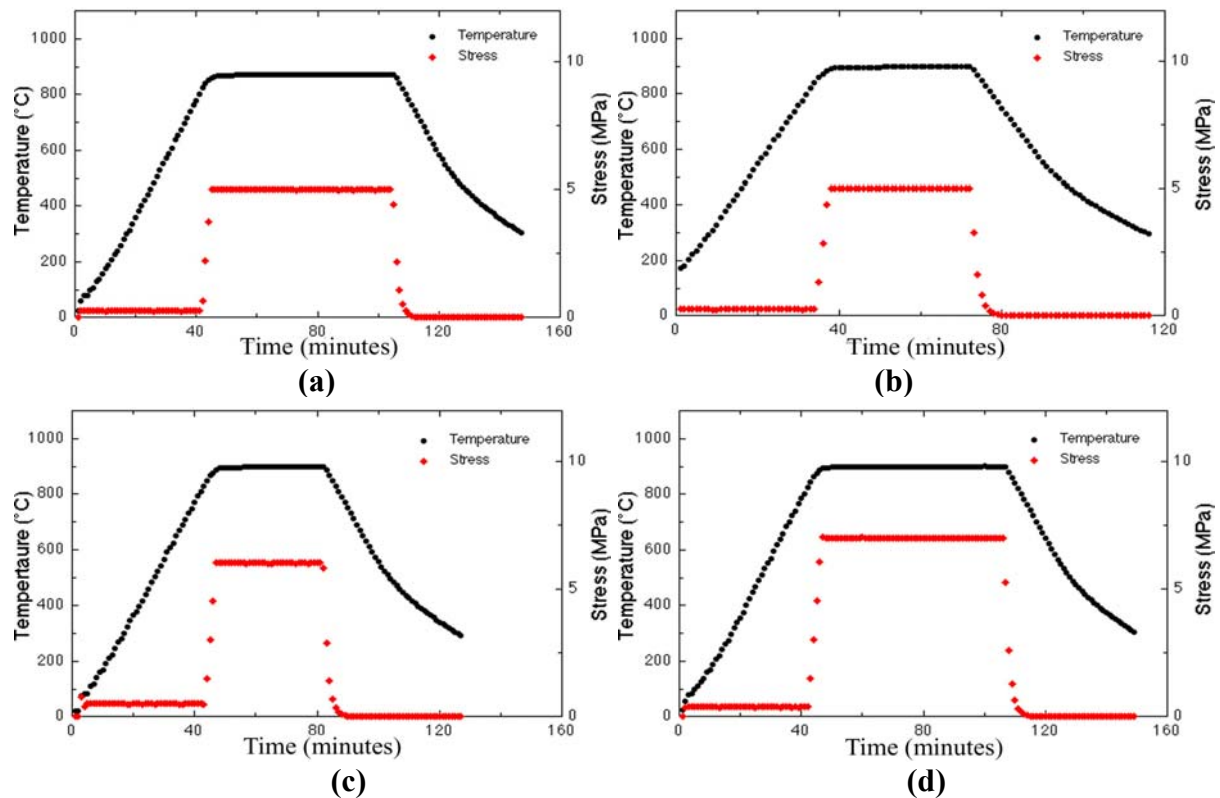
(e)

Figure 4.52 – SEM micrographs from the fracture surfaces of the welded joints. (a) DM11 (1500 rpm/136MPa). (b) DM12 (3000rpm/136MPa). (c) DM13 (4500rpm/136MPa). (d) DM14 (1500 rpm/272MPa). (e) DM16 (4500rpm/272MPa). DM15 is not shown (notches in base material).

### 4.3 Metallurgical and Mechanical Characterisation of the Ti6Al4V+10 wt.% TiC Diffusion Bonded Joints

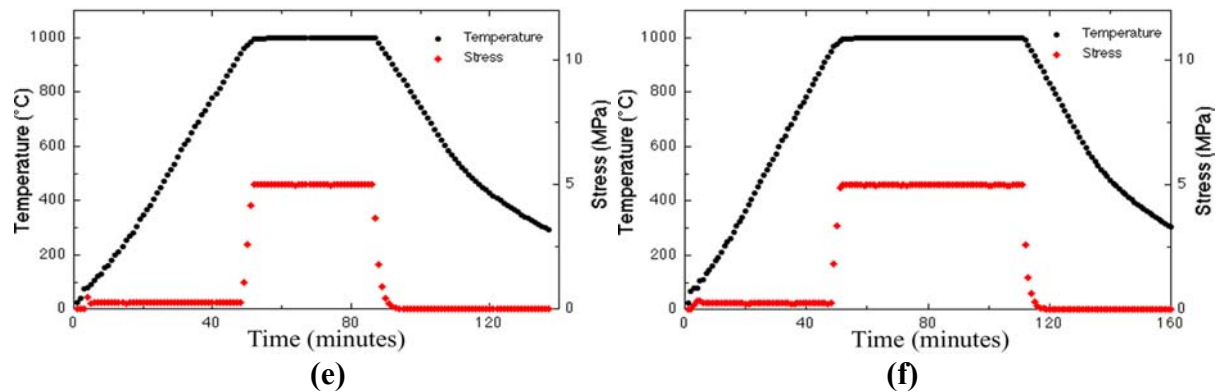
#### 4.3.1 Diffusion Bonding

Figure 4.53 shows the temperature and pressure cycles of the six diffusion bonding conditions. There is no evidence that the  $\beta$  transus temperature of the composite has been reached (maximum temperatures used were 1000°C and there is no data concerning the  $\beta$  transus temperature of the Ti6Al4V+10 wt.% TiC alloy). It is suggested that all the bonding process has been performed high in the  $\alpha+\beta$  field confirming the microstructure found in all the bonding conditions (same as in the base material, i.e., no phase transformation has occurred). The bonding cycle was of the same type for all the samples: heating rate of 20°C/min in vacuum to 30°C below the chosen bonding temperature under a pressure of approximately 0.25 MPa, heating rate of 10°C/min to the selected bonding temperature, increasing the applied pressure to the selected bonding pressure, with a rate of 1.5 MPa/min, for the selected bonding time. After finishing the bonding process the cooling rate was approximately 20°C/min in vacuum down to room temperature which has not induced any subsequent phase transformations on the bonded joints.



**Figure 4.53 – Diffusion bonding temperature and pressure cycle for all investigated conditions. (a) DB1 (875°C/5 MPa/60 min). (b) DB2 (900°C/5 MPa/35 min). (c) DB3 (900°C/6 MPa/35 min). (d) DB4 (900°C/7 MPa/60 min). (e) DB5 (1000°C/5 MPa/35 min). (f) DB6 (900°C/6 MPa/60 min).**





**Figure 4.53 – Diffusion bonding temperature and pressure cycle for all investigated conditions. (a) DB1 (875°C/5 MPa/60 min). (b) DB2 (900°C/5 MPa/35 min). (c) DB3 (900°C/6 MPa/35 min). (d) DB4 (900°C/7 MPa/60 min). (e) DB5 (1000°C/5 MPa/35 min). (f) DB6 (900°C/6 MPa/60 min).**

### 4.3.2 Metallurgical Characterisation of the Diffusion Bonded Joints

The microstructure of the bonded joints consists of platelike  $\alpha$  (equiaxed  $\alpha$  grains have also been reported in some regions close to the TiC particles) and intergranular  $\beta$  with TiC particulate distributed in the matrix which is the same microstructure found in base material indicating that no metallurgical reaction has taken place during the bonding process.

The diffusion bonds made at 875°C/5MPa with a bonding time of 60 minutes (DB1) showed unbonded areas as well as a clearly visible bond interface (see Fig. 4.54a) indicating that bonding time, temperature and/or pressure were not enough to allow diffusion across the bond interface from the mating surfaces in order to have a defect-free joint. The original interface can be also clearly seen since the black line located at the middle of the micrograph is the gap between the mating surfaces. The samples joined at 900°C/5MPa and 900°C/6MPa with a bonding time of 35 minutes, DB2 and DB3, respectively, showed a visible bond line and presented in some parts unbonded areas, Figs. 4.54b and 4.54c. Once again, the samples have not been fully bonded since the original interface is clearly visible (the black line at the middle of the micrographs, Figs. 4.54b and 4.54c, is the gap between the mating surfaces). These results showed that even increased temperature and pressure (compared to DB1) were not enough to produce defect-free bonds. The condition DB4 (900°C/7 MPa/60 minutes) presented a visible bond interface (remaining voids) in some parts but no unbonded areas were found showing that an increase in the three key bonding parameters compared to the initial conditions was beneficial to the bonding process, Fig. 4.54d. The best results were obtained with bonds made at 1000°C/5MPa and bonding times of 35 and 60 minutes (DB5 and DB6, respectively). It presented no unbonded areas, cracks or any kind of segregation and the bond interface was almost imperceptible (few remaining voids in some areas away from the weld centre), Figs. 4.54e and 4.54f. This clearly demonstrated that an increase of 100°C,

keeping pressure constant and maintaining the bonding times in the range studied were enough to ensure defect-free bonds showing the importance of this parameter. Indeed, diffusion varies exponentially with temperature (see Eq.2.9) and a small increase on its value strongly influences the final condition of the bonded joint.

Comparing results obtained for conditions DB2 and DB3 (Figs. 4.54b and 4.54c), one can observe the influence of varying the pressure at constant temperature. DB3 (higher pressure – 6MPa) showed the best results mainly because the first stage of bonding formation is strongly influenced by the amount of deformation induced causing deformation of the mating surfaces and asperity collapse. Indeed, void elimination at the bond interface is strongly affected by bonding pressure and mating surface condition (surface roughness) [146]. The bonding pressure is critical in the beginning of the process in order to establish a point-to-point contact across which diffusion can occur; the higher the pressure, the more points and contact area, so the more diffusion can occur for any particular temperature. Later in the process (stages II and III), pressure can also help accelerate bonding process by causing creep and/or sufficient plastic deformation at the dynamic recrystallisation temperature [88].

Time influences the distance in which diffusion occurs and increasing it increases the distance (Eq. 2.10). Additionally, the time required for complete the bonding decreases with increasing the applied pressure. From Figs. 4.54e and 4.54f it can be observed that bonding in DB5 and DB6 was completed after 35 minutes (almost no remaining voids) and after that certain time grain boundary migration (stage III) has occurred beyond the bond interface since there was almost no difference between both conditions concerning the presence of voids.

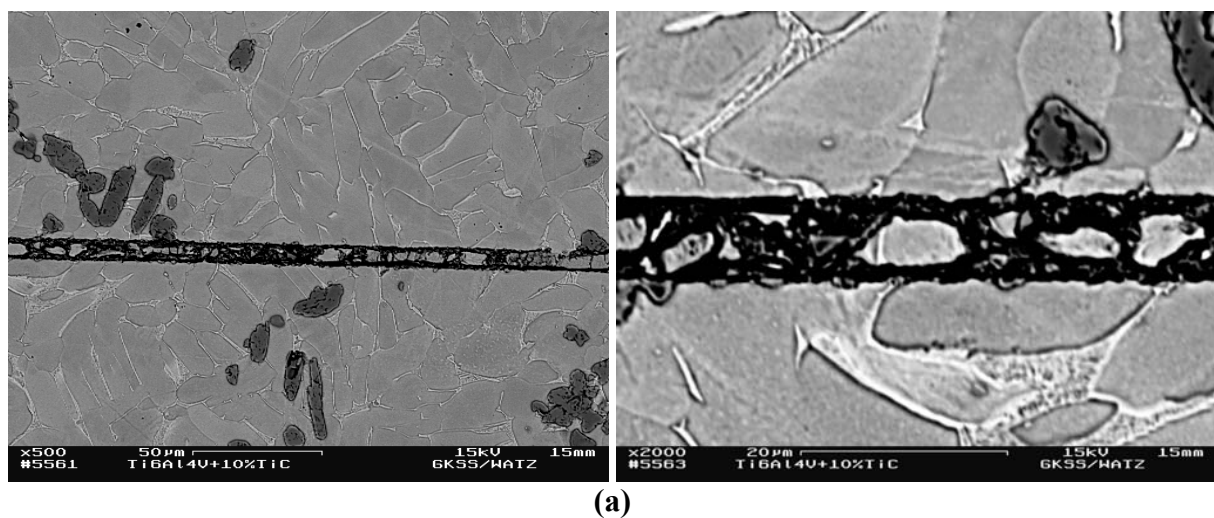


**Figure 4.54 – SEM micrographs of the bonded conditions. (a) DB1 (875°C/5MPa/60min). (b) DB2 (900°C/5MPa/35min). (c) DB3 (900°C/6MPa/35min). (d) DB4 (900°C/7MPa/60min). (e) DB5 (1000°C/5MPa/35min). (f) DB6 (1000°C/5MPa/60min).**

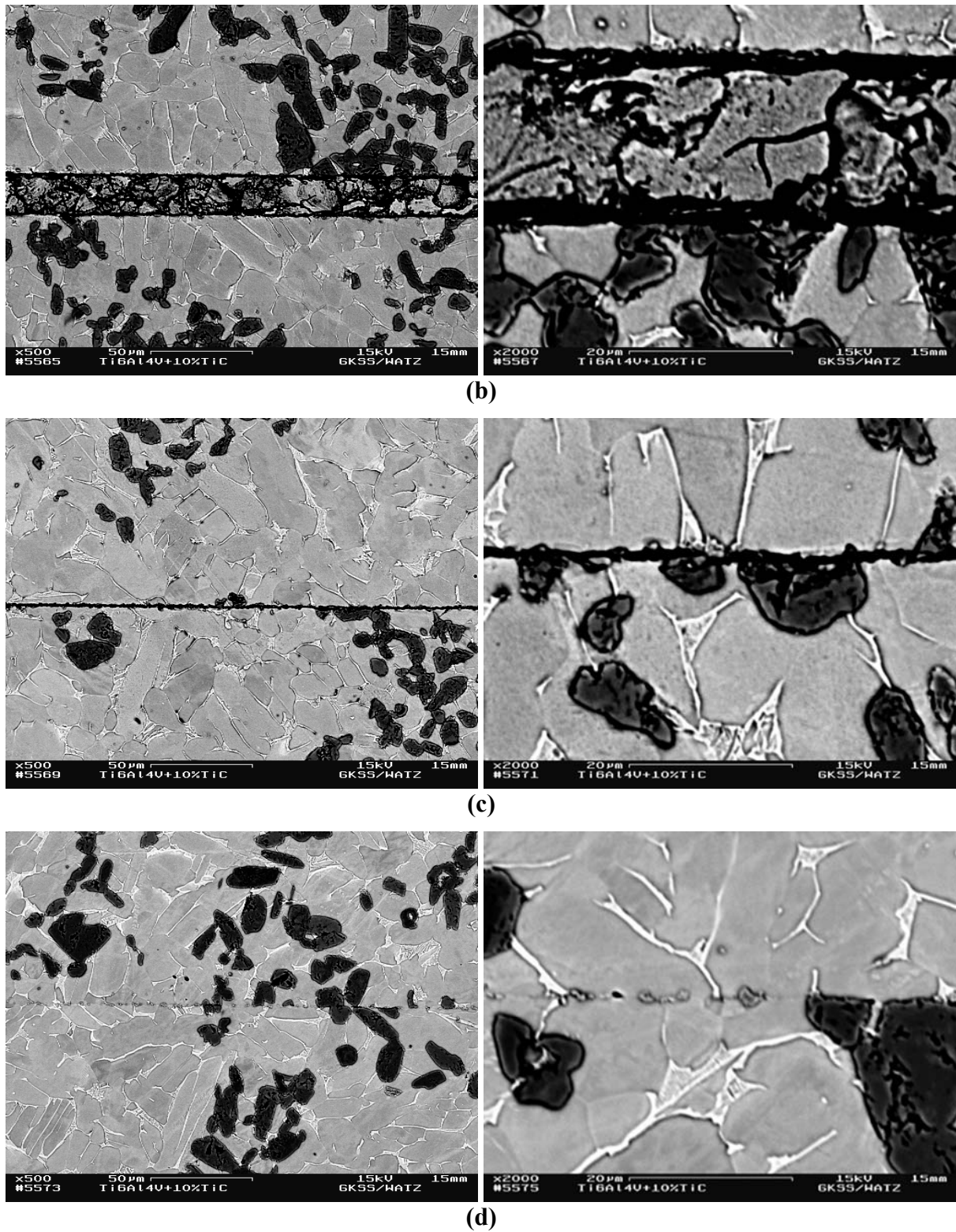


**Figure 4.54 – SEM micrographs of the bonded conditions. (a) DB1 (875°C/5MPa/60min). (b) DB2 (900°C/5MPa/35min). (c) DB3 (900°C/6MPa/35min). (d) DB4 (900°C/7MPa/60min). (e) DB5 (1000°C/5MPa/35min). (f) DB6 (1000°C/5MPa/60min).**

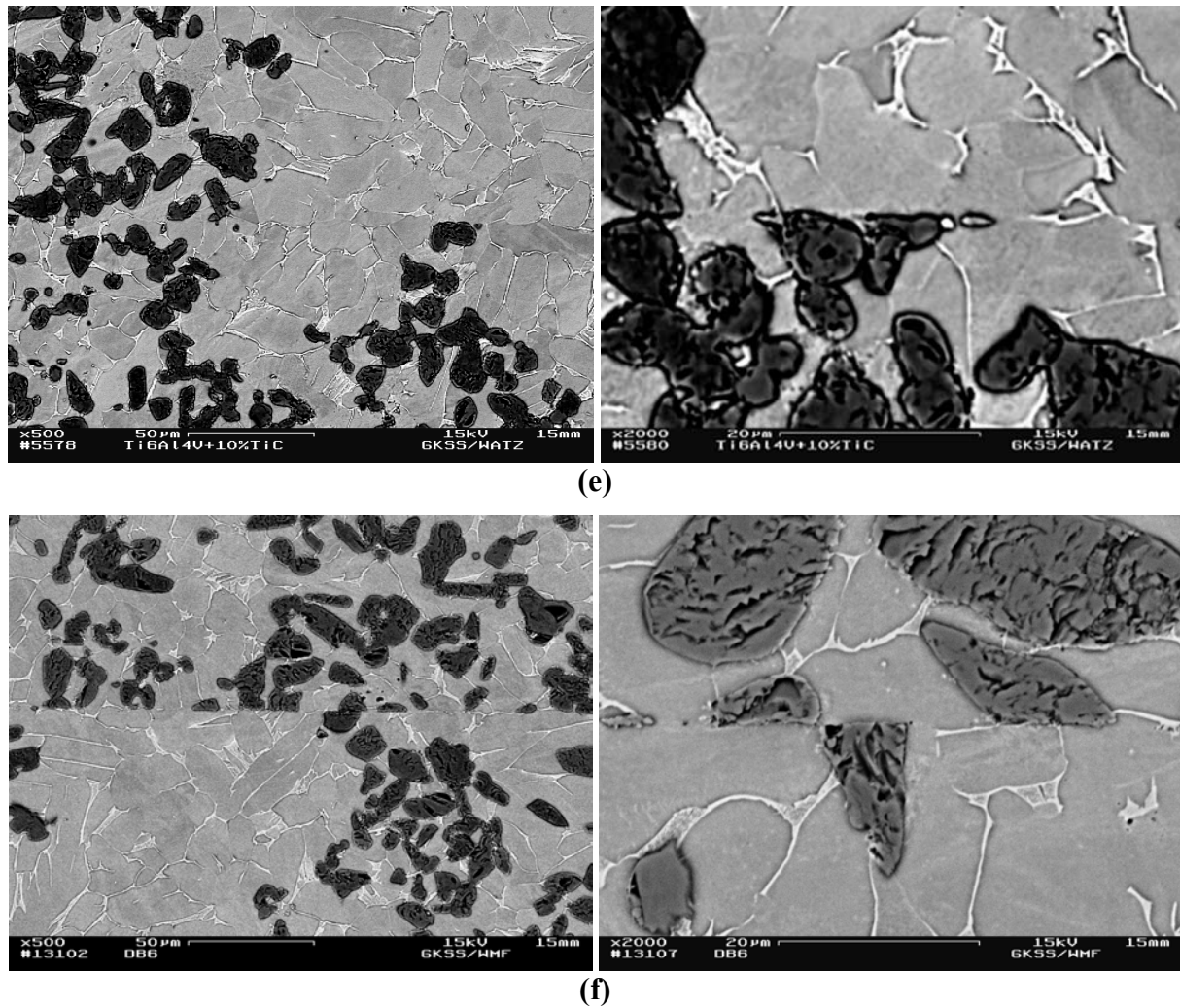


**Figure 4.54 – SEM micrographs showing the bonded conditions. (a) DB1 (875°C/5MPa/60min). (b) DB2 (900°C/5MPa/35min). (c) DB3 (900°C/6MPa/35min). (d) DB4 (900°C/7MPa/60min). (e) DB5 (1000°C/5MPa/35min). (f) DB6 (1000°C/5MPa/60min).**

An important feature of composite diffusion bonding is that since the initial steps of bonding include plastic deformation on loading and that the ceramic particle has much higher stiffness than the matrix alloy at the bonding temperature, the combination of these factors can prevent plastic and creep deformation at the bond interface which may cause insufficient bonding in joining the composite (particle/particle contact). Such behaviour has not been found while joining particle reinforced Ti6Al4V/TiC, Fig. 4.55, and bonding was complete in the TiC particles and most of the remaining voids are present in the matrix alloy.



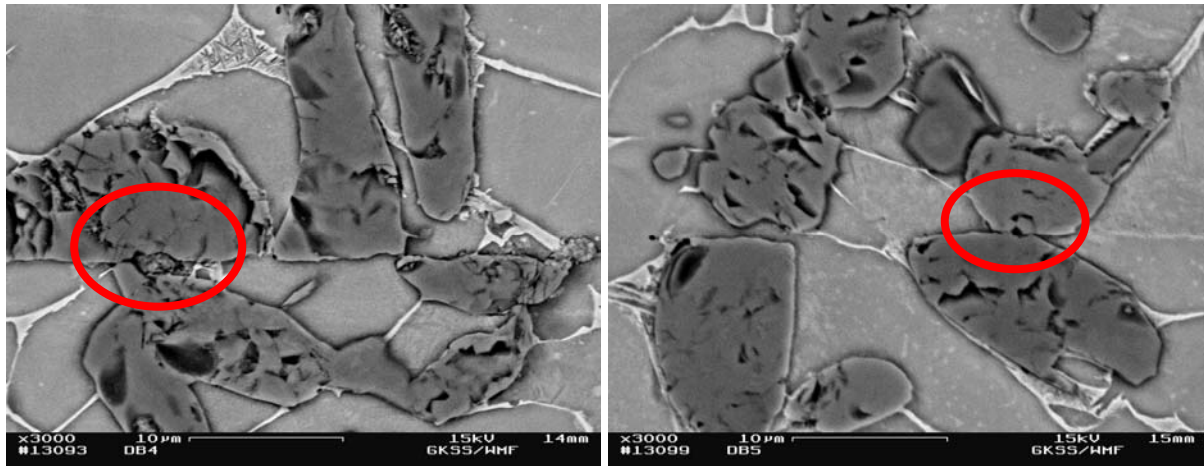


**Figure 4.55 – Particle/particle contact at the joint. Condition DB5 (1000°C/5MPa/35 min).**

As can be observed from Fig. 4.54, under all the bonding conditions investigated, no drastic microstructural changes have occurred indicating that even using high temperatures (1000°C) the  $\beta$ -transus temperature of the base material composite has not been reached. The composite microstructure remained the same, platelike  $\alpha$  (as well as equiaxed  $\alpha$  in some regions) and intergranular  $\beta$  with TiC randomly distributed, without grain growth or dynamic recrystallisation (typical features of other titanium alloys [11,153-159]), and the only modification that was clearly visible was the presence of remaining voids at the mating surfaces resulted from inefficient bonding parameters.

### 4.3.3 Metallurgical Characterisation of the Diffusion Bonded Joints

#### 4.3.3.1 Microhardness

Microhardness profiles were performed across the diffusion bonded joints using the same procedure as for the friction welds. The same difficulties found in the friction welds has also been found here concerning the presence of the TiC particles; therefore, five indentation lines have been made and the average values for each point were the final hardness values. Figure 4.56 shows the hardness profiles performed across the bonded joints for three selected conditions (DB4, DB5 and DB6). It can be clearly observed that there was no drastic variation on the microhardness profile since no microstructural transformation induced by the diffusion bonding process has occurred; however the hardness values presented by the base material are slightly higher than the ones presented by the bonded joints indicating that it could have occurred some softening or relaxation process due to subtle changes in the microstructure induced by the bonding temperatures. The base material hardness values were the ones expected for the microstructure found – platelike  $\alpha$  (equiaxed  $\alpha$  in some regions) and intergranular  $\beta$  [61].

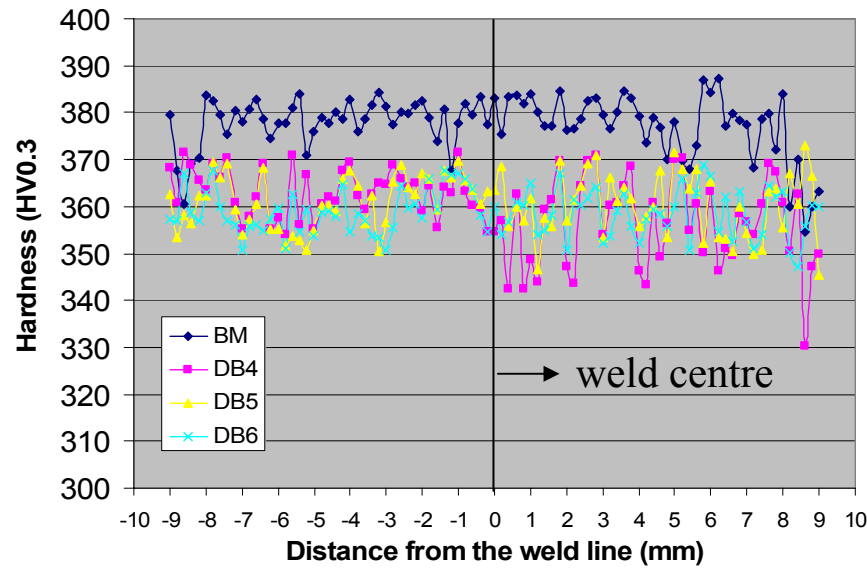


Figure 4.56 – Microhardness profiles of the diffusion bonding conditions (DB4, DB5 and DB6).

#### 4.3.3.2 Microflat Tensile Tests

Microflat tensile tests have been accomplished for five specimens from each condition – diffusion bonded joints (DB4, DB5 and DB6) and base material. The other conditions have not been tested since the bonding parameters were insufficient or inadequate to achieve bonding along the mating surfaces and bonding was not complete (gap between the mating surfaces, see Figs. 4.54a to 4.54c). Table 4.26 presents the  $R_m$  and STD for the base material and bonded joints as well as the joint efficiency based on the  $R_m$ . Here it is possible to see that diffusion bonding of Ti6Al4V+10 wt.% TiC has produced welds retaining almost the same strength of the base material and even the worst condition has displayed almost 76% of the original properties. Figure 4.57 presents the typical tensile behaviour displayed by the microflat tensile specimens of the base material and bonded joints. All specimens have fractured without yielding since the TiC particles have drastically reduced the ductility due to the elastic restraint imposed on the matrix by the particulate and the subsequent stress concentration around the particulate (constraint imposed on the plastic flow by the particles) due to their elastic modulus difference. The presence of clustering in some areas of the composite has also contributed for such behaviour. Another important feature is the presence of microcracks at the non-polished lateral surfaces which could have also contributed to the low tensile behaviour (no yielding and elongation). A large scatter in the  $R_m$  (see Fig. 4.58) has been observed under all conditions studied mainly due to the microstructural inhomogeneity (non-uniform TiC particles distribution and remaining voids). As expected one can observe that the specimens extracted from DB5 and DB6 displayed the best results since no drastic microstructural change has occurred at the bonding line and almost no voids

were present at the mating surfaces (Figs. 4.54e and f). Condition DB4 had the worst results since there were some remaining voids at the bonding line and the presence of such discontinuities interfered negatively in the tensile behaviour propitiating a preferable crack path leading to a poor tensile strength behaviour (Fig. 4.54d).

**Table 4.26 – Microflat tensile results of the base material and bonded conditions as well as the joint efficiency based on  $R_m$ .**

Condition	$R_m$ (MPa)	Joint Efficiency based on $R_m$ (%)
BM	$846 \pm 65$	*
DB4	$646 \pm 34$	76.4
DB5	$840 \pm 38$	99.3
DB6	$797 \pm 51$	94.2

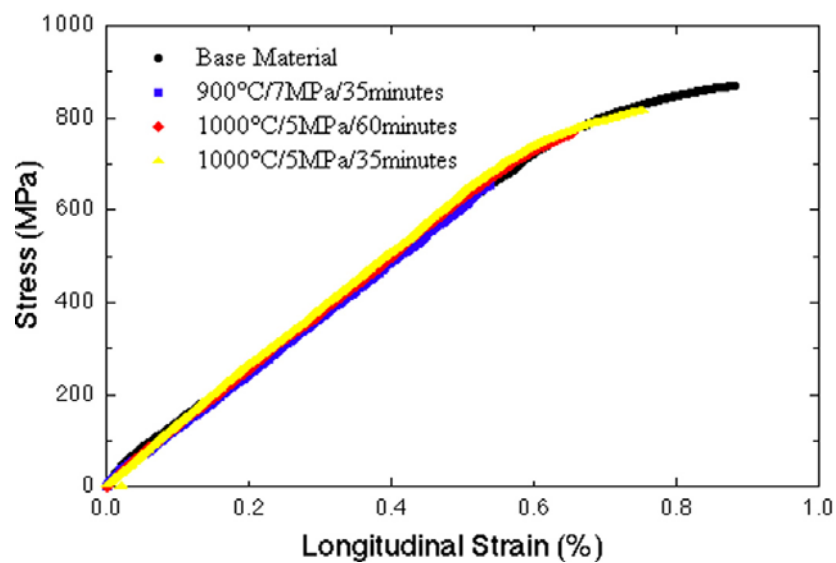


**Figure 4.57 – Tensile strength behavior of the diffusion bonding and base material conditions.**

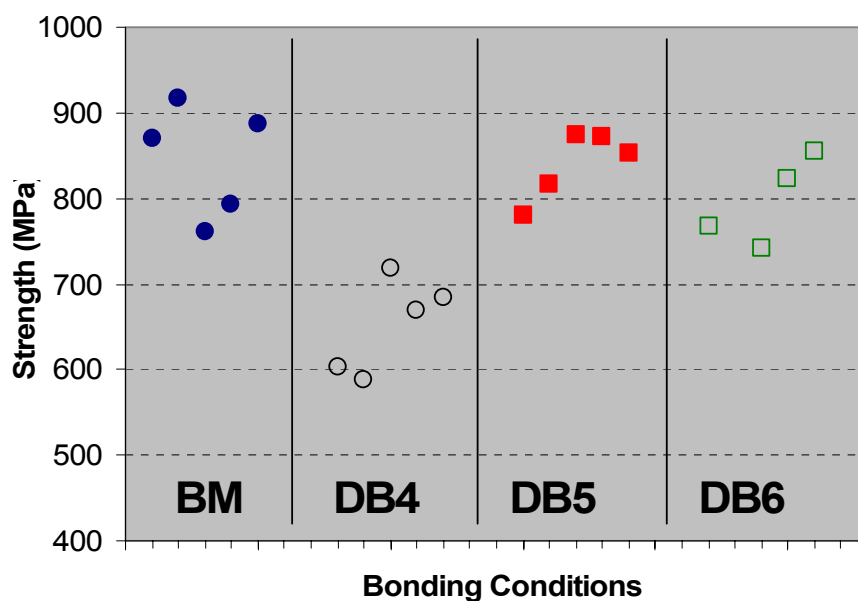


**Figure 4.58 – Tensile strength values of all diffusion bonding and base material specimens.**

According to Çam et al [187] the tensile strength of the microflat specimens compared to the tensile strength determined by testing standard specimens is different; the former having a lower value. Such behaviour has been found in all tested conditions since the  $R_m$  of the base material was 967 MPa (standard tensile test) and the micro flat base material  $R_m$  was 846 MPa, see Fig. 4.59. Such difference of 121 MPa might be a result of non-polished surfaces of the micro tensile specimens since surface microcracks can be present after machining by spark erosion reducing considerably the tensile properties. It is well known that the presence of damaged areas (apart from particle clustering and large particles) prior testing in composites materials is very detrimental to the tensile behaviour; therefore the presence of these microcracks (found in all conditions after metallographic preparation of the lateral surfaces) considerably reduces the  $R_m$  of the bonded conditions. Hence, it is not possible to compare standard base material  $R_m$  values with the ones found in this investigation for the base material and bonded conditions. Furthermore, since this is a non-standardised test the  $R_m$  values for the base material and bonded conditions are only comparable among each other and can not be considered absolute  $R_m$  values.

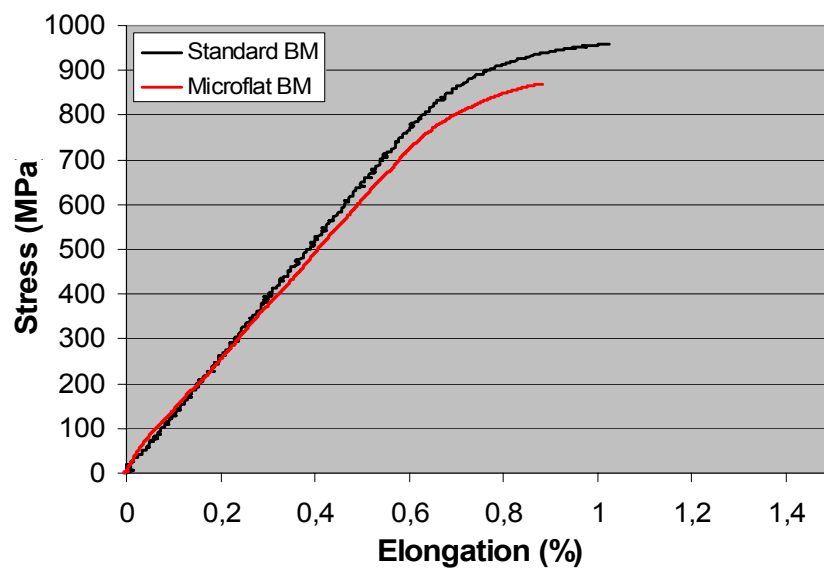


**Figure 4.59 – Comparison between standard tensile testing and microflat tensile testing.**

The fracture mechanism of the base material as well DB5 and DB6 is the same one as that of the friction welded joints (nucleation at the TiC particles, growth, followed by failure in the matrix by void coalescence) since no microstructural change has occurred during the bonding process, see Figs. 4.60 and 4.61. The primary features of the fracture surfaces were the same as those found in the tensile tests (particle fracture– PF in Fig. 4.61 and ductile fracture – DF in Fig. 4.61). It is also possible to observe the presence of secondary cracking (SC in Fig. 4.61) in the particles confirming internal damage accumulation at the particle.

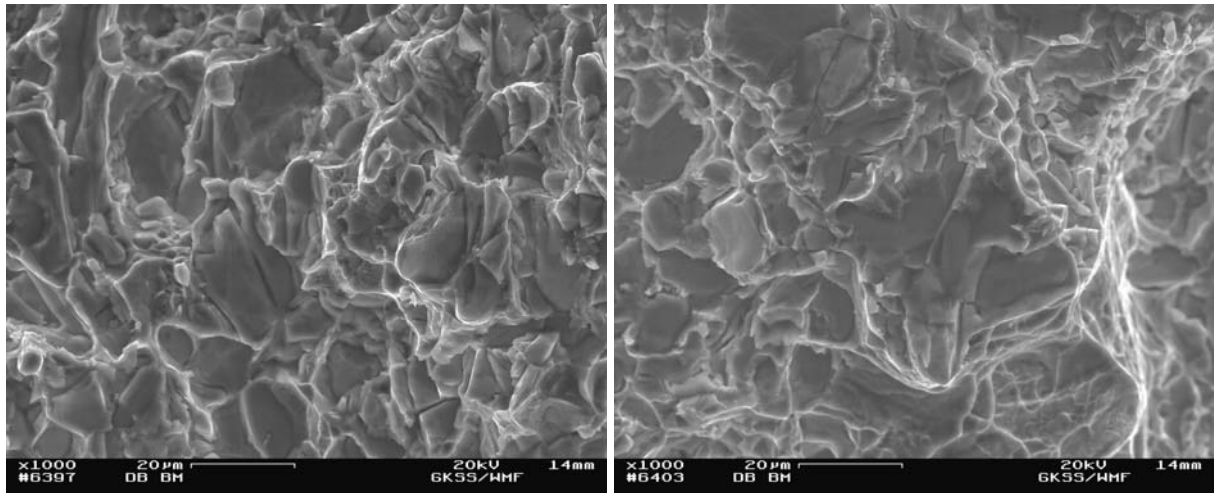
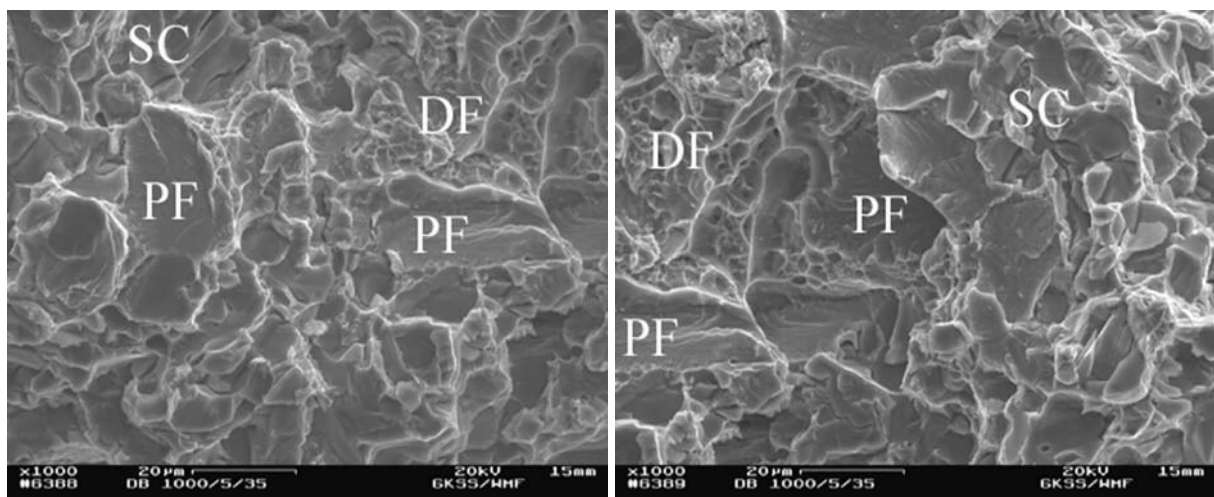
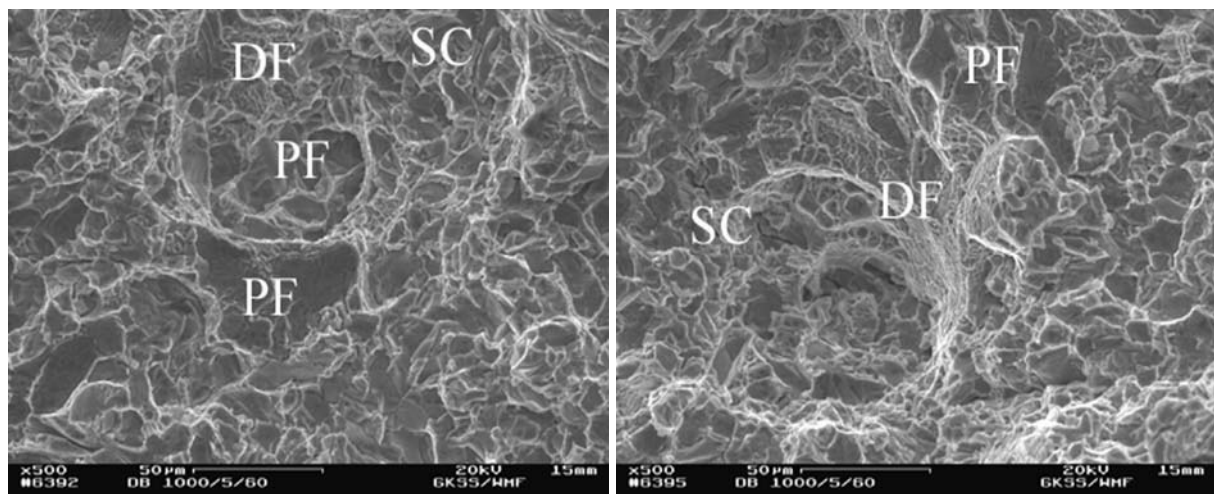


Figure 4.60 – SEM micrographs taken from the fracture surface of the base material specimens.



(a)



(b)

Figure 4.61 – SEM micrographs from the microflat tensile fracture surfaces of the bonded joints. (a) DB5 (1000°C/5MPa/35min). (b) DB6 (1000°C/5MPa/60min). PF: Particle fracture. SC: Secondary cracking. DF: Ductile fracture.

Condition DB4 has presented a different fracture behaviour since remaining voids were already present in the specimen (along the whole bonding interface) due to inefficient diffusion bonding parameters. Such irregularities have represented a preferable crack path because prior to the tensile loading these internal defects were already present thereby contributing for the reduction of the tensile strength and helping the acceleration of the damage process. It can be seen from Figure 4.62 that flat and some rough regions are present at the fracture surface of the microflat tensile specimens. The rough regions correspond to the fracture in the composite (particle fracture – PF in Fig. 4.62); whereas, the flat regions (FS in Fig. 4.62), which predominate in the fracture surface, correspond to the fracture along the bond line (the remaining voids represent a preferable crack path). Ductile fracture (coalescence of microvoids) has only been observed in a few areas especially where the spacing between the voids and the interparticle spacing was large. Secondary cracking (SC in Fig. 4.62) has also been observed confirming the brittle nature of the composite.

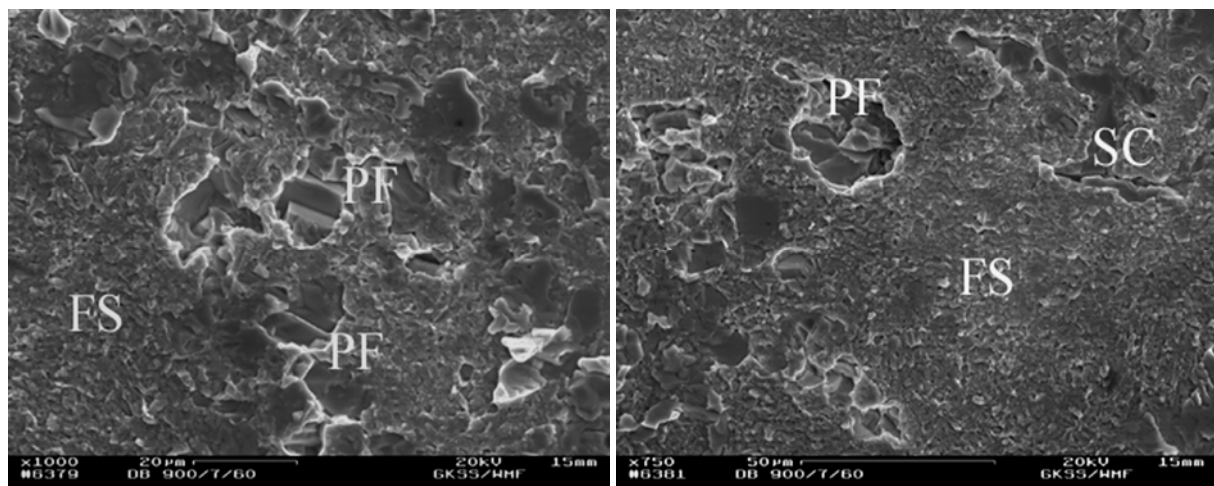


**Figure 4.62 – SEM micrographs from the microflat tensile fracture surfaces of condition DB4 (900°C/7MPa/60min.). PF: Particle fracture. SC: Secondary cracking. FS: Flat surface (fracture along the bonding line).**

## 5 CONCLUSIONS

The friction welding aspects of the Ti-6Al-4V+10 wt.% TiC alloy as well as the metallurgical and mechanical properties of the base material and friction welded joints were investigated. The following conclusions can be presented:

1. Friction welding has been successfully applied to the composite Ti6Al4V + 10 wt.% TiC.
2. Ti-6Al-4V+10 wt.% TiC friction welding microstructure consists of 2 zones: transformed and recrystallized zone (TRZ), with acicular  $\alpha$  and redistributed TiC particles and the heat affected zone (HAZ) which contains  $\alpha$ -Widmanstätten (close to the base material region) and acicular  $\alpha$  (close to the TRZ region) and TiC particles. The microstructure of the base material zone consists of platelike  $\alpha$  (equiaxed  $\alpha$  in regions close to the TiC particles) and intergranular  $\beta$  plus TiC particles.
3. The joint tensile strength was optimized utilizing both low rotational speed and pressure.
4. There is a wide operating window for production of satisfactory joints concerning the mechanical properties (tensile and fracture toughness properties) of friction-welded Ti6Al4V + 10 wt.% TiC joints.
5. Wider and thinner transformed regions (TRZ and HAZ) have been found when using high rotational speeds and high pressure, respectively.
6. The micromechanisms of fracture of the base material and friction welded joints are the same, i.e., nucleation of voids at the TiC particles, growth of these voids followed by ductile failure of the matrix by coalescence of microvoids. The fracture toughness specimens present a second micromechanism of fracture represented by extensive microcracking at and near the crack tip actuating together with those described above.
7. The particle size and distribution strongly affects the mechanical behaviour of both base material and friction welded joints due to increased stress levels in the matrix between the particles and high triaxiality in the matrix between the particles.
8. It was not possible to determine the fracture toughness behaviour according to the Hahn and Rosenfield model due to the inhomogeneity distribution and size of the particles as well as an elastic behaviour of the studied composite (both base material and friction welded joints).

The following conclusions can be drawn from the metallurgical and mechanical investigations conducted on the diffusion bonding of Ti-6Al-4V+10 wt.% TiC:

1. No microstructural change or transformation has been found due to the diffusion bonding process. The 'post-weld' microstructure remained the same as before welding: platelike  $\alpha$  (equiaxed  $\alpha$  in regions close to the TiC particles) and intergranular  $\beta$  with TiC particles randomly distributed in the matrix.
2. Defect-free bonds can be achieved using bonding conditions of 1000°C, 5MPa in both bonding times of 35 and 60 minutes.
3. Temperature is a key parameter concerning the diffusion bonding process, since an increase in its values have increased the weld quality avoiding the formation of unbonded areas as well as remaining voids.
4. The best tensile strength properties were displayed by joints made at 1000°C, 5 MPa and 35 minutes.
5. The composite failure is controlled by fracture of the reinforcement which is followed by ductile fracture of the matrix. The presence of remaining voids in the diffusion bonding line interferes negatively in this fracture mechanism since it represents a preferable crack path.



## 6 SUGGESTIONS FOR FUTURE WORK

The suggestions for further investigation are concentrated in a detailed metallurgical characterization of the friction welded joints and the determination of the thermal properties of the friction welding process as well as the possibilities of industrial application of both processes and base material including dissimilar configuration.

Further investigation of two important features found in TRZ (grain boundary phase and small TiC particles) using Transmission Electron Microscope (TEM) is necessary in order to understand the complex metallurgical transformations taking place after the friction welding process. On one hand such information is necessary in order to investigate the real influence of such features in the mechanical behaviour (whether there is such influence) as well as the influence of the friction welding parameters over the presence of these features. On the other hand it is important to understand the kind of interaction between the matrix and the particulate; if it is a mechanical interaction that can be controlled by the welding parameters or a metallurgical interaction that can be controlled by the thermal and diffusion properties of the composite.

The thermal history of the friction welding process should also be investigated; however care must be taken in choosing the measuring system since problems have been found in this work while investigating the thermal phenomena with thermocouples. Due to practical difficulties imposed by extensive material displacement therein as well as friction surfaces non-uniform heating it is very difficult to predict temperature and temperature variations for friction surfaces and HAZ.

For a wider industrial application of both welding processes additional information on the possibilities of dissimilar welding combination would be needed. Initial tests have been conducted in GKSS Forschungszentrum with good results using Ti6Al4V+10 wt,% TiC and Ti6Al4V. Such combination could be very useful in the aeronautic industry especially in applications where creep and corrosion properties are necessary, e.g., blades and vanes.

## 7 REFERENCES

- [1] M.J. Donachie Jr., "Introduction to Titanium and Titanium Alloys", *Titanium and Titanium Alloys* (Ed. M. J. Donachie Jr., ASM, Materials Park, Ohio 1982), pp. 3-9.
- [2] E.W. Collings, "Physical Metallurgy of Titanium Alloys", *Materials Properties Handbook: Titanium Alloys* (Ed. R.R. Boyer, G. Welsch, E.W. Collings, ASM, Materials Park, Ohio 1994), pp. 3-122.
- [3] J.D. Destefani, "Introduction to Titanium and Titanium Alloys", *Properties and Selection: Nonferrous Alloys and Special-Purpose Materials ASM Metals Handbook vol. 2*, (ASM, Materials Park, Ohio 1995), pp. 586-591.
- [4] C.S. Shira, F.H. Froes, "Advanced Material in Golf Clubs: The Titanium Phenomenon", *The Journal of The Minerals, Metals and Materials Society* **49**(5) (1997) 35-37.
- [5] S.M. Abkowitz, P.F. Weinrauch, H.L. Heussi, S. Abkowitz, "P/M Titanium Matrix Composites: From War Games to Fun Games" in: *Titanium '95 Science and Technology* (TMS, Warrendale, PA, 1995), pp. 2722-2730.
- [6] *Materials Properties Handbook: Titanium Alloys* (Ed. R.R. Boyer, G. Welsch, E.W. Collings, ASM, Materials Park, Ohio 1994), pp. 483-636.
- [7] S.R. Seagle, L.J. Bartlo, "Physical Metallurgy and Metallography of Titanium Alloys", *Titanium and Titanium Alloys* (Ed. M. J. Donachie Jr., ASM, Materials Park, Ohio 1982), pp. 23-32.
- [8] L.S. Smith, M.F. Gittos, "High Productivity Pipe Welding of Ti-6Al-4V Alloys", TWI Research Report 660/1998 (1998).
- [9] S.J. Chen, J.H. Devletian, "Microstructure and Mechanical Properties of Electroslag Welds in Ti-6Al-4V Alloy", *Welding Journal*, **69**(9) (1990) 319s-325s.
- [10] W.A. Baeslack III, J.R. Davis, C.E. Cross, "Selection and Weldability of Conventional Titanium Alloys", *Welding, Brazing and Soldering ASM Handbook Vol. 6*, (ASM, Materials Park, Ohio 1995), pp. 507-523.
- [11] G. Çam, M. Koçak, "Progress in Joining of Advanced Materials", GKSS Report: GKSS 98/E/55, (1998).
- [12] K.K. Chawla, "Metal Matrix Composites", *Materials Science and Technology - A Comprehensive Treatment - Structure and Properties of Composites Volume 13*, (Ed. R.W. Cahn, P. Haasen, E.J. Kramer, VCH Publishers Inc., New York, NY, 1993) p. 121-182.
- [13] S. Mall, T. Fecke, M.A. Foringer, "Introduction", *Titanium Matrix Composites: Mechanical Behaviour*, (Ed. S. Mall, T. Nicholas, Technomic Publishing Company Inc.,

Lancaster, PA, 1998) p. 1-22.

[14] S.M. Abkowitz, P.F. Weinrauch, H.L. Heussi, S. Abkowitz, "The Commercial Application of Low-Cost Titanium Composites", *The Journal of The Minerals, Metals and Materials Society*, **47**(8) (1995) 40-41.

[15] C.M. Ward-Close, C. Loader, "PVD Processing of Fibre Reinforced Composites", *Recent Advances in Titanium Metal Matrix Composites*, (Ed. F.H. Froes, J. Storer, The Minerals, Metals and Materials Society, Warrendale, PA: 1995), 19-32.

[16] S. Lampman, "Wrought Titanium and Titanium Alloys", *Properties and Selection: Nonferrous Alloys and Special-Purpose Materials ASM Metals Handbook vol. 2*, (ASM, Materials Park, Ohio 1995), pp. 592-633.

[17] R.N. Caron, J.T. Staley, "Effects of Composition, Processing and Properties of Nonferrous Alloys", *Materials Selection and Design ASM Metals Handbook vol. 20*, (ASM, Materials Park, Ohio 1997), pp. 382-404.

[18] J.K. Gregory, *Handbook of Fatigue Crack Propagation in Metallic Structures*, (Elsevier Science B.V., Amsterdam 1994) 281-322.

[19] H. Baker, "Introduction to Alloy Phase Diagrams", *Alloy Phases Diagrams ASM Metals Handbook vol. 3*, (ASM, Materials Park, Ohio 1997), pp. 1.1 - 1.30.

[20] R. Gilbert, C.R. Shannon, "Heat Treating of Titanium and Titanium Alloys", *Heat Treating ASM Metals Handbook vol. 4*, (ASM, Materials Park, Ohio 1995), pp. 913-923.

[21] R.R. Boyer, "Titanium and Titanium Alloys", *Metallography and Microstructures ASM Metals Handbook vol. 9*, (ASM, Materials Park, Ohio 1995), pp. 458-475.

[22] F. Torster, J.F. dos Santos, G. Hutt, M. Koçak, "The Use of Titanium Alloys for Dynamic Risers: A Literature Review", GKSS Report: GKSS 97/E/38 (1997).

[23] C.R. Brooks, *Heat Treatment, Structure and Properties of Nonferrous Alloys*, (ASM, Materials Park, Ohio 1982) 329-387.

[24] L. Wagner, J.K. Gregory, "Thermomechanical Surface Treatment of Titanium Alloys" in: 2<sup>nd</sup> ASM Heat Treatment and Surface Engineering Conference in Europe, Dortmund 1993, (ASM, Materials Park, Ohio 1993).

[25] *Fatigue and Fracture ASM Metals Handbook vol. 19*, (ASM, Materials Park, Ohio 1996), pp. 829-853.

[26] "Alpha-Beta Alloys", *Materials Properties Handbook: Titanium Alloys* (Ed. R.R. Boyer, G. Welsch, E.W. Collings, ASM, Materials Park, Ohio 1994), pp. 451-763.

[27] J.C. Williams, J.C. Chesnutt and A.W. Thompson, "The Effects of Microstructure on Ductility and Fracture Toughness of  $\alpha+\beta$  Titanium Alloys" in: Proceedings of the 1987 TMS-

- AIME Annual Symposia on "Effect of Microstructure on Fracture Toughness and Fatigue Crack Growth rate in Titanium Alloys", Denver, USA, 1987, pp.255-271.
- [28] G. Lütjering, A. Gysler and L. Wagner, "Crack Propagation in Ti-Alloys" in: 'Sixth World Conference on Titanium', Cannes, France, 1988, pp. 71-80.
- [29] R.R. Boyer, R. Bajoratis, W.F. Spurr, "The Effects of Thermal Processing Variations on the Properties of Ti-6Al-4V" in: Proceedings of the 1987 TMS-AIME Annual Symposia on "Effect of Microstructure on Fracture Toughness and Fatigue Crack Growth rate in Titanium Alloys", Denver, USA, 1987, pp. 149-157.
- [30] K. K. Murthy, S. Sundaresan, "Fracture Toughness of Ti-6Al-4V after Welding and Postweld Heat Treatment", *Welding Journal*, **76**(2) (1997) 81s-91s
- [31] D.B. Miracle, S.L. Donaldson, "Introduction to Composites", *Composites ASM Handbook Vol. 21*, (ASM, Materials Park, Ohio 1995), p. 3-17.
- [32] G.S. Cole, A.M. Sherman, "Lightweight Materials for Automotive Applications", *Materials Characterization*, **35** (1995) 3-9.
- [33] H. Persson, "Guidelines for Joining of Metal Matrix Composites" MMC-Assess Thematic Network, Volume 8, 2002, pp. 3/12.
- [34] W.H. Hunt Jr., D.B. Miracle, "Automotive Applications of Metal Matrix Composites", *Composites ASM Handbook Vol. 21*, (ASM, Materials Park, Ohio 1995), p. 1029-1032.
- [35] K.M. Mussert, "A Fracture Mechanical Study of Precipitation Hardenable Aluminum-Based Metal Matrix Composites", PhD Thesis, Delft, 2000 (Delft University Press, Delft, The Netherlands 2000).
- [36] *Composite Materials Handbook - Volume 4 - Metal Matrix Composites* Department of Defense Handbook MIL-HDBK-17-4 (1999).
- [37] R.R. Kieschke, H.E. Deve, C. McCollough, C.J. Griffin, "Processing of Tow-Based Titanium Composites", *Recent Advances in Titanium Metal Matrix Composites*, (Ed. F.H. Froes, J. Storer, The Minerals, Metals and Materials Society, Warrendale, PA: 1995), 19-32.
- [38] T.M.T. Godfrey, A. Wisbey, P.S. Goodwin, K. Bagnall, C.M. Ward-Close, "Microstructure and Tensile Properties of Mechanically Alloyed Ti-6Al-4V with Boron Additions", *Materials Science and Engineering A*, **A282** (2000) 240-250.
- [39] "Innovative Engineered Materials - Creative Manufacturing Technology", Dynamet Technology Inc. Technical Catalogue.
- [40] S. Abkowitz, P. Weihrauch, "Trimming the Cost of MMCs", *Advanced Materials and Processes*, **136**(7) (1989) pp. 31-34.

- [41] S.J. Zhu, D. Mukherji, W. Chen, Y.X. Lu, Z.G. Wang, R.P. Wahi, "Steady State Creep Behaviour of TiC Particulate Reinforced Ti-6Al-4V Composite", *Materials Science & Engineering A* **A256** (1998) 301-307.
- [42] D.G. Konitzer, M.H. Loretto, "Interfacial Interactions in Titanium-Based Metal Matrix Composites", *Materials Science & Engineering A* **A107** (1989) 217-223.
- [43] G. Liu, D. Zhu, J.-K. Shang, "Temperature Dependence of Fracture Toughness in TiC-Particulate Reinforced Ti-6Al-4V Matrix Composite", *Scripta Metallurgica et Materialia* **28** (1993) 729-732.
- [44] J.-K. Shang, R.O. Ritchie, "Monotonic and Cyclic Growth in a TiC-Particulate-Reinforced Ti-6Al-4V Metal-Matrix Composite", *Scripta Metallurgica et Materialia* **24** (1990) 1691-1694.
- [45] S.J. Zhu, Y.X. Lu, Z.G. Wang, J. Bi, "Cyclic Creep Behaviour of TiC (Particulate) Ti-6Al-4V Composite in the Temperature Range of  $0,4-0,5 T_m$ ", *Journal of Materials Science Letters*, **11** (1992) 630-632.
- [46] M.H. Loretto, D.G. Konitzer, "The Effect of Matrix Reinforcement Reaction on Fracture in Ti-6Al-4V-Base Composites", *Metallurgical and Materials Transactions A*, **21A** (1990) 1579-1587.
- [47] D.G. Konitzer, M.H. Loretto, "Microstructural Assessment of Ti6Al4V-TiC Metal-Matrix Composite", *Acta Metallurgica* **37**(2) (1989) 397-406.
- [48] G.Liu, D. Zhu, J.K. Shang, "Enhanced Fatigue Crack Growth Resistance at Elevated Temperature in TiC/Ti-6Al-4V Composite: Microcrack-Induced Crack Closure", *Metallurgical and Materials Transactions A* **26A** (1995) 159-166.
- [49] J.H. Zhu, P.K. Liaw, J.M. Corum, H.E. McCoy Jr, "High Temperature Mechanical behaviour of Ti-6Al-4V Alloy and TiC<sub>p</sub>/Ti-6Al-4V Composite", *Metallurgical and Materials Transactions A* **30A** (1999) 1569-1578.
- [50] D.E. Alman "Properties of Metal-Matrix Composites", *Composites ASM Handbook Vol. 21*, (ASM, Materials Park, Ohio 2001), p. 849.
- [51] A.J. Wagoner Johnson, K.S. Kumar, C.L. Briant, "Deformation Mechanisms in Ti-6Al-4V/TiC Composites", *Metallurgical and Materials Transactions A* **34A** (2003) 1869-1877.
- [52] M. Gu, W. Jiang, G. Zhang, "Quantitative Analysis of Interfacial Chemistry in TiC/Ti Composite Using Electron-Energy-Loss Spectroscopy", *Metallurgical and Materials Transactions A* **26A** (1995) 1595-1597.
- [53] *Alloy Phase Diagrams ASM Handbook Vol.3*, (ASM, Materials Park, Ohio 1995), p.

2.114.

[54] P.Wanjara, R.A.L. Drew, J. Root, S. Yue., "Evidence for Stable Stoichiometric Ti<sub>2</sub>C at the Interface in TiC Particulate Reinforced Ti Alloy Composites", *Acta Materialia* **48**(3) (2000) pp. 1443-1450.

[55] [www.oit.doe.gov/nice3/factsheets/dynamet2.pdf](http://www.oit.doe.gov/nice3/factsheets/dynamet2.pdf), "Increased Productivity and Reduced Energy Consumption in Metal Casting using Titanium Matrix Composite Tooling", 21.11.2002.

[56] [www.titanium.org/PDF/Newsletters/ausgustnews2003.pdf](http://www.titanium.org/PDF/Newsletters/ausgustnews2003.pdf), "Dynamet Receives DOE Grant and MPIF Grand Prize" in The Newsletter Dedicated to Titanium – Volume 2002, Issue VI, August.

[57] "Opportunities for Low Cost Titanium in Reduced Fuel Consumption, Improved Emissions and Enhanced Durability Heavy-Duty Vehicles", Technical Report performed for US Department of Energy and Oak Ridge National Laboratory available at [www.ms.ornl.gov/programms/energyeff/HVPM/Kraft-Titanium.pdf](http://www.ms.ornl.gov/programms/energyeff/HVPM/Kraft-Titanium.pdf) July 2002, pp.1-47.

[58] J.C. Thesken, B.A. Lerch, S.M. Arnold, "Particulate Titanium Matrix Composites Tested Show Promise for Space Propulsion Applications", Technical Report performed by NASA available at [www.grc.nasa.gov/WWW/RT2002/5000/5920thesken2.html](http://www.grc.nasa.gov/WWW/RT2002/5000/5920thesken2.html)

[59] W.S. Miller, F.J. Humphreys, "Strengthening Mechanisms in Particulate Metal Matrix Composites", *Scripta Metallurgica et Materialia*, **25** (1991) pp. 33-38.

[60] T.P. Johnson, J.W. Brooks, M.H. Loretto, "Mechanical Properties of a Ti-Based Metal Matrix Composite Produced by a Casting Route", *Scripta Metallurgica et Materialia*, **25** (1991) pp. 785-789.

[61] *Materials Properties Handbook: Titanium Alloys* (Ed. R.R. Boyer, G. Welsch, E.W. Collings, ASM, Materials Park, Ohio 1994), pp. 493.

[62] C.A. Smith, "Discontinuous Reinforcements for Metal-Matrix Composites", *Composites ASM Handbook Vol. 21*, (ASM, Materials Park, Ohio 1995), pp. 51-55.

[63] *Materials Properties Handbook: Titanium Alloys* (Ed. R.R. Boyer, G. Welsch, E.W. Collings, ASM, Materials Park, Ohio 1994), pp. 516.

[64] T.J.A. Doel, P. Bowen, "Tensile Properties of Particulate-Reinforced Metal Matrix Composites", *Composites Part A*, **27A** (1996) pp. 655-665.

[65] D. Zhao, F.R. Tuler and D.J. Lloyd, "Fracture at Elevated Temperatures in a Particle Reinforced Composite", *Acta Metall. Mater.*, **42**(7) (1994) pp. 2525-2533.

[66] T.L. Anderesen, *Fracture Mechanics*, (Elsevier Press), pp.265-305.

[67] D.J. Lloyd, "Aspects of Fracture in Particulate Reinforced Metal Matrix Composites",

*Acta Metallurgica et Materialia*, 1991, **39**(1), pp. 59-71.

[68] C.P. You, A.W. Thompson, I.M. Bernstein, "Proposed Failure Mechanism in a Discontinuously Reinforced Aluminum Alloy", *Scripta Metallurgica*, 1987, **21**, pp. 181-185.

[69] T. W. Clyne, P. J. Withers, *An Introduction to Metal Matrix Composites*, (Cambridge University Press, Cambridge, Great Britain, 1993) pp. 219-276.

[70] J.D. Evansen, A.S. Verk, "The Influence of Particle Cracking on the Fracture Strain of some Al-Si Alloys", *Scripta Metallurgica*, 1981, **15**, pp. 1131-1133.

[71] L.M. Brown, J.D. Embury, "The Initiation and Growth of Voids at Second Phase Particles", in: Proceedings of the ICSMA III, Cambridge, UK, 1973, pp.164-168.

[72] P.F. Thomason, "A Theory for Ductile Fracture by Internal Necking of Cavities", *Journal of the Institute of Metals*, 1968, **96**, pp. 360-364.

[73] A.F. Whitehouse and T.W. Clyne, "Cavity Formation during Tensile Straining of Particulate and Short Fibre MMCs", *Acta Metallurgica et Materialia*, 1993, **41**, pp. 1701-1711.

[74] B.S. Mujamdar, A.B. Pandey, "Deformation and Fracture of a Particle-Reinforced Aluminum Alloy Composite: Part II. Modeling", *Metallurgical and Materials Transactions A* **31A** (2000) 937-950.

[75] P. Mummery, B. Derby, "The Influence of Microstructure on the Fracture Behaviour of Particulate Metal Matrix Composites", *Materials Science and Engineering A*, 1991, **A135**, pp. 221-224.

[76] M.J. Hadianfard, J. Healy, Y.-W. May, "Fracture Characteristics of a Particulate-Reinforced Metal Matrix Composite", *Journal of Materials Science*, 1994, **29**, pp. 2321-2327.

[77] M. Manoharan, J.J. Lewandowski, "In Situ Deformation Studies of an Aluminium Metal-Matrix Composite in a Scanning Electron Microscope", *Scripta Metall.*, 1989, **23**(10), pp. 1801-1804.

[78] Y. Flom, R.J. Arsenault, "Effect of Particle Size on Fracture Toughness of SiC/Al Composite Material", *Acta Metallurgica*, 1989, **37**, pp. 2413-2423.

[79] M. Manahoran, J.J. Lewandowski, "Effects of Aging Condition on the Fracture Toughness of 2XXX and 7XXX Series Aluminum Alloy Composites", *Scripta Metallurgica*, **23** (1989) pp. 301-304.

[80] J.J. Lewandowski, C. Liu, W.H. Hunt Jr, "Effects of Matrix Microstructure and Particle Distribution on Fracture of an Aluminum Metal Matrix Composite", *Materials Science and Engineering A*, 1989, **A107**, pp. 241-255.

[81] R. Dixon "Introduction to Solid-State Welding", *Welding, Brazing and Soldering ASM*

- Handbook Vol. 6*, (ASM, Materials Park, Ohio 1995), pp. 141-142.
- [82] G.E. Linnert, *Welding Metallurgy Carbon and Alloy Steels Vol. 1 Fundamentals*, (AWS, Miami, Florida, 1994) pp. 1-940.
- [83] J.W. Elmer, D.D. Kautz, "Fundamentals of Friction Welding", *Welding, Brazing and Soldering ASM Handbook Vol. 6*, (ASM, Materials Park, Ohio 1995), pp. 150-155.
- [84] S. Tsang, "Friction Welding", *Welding, Brazing and Soldering ASM Handbook Vol. 6*, (ASM, Materials Park, Ohio 1995), pp. 315-317.
- [85] ANSI/AWS C6.1-89 American National Standard, "Recommended Practices for Friction Welding", (AWS, Miami, Florida 1989) pp. 1-27.
- [86] V. I. Vill, *Friction Welding of Metals*, (AWS, New York, New Jersey, 1962) pp. 1-114.
- [87] American Welding Society (AWS), *Welding Handbook Vol. 2*, (AWS, Miami, Florida 1989), pp. 740-763.
- [88] R. W. Messler, *Principles of Welding - Processes, Physics, Chemistry and Metallurgy*, (John Wiley and Sons Inc., New York, New Jersey, 1999), pp. 1-662.
- [89] B. Crossland, "Friction Welding", *Contemporary Physics*, **12**(6) (1971) 559-574.
- [90] D. Pauly, G.R. Blakemore, J.F. dos Santos, D. Gibson, "A Preliminary Study on the Application of Friction Welding in Structural Repairs", GKSS Report: GKSS 98/E/15, (1998), pp. 9-36.
- [91] G. Pinheiro, A. Meyer and J.F. dos Santos, "A Literature Review on Friction Welding", GKSS Internal Report (Materials Research - Joining Technology) (2000), pp. 1-47.
- [92] C. R. G. Ellis, "Continuous Drive Friction Welding of Mild Steel", *Welding Journal*, **51**(4) (1972) 183s-197s.
- [93] T. Stotler, "Procedure, Development and Practice Considerations for Inertia and Direct-Drive Friction Welding", *Welding, Brazing and Soldering ASM Handbook Vol. 6*, (ASM, Materials Park, Ohio 1995), pp. 888-892.
- [94] D. E. Spindler, "What Industry Needs to Know about Friction Welding", *Welding Journal*, **73**(3) (1994) 37-42.
- [95] C. Maldonado, T.H. North "Particle Fracture in Metal-Matrix Composite Friction Joints", *Journal of Materials Science*, **32** (1997) 4739-4748
- [96] G.J. Bendzsak, T.H. North, Z. Li, "Numerical Model for Steady-State Flow in Friction Welding", *Acta Materialia* **45**(4) (1997) 1735-1745.
- [97] O.T. Midling, O. Grong, " A Process Model for Friction Welding of Al-Mg-Si Alloys and Al-SiC Metal Matrix Composites- I. HAZ Temperature and Strain Rate Distribution",



*Acta Metallurgica et Materialia* **42(5)** (1994) 1595-1609.

- [98] T.H. North, G.J. Bendzsak, Z. Li, Y. Zhai, "Particle Fracture, Retention and Fluid Flow in Metal Matrix Composite Friction Joints", *Metallurgical and Materials Transactions A* **28A(11)** (1997) 2371-2384.
- [99] F.D. Duffin, A.S. Bahrani, "The Mechanics of Friction Welding Mild Steel", *Metal Construction*, **8(6)** (1976) 267-271.
- [100] A. Meyer, "Friction Hydro Pillar Processing - Bonding Mechanism and Properties", PhD Thesis, Geesthacht, 2002, to be published.
- [101] K.K. Wang, P. Nagappan, "Transition Temperature Distribution in Inertia Welding of Steels", *Welding Journal*, **49(9)** (1970) 419s-426s.
- [102] M. Futamata, A. Fuji, "Friction Welding of Titanium and SUS 304L Austenitic Stainless Steel", *Welding International*, **4(10)** (1990) 768-774.
- [103] C.G. Nessler, D.A. Rutz, R.D. Eng, P.A. Vozzela, "Friction Welding of Titanium Alloys", *Welding Journal*, **50(9)** (1971) 379s-385s.
- [104] Y. Zhou, Z. Li, L. Hu, A. Fuji, T.H. North, "Mechanical Properties of Particulate MMC/AISI 304 Friction Joints", *ISIJ International*, **35(10)** (1995) 1315-1321.
- [105] Y. Zhou, J. Zhang, T.H. North, Z. Wang, "The Mechanical Properties of Friction Welded Aluminum-Based-Metal-Matrix Composite Materials", *Journal of Materials Science*, **32(0)** (1997) pp. 3883-3889
- [106] T. Shinoda, K. Tanada, Y. Katoh, T. Shimizu, "Study of Thermal Phenomena During Friction Welding and the Mechanical Properties of an Aluminium Alloy", *Welding International*, **8(5)** (1994) pp. 349-353.
- [107] Z. Li, C. Maldonado, T.H. North, B. Altshuller, "Mechanical and Metallurgical Properties of MMC Friction Welds", *Welding Journal*, **76(9)** (1997) 367s-373s.
- [108] V.K. Lebedev, I.A. Chernenko, "Friction Welding", *Sov. Tech. Rev. C. Weld. Surf.*, **4** (1992) 59-168.
- [109] M. W. Mahoney, C.C. Bampton, "Fundamentals of Diffusion Bonding", *Welding, Brazing and Soldering ASM Handbook Vol. 6*, (ASM, Materials Park, Ohio 1995), pp. 156-159.
- [110] American Welding Society (AWS), *Welding Handbook Vol. 2*, (AWS, Miami, Florida 1989), pp. 814-837.
- [111] N. F. Kazakov, *Diffusion Bonding of Materials*, (Mir Publishers, MoscowRussia, 1999), pp. 1-304.
- [112] S. B. Dunkerton, "Procedure Development and Practice Considerations for Diffusion

- Welding", *Welding, Brazing and Soldering ASM Handbook Vol. 6*, (ASM, Materials Park, Ohio 1995), pp. 883-887.
- [113] J. Pilling, "The Kinetics of Isostatic Diffusion Bonding in Superplastic Materials", *Materials Science and Engineering*, **100** (1988) 137-144
- [114] C. L. Cline, "An Analytical and Experimental Study of Diffusion Bonding", *Welding Journal*, **45** (1966) 481-489.
- [115] A. Hill, E.R. Wallach, "Modelling Solid-State Diffusion Bonding", *Acta Metall.*, **37**(9) (1989) 2425-2437.
- [116] M.M. Schwartz, *Joining of Composite-Matrix Materials*, (ASM, Materials Park, Ohio 1995) pp. 1-182.
- [117] F.L. Matthews, R.D. Rawlings, *Composite Materials: Engineering and Science*, (Ed. CRC Press, Boca Raton, Florida 1999), pp. 1-465.
- [118] A. Hirose, Y. Matsuhiro, M. Kotoh, S. Fukumoto, K.F. Kobayashi, "Laser Beam Welding of SiC Fibre-Reinforced Ti-6Al-4V Composite", *Journal of Materials Science*, **28**(2) (1993) 349-355.
- [119] S. Fukumoto, A. Hirose, K.F. Kobayashi, "Application of Laser Beam Welding to Joining of Continuous Fibre-Reinforced Composite to Metal", *Materials Science and Technology*, **9**(3) (1993) 264-271.
- [120] C.A. Blue, S.G. Warriar, M.T. Robson, R.Y. Lin, "Rapid Infrared Joining Takes on the Advanced Materials", *Welding Journal*, **72**(6) (1993) 51-54.
- [121] C.A. Blue, R.A. Blue, R.Y. Lin, J.-F. Lei, W.D. Williams, "Joining of SCS-6/Beta 21S Titanium Composite", *Processing of Advanced Materials*, **4**(2) (1994) 105-110.
- [122] TWI Report N° 530, "Bonding of SiC Fibre Reinforced Ti-6Al-4V MMC Sheet by Resistance Heating", TWI 530/December (1995).
- [123] T. Mohandas, V.K. Karma, V.V. Kutumbarao, D. Banerjee, "Low Cycle of Fatigue Behaviour of Electron Beam and Friction Welded Joints of an  $\alpha+\beta$  Titanium Alloy", *Scripta Materialia*, **35** (2) (1996) pp. 187-192.
- [124] D. Sun, Z. Ren, Z. Zhou, T. North, Y. Zhai, S. Sathian, "Microstructural Features of Friction-Welded Ti-6Al-4V Joint", *Journal of Materials Science and Technology*, **16** (1) (2000), pp. 59-62.
- [125] P.L Threadgill, "Developments in Solid State Welding of Titanium" in: Proceedings of the Non Aerospace Applications of Titanium symposium presented at the 1998 TMS Annual Meeting, San Antonio, USA (Ed. F.H. Froes, P.G Allen, M.Niinomi, The Minerals, Metals and Materials Society, Warrendale, PA: 1998).

- [126] F. Torster, J.F. dos Santos, G. Hutt, M. Koçak, "Metallurgical and Mechanical Properties of Radial Friction Welded Ti-6Al-4V-0.1Ru Risers" in: Proceedings of the 17<sup>th</sup> International Conference on Offshore Mechanics and Arctic Engineering - OMAE 1998, Lisbon, Portugal. (ASME, New York, NY, 1998).
- [127] E.D. Nicholas, "Radial Friction Wleding", *Welding Journal*, **62**(7) (1983) 17-29.
- [128] F. Torster, J.F. dos Santos, G. Hutt, M. Koçak, "Mechanical Properties of Ti-6Al-4V-0.1Ru Riser Pipes Joined by Radial Friction Welding " in: Proceedings of the Non Aerospace Applications of Titanium symposium presented at the 1998 TMS Annual Meeting, San Antonio, USA (Ed. F.H. Froes, P.G Allen, M.Niinomi, The Minerals, Metals and Materials Society, Warrendale, PA: 1998).
- [129] J. Ruge, K. Thomas, C. Eckel and S. Sundaresan "Joining of Copper to Titanium by Friction Welding", *Welding Journal*, **65**(8) (1986) 28-31.
- [130] A. Fuji, M. Kimura, K. Ameyama, M. Aki "Mechanical Properties of Titanium-5083 Aluminium Alloy Friction Joints", *Materials Science and Technology*, **13**(8) (1997) pp.673-678.
- [131] A. Fuji, T.H. North, M. Kimura, K. Ameyama, "Effect of Friction Welding on Characteristics of Pure Titanium/A5083 Aluminum Alloy Joint", *Materials Science Research International*, **1**(3) (1995) pp. 188-192.
- [132] M. Futamata, A. Fuji "Friction Welding of Titanium and SUS 304L Austenitic Stainless Steel", *Welding International*, **4**(10) (1990) pp.768-774.
- [133] M. Futamata, T.H. North, K. Ameyama, A. Fuji, "Improving Tensile Strength and Bend Ductility of Titanium/AISI 304L Stainless Steel Friction Welds", *Materials Science and Technology*, **8**(3) (1992) pp.219-234.
- [134] F. Sassani, J.R. Neelam, "Friction Welding of Incompatible Materials", *Welding Journal*, **67**(11) (1988) 264s-270s.
- [135] A. Hasui, Y. Kira, "Friction Welding of Titanium and Plain Carbon Steel", *Quarterly Journal of the Japan Welding Society*, **1**(3) (1983) 64-69.
- [136] G. Hutt, "Titanium Dynamic Riser Systems", *Titanium World*, **2**(4) (1995), pp.25-27.
- [137] W.A. Baeslack III, T.F. Broderick, M. Juhas, H.L. Fraser, "Characterization of Solid-Phase Welds Between Ti-6Al-2Sn-4Zr-2Mo-0.1Si and Ti-13.5Al-21.5Nb Titanium Aluminide", *Materials Characterization*, **33** (1994) pp. 357-367.
- [138] O.T. Midling, O. Grong, M. Camping, "A First Report on the Microstructure Integrity and Mechanical Performance of Friction Welded Al-SiC Composites" in: Proceedings of the 12<sup>th</sup> Riso International Symposium on Materials Science, Riso International Laboratory,

Denmark, 1991, pp. 529-534.

[139] M.J. Cola and W A. Baeslack, "Inertia Friction Welding of a Particulate-Reinforced Aluminium-Matrix Composite" in: Proceedings of the 3<sup>rd</sup> International SAMPE Conference, Toronto, Canada, M424, 3.

[140] T.H. North, "Friction Joining of Particle-Reinforced Composites" in: Proceedings of the 5<sup>th</sup> International Symposium of the Japanese Welding Society, Nagoya, Japan, JWS, 1996, pp. 673-682.

[141] C. Pan, J. Hu, Z. Li, T.H. North, "TEM Observation of the Microstructural Features of Dissimilar 6061 MMC/AISI 304 Stainless Steel Friction Joints", *Journal of Materials Science*, 1996, **31**, pp. 3667-3674.

[142] A.A.M. da Silva, A. Meyer, J.F. dos Santos, C.E.F. Kwietniewski, T.R. Strohaecker, "Mechanical and Metallurgical Properties of Friction Welded TiC Particulate Reinforced Ti-6Al-4V", *Composites Science and Technology*, in press, 2004.

[143] A.A.M. da Silva, T.R. Strohaecker, J.F. dos Santos, A. Meyer, C.E.F. Kwietniewski, S. Abkowitz, "Friction Welding of a Titanium Matrix Composite Ti-6Al-4V+10%TiC" In: Proceedings of the 6th International Conference on Trends in Welding Research, 2002, Pine Mountain, United States, 2002, p. 334-336.

[144] A.A.M. da Silva, C.E.F. Kwietniewski, J.F. dos Santos, A. Meyer, S. Abkowitz, T.R. Strohaecker, "Friction Welding of a Titanium Matrix Composite Ti-6Al-4V+10%TiV" In: Sub-Commission IX NF "Weldability of Non-Ferrous Materials", Geesthacht, Germany. IIW IX-2044-02, 2002.

[145] A.A.M. da Silva, A. Meyer, J.F. dos Santos, S. Abkowitz, T.R. Strohaecker, "Properties of Friction Welded TiC Particulate Reinforced Ti-6Al-4V+10%TiC Metal Matrix Composite" In: IX International Conference on Composites Engineering, 2002, San Diego, United States. 2002, p.151 – 152.

[146] S. Fukomoto, A. Hirose, K.F. Kobayashi, "Diffusion Bonding of SiC/Ti-6Al-4V Composite to Ti-6Al-4V Alloy and Fracture Behaviour of Joint", *Materials Science and Technology*, **9**(6) (1993) 520-527.

[147] A. Hirose, M. Kotoh, S. Fukomoto, K.F. Kobayashi, "Diffusion Bonding of SiC fibre Reinforced Ti-6Al-4V Alloy", *Materials Science and Technology*, **8**(9) (1992) 811-815.

[148] A.A.M da Silva, J.F. dos Santos, T.R Strohaecker, A. Reguly, "Properties of Diffusion Bonded TiC Particulate Reinforced Ti-6Al-4V Metal Matrix Composite", Proceedings of the 10<sup>th</sup> World Conference on Titanium, Hamburg, Germany (Ed. G. Lutjering DGM) July 2003.

[149] A.A.M da Silva, J.F. dos Santos, T.R Strohaecker, A. Reguly, "A Study on the

Structure/Property Relationships of Diffusion Bonded TiC-Particulate Reinforced Ti-6Al-4V Metal Matrix Composite”, *Science and Technology of Welding and Joining*, (2004), to be published.

[150] A.A.M da Silva, J.F. dos Santos, T.R Strohaecker, “Properties and Fracture Analysis of Diffusion Bonded TiC Particulate Reinforced Ti-6Al-4V Metal Matrix Composite”, Proceedings of the 11<sup>th</sup> European Conference on Composites Materials, Rhodes, Greece (Ed.) June 2004.

[151] A. B. Tomkings, R.M. Cotgrove, "Joining of Advanced Inorganic Structural Materials", Final Report ERA Report 96-0139R, ERA Technology Limited, Surrey, England, 1996, 1-126.

[152] T. Onzawa, A. Suzumura, J.-H. Kim, K. Takagami, "Joining Titanium-Matrix Composites Reinforced with SiC-CVD Fibre", *Welding International*, **6**(9) (1992) 707-712.

[153] G. Çam, H. Clemens, R. Gerling, M. Koçak, "Diffusion Bonding of Fine Grained  $\gamma$ -TiAl Sheet", *Z. Metallkd.*, **90** (1999) pp. 284-286.

[154] G. Çam, J. Müllauer, M. Koçak, "Diffusion Bonding of Two Phase  $\gamma$ -TiAl Alloys with Duplex Microstructure", *Science and Technology of Welding and Joining*, **2** (1997) pp. 213-219.

[155] G. Çam, K.-H. Bohm, J. Müllauer, M. Koçak, "Microstructural Development During Diffusion Bonding of  $\gamma$ -TiAl" in: Proceedings of the International Welding Technology '96 Symposium, Istanbul, Turkey, 1996, pp. 25-35.

[156] G. Çam, K.-H. Bohm, J. Müllauer, M. Koçak, "The Fracture Behavior of Diffusion-Bonded Duplex Gamma TiAl", *The Journal of The Minerals, Metals and Materials Society*, **48**(11) (1996) 66-68.

[157] G. Çam, H. Clemens, R. Gerling, M. Koçak, "Diffusion Bonding of  $\gamma$ -TiAl Sheets", *Intermetallics*, **7** (1999) pp. 1025-1031.

[158] G. Çam, R. Gerling, K.-H. Bohm, M. Koçak, "Diffusion Bonding of Rolled  $\gamma$ -TiAl-Alloys", GKSS Report: GKSS 98/E/29 (1998).

[159] G. Çam, M. Koçak, "Diffusion Bonding of Investment Cast  $\gamma$ -TiAl", *Journal of Materials Science*, **34** (1999) pp. 3345-3354.

[160] J. Pilling, N. Ridley, M.F. Islam, “On the Modelling of Diffusion Bonding in Materials: Superplastic Super Alpha-2”, *Materials Science and Engineering A*, **A205** (1996) pp. 72-78.

[161] M. Holmquist, V. Recina, B. Pettersson, "Tensile and Creep Properties of Diffusion

- Bonded Titanium Alloy IMI 834 to Gamma Titanium Aluminide IHI Alloy 01A", *Acta Materialia*, **47** (6) (1999) pp. 1791-1799.
- [162] M. Holmquist, V. Recina, J. Ockborn, B. Pettersson, E. Zumalde, "Hot Isostatic Diffusion Bonding of Titanium Alloy Ti-6Al-4V to Gamma Titanium Aluminide IHI Alloy 01A", *Scripta Materialia*, **39** (8) (1998) pp. 1101-1106.
- [163] P. He, J.C. Feng, B.G. Zhang, Y.Y. Qian, "A New Technology for Diffusion Bonding Intermetallic TiAl to Steel with Composite Barrier Layers", *Materials Characterization*, **50** (2003) pp. 878-92.
- [164] G. Çam, D. Dobi, M. Koçak, L. Heikinheimo, M. Sirén, "Characterization of the Diffusion Bonded Interface Between Ti and Al", GKSS Internal Report, GKSS 95/E/23, Geesthacht, Germany, 1995.
- [165] N. Orhan, T. I. Khan, M. Eroglu, "Diffusion Bonding of a Microduplex Stainless Steel to Ti-6Al-4V", *Scripta Materialia*, **45** (2001) pp. 441-446.
- [166] M. Koçak, M. Pakdil, G. Çam, "Fracture Behaviour of Diffusion Bonded Titanium Alloys with Strength Mismatch", *Science and Technology of Welding and Joining*, **7**(4) (2002) pp. 187-196.
- [167] M.F. Islam, M.O. Alam, "Interface Characteristics of Isostatic Diffusion Welding Between Dissimilar Titanium Alloys", Proceedings of the Symposium by Reactive Metals Committee of the Light Metals Division of TMS 1997 Materials Week, Indianapolis, USA, 14 to 18/09 1997.
- [168] M. Ghosh, K. Bhanumurthy, G.B. Kale, J. Krishnan, S. Chatterjee, "Diffusion Bonding of Titanium to 304 Stainless Steel", *Journal of Nuclear Materials*, **322** (2003) pp. 235-241.
- [169] M. Ghosh, S. Chatterjee, B. Mishra, "The Effect of Intermetallics on the Strength Properties of Diffusion Bonds Formed Between Ti-5.5Al-2.4V and 304 Stainless Steel", *Materials Science and Engineering A*, **A363** (2003) pp. 268-274.
- [170] M. Ghosh, S. Chatterjee, "Diffusion Bonded Transition Joints of Titanium to Stainless Steel With Improved Properties", *Materials Science and Engineering A*, **A358** (2003) pp. 152-158.
- [171] A. Ureña, J.M. Gómez de Salazar, M.D. Escalera, "Diffusion Bonding of an Aluminium-Copper Alloy Reinforced with Silicon Carbide Particles (AA2014/SiC/13p) using Metallic Interlayers", *Scripta Materialia*, **35**(11) (1996) pp. 1285-1293.
- [172] C.S. Lee, H. Li, R.S. Chandel, "Vacuum-free Diffusion Bonding of Aluminium Metal-Matrix Composite", *Journal of Materials Processing Technology*, **89-90** (1999) pp. 326-330.

- [173] C.S. Lee, H. Li, R.S. Chandel, "Stimulation Model for the Vacuum-free Diffusion Bonding of Aluminium Metal-Matrix Composite", *Journal of Materials Processing Technology*, **89-90** (1999) pp. 344-349.
- [174] X.-P Zhang, L. Ye, Y.-W. Mai, G.-F Quan, W. Wei, "Investigation on Diffusion Bonding Characteristics of SiC Particulate Reinforced Aluminium Metal Matrix Composites (Al/SiC<sub>p</sub>-MMC), *Composites: Part A*, **30** (1999) pp. 1415-1421.
- [175] D. H. Phillips, "Selection and Weldability of Advanced Titanium-Base Alloys", *Welding, Brazing and Soldering ASM Handbook Vol. 6*, (ASM, Materials Park, Ohio 1995), pp. 524-527.
- [176] ASTM E 3-95 "Standard Practice for Preparation of Metallographic Specimens", *Annual Book of ASTM Standards Vol 03.03*, (ASTM, Philadelphia, 2000), pp.1-8.
- [177] ASTM E 340-95 "Standard Test Method for Macroetching Metals and Alloys", *Annual Book of ASTM Standards Vol 03.03*, (ASTM, Philadelphia, 2000), pp.385-395.
- [178] Image C for Windows User Guide.
- [179] Leica QWin User Guide – Image Processing and Analysis System, vols. 1 and 2. Leica Imaging Systems Ltda. 1996.
- [180] J.L. Hubbard, "Microscopy and Image Analysis", *Materials Characterization ASM Handbook Vol.10*, (ASM, Materials Park, Ohio 1996), pp. 225-230.
- [181] ASTM E 112-96 "Standard Test Methods for Determining Average Grain Size", *Annual Book of ASTM Standards Vol 03.03*, (ASTM, Philadelphia, 2000), pp.240-263.
- [182] ASTM E 384-99 "Standard test method for Microindentation Hardness Materials", *Annual Book of ASTM Standards Vol 03.03*, (ASTM, Philadelphia, 2000), pp.406-429.
- [183] ASTM E 8M-00a "Standard Test Methods for Tension Testing of Metallic Materials (Metric)", *Annual Book of ASTM Standards Vol 03.03*, (ASTM, Philadelphia, 2000), pp.56-76.
- [184] EN 10002-1 "Tensile Testing of Metallic Materials - Method of Test at Ambient Temperature", (CEN - European Committee for Standardization, Brussels, 1991), pp.1-19.
- [185] ASTM E 21-92 "Standard Test Methods for Elevated Temperatures Tension Tests of Metallic Materials", *Annual Book of ASTM Standards Vol 03.03*, (ASTM, Philadelphia, 2000), pp.130-137.
- [186] EN 10002-5 "Tensile Testing of Metallic Materials - Method of Test at Elevated Temperature", (CEN - European Committee for Standardization, Brussels, 1992), pp.1-18.
- [187] G. Çam, S. Riekehr, M. Koçak, "Determination of Mechanical Properties of Laser Welded Joints with Microtensile Specimens" in: ASM International European Conference on

- Welding and Joining Science and Technology, Madrid, Spain, (ASM International, 1998).
- [188] ASTM E 399-90 "Standard Test Method for Plain-Strain Fracture Toughness of Metallic Materials", *Annual Book of ASTM Standards Vol 03.03*, (ASTM, Philadelphia, 2000), pp.431-461.
- [189] EFAM GTP 94 "The GKSS Test Procedure for Determining the Fracture Behaviour of Materials", GKSS Internal Report: GKSS 94/E/60, (1994).
- [190] S. Ranganath, "A Review on Particulate-Reinforced Titanium Matrix Composites", *Journal of Materials Science*, **32** (1997) pp. 1-16.
- [191] C. Badini, G. Ubertalli, D. Puppò, P. Fino, "High Temperature Behaviour of a Ti-6Al-4V/TiCp Composite Processed by BE-CIP-HIP Method", *Journal of Materials Science*, **35** (2000) pp. 3903-3912.
- [192] "Processing of Metal-Matrix Composites", *Composites ASM Handbook Vol. 21*, (ASM, Materials Park, Ohio 1995), pp. 579-588.
- [193] *Materials Properties Handbook: Titanium Alloys* (Ed. R.R. Boyer, G. Welsch, E.W. Collings, ASM, Materials Park, Ohio 1994), pp. 1141.
- [194] A. Razaghian, D. Yu, T. Chandra, "Fracture Behaviour of a SiC-Particle-Reinforced Aluminium Alloy at High Temperature", *Composites Science and Technology*, **58** (1998), 293-298.
- [195] J. Segurado, C. González, J. Llorca, "A Numerical Investigation of the Effect of Particle Clustering on the Mechanical Properties of Composites", *Acta Materialia*, **51** (2003) pp. 2355-2369.
- [196] V. de Castro, T. Leguey, M.A. Monge, A. Muñoz, R. Pareja, M. Victoria., "Discontinuously Reinforced Titanium Matrix Composites for Fusion Applications", *Journal of Nuclear Materials*, **307-311** (2002) pp. 691-695.
- [197] L. Mishnaevski Jr, K. Derrien, D. Baptiste, "Effect of Microstructure of Particle Reinforced Composites on the Damage Evolution: Probabilistic and Numerical Analysis", *Composites Science and Technology*, (2004) in press.
- [198] Y. Brechet, J.D. Embury, S. Tao, L. Luo, "Damage Initiation in Metal Matrix Composites", *Acta Metallurgica et Materialia*, 1991, **39**(8), pp. 1781-1786.
- [199] J. Llorca and C. Gonzalez, "Microstructural Factors Controlling the Strength and Ductility of Particle-Reinforced Metal-Matrix Composites", *Journal of Mechanics and Physics of the Solids*, 1998, **46**, pp. 1-28.
- [200] H. Berns, C. Broeckmann, A. Fischer, D. Weichert, "Influence of Second Phase Particles to the Fracture Toughness of Hard Metallic Materials", *Localized Damage II – Vol.*



- I: Fatigue and Fracture Mechanics*, Eds. M.H. Aliabadi, D.J. Cartwright, H. Nisitani. Computational Mechanics Publications, 1989, pp. 473-485.
- [201] T.W. Clyne, “An Introductory Overview of MMC Systems, Types, and Developments” in: *Comprehensive Composite Materials – Volume 3*, Eds. A. Kelly, C. Zweben, T.W. Clyne, Elsevier Science Ltd., Oxford, UK, 2000, p. 22.
- [202] J.D. Boyd and D.J. Lloyd, “Clustering in Particulate MMCs”, in: *Comprehensive Composite Materials – Volume 3*, Eds. A. Kelly, C. Zweben, T.W. Clyne, Elsevier Science Ltd., Oxford, UK, 2000, p. 147.
- [203] J.J. Lewandowski, “Fracture and Fatigue of Particulate MMCs”, in: *Comprehensive Composite Materials – Volume 3*, Eds. A. Kelly, C. Zweben, T.W. Clyne, Elsevier Science Ltd., Oxford, UK, 2000, p. 166.
- [204] T.J.A. Doel, P. Bowen, "Effect of Particle Size and Matrix Aging Condition on Toughness of Particle Reinforced Aluminium Based Metal Matrix Composites“, *Materials Science and Technology*, 1996, **12**, pp. 586-594.
- [205] V.G. Voinov, “Mechanisms of Joint Formation in Friction Welding”, *Welding Production*, **15** (1968) pp. 8-13.
- [206] ASM Committee on Metallography of Titanium and Titanium Alloys “Microstructure of Titanium and Titanium Alloys”, *Titanium and Titanium Alloys* (Ed. M. J. Donachie Jr., ASM, Materials Park, Ohio 1982), pp. 33-44.
- [207] H.E. Exner, "Scanning Electron Microscopy", *Metallography and Microstructures ASM Handbook Vol.9*, (ASM, Materials Park, Ohio 1995), pp. 89-102.
- [208] ISO/TTA 2 “Tensile Tests for Discontinuously Reinforced Metal Matrix Composites at Ambient Temperatures”, Standard – Technology Trends Assessment, (1997) pp. i – 16.
- [209] A.C.C Insfran, “Microstructural and Fracture Toughness Evaluation of Power Beam Welded C – Mn Steels”, PhD Thesis, Hamburg, 1999 (Technischen Universität Hamburg Harburg, Hamburg, Germany 1999).
- [210] G.T. Hahn, A.R. Rosenfield, “Metallurgical Factors Affecting Fracture Toughness of Aluminum Alloys”, *Metallurgical Transactions A*, 1976, **6A**, pp. 653-670.

## LIST OF FIGURES

Figure 2.1 - Examples of reinforcements in composites. (a) Continuous reinforcement (fibres). (b) Discontinuous reinforcement (whiskers). (c) Discontinuous reinforcement (particulate) [35].	11
Figure 2.2 – Schematic representation of the different stages in the CHIP process [5,39].	14
Figure 2.3 - Ti6Al4V and Ti6Al4V+10%TiC elastic modulus vs. temperature [14].	17
Figure 2.4 – Equilibrium Ti-C binary phase diagram [53].	20
Figure 2.5 – Fracture process in ductile metals. (a) Inclusions in a ductile matrix (like ceramic reinforcements in a ductile matrix). (b) Void nucleation according to the correspondent void initiation mechanism. (c) Void growth. (d) Strain localization between the voids. (e) Necking between the voids. (f) Void coalescence and fracture. [66]	21
Figure 2.6 – Schematic representation illustrating the fracture mechanics model for estimating the strain to failure of a composite.	23
Figure 2.7 –Crack initiation/propagation during tensile failure of MMCs. (a) Void formation in high hydrostatic tension regions. (b) Void coalescence by ductile tearing. (c) Failure. [69]	23
Figure 2.8 – Mechanism of microcracks linking in front of the main crack by void growth [76].	24
Figure 2.9 - Ti6Al4V+20% TiC fracture toughness temperature dependence [43].	25
Figure 2.10 – Metal surface under normal atmospheric conditions [82].	27
Figure 2.11 - Basic steps in the friction welding process [84,86].	28
Figure 2.12 – Characteristics of the direct drive friction welding parameters [87].	29
Figure 2.13 - Characteristics of the inertia friction welding parameters [87].	30
Figure 2.14 - Schematic illustration of plastified material concentration (green areas indicate concentration – 0.5 to 0.7 of the radius) during rubbing stage after different rubbing durations [100]. Outer part shows oxidation due to heating; while the inner region shows unaffected surface (machining marks)	33
Figure 2.15 - Schematic illustration of the friction surfaces during heating phase [100]. Plastified ring area extends initially towards the rotational centre and then to the outer regions.	33
Figure 2.16 - Friction welding parameters and phase division [91].	34
Figure 2.17 - Schematic representation showing the effect of the welding parameters on the HAZ shape and width. (A) Rotational speed and (B) pressure [84].	36
Figure 2.18 - Metallurgical stages sequence in the bonding process. (a) Initial contact: limited to a few asperities. (b) Stage I: deformation of surface asperities by plastic flow and creep, a thinner oxide layer with large voids results. (c) Stage II: grain boundary diffusion of atoms to voids and grain boundary migration. (d) Stage III: volume diffusion of atoms to the voids [109].	40
Figure 2.19 - Paths of material transfer generated during the bonding process. (a) Surface mechanisms. (b) Interface mechanisms. (c) Bulk deformation mechanisms [109,115].	42

Figure 2.20 - Dynamic recrystallisation process in the vicinity of the original interface between two materials being welded using pressure at temperatures above $0.4 T_{MPabsolute}$ . Grain refinement is observed at the centre region. [88] .....	50
Figure 2.21 - Relation between bonding conditions and joint tensile properties. (a) Bonding pressure ( $T= 1143^{\circ}C$ and $t= 5minutes$ ). (b) Bonding temperature ( $P= 12MPa$ , $t= 5minutes$ ) [152]. .....	52
Figure 3.1 - Experimental procedure flow chart. ....	53
Figure 3.2 - HMS 3000 friction welding machine. ....	55
Figure 3.3 - Friction welding system used to perform the friction welding process. ....	55
Figure 3.4 - Configuration of the studs (dimensions in mm) for the friction welding process. ....	56
Figure 3.5 - Flowchart showing the procedure used to investigate the initial parameter matrix.....	57
Figure 3.6 - Diffusion bonding equipment and experimental setup of the diffusion bonding process used in this investigation. ....	58
Figure 3.7 – Configuration of the diffusion bonding specimens. ....	59
Figure 3.8 - Convex hull perimeter used during the mean Ferret diameter measurements [180]. ....	62
Figure 3.9 – Location of the tensile specimen in the friction welding specimens.....	64
Figure 3.10 - Geometry of the tensile specimens used to investigate the tensile properties for the friction welding process (dimensions in mm). ....	64
Figure 3.11 - Equipment utilized to perform the tensile tests at room temperature. (a) General view. (b) Detail of specimen positioning and extensometer. ....	65
Figure 3.12 - Equipment utilized to perform the tensile tests at high temperature. (a) General view. (b) Detail of specimen positioning. ....	65
Figure 3.13 - Schematic representation of the extraction of the microflat tensile specimens. ....	66
Figure 3.14 - Microflat tensile testing machine and laser extensometer. ....	66
Figure 3.15 - SENB specimens for fracture toughness testing (dimensions in mm).....	67
Figure 3.16 – Fracture toughness testing notch positions. (a) Base material. (b) FW joint centre.....	67
Figure 3.17 - Optical microscopes utilized to monitor fatigue precrack growth and experimental setup to open the fatigue precracks. ....	68
Figure 4.1 – Particle distribution of the CHIP-processed Ti6Al4V+10 wt.% TiC composite. OM.....	69
Figure 4.2- Base material (Ti6Al4V+10 wt.% of TiC) microstructure. SEM.....	70
Figure 4.3 - Schematic representation of platelike $\alpha$ and intergranular $\beta$ formation in a Ti6Al4V alloy by slow cooling from above the $\beta$ transus temperature [23]. ....	71
Figure 4.4 - Position of the different points at the composite for the EDS analysis. SEM. ....	72
Figure 4.5 –Chemical composition profile analysed by EDS (line indicated by the arrow). SEM.....	72
Figure 4.6 – SEM high magnification micrograph showing no evidence of interaction between the TiC particle and the Ti6Al4V matrix. ....	73
Figure 4.7 - Micrographs used to investigate the base material particle characteristics. ....	73
Figure 4.8 –Mean Ferret diameter distribution of the base material condition. ....	74

Figure 4.9 –Nearest neighbour distance distribution of the base material condition. ....	75
Figure 4.10 - Hardness variation due to the TiC particles presence. (a) base material, 352 HV0.3; (b) base material + TiC particles, 413 HV0.3 and (c) TiC particle, 551 HV0.3. ....	76
Figure 4.11 – Hardness distribution of the base material (Ti6Al4V+10 wt.% TiC). ....	76
Figure 4.12 – SEM micrographs taken from the base material fracture surface. ....	78
Figure 4.13 - Tensile behaviour according to different testing temperatures (base material zone). ....	80
Figure 4.14 - SEM micrographs taken from the fracture surfaces of the tensile specimens tested at 200°C. PF: Particle fracture. SC: Secondary cracking. DF: Ductile fracture. ....	81
Figure 4.15 - SEM micrographs taken from the fracture surfaces of the tensile specimens tested at 375°C. PF: Particle fracture. SC: Secondary cracking. DF: Ductile fracture. ....	81
Figure 4.16 – SEM micrographs showing the location of the notches in the fracture toughness specimens of the friction welding conditions. (a) DM12-6 (3000 rpm/136 MPa). (b) DM 15-7 (3000 rpm/272 MPa). (c) DM16-4 (4500 rpm/272 MPa). ....	82
Figure 4.17 – Fracture toughness behaviour of the Ti6Al4V+10 wt.% TiC base material. ....	84
Figure 4.18 – SEM micrographs showing the crack path geometry of the base material. Etched. ....	84
Figure 4.19 – Example of preferable crack path due to poor reinforcement distribution. ....	85
Figure 4.20 – Influence of the plastic zone size on the fracture toughness behaviour of particulate reinforced composites. (a) Small plastic zone size (few or no particles inside). (b) Large plastic zone size (large amount of particles inside) [69]. ....	87
Figure 4.21 - SEM micrographs taken from the fracture surfaces of the base material. ....	88
Figure 4.22 – Welding process diagrams. (a) Condition DM 08: friction pressure 136MPa; forging pressure 544MPa; rotational speed 4500rpm; burn-off 3mm. (b) Condition DM 16-2: friction pressure 272MPa; forging pressure 408MPa; rotational speed 4500rpm; burn-off 2mm. ....	89
Figure 4.23 - Initial parameter matrix of the Ti6Al4V + 10 wt.% of TiC alloy friction welding. ....	90
Figure 4.24 – Secondary parameter matrix of the Ti6Al4V + 10 wt.% of TiC friction welding. Two friction welding parameters have been held constant (forging pressure 408 MPa and burn-off 2mm), while two have been varied (friction pressure and rotational speed). ....	91
Figure 4.25 – Friction welding macrostructure (BM, HAZ and TRZ). (a) DM11 (1500 rpm/136 MPa), (b) DM12 (3000 rpm/136 MPa), (c) DM13 (4500 rpm/136 MPa), (d) DM14 (1500 rpm/272 MPa), (e) DM15 (3000 rpm/272 MPa) and (f) DM16 (4500 rpm/272 MPa). Etch. OM. ....	91
Figure 4.26 – Influence of rotational speed over the friction welded area. ....	93
Figure 4.27 – Influence of friction pressure versus the friction welded area. ....	94
Figure 4.28 – SEM micrographs of the HAZ microstructure – Widmanstätten $\alpha$ (acicular $\alpha$ ) and intergranular $\beta$ with TiC particles. ....	95

Figure 4.29 – Transition zone between HAZ and BM. Widmanstätten $\alpha$ and intergranular $\beta$ (HAZ) as well as platelike $\alpha$ and intergranular $\beta$ (BM) with TiC particles. (a) DM12 (3000 rpm/136 MPa). (b) DM11 (1500 rpm/136 MPa). (c) DM12. (d) DM16 (4500 rpm/272 MPa). .....	95
Figure 4.30 – SEM micrographs taken from TRZ. (a) DM11 (1500 rpm/136 MPa); (b) DM12 (3000 rpm/136 MPa); (c) DM13 (4500 rpm/136 MPa); (d) DM14 (1500 rpm/272 MPa); (e) DM15 (3000 rpm/272 MPa); (f) DM16 (4500 rpm/272 MPa). .....	98
Figure 4.31 – SEM micrograph showing small TiC particles. DM13 (4500 rpm/136 MPa). Etch.....	99
Figure 4.32 – EDS analysis at the particles found in the TRZ region. (a) DM11 (1500 rpm/136 MPa) and (b) DM12 (3000 rpm/136 MPa). .....	101
Figure 4.33 – EDS analysis in TRZ. (a) DM12. (b) DM14.....	102
Figure 4.34 Examples of micrographs used to investigate the particle characteristics of the friction welding joints. (a) DM12 (3000 rpm/136 Mpa). (b) DM13 (4500 rpm/136 Mpa). OM.....	103
Figure 4.35 – Mean Ferret diameter distribution according to friction welding rotational speed.....	105
Figure 4.36 – Mean Ferret diameter distribution according to friction welding pressure.....	105
Figure 4.37 – Hardness distribution of all the welded conditions investigated.....	106
Figure 4.38 – Tensile behaviour of the friction welded joints and base material.....	108
Figure 4.39 – Fracture position of the friction welded tensile specimens.....	109
Figure 4.40 –Tensile strength behaviour of the friction welded joints and base material.....	109
Figure 4.41 –SEM micrographs of the longitudinal sections of the fracture surfaces. (a) DM11-2 (1500rpm/136MPa), (b) DM12-3 (3000rpm/136MPa), (c) DM13-2 (4500rpm/136MPa), (d) DM14-3 (1500rpm/272MPa), (e) DM15-2 (3000rpm/272MPa), (f) DM16-2 (4500rpm/272MPa). .....	110
Figure 4.42 – Secondary electron micrographs taken the friction welded joints fracture surfaces. (a) DM11 (1500 rpm/136 MPa), (b) DM12 (3000 rpm/136 MPa), (c) DM13 (4500 rpm/136 MPa), (d) DM14 (1500 rpm/272 MPa),(e) DM15 (3000 rpm/272 MPa), (f) DM16 (4500 rpm/272 MPa). .....	113
Figure 4.43 – SEM micrographs showing the fracture surfaces and longitudinal sections from the different regions in the friction welded conditions. (a) Base material. (b) HAZ. (c) TRZ.....	115
Figure 4.44 – Fracture toughness behaviour of the friction welded joints.....	116
Figure 4.45 – SEM micrographs showing the crack path geometry of the friction welded joints. (a) DM13 (4500 rpm/136 MPa). (b) DM14 (1500 rpm/272 MPa). .....	116
Figure 4.46 – Crack path behaviour of condition DM13. (a) Before fatigue precracking. (b) After fatigue precracking. (c) to (f) After initiation of the fracture toughness testing. Plastic zone as well as crack path are inside the friction welded region.....	118
Figure 4.47 – Crack path deviation in the welded joints. (a) DM11-5. (b) DM14-7. (c) DM16-4. ....	119
Figure 4.48 – Crack tip plasticity behaviour. (a) homogeneous and (b) mismatched materials. ....	119
Figure 4.49 – Crack path behaviour of condition DM14. (a) Before fatigue precracking. (b) After fatigue precracking. (c) to (f) After initiation of the fracture toughness testing. Plastic zone as well as crack path are inside different regions (TRZ, HAZ and base material). .....	120

Figure 4.50 – Comparison between tested and calculated $K_{IC}$ values.....	124
Figure 4.51 – Micrographs showing the sequence of the image analysis performed in condition DM12-4 (3000 rpm/136 MPa and $K_{IC}$ value of 36.33 MPa*m <sup>1/2</sup> ). (a) SEM micrograph showing the area analysed. (b) and (c) Micrographs presenting the particles identified by the software.....	125
Figure 4.52 – SEM micrographs from the fracture surfaces of the welded joints. (a) DM11 (1500 rpm/136MPa). (b) DM12 (3000rpm/136MPa). (c) DM13 (4500rpm/136MPa). (d) DM14 (1500 rpm/272MPa). (e) DM16 (4500rpm/272MPa). DM15 is not shown (notches in base material). .....	128
Figure 4.53 – Diffusion bonding temperature and pressure cycle for all investigated conditions. (a) DB1 (875°C/5 MPa/60 min). (b) DB2 (900°C/5 MPa/35 min). (c) DB3 (900°C/6 MPa/35 min). (d) DB4 (900°C/7 MPa/60 min). (e) DB5 (1000°C/5 MPa/35 min). (f) DB6 (900°C/6 MPa/60 min).....	130
Figure 4.54 – SEM micrographs showing the bonded conditions. (a) DB1 (875°C/5MPa/60min). (b) DB2 (900°C/5MPa/35min). (c) DB3 (900°C/6MPa/35min). (d) DB4 (900°C/7MPa/60min). (e) DB5 (1000°C/5MPa/35min). (f) DB6 (1000°C/5MPa/60min). .....	133
Figure 4.55 – Particle/particle contact at the joint. Condition DB5 (1000°C/5MPa/35 min).....	134
Figure 4.56 – Microhardness profiles of the diffusion bonding conditions (DB4, DB5 and DB6). ...	135
Figure 4.57 – Tensile strength behavior of the diffusion bonding and base material conditions.....	136
Figure 4.58 –Tensile strength values of all diffusion bonding and base material specimens. ....	136
Figure 4.59 – Comparison between standard tensile testing and microflat tensile testing.....	137
Figure 4.60 – SEM micrographs taken from the fracture surface of the base material specimens. ....	138
Figure 4.61 – SEM micrographs from the microflat tensile fracture surfaces of the bonded joints. (a) DB5 (1000°C/5MPa/35min). (b) DB6 (1000°C/5MPa/60min). PF: Particle fracture. SC: Secondary cracking. DF: Ductile fracture.....	138
Figure 4.62 – SEM micrographs from the microflat tensile fracture surfaces of condition DB4 (900°C/7MPa/60min.). PF: Particle fracture. SC: Secondary cracking. FS: Flat surface (fracture along the bonding line).....	139

## LIST OF TABLES

Table 2.1 - Tensile data for various microstructural conditions [26].	9
Table 2.2 - High- and room-temperature tensile tests results for the Ti6Al4V matrix alloy and the reinforced Ti6Al4V + 10% TiC alloy [40].	15
Table 2.3 - Mechanical properties comparison of Ti6Al4V, Ti6Al4V+10%TiC and Ti6Al4V+20%TiC alloys [5,14,39,40].	17
Table 2.4 – Comparison between the process parameters of the direct drive friction welding system relative to the inertia friction welding system [84,91].	30
Table 2.5 - Qualitative rating for joining adaptability, applications and selection of different joining processes (solid state welding and fusion welding processes) [36].	46
Table 3.1 - As-received base material chemical composition.	54
Table 3.2 - Friction welding parameters of initial matrix.	57
Table 3.3 - Secondary matrix of the friction welding parameters. All conditions have been welded with a forging pressure of 408 MPa and a burn-off of 2 mm.	58
Table 3.4 - Diffusion bonding parameters.	60
Table 4.1 - Results of the EDS analysis in six different points of the composite.	72
Table 4.2 - Mean Ferret diameter results of the base material.	74
Table 4.3 – Tensile properties of the base material.	77
Table 4.4 - Tensile test results at high temperature (200°C) for the base material composite.	80
Table 4.5 – Tensile test results at high temperature (375°C) for the base material composite.	80
Table 4.6 - Notch location according to the different friction welding zones in the fracture toughness specimens.	83
Table 4.7 – Results of fracture toughness of the base material (Ti6Al4V + 10 wt.% TiC).	83
Table 4.8 – Area of the friction welded joints.	93
Table 4.9 – Results from the EDS analysis at the particles found in the TRZ region.	101
Table 4.10 – ASTM Beta grain size determination for all the investigated friction welding conditions in the weld centre and close to the HAZ region.	103
Table 4.11 – Results for the shape factor of the friction welding conditions investigated.	104
Table 4.12 – Results for the mean Ferret diameter of the friction welding conditions.	104
Table 4.13 – Area fraction of the TiC particles after the friction welding process.	105
Table 4.14 – Individual particle area determination for all the welded conditions.	106
Table 4.15 – Results of the tensile tests performed in the friction welded conditions.	107
Table 4.16 – Joint efficiency (based on $R_m$ values) presented by the friction welded joints.	108
Table 4.17 – Fracture location of the friction welded tensile specimens.	111
Table 4.18 – Results of fracture toughness of the friction welding and base material conditions.	116
Table 4.19 – Influence of the interparticle spacing on the fracture toughness behaviour.	121

Table 4.20 – Plastic zone size and interparticle spacing of the friction welded joints. .... 121

Table 4.21 – Parameters used to calculate the fracture toughness of the base material and friction welded joints according to the Hahn and Rosenfield model. .... 123

Table 4.22 – Comparison (in % values) of measured and calculated  $K_{IC}$  values. .... 123

Table 4.23 – Parameters used to calculate the  $K_{IC}$  of the base material and welded joints by the Hahn and Rosenfield model according to the image analysis performed close to the crack front..... 124

Table 4.24 – Calculated fracture toughness values of the base material and friction welded joints (Hahn and Rosenfield model) after the image analysis performed close to the crack front..... 126

Table 4.25 – Comparison between measured and calculated  $K_{IC}$  (global and local analysis) values according to the Hahn and Rosenfield model..... 126

Table 4.26 – Microflat tensile results of the base material and bonded conditions as well as the joint efficiency based on  $R_m$ . .... 136



---

**CURRICULUM VITAE – ANTONIO AUGUSTO MONACO DA SILVA**
**Personal Details**


---

Address	Johannes-Ritter-Strasse, 100 21502 Geesthacht
Date and place of birth	07.04.1974 / Porto Alegre, Brazil
Nationality	Brazilian

**University**


---

1993 - 1998	Metallurgical Engineering at the Federal University of Rio Grande do Sul (UFRGS) - Porto Alegre, Brazil
1998 - 2000	Master in Metallurgical Engineering/Materials Science (M.Sc.) in the Post-Graduation Program in Metallurgical, Mining and Materials Engineering (PPGEM/UFRGS) – Porto Alegre, Brazil

**Professional / research experience**


---

Sept. 1994 – Mar. 1998	Research Assistant in the Laboratório de Metalurgia Física (LAMEF/UFRGS), Porto Alegre, Brazil
Mar. 1998 – May 1998	Trainee in Aços Finos Piratini – Grupo Gerdau, Charqueadas, Brazil.
Aug. 1998 – Dec. 2000	M.Sc. student in the Laboratório de Metalurgia Física (LAMEF/UFRGS), Porto Alegre, Brazil
Mar. 2001 – Mar. 2003	Engineer for research and development in the Institute for Materials Research (Joining Technology group) of GKSS Forschungszentrum Geesthacht GmbH.
Mar. 2003 – June 2003	Engineer for research and development in the Laboratório de Metalurgia Física (LAMEF/UFRGS), Porto Alegre, Brazil
July 2003 - today	Engineer for research and development in the Institute for Materials Research (Joining Technology group) of GKSS Forschungszentrum Geesthacht GmbH.